16CTAP-C098306-02

나노압입을 이용한 구조용 강재 용접부의 미세구조 파악 및 정량적 건전성 지표 개발 연구 최종보고서

2017

국토교통부

Infrastructure R&D Report

보안 과제( ), 일반 과제(○) / 공개(○), 비공개( )
국토교통기술촉진연구사업 제2차 연도 최종보고서

R&D / 16CTAP-C098306-02

나노압입을 이용한 구조용 강재 용접부의 미세구조 파악 및 정량적 건전성 지표 개발 연구 최종보고서

2017. 07. 23.

주관연구기관 / 세종대학교 산학협력단
위탁연구기관 / 경남대학교 산학협력단

국 토 교 통 부
(전문기관) 국토교통과학기술진흥원

제 출 문

국토교통부장관(국토교통과학기술진흥원장) 귀하

'나노압입을 이용한 구조용 강재 용접부의 미세구조 파악 및 정량적 건전성 지표 개발 연구'(연구개발 기간 : 2015.06.24 ~ 2017.06.23) 과제의 최종보고서 10부를 제출합니다.

2017. 07. 23.

주관연구기관명 : 세종대학교 산학협력단 (김선재) (인)

주관연구기관책임자 : 김승억

국토교통부소관 연구개발사업 운영규정 제38조에 따라 최종보고서 열람에 동의합니다.

보고서 요약서

<table>
<tr><td>과제고유번호</td><td>16CTAP-C098306-02</td><td>해 당 단 계
연 구 기 간</td><td>2016.06.24
-
2017.06.23</td><td>단 계 구 분</td><td>2차년도 /
2차년도</td></tr>
<tr><td rowspan="2">연 구 사 업 명</td><td>중사업명</td><td colspan="4">국토교통기술촉진연구사업</td></tr>
<tr><td>세부사업명</td><td colspan="4">국토교통기술촉진연구사업</td></tr>
<tr><td rowspan="2">연 구 과 제 명</td><td>대과제명</td><td colspan="4">국토교통기술촉진연구사업</td></tr>
<tr><td>세부과제명</td><td colspan="4">나노압입을 이용한 구조용 강재 용접부의 미세구조 파악 및 정량적 건전성 지표 개발 연구</td></tr>
<tr><td rowspan="2">연 구 책 임 자</td><td rowspan="2">김승억</td><td>해 당 단 계 참 여 연 구 원 수</td><td>총: 17명
내부: 3명
외부: 14명</td><td>해 당 단 계 연 구 개 발 비</td><td>정부 : 200,000천원
기업 : 천원
정부 외 : 천원
계 : 200,000천원</td></tr>
<tr><td>총 연 구 기 간 참 여 연 구 원 수</td><td>총: 16명
내부: 3명
외부: 13명</td><td>총연구개발비</td><td>정부 : 200,000천원
기업 : 천원
정부 외 : 천원
계 : 200,000천원</td></tr>
<tr><td>연 구 기 관 명 및
소 속 부 서 명</td><td colspan="3">세종대학교 산학협력단</td><td>참 여 기 업 명</td><td></td></tr>
<tr><td>국제공동연구</td><td colspan="3">상대국명 :</td><td colspan="2">상대국 연구기관명 :</td></tr>
<tr><td>위 탁 연 구</td><td colspan="3">연구기관명 : 경남대학교 산학협력단</td><td colspan="2">연구책임자 : 김정중</td></tr>
<tr><td colspan="4">요약</td><td>보고서 면수</td><td>151</td></tr>
</table>

■ 연구목표 : 피로도와 잔류응력을 고려한 용접연결부의 건전성을 정량적으로 검증할 수 있는 건전성 지표 개발

1. 나노압입에 의한 구조용 강재 용접부의 미세구조 구성성분비 파악 기법 개발
- 기존 나노압입 분석방법 연구
- 나노압입에 의한 미세구조와 SEM 촬영사진에 의한 미세구조 분석 : SS400, SM490 강재로 용접부 제작, 나노압입 실험 및 SEM촬영, 사전 조사된 기존의 분석 방법으로 결과 분석, 나노압입과 SEM 촬영결과로부터 강재 미세구조의 구성비 결정
- 용접열에 의한 용접부 열 영향지역의 미세구조 변화 연구

2. 나노압입에 의한 구조용 강재의 탄성계수, 항복응력, 경화지수 도출 기법 개발
- 유한요소모형 개발, 강재의 기계적 성질을 이용하여 검증
- 구조용 강재의 나노압입 결과로부터 항복강도와 경화지수 산정을 위한 알고리즘 개발

3. 구조용 강재의 잔류응력에 따른 강재 미세구조의 특성변화 파악
- 잔류응력 도입장치 개발
- 인장과 압축 각각 다섯가지 등급의 잔류응력을 가진 SS400, SM490 강재에 대하여 나노압입 수행 후 미세구조의 구성성분비, 탄성계수, 항복강도, 경화지수 산출

4. 구조용 강재 용접부의 피로도에 따른 강재 미세구조의 특성변화 파악

- 용접부를 포함한 SS400, SM490 강재에 대한 세 가지 단계의 피로도에 대하여 피로실험 수행 후 시편의 인장강도 측정
- 용접 연결부 (WM, HAZ, BM)에 나노압입 수행 후 구성성분비, 탄성계수, 항복강도, 경화지수 산출

5. 피로도와 잔류응력을 고려한 용접연결부의 정량적 건전성 지표 개발

- 실험결과들을 정리하여 잔류응력과 피로도에 따른 강재와 용접부 미세구조의 특성변화 분석
- 피로와 열에 의한 손상에 의한 용접부의 건전성을 정량화 할 수 있는 지표를 개발

〈 요약문 〉

연구의 목적 및 내용	■ 본 연구의 최종목표는 피로도와 잔류응력을 고려한 용접연결부의 건전성을 정량적으로 검증할 수 있는 건전성 지표를 개발하는 것임 ■ 본 연구의 연차별 목표는 다음과 같음 - 1차년도 : 나노압입에 의한 구조용 강재의 미세구조 및 기계적 성질 도출기법 개발 - 2차년도 : 피로도와 잔류응력에 따른 미세구조 파악 및 용접연결부의 정량적 건전성 지표 개발 본 연구의 연도별 연구내용 및 범위는 다음과 같이 요약할 수 있다. ■ 나노압입에 의한 구조용 강재 용접부의 미세구조 구성성분비 파악기법 개발 - 기존 나노압입 분석방법 연구 - 세라믹의 미세구조 분석법 (미국 MIT) 벤치마킹 - 구조용강 용접부에 적용 - 미세구조 구성성분비 도출 - SEM, 광학현미경 촬영 사진과 화학성분비 분석으로 결과 검증 ■ 나노압입에 의한 구조용 강재의 탄성계수, 항복응력, 경화지수 도출기법 개발 - 기존 나노압입 분석방법 연구 - 유한요소해석과 차원해석에 의한 기법 (미국 U. of Michigan) 벤치마킹 - 구조용강에 대한 유한요소해석과 차원해석 수행-산출식 결정 - 구조용강 SS400, SM490 용접부에 적용 - 항복응력, 경화지수 결정 - 인장실험 결과와 비교하여 산출식 검증 ■ 구조용 강재의 잔류응력에 따른 강재 미세구조의 특성변화 파악 - 잔류응력 도입장치 개발 및 검증 - 나노압입 실험 : 잔류응력이 도입된 강재의 미세구조 구성성분비 도출 - 항복응력, 경화지수 결정 - 기존 연구와 결과 검증 - 잔류응력과 미세구조 구성성분비, 기계적 성질간의 관계 정립 ■ 구조용 강재 용접부의 피로상태에 따른 강재 미세구조의 특성변화 파악 - 용접부를 포함한 SS400, SM490 강재의 피로실험 - 나노압입 실험 : 피로실험된 용접부의 미세구조 구성성분비 도출 - 피로실험된 용접부의 항복응력, 경화지수 결정 - 인장실험으로 결과 검증 - 피로도와 미세구조 구성성분비, 기계적 성질간의 관계 정립 ■ 피로도와 잔류응력을 고려한 용접연결부의 정량적 건전성 지표 개발 - 잔류응력과 피로도에 따른 나노압입 결과의 확률적 분석 - 피로도와 잔류응력을 고려한 용접부 건전도 지수 결정

연구개발성과	■ 본 연구를 통해 4편의 SCI급 논문 및 2건의 특허를 출원함 ✓ 1차년도 - (논문) 나노압입에 의한 구조용 강재 용접부의 미세구조 구성성분비 파악 기법 - (논문) 나노압입에 의한 구조용 강재의 탄성계수, 항복응력, 경화지수 도출 기법 ✓ 2차년도 - (특허, 논문) 구조용 강재의 잔류응력에 따른 강재 미세구조의 특성변화 파악 - (특허) 구조용 강재 용접부 피로도에 따른 강재 미세구조의 특성변화 파악 - (논문) 피로도와 잔류응력을 고려한 용접연결부의 정량적 건전성 지표 개발
연구개발성과의 활용계획 (기대효과)	■ 기술적 기대효과 - 나노기술을 활용하여 용접부의 탄소성 성질을 산정하는 방법을 결정 - 구조용 강재의 잔류응력에 따른 미세구조의 특성변화를 파악하여, 잔류응력 측정기술 확보 - 구조용 강재 용접연결부의 피로도에 따른 미세구조의 특성변화를 파악하여, 용접부 피로도 측정기술 확보 - 강구조 용접부의 응력집중 현상과 연계하여 용접 연결부의 건전성을 확인할 수 있는 비파괴 검사 기술 개발 - 강구조 용접부의 건전성 평가에 대해 기존 선진국 기술과 대등한 위치를 확보하여 보다 정확하고 합리적인 안전 및 유지관리 기술 확보 ■ 경제적 · 산업적 기대효과 - 비파괴 검사 장비를 개발하여 저렴하게 용접연결부의 안전성 평가 - 효율적인 용접연결부의 건전성 평가를 통해 강구조물의 재해 및 붕괴에 따른 인명과 경제적 손실 예방 - 나노기술을 이용한 강구조 용접부의 비파괴 검사 장비를 개발하여 수출 가능

핵심어 (5개 이내)	나노압입	용접부	구조용 강재	미세구조	피로

〈 SUMMARY 〉

Purpose & Contents	■ A goal of this research is to develop quantitatively verifiable soundness index as to soundness of weld joints that considering fatigue and residual stress. ■ The yearly research goal is summarized as follows: - 1st year : Development of technique of obtaining mechanical property and microstructure in structural steel using nanoindentation - 2nd year : Development of quantitative soundness index of weld joints and microstructure based on fatigue and residual stress The yearly research contents are summarized as follows: ■ Recognition technique of microstructure composition in structural steel weld zone using nanoindentation - Research of previous nanoindentation analysis method - Benchmarking of microstructure analysis method of ceramic - Application of structural steel weld zone - Elicitation of composition of microstructure - Result verification based on the chemical composition analysis and photographs of SEM ■ Elicitation techniques of elastic modulus, yield stress, hardening index of structural steel weld zone using nanoindentation - Research of previous nanoindentation analysis method - Benchmarking of technique by FEM and dimensional analysis - FEM and dimensional analysis for structural steel : Decision of calculation formula - Decision of yield stress and hardening index - Verification of formular as compared with results of tensile test ■ Change of characteristics in structural steel microstructure by residual stress - Develope and verification of residual stress introduction system - Nanoindentation test : Elicitation of microstructure composition in structural steel using residual stress - Decision of yield stress and hardening index - Result verification of previous research - Arrangement of relationship of mechanical property, microstructure composition and residual stress ■ Change of characteristics in structural steel microstructure based on structural steel weld zone - Fatigue test of SS400, SM490 structural material containing weld zone

	- Nanoindentation test : Elicitation of microstructure composition in weld zone based on fatigue test - Decision of yield stress and hardening index in weld zone based on fatigue test - Result verification based on tensile test - Arrangement of relationships of mechanical property, microstructure composition and fatigue ■ Development of quantitative soundness index in weld joints considering fatigue and residual stress - Probabilistic analysis of nanoindentation test based on fatigue and residual stress - Decision of soundness index in weld zone considering fatigue and residual stress
Results	■ 4 SCI journal papers, 2 patent applications ✓ First year - (Journal) Technique to grasp the microstructure component ratio of welded part of structural steel by nano indentation - (Journal) Derivation technique of the elastic modulus, yield stress, hardening accelerator of steel in nano indentation structure ✓ Second year - (Patent, Journal) Characteristic change identification of steel microstructure by residual stress of structural steel - (Patent) Characteristi change identification of steel microstructure in fatigue of structural steel weld - (Journal) Development of quantitative soundness index of weld connection considering fatigue and residual stress
Expected Contribution	■ Technical contributions - Decision of method to determine the elastic and plastic properties in weld zone using nanotechnology - Development of measurement technology of residual stress by realizing change of characteristics in microstructure based on residual stress of structural steel - Development of measurement technology of weld zone fatigue by realizing change of characteristics in microstructure based on fatigue stress of structural steel - Development of non-destructive testing technology that can check into soundness of weld joints - Acquisition of accurate and resonable maintenance technology about soundness of steel structure weld zone ■ Economic · Industrial contributions - Economical safety evaluation of weld joints by developing non-destructive testing equipment - prevention of life and economic loss resulting from failure of

	steel structure through effective soundness evaluation of weld joints - Exportation of equipment as developing non-destructive testing equipment of steel structure weld zone using nanoindentation				
Keywords	Nanoindentation	Weld Zone	Structural Steel	Microstructure	Fatigue

〈 CONTENTS 〉

Chapter 1. INTRODUCTION ····· 13

Section 1. Purpose ····· 13

1. Background ····· 13

2. Nanoindentation ····· 14

Section 2. Need ····· 15

Section 3. Scope ····· 15

1. Stage ····· 15

2. Goal ····· 16

Chapter 2. Status of domestic and overseas technology development ····· 29

Section 1. Research trends and academic achievements in related fields ····· 29

1. National Research and Development Project ····· 29

2. Research Trends and Academic Flow Analysis in Domestic and Foreign Related Fields ····· 30

Section 2. Patent Trends Related to Domestic and Foreign ····· 30

Section 3. Domestic and overseas market analysis and industry trend ····· 32

Section 4. Concluding Remarks ····· 33

Chapter 3. Research performance and achievements ····· 34

Section 1. Detailed contents of research results ····· 34

1. Flow chart ····· 34

2. Details of research by research and development stage ····· 35

Section 2. Contents of step-by-step research ····· 37

1. Major Research Contents ····· 37

Chapter 4. Achievement of goal and contribution to relevant field ····· 61

Section 1. Goal Achievement ····· 61

1. Research performance targets and performance indicators ····· 61

2. Achievement of research and development goal ····· 64

Section 2. Contribution of related field ····· 67

1. Core Achievements ····· 67

Chapter 5. Plan to utilize R & D achievements ····· 69

Section 1. Use of research results ····· 69

Section 2. Benefit ····· 71

1. Technical aspects ····· 71
2. Economic and industrial aspects ····· 71
3. Social aspect ····· 71
Chapter 6. Overseas science and technology information collected during the research process ····· 72
Section 1. Nano indentation data analysis ····· 72
1. Nano indentation overseas journals data analysis ····· 72
2. Nano indentation development status analysis ····· 73
Chapter 7. Security rating of R & D achievement ····· 74
Section 1. Classification of Security Classes ····· 74
Section 2. Reason for decision ····· 74
Chapter 8. Status of research facilities and equipment registered in the National Science and Technology Comprehensive Information System ····· 75
Chapter 9. Implementation of safety measures in laboratories due to R & D tasks ····· 76
Section 1. Laboratory safety measures implementation plan ····· 76
1. Laboratory safety inspection system and implementation ····· 76
2. Education training ····· 76
Section 2. Research facilities and import declaration status ····· 77
Chapter 10. Representative research achievements of R & D tasks ····· 78
Chapter 11. Others ····· 80
Chapter 12. References ····· 81
Appendix ····· 82

〈 목 차 〉

제1장. 연구개발과제의 개요 ····· 13

1절. 연구개발 목적 ····· 13

1. 연구개발의 배경 ····· 13

2. 나노압입(Nanoindentation) ····· 14

2절. 연구개발의 필요성 ····· 15

3절. 연구개발 범위 ····· 15

1. 연구개발 단계 ····· 15

2. 연구개발 목표 ····· 16

제2장. 국내외 기술 개발 현황 ····· 29

1절. 관련 분야의 국내외 연구동향 및 학술적 성과 ····· 29

1. 국가 연구개발사업 유사연구 실적 ····· 29

2. 관련분야의 국내외 연구동향 및 학술적 흐름 분석 ····· 30

2절. 국내외 관련 기술 특허 동향 ····· 30

3절. 국내외 시장분석 및 산업동향 ····· 32

4절. 종합결론 ····· 33

제3장. 연구 수행 내용 및 성과 ····· 34

1절. 연구성과별 세부추진내용 ····· 34

1. 연구개발 흐름도 ····· 34

2. 연구개발 단계에 따른 세부연구내용 ····· 35

2절. 단계별 연구수행 내용 ····· 37

1. 주요 연구내용 ····· 37

제4장. 목표 달성도 및 관련 분야 기여도 ····· 61

1절. 목표 달성도 ····· 61

1. 연구 성과목표 및 성과지표 ····· 61

2. 연구개발 목표 달성도 ····· 64

2절. 관련 분야 기여도 ····· 67

1. 연구개발 핵심성과 ····· 67

제5장. 연구개발성과의 활용 계획 ····· 69

1절. 연구결과의 활용방안 ····· 69

2절. 기대효과 ····· 71

1. 기술적 측면 ····· 71
2. 경제적 · 산업적 측면 ····· 71
3. 사회적 측면 ····· 71
제6장. 연구 과정에서 수집한 해외 과학기술 정보 ····· 72
1절. 나노압입 자료 분석 ····· 72
1. 나노압입 해외 학술지 자료 분석 ····· 72
2. 나노압입 개발 현황 분석 ····· 73
제7장. 연구개발성과의 보안등급 ····· 74
1절. 보안등급의 분류 ····· 74
2절. 결정사유 ····· 74
제8장. 국가과학기술종합정보시스템에 등록한 연구시설 · 장비 현황 ····· 75
제9장. 연구개발과제 수행에 따른 연구실 등의 안전 조치 이행 실적 ····· 76
1절. 연구실 안전조치 이행계획 ····· 76
1. 연구실 안전 점검 체계 및 실시 ····· 76
2. 교육 훈련 ····· 76
2절. 연구시설 및 수입신고 현황 ····· 77
제10장. 연구개발과제의 대표적 연구 실적 ····· 78
제11장. 기타 사항 ····· 80
제12장. 참고 문헌 ····· 81
부록 ····· 82

제1장. 연구개발과제의 개요

1절. 연구개발 목적

1. 연구개발의 배경

- 본 연구에서는 강구조물 연결부와 주변 응력 집중부의 비파괴 검사 장비 개발에 필요한 원천기술의 확보를 목적으로 나노압입 방법을 이용한 강구조 용접 연결부의 기계적 특성 산출방안을 연구하고자 함
- 그림 1과 같이 강구조물의 붕괴는 대형 인명 피해와 재산 피해를 동반함. 강구조물의 붕괴는 응력집중이 높은 연결부와 연결부 부근의 파괴에서 비롯되므로, 연결부와 주변 응력 집중 예상 부재에 대한 검사와 유지관리는 강구조물의 사용 기간에 걸쳐 지속적으로 이루어져야 함



그림 1. 강구조물의 붕괴

- 강재의 연결에 있어 용접은 볼팅에 의한 방법보다 활용성과 경제성이 높아 강구조물의 건설에 많이 사용되고 있으나 용접부는 일반적으로 강구조물에서 가장 취약한 부분임. 이는 용접부의 용접 결함, 재료의 불균질 그리고 용접열에 의한 강재의 구성성분 변화에 대한 정보가 부족하기 때문임
- 일반적으로 용접부는 그림 2와 같이 용접모재 (Weld Metal, WM), 열영향지역 (Heat Affected Zone, HAZ), 모재 (Base Metal,BM)로 구분할 수 있음

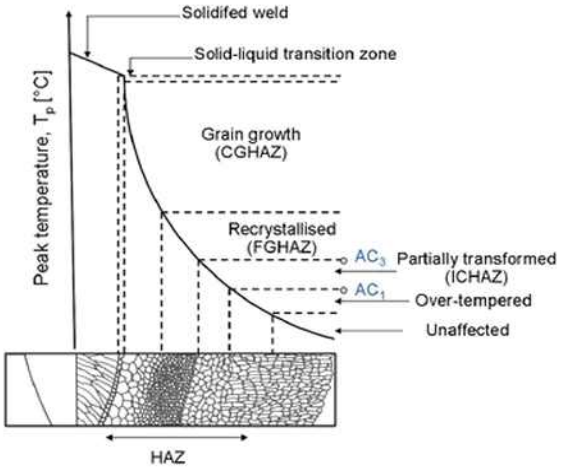


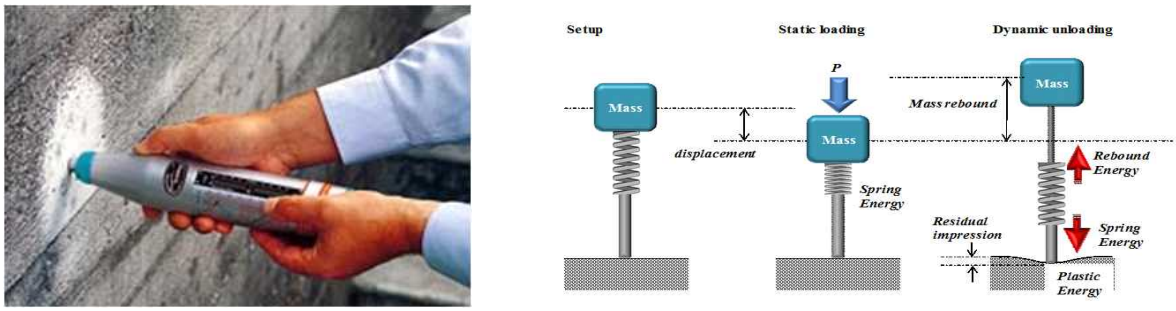
그림 2. 용접부의 구분

- 용접열에 의해 영향을 받는 강재부위는 열에 의해 그 구성성분이 변화하며 구성성분의 변화는 강재의 기계적 성질, 즉, 탄성계수, 경도, 항복강도의 변화를 발생시킴
- 용접열에 의해 영향을 받는 영역 (HAZ)에 대한 구조용 강재의 기계적 성질은 현재까지 파악되지 않고 있으며, 강구조의 설계에도 반영되어 있지 않음

- 이러한 설계상의 불확실성은 향후 강구조물 붕괴의 원인이 될 수도 있으므로, 설계상의 불확실성을 제거할 수 있는 원천기술의 개발이 필요함

2. 나노압입 (Nanoindentation)

- 표면경도를 이용하여 재료의 기계적 성질을 규명하는 기법을 압입(Indentation) 기법이라고 함
- 건설 분야에서 우리에게 가장 친숙한 압입기법은 그림 3과 같은 슈미트 햄머를 이용하여 콘크리트의 강도를 측정하는 것임. 슈미트 햄머를 이용한 압입기법은 동적인 하중을 재하하여 표면경도와 강도사이의 관계를 이용하여 강도를 측정하는 방법임



(a) (b)

그림 3. (a) 슈미트 햄머를 이용한 강도측정과 (b) 측정원리

- 그림 4에 나타낸 나노압입 기법은 Sub-micron 범위에서 기계적 실험의 다른 방법과 비교했을 때 매우 작은 흔적만 남기는 비파괴 검사법이며, 나노압입의 결과를 분석하여 재료의 탄성계수, 경도, 항복강도, 경화계수를 산정할 수 있음
- 따라서 구조용 강재에 대해 강재를 구성하는 미세구조인 페리트(ferrite), 펄라이트(pearlite), 시멘타이트(cementite)의 탄성계수, 항복강도 등을 산출할 수 있으며, 이러한 결과를 분석하여 미세구조의 구성성분비를 도출할 수 있음

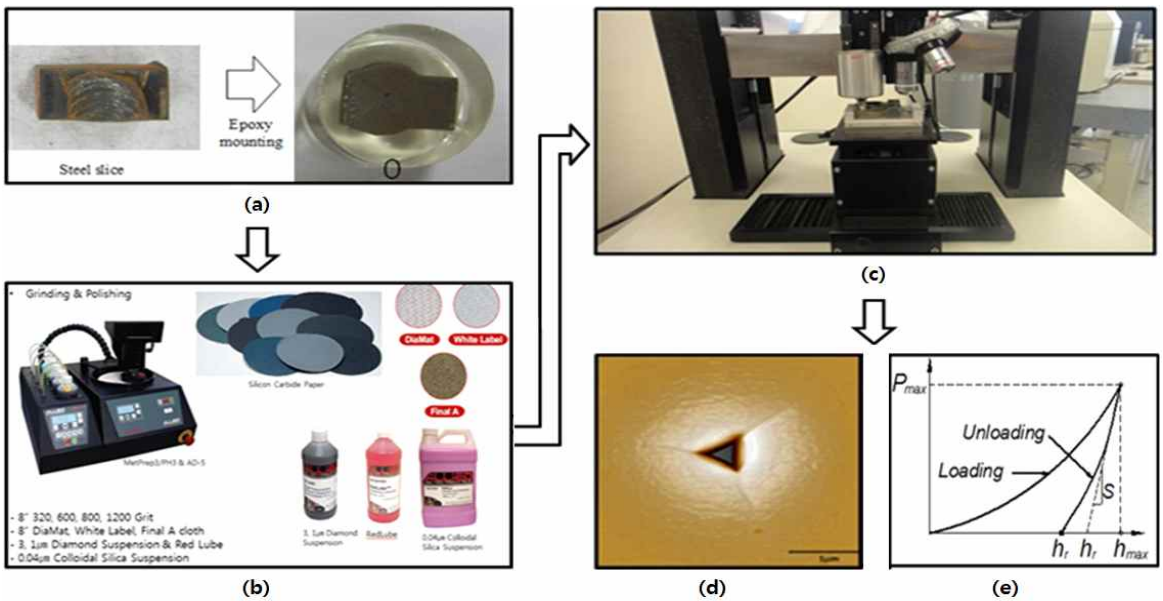


그림 4. 나노압입 기법 (a) 샘플 준비 (b) 샘플 연마 (c) 나노압입 시험 (d) 압흔 (e) P-h 곡선 도출

2절. 연구개발의 필요성

- 나노압입기술은 재료의 기계적 물성치를 측정하기 위한 방법의 하나로 측정의 간편함과 시편 준비의 편리함 때문에 현재 가장 널리 사용되고 있음
- 미소소재 즉, 특성 길이가 1μm 이하인 주조물은 인장시험용 시편을 제작하기가 매우 어려움
- 미소소재에 대한 인장 시험용 시편을 만들기 위해서는 MEMS 제작에서 이용되는 미소가공기술을 적용하지만 제작하고자 하는 시편의 크기, 형상, 재료에 따라 많은 노력과 비용을 필요로 함
- 반면 압입기술은 시험 방법이 매우 간단하고 시편 형상에 대한 제약이 거의 없으므로 각종 코팅 소재, 반도체 및 MEMS 등에서 사용되는 미소 소재 등에 활발하게 적용되고 있음
- 나노기술을 이용한 재료의 기계적 성질 산정 기법은 이론적 측면과 실험적 측면에서 검증이 된 단계이므로, 지금이야말로 건설 분야에 사용되는 구조용 강에 대한 기계적 성질 산정에 적합한 나노기술의 원천기술 개발의 최적 시기임
- 향후 강구조 연결부의 응력집중 현상과 연계하여 강구조 연결부의 건전성을 측정 하는 장비개발을 통해 구조물의 진단기술로 확장하고자 함

3절. 연구개발 범위

1. 연구개발 단계

- 본 연구는 기존의 나노압입 기법을 구조용 강재의 용접열에 의한 미세구조 구성성분비 변화를 파악하는 연구에 적용하는 것으로써 공법·기법 유형에 해당함
- 최종적으로 본 연구에서는 피로도와 잔류응력을 고려한 용접연결부의 정량적 건전성 지표 개발을 위해 실험적 연구를 수행할 것으로써 연구개발 단계를 TRL 3으로 설정하였음

구분		표기	단계별 설명
기초연구 단계	TRL 1	☐	
	TRL 2	☐	
실험 단계	TRL 3	☑	
	TRL 4	☐	
시작품 단계	TRL 5	☐	
	TRL 6	☐	
실용화 단계	TRL 7	☐	
	TRL 8	☐	
사업화 단계	TRL 9	☐	

2. 연구개발 목표

가. 최종목표

- 본 연구의 최종목표는 피로도와 잔류응력을 고려한 용접연결부의 건전성을 정략적으로 검증할 수 있는 건전성 지표를 개발하는 것임
  - ✓ 1차년도 : 나노압입에 의한 구조용 강재의 미세구조 및 기계적 성질 도출기법 개발
  - ✓ 2차년도 : 피로도와 잔류응력에 따른 미세구조 파악 및 용접연결부의 정량적 건전성 지표 개발

나. 최종목표의 성격 및 설정근거

- 최종목표의 성격
  - ✓ 본 연구에서는 기 정립된 나노압입 기법의 이론을 바탕으로 나노압입에 의한 구조용 강재 용접부의 탄소성 성질을 도출하는 기법을 개발하며, 피로도와 잔류응력을 고려한 용접연결부의 정량적 건전성 지표 개발을 위해 실험적 연구를 수행하는 실험적 증명 단계에 해당함
- 최종목표의 설정근거
  - ✓ 나노기술의 발전과 더불어 나노압입 기술에 대한 이론적인 검증은 완료된 상태이며 나노압입 기법은 검증된 이론을 바탕으로 이미 다양한 공학 분야에서 재료의 특성치를 파악하기 위한 방법으로 사용되고 있음
  - ✓ 나노압입 기법을 건설분야에 적용하기 위해서는 기존의 나노압입 분석기법을 건설재료의 성질에 맞게 개선하고 검증하여야 함. 따라서 본 연구의 1차년도 최종목표를 기존의 나노압입 분석기법을 구조용 강재의 성질에 맞게 개선하고 검증하는 것으로 설정하였음
  - ✓ 또한 건설분야에 있어서 구조용 강재 용접부의 잔류응력과 피로는 기존의 비파괴 기술로 측정할 수 없음. 나노압입 기법에 의해 기존에 수행할 수 없었던 미세구조의 기계적 특성 분석이 가능하며, Sub-micro크기의 흔적만을 남기는 나노압입 기법을 이용하여 구조용 강재 용접부의 잔류응력과 피로를 측정할 수 있다면, 나노압입 기법을 활용한 강재 용접부의 비파괴 검사 장비의 개발이 가능할 것임
  - ✓ 이러한 활용성에 근거하여 본 연구의 2차년도 최종목표를 구조용 강재 용접부의 잔류응력과 피로도에 따른 강재 미세구조의 특성변화와 이를 고려한 용접부의 건전성 지표 개발로 설정하였음

다. 연차별 연구목표 및 내용

- 연구목표 및 내용

연차	연구목표	주요연구내용
1차년도	• 나노압입에 의한 구조용 강재의 미세구조 및 기계적 성질 도출기법 개발	✓ 나노압입에 의한 구조용 강재 용접부의 미세구조 구성성분비 파악기법 개발 ✓ 나노압입에 의한 구조용 강재의 탄성계수, 항복응력, 경화지수 도출기법 개발
2차년도	• 피로도와 잔류응력에 따른 미세구조 파악 및 용접연결부의 정량적 건전성 지표 개발	✓ 구조용 강재의 잔류응력에 따른 강재 미세구조의 특성변화 파악 ✓ 구조용 강재 용접부의 피로상태에 따른 강재 미세구조의 특성변화 파악 ✓ 피로도와 잔류응력을 고려한 용접연결부의 정량적 건전성 지표 개발

(1) 1차년도 주요 연구내용

■ **나노압입에 의한 구조용 강재 용접부의 미세구조 구성성분비 파악기법 개발**

- 나노압입은 재료의 표면에 압입기(indenter)로 일정한 압입하중까지 압입을 가하고, 다시 하중을 제거하며 압입깊이를 측정하는 것으로써 이로부터 그림 5와 같은 가력(loading)-제력(unloading) 곡선을 얻을 수 있음. 그림에서 x축은 압입깊이이며, y축은 압입하중임
- 나노압입시 재하된 하중에 의하여 강재는 탄성과 소성변형이 함께 일어나는 반면, 하중을 제거할 때는 탄성에 의한 복원만이 이루어지고 소성에 의한 변형은 결과적으로 압입흔적(indentaion residue)으로 남음. 이러한 원리를 이용하여 나노압입에 의한 강재의 탄성계수와 경도를 측정할 수 있음

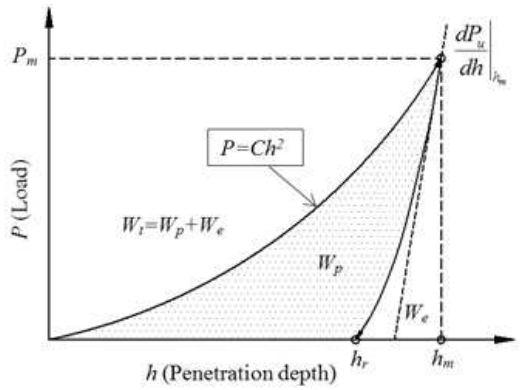
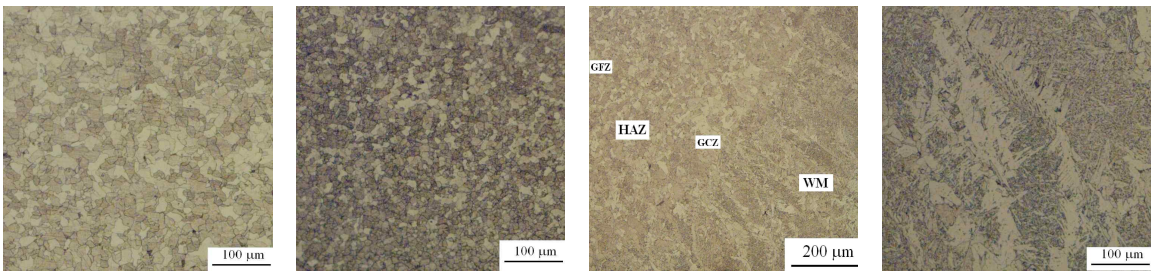


그림 5. 나노압입 가력(Loading)-제력(Unloading) 곡선

- 구조용 강재는 페리트(ferrite), 펄라이트(pearlite), 시멘타이트(cementite)와 같은 미세구조로 구성되며, 강재내 미세구조의 구성성분비는 구조용 강재의 기계적 성질에 가장 큰 영향을 미치기 때문에 미세구조의 구성 성분비를 파악하여 강재의 기계적 성질을 산정할 수 있음
- 나노 크기의 압입을 수행했을 경우 그림 6과 같은 강재의 미세구조 각각에 대한 압입이 수행되어 졌다고 볼 수 있으며 일반적으로 알려진 미세구조의 탄성계수와 경도는 표 1과 같음



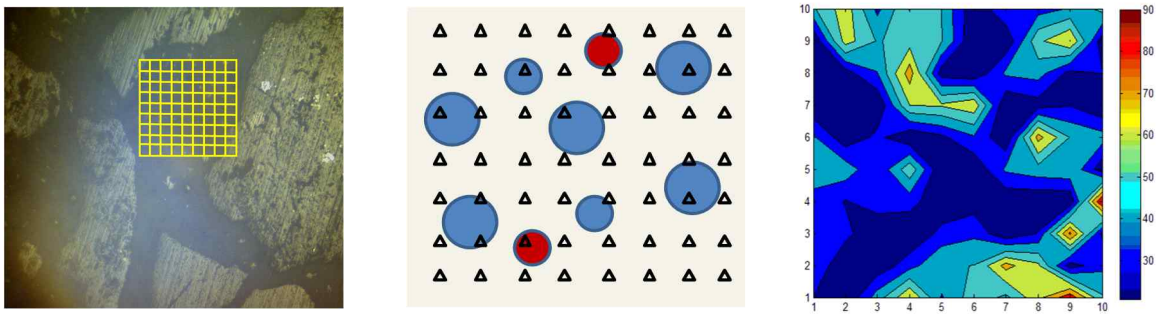
(a) (b) (c) (d)

그림 6. SEM으로 촬영된 미세구조 사진 (a) 일반강재 SS400 (b) 용접열에 의한 변형 (c) 열영향 영역과 용접재 접촉면 (d) 용접재

Properties	ferrite	cementite
탄성계수 (GPa)	177.1 - 234.2	384 - 395
경도 (GPa)	3.75 - 5.85	10.0 - 13.2

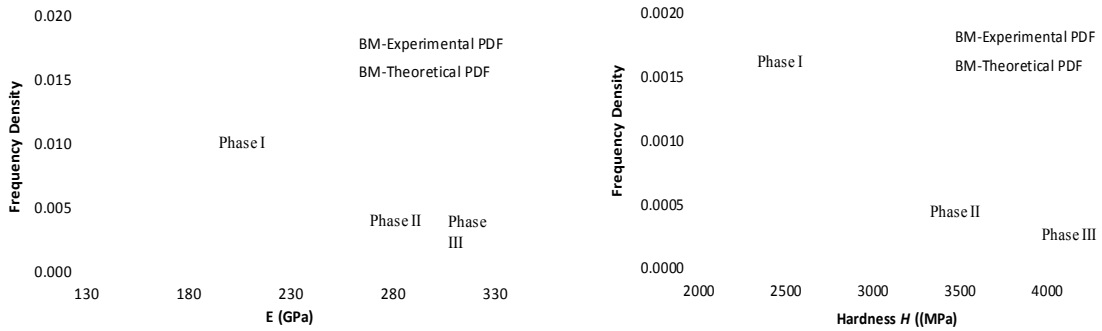
표1. 일반적인 강재 미세구조의 탄성계수와 경도

- 그림 7 (a)와 같이 그리드를 구성하여 100회의 나노압입을 수행하면 100개의 탄성계수와 경도 값들을 얻을 수 있음. 각각의 탄성계수와 경도는 강재 내에 존재하는 다양한 미세구조 중 하나의 특성이라 할 수 있음
- 이를 바탕으로 100개의 탄성계수와 경도 값들을 그림 8 (a)와 (b) 같은 탄성계수와 경도에 따른 빈도함수(frequency function)로 나타낼 수 있음. 이 빈도함수를 정규분포 함수의 합으로 가정하여 분해(deconvolution)하면, 각각의 미세구조의 구성 성분비를 도출할 수 있음



(a) (b) (c)

그림 7. (a) 압입지점 그리드 (b) 예상되는 미세구조 압입 지점
(c) 압입결과에 따른 매핑 (Mapping)



(a) (b)

그림 8. (a) 탄성계수 (b) 경도에 의한 미세구조의 구성비 분석

- 분석결과는 표 2와 같이 미세구조의 구성성분비로 나타나며 이러한 분석결과를 이용하여 그림 7 (c)와 같이 미세구조를 도식화 (mapping) 할 수 있음. 이 기법은 강재내의 잔류응력의 분포를 도식화하는데도 쓰일 수 있음

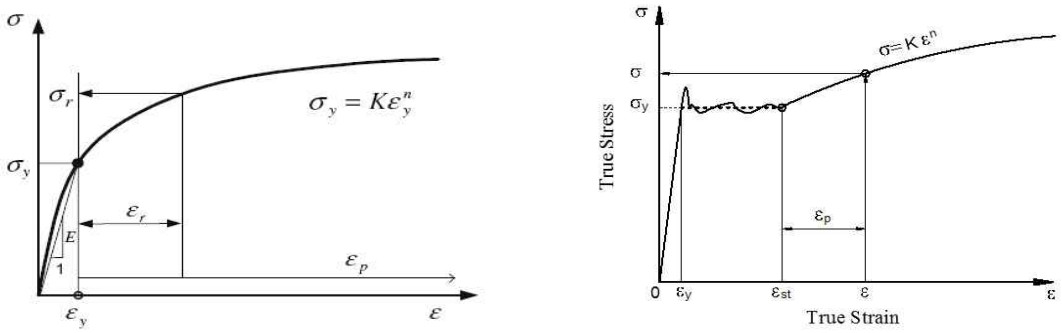
위치	계수	미세구조 1		미세구조 2		미세구조 3	
		탄성계수		경도		탄성계수	
강재	평 균 (GPa)	206	2.49	280	3.48	320	4.1
	편 차 (%)	13	10	4	3	2	3
	구 성 비 (%)	89	90	5	6	6	4

표 2. 강재 미세구조의 구성성분비

- 1차년도 1단계 연구에서는 SS400, SM490 구조용 강재의 용접부의 미세구조 구성성분비를 파악할 것임. 실험체 제작은 다음과 같이 이루어짐. 먼저, 선정된 강재에 대하여 수동 아크 용접 (Manual Metal Arc Welding) 방법을 활용하여 맞대기 용접 (Butt Welding)에 의해 용접부를 생산할 것이며 추가적인 열의 영향을 제거하기 위해 수압절단을 이용하여 나노압입에 필요한 용접부를 포함한 시편을 잘라낼 것임
- 이렇게 잘려진 시편은 일반강재 (Base Metal), 열영향부 (Heat Affected Zone), 용접재 (Weld Metal)을 모두 포함하며 각각의 영역에 나노압입을 수행하여 탄성계수와 경도의 빈도함수로부터 미세구조의 구성성분비를 결정할 것임. 결과를 검증하기 위해 광학현미경과 SEM촬영, 화학 성분검사를 수행할 것임

■ 나노압입에 의한 구조용 강재의 탄성계수, 항복응력, 경화지수 도출기법 개발

- 나노압입에 의해 강재의 소성특성을 파악하는 기존의 방법은 강재의 진응력(true stress)-변형률 선도를 그림 9 (a)와 같이 가정함
- 이러한 응력-변형률 선도는 일반적으로 알루미늄이나 프레스트레싱 텐던의 경우에 해당함. 구조용 강재의 진응력(true stress)-변형률 선도는 그림 9 (b)와 같이 나타나며, 항복 후 일정구간의 완전소성 구간을 가짐



(a) (b)

그림 9. 진응력-변형률 선도 (a) 알루미늄, 프레스트레싱 텐던 (b) 구조용 강재

- 나노압입에 의한 하중 재하시 탄성과 소성변형이 함께 일어나므로, 앞 절의 그림 8 (b)에 보인 나노압입의 가력(loading)곡선 P = Ch2은 재료의 탄성계수, 항복응력, 경화지수 (n)의 함수로 가정할 수 있음. 이들의 관계를 차원해석에 의해 다음과 같은 무차원 함수 Π1으로 표현할 수 있음

$$\frac{E_r}{C} = \Pi_1\left(\frac{E_r}{\sigma_y}, n\right)$$

- 제력(unloading)곡선의 초기 접촉강성 S는 재료의 탄성계수와 압입기와 강재가 접촉하는 면적의 넓이 Ac의 함수이며 접촉면적 Ac는 최대압입깊이와 압입하중의 함수로 재료의 소성 성질과 관련이 있음. 이들의 관계는 차원해석에 의해 다음과 같은 무차원 함수 Π2로 표현할 수 있음

$$\frac{S}{E_r h_m} = \Pi_2\left(\frac{\sigma_y}{E_r}, n\right)$$

- 본 연구실에서는 그림 10과 같은 나노압입 실험에 대한 유한요소 해석모델을 개발하여, 차원해석 결과의 벤치마킹 연구를 수행하였음 (그림 11, 12). 다양한 n값과 Er/σy 값에 대하여 해석을 수행하여 그림 11과 같은 결과를 도출하였음

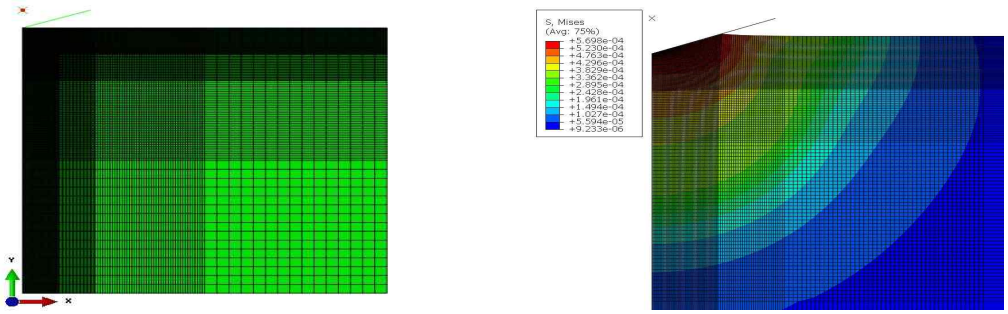
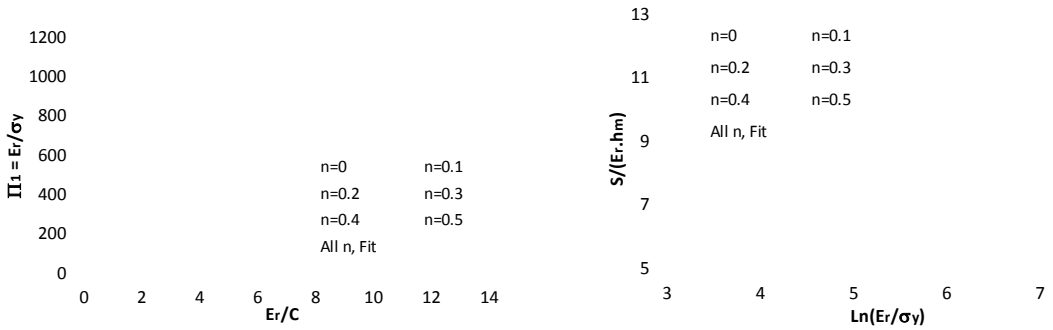


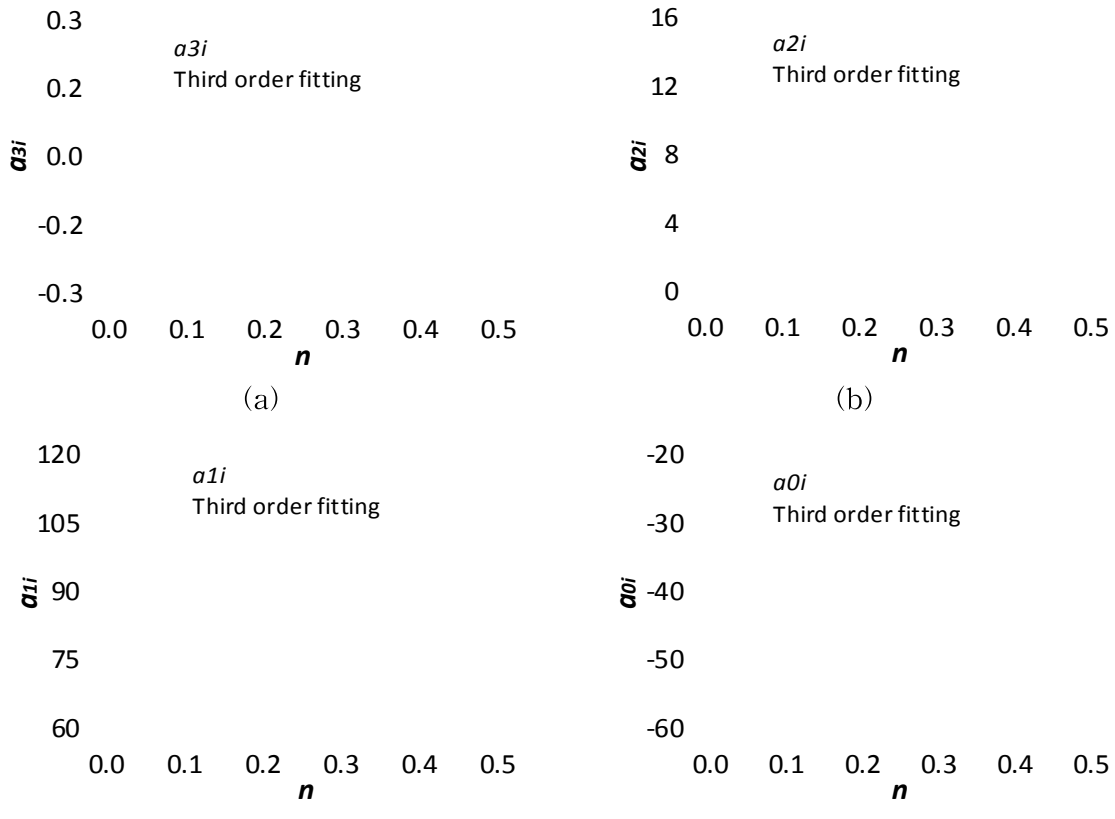
그림 10. 나노압입 실험의 유한요소 해석모델



(a) (b)

그림 11. 유한요소 해석결과 (a) 무차원 함수 Π1 (b) 무차원 함수 Π2

- 그림 11 (a)에 보인 6개의 n값에 따른 곡선을 각각 Er/C의 3차식으로 회귀분석하여 6개의 3차 다항식을 얻었음. 이렇게 얻어진 6개 다항식의 3차항 계수, 2차항 계수, 1차항 계수, 상수항을 다시 n에 대한 3차식으로 회귀분석하여 그림 12와 같은 결과를 얻었음



(a) (b)

(c) (d)

그림 12. 무차원 함수 Π1 계수의 경화지수 n에 대한 회귀분석 (a) 3차항 계수 (b) 2차항 계수 (c) 1차항 계수 (d) 상수항

- 결과적으로 무차원 함수 Π1 ,Π2 가 결정되며, 나노압입 결과로부터 Er, C, S, hm을 결정한 후 무차원 함수 Π1과 Π2를 풀면, 항복응력 σ_y와 경화지수 n을 결정할 수 있음
- 이상에서 살펴본 바와 같이 기존의 나노압입의 결과로부터 항복응력과 경화지수를 결정하는 차원해석에서는 완전소성 구간을 고려하지 않고 있음
- 결과적으로 SS400, SM490과 같은 구조용 강재의 나노압입 결과로부터 항복응력과 경화지수를 도출하기 위해서는 완전소성구간의 끝과 경화구간의 시작이 나타나는 변형률 εst = αεy에 대한 영향을 차원해석에 고려해야 함. 일반적으로 α는 7~23의 값으로 알려져 있음
- 1차년도 2단계 연구에서는 구조용 강재에 대한 유한요소해석 모형을 개발 검증하여 완전소성 구간을 포함한 차원해석을 수행할 것임. 이로부터 나노압입 결과를 이용하여 구조용 강재의 항복응력, 경화지수, α를 결정하는 세 개의 무차원 식 Π1, Π2, Π3을 제안할 것임. 제안된 식을 검증하기 위하여 SS400, SM490 구조용 강재의 인장강도 실험을 수행할 것임

(2) 2차년도 주요 연구내용

■ **구조용 강재의 잔류응력에 따른 강재 미세구조의 특성변화 파악**

- 강재의 열 절단(flame cut) 및 용접에 의해 강재에는 인장과 압축의 잔류응력이 발생함. 이러한 잔류응력의 크기는 100~400 MPa 정도로 강재의 항복응력을 상회하기도 함
- 그림 13에 미국표준인 ASTM 36에서 제시하고 있는 용접부를 가지는 열 절단된 강재 플랜지의 잔류응력 분포를 나타내었음. 400 MPa의 인장응력(+)과 140 MPa의 압축응력(-)이 잔류하고 있음을 확인할 수 있음

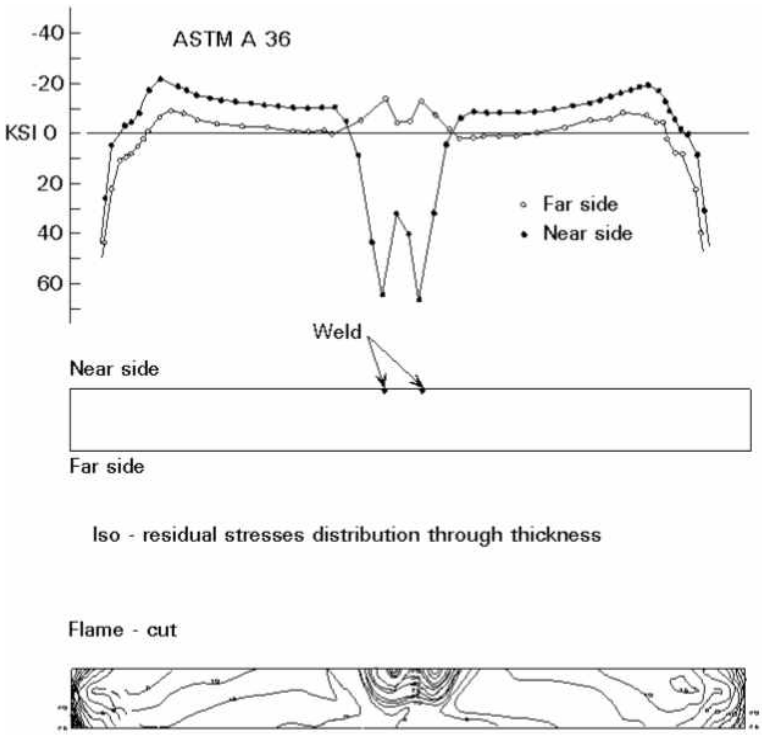


그림 13. ASTM에서 제시하고 있는 플랜지의 잔류응력 분포 (1 ksi=6.9 MPa)

- 잔류응력의 측정은 일반적으로 그림 14과 같이 잔류응력부에 환형 코어 (Ring core)를 뚫어 풀어지는(release) 변형률을 계측하는 파괴검사 방법을 사용하고 있음

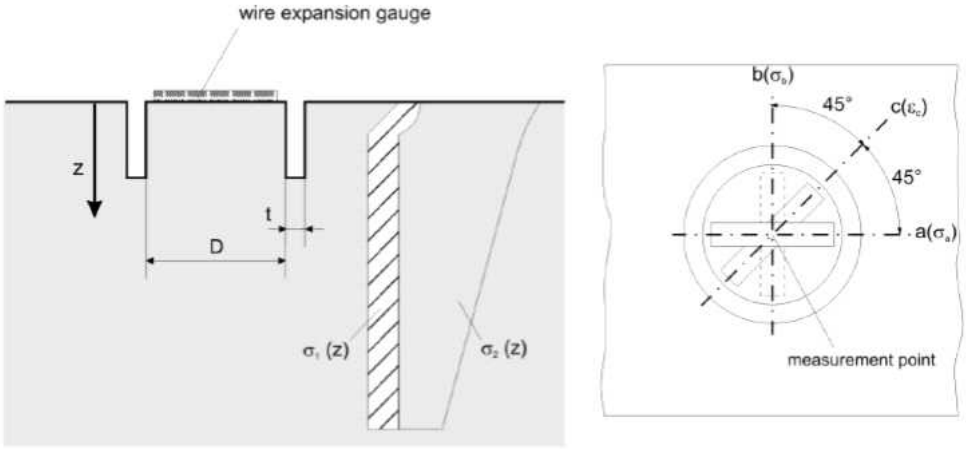
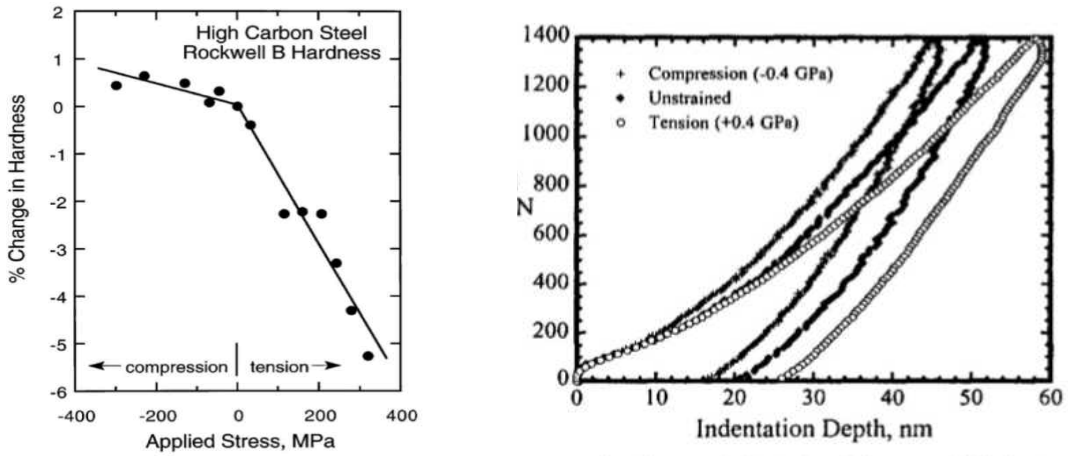


그림 14. Ring core 방법을 이용한 잔류응력 측정법

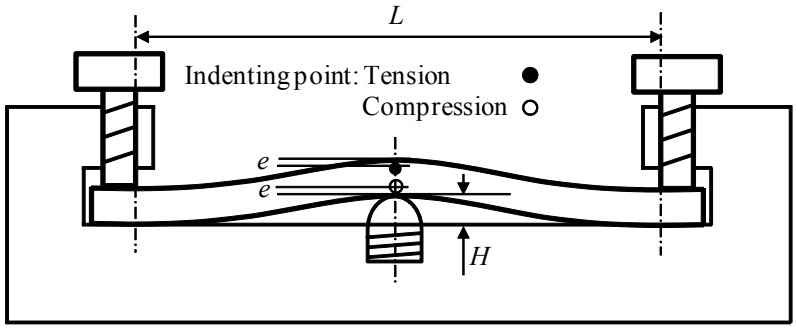
- 반면 나노압입에 의하여 잔류응력을 측정할 경우 sub-micro크기의 흔적을 남기므로, 비파괴 검사 방법으로 활용될 수 있음
- 그림 15 (a)에 압축과 인장 잔류응력의 크기에 따른 강재의 표면경도 변화를 나타내었으며, (b)에 나노압입에 의한 가력-제력곡선의 차이를 나타내었음



(a) (b)

그림 15. 압축과 인장 잔류응력의 크기에 따른 (a) 강재의 표면경도 변화, (b) 가력-제력곡선의 변화

- 이러한 잔류응력과 재료성질의 관계를 활용하여, 본 연구에서는 그림 16와 같이 나노압입 시 응력을 유지할 수 있는 장치를 제작하여, 작용 인장 및 압축 응력 상태의 강재에 대하여 나노압입을 수행하고 그 결과를 분석할 것임
- 잔류응력과 강재의 기계적 특성, 미세구조와의 관계를 파악할 것이며 실험이 성공적일 경우, 그림 16의 장치를 특허출원할 예정임



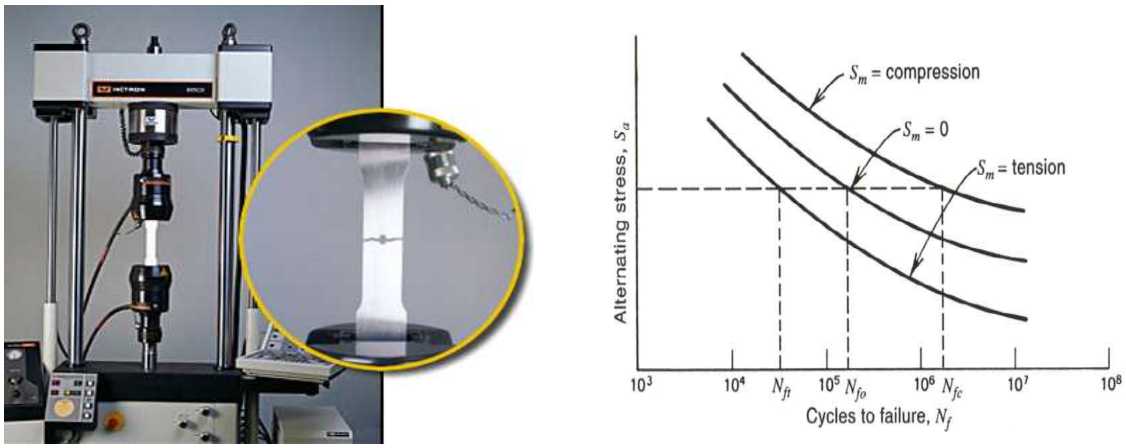
두께 t = 2 mm, e = 0.1 mm, 길이 L=240 mm, E = 210 GPa 인 시편에 대하여,

H (mm)	1	2	3	4	5
σ (MPa)	78.75	157.5	236.25	315	393.75

그림 16. 나노압입 시 잔류응력 도입을 위한 장치 제안

■ 구조용 강재 용접부의 피로상태에 따른 강재 미세구조의 특성변화 파악

- 일반적으로 강구조물의 피로에 대한 설계는 강구조물 사용 시 부재에 작용하는 응력을 강재의 내구한계(endurance limit) 이내로 제한하는 것이며 강재의 내구한계는 그림 17과 같이 피로실험을 수행하여 결정할 수 있음. 평균응력 S에 대하여 파단이 발생하는 반복횟수를 결정하는 실험임



(a) (b)

그림 17. (a) 피로실험 (b) S-N 곡선

- 다양한 평균응력 S에 대하여 실험을 수행하면 그림 18과 같은 S-N곡선을 얻을 수 있으며, 내구한계를 결정할 수 있음
- 그림 18에서 보이는 것처럼 평균응력이 항복응력의 50%이하이면 반복하중에 의해 파단이 발생하지 않는 것으로 간주하며 일반적으로 항복응력의 40%에서 60%사이가 구조용 강재의 내구한계의 범위로 알려져 있음

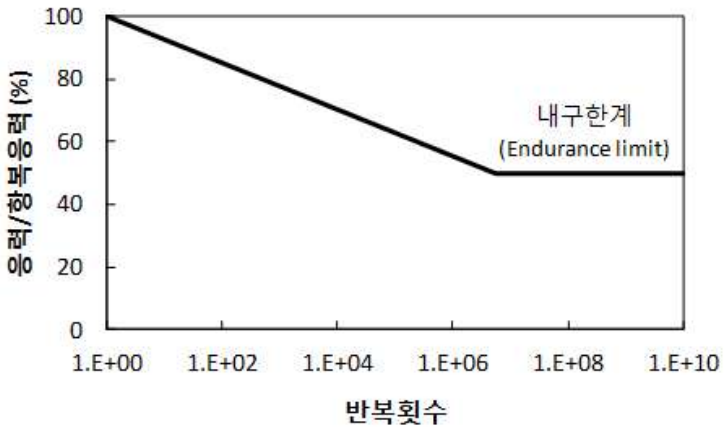
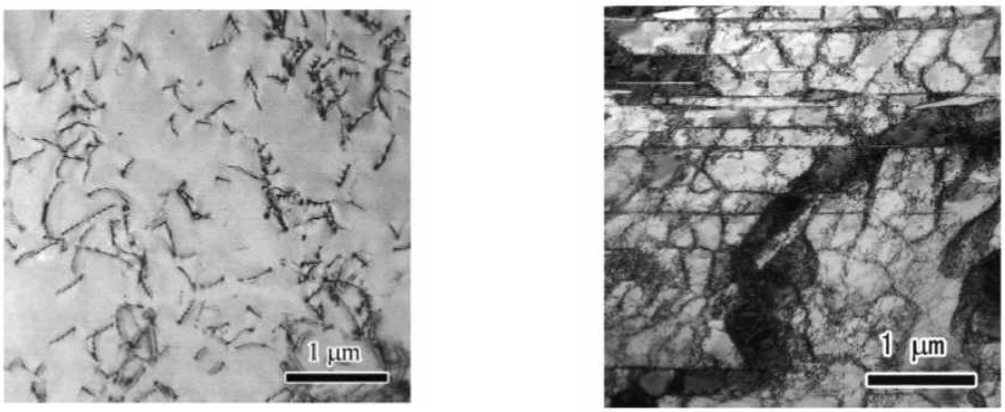


그림 18. 내구한계 결정을 위한 S-N 곡선

- 대부분의 강구조물 설계는 이러한 내구한계를 고려하여 설계되어졌으나, 이미 상당한 크기의 잔류응력이 존재하고 있는 강재 용접부의 피로에 대한 건전성은 불확실한 실정임
- 전자파나 자기력을 이용한 기존의 피로 탐지 기술은 피로에 의한 미세균열이 발생된 이후에야 탐지가 가능하기 때문에 피로에 의한 용접부의 파괴를 예방하기 위해서는 피로에 따른 용접부의 항복응력, 탄성계수, 경화지수의 변화를 지속적으로 모니터링 하여야 함



(a) (b)

그림 19. 피로실험 (a) 전, (b) 후의 SEM 이미지

- 그림 19에서 보여지는 것처럼 피로에 의해 강재내의 미세구조는 많은 변화를 일으키고 그림 20에 보인 것처럼 피로정도 (반복하중 횟수)에 따라 강재의 기계적 성질도 변화할 것임

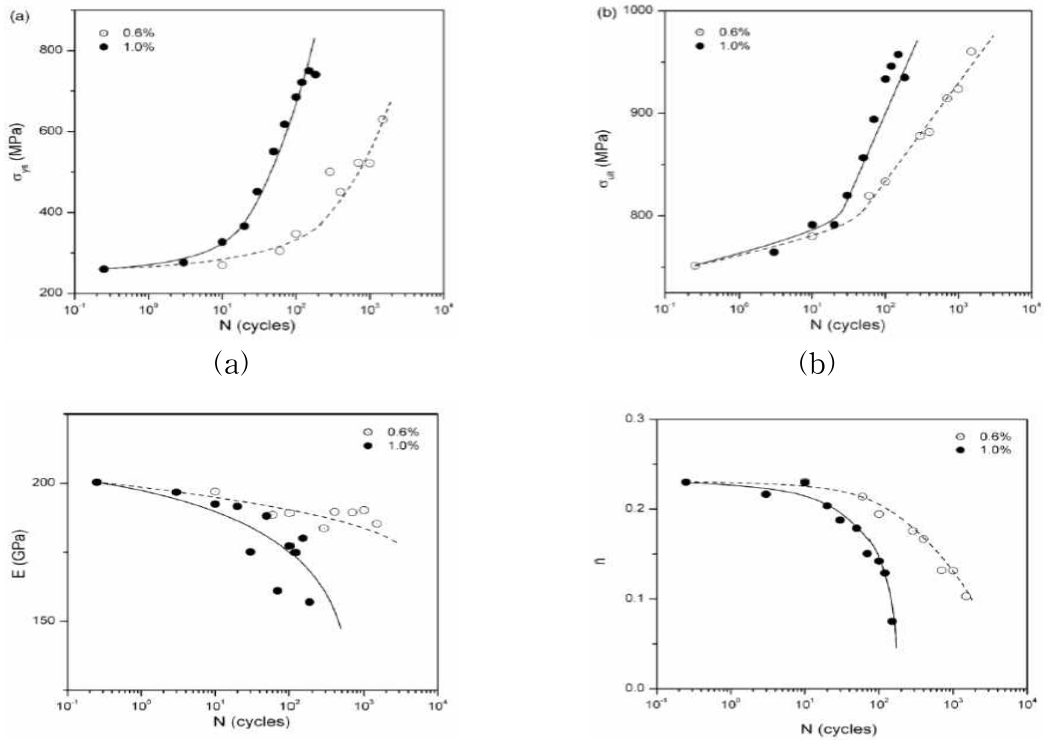


그림 20. 피로도에 따른 강재의 기계적 성질 변화 (a) 항복응력, (b)극한응력, (c) 탄성계수, (d) 경화지수

- 본 연구에서는 그림 21과 같이 용접부를 포함한 시편과 포함하지 않는 시편을 제작하여 피로 실험을 수행할 것이며 각각의 시편에 대하여 항복응력 대비 40%로 내구한계 이내의 평균응력을 사용하여 반복횟수 105, 106, 107의 피로실험을 수행할 것임
- 피로실험 후 용접부에 대해 나노압입과 광학현미경, SEM촬영을 수행하여 미세구조의 변화를 확인할 것이며 탄성계수, 항복응력, 경화지수의 변화를 산정할 것임. 또한 직접 인장강도 실험으로부터 결정된 탄성계수, 항복강도, 경화지수는 나노압입에 의해 결정된 값들과 비교하고 분석할 것임

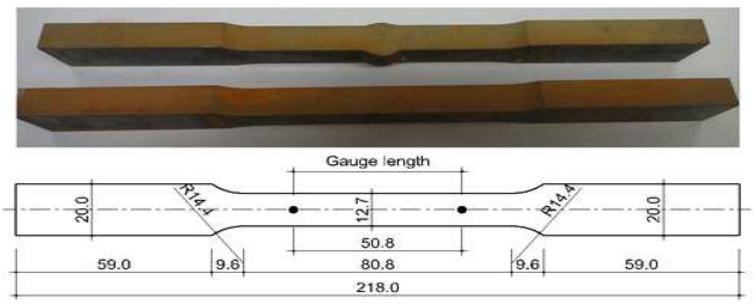
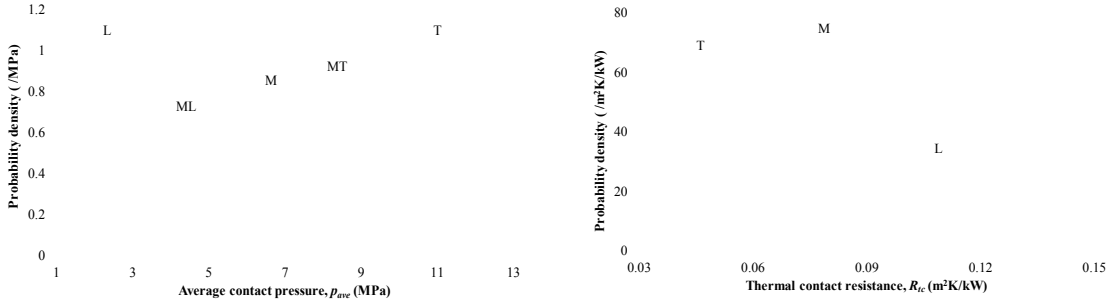


그림 21. 용접부를 포함한 강재와 포함하지 않는 시편

■ 피로도와 잔류응력을 고려한 용접연결부의 정량적 건전성 지표 개발

- 제안된 기법들을 강재 용접부의 비파괴 검사를 위한 방안으로 발전시키기 위해 용접부의 건전성을 정량적으로 나타낼 수 있는 지표를 제안할 것임
- 확률분포를 이용한 일반적인 통계기법이 사용될 것이며, 그림 22는 볼트 연결부의 접촉압력과 접촉열저항 측정결과에 따른 연결부의 건전성을 나타내는 지표를 보여줌.
- 접촉압력이 클수록, 접촉 열저항이 작을수록 볼트 연결부의 연결이 견고함(tight, T)을 나타내며 유사한 방법으로, 나노압입에 의해 측정된 강재의 피로상태, 잔류응력, 항복응력을 이용하여 용접 연결부의 상태를 나타내는 지표를 제안할 것임



(a) (b)

그림 22. 연결부의 (a) 접촉압력과 (b) 접촉열저항에 따른 건전성 지표

- 본 연구가 성공적으로 수행될 경우 구조용 강재의 다양한 잔류응력과 피로도에 따라 각각의 미세구조의 기계적 성질과 성분비의 분포가 결정될 것임
- 잔류응력과 피로도에 따라 분석될 강재와 용접부의 미세구조의 기계적 성질을 표 3에서 6까지 정리하였음. 표에서 f는 미세구조의 구성성분비임
- 표 3과 같이 Low, Mid, High 잔류응력 상태에 대한 실험을 수행할 것이며, 표 4~6의 피로도 Low, Mid, High에 대한 분석 결과는 각각 반복횟수 105, 106, 107의 강재에 대한 용접재(WM), 열영향지역(HAZ), 모재(BM)의 실험결과임. "✓" 표시된 부분에는 평균과 표준편차가 결정될 것임

잔류응력	미세구조 1				미세구조 2				미세구조 3			
	E_r	σ_y	n	f	E_r	σ_y	n	f	E_r	σ_y	n	f
Low	✓	✓	✓	✓	✓	✓	✓	✓	✓	✓	✓	✓
Mid	✓	✓	✓	✓	✓	✓	✓	✓	✓	✓	✓	✓
High	✓	✓	✓	✓	✓	✓	✓	✓	✓	✓	✓	✓

표3. 잔류응력 크기에 따른 강재 미세구조의 기계적 성질과 구성성분비

피로도	미세구조 1				미세구조 2				미세구조 3			
	E_r	σ_y	n	f	E_r	σ_y	n	f	E_r	σ_y	n	f
Low	✓	✓	✓	✓	✓	✓	✓	✓	✓	✓	✓	✓
Mid	✓	✓	✓	✓	✓	✓	✓	✓	✓	✓	✓	✓
High	✓	✓	✓	✓	✓	✓	✓	✓	✓	✓	✓	✓

표4. 피로도 크기에 따른 용접부 WM의 미세구조의 기계적 성질과 구성성분비

피로도	미세구조 1				미세구조 2				미세구조 3			
	E_r	σ_y	n	f	E_r	σ_y	n	f	E_r	σ_y	n	f
Low	✓	✓	✓	✓	✓	✓	✓	✓	✓	✓	✓	✓
Mid	✓	✓	✓	✓	✓	✓	✓	✓	✓	✓	✓	✓
High	✓	✓	✓	✓	✓	✓	✓	✓	✓	✓	✓	✓

표5. 피로도 크기에 따른 용접부 HAZ의 미세구조의 기계적 성질과 구성성분비

피로도	미세구조 1				미세구조 2				미세구조 3			
	E_r	σ_y	n	f	E_r	σ_y	n	f	E_r	σ_y	n	f
Low	✓	✓	✓	✓	✓	✓	✓	✓	✓	✓	✓	✓
Mid	✓	✓	✓	✓	✓	✓	✓	✓	✓	✓	✓	✓
High	✓	✓	✓	✓	✓	✓	✓	✓	✓	✓	✓	✓

표6. 피로도 크기에 따른 용접부 BM의 미세구조의 기계적 성질과 구성성분비

- 최종실험 결과를 정리하여 그림 22에 보인 관계와 같이 정립하면, 비파괴 검사의 판정 기준으로 사용할 수 있는 용접부 건전성의 정량적 지표를 산정할 수 있음
- 예를 들어 용접부에 나노압입 실험을 수행하여 미세구조1, 2, 3 의 Er, σy, n, f의 값을 산정할 수 있음. 이들 12개의 값이 잔류응력, WM 피로도, HAZ 피로도, BM 피로도에 대하여 모두 “Low”의 범위에 들어갈 경우 용접부의 건전도는 1.0, 모두 “High”의 범위에 들어갈 경우 용접부의 건전도는 0으로 나타낼 수 있음

제2장. 국내외 기술 개발 현황

1절. 관련 분야의 국내외 연구동향 및 학술적 성과

1. 국가 연구개발사업 유사연구 실적

가. 연구개발과제의 중복방지를 위한 조사 및 검토결과

- 나노압입과 관련된 연구 과제를 자체적으로 조사한 결과는 다음 표와 같음. 6개 과제 모두 나노압입 관련 연구내용을 포함하고 있으며, 구조용 강의 용접부 물성치 해석 관련 내용은 본 연구가 시초임. 따라서 구조용 강의 특성에 따른 개선과 실험적 연구가 추후 많이 필요함

(단위 : 억원)

부처명	사업명	과제명	예산	비 고
국토교통부	국토교통기술촉진연구사업	나노압입을 이용한 구조용 강재 용접부의 미세구조 파악 및 정량적 건전성 지표 개발 연구 (2015년 ~ 2017년)	4.00	해당 연구
교육과학기술부	중견연구자 지원사업	나노소재 국부 고유 역학특성 평가를 위한 이론/실험/수치해석 융합기술 (2009년 ~ 2012년)	3.87	
교육과학기술부	국가연구개발사업	10nm급 측정 원천기술 개발 (2008년 ~ 2012년)	20.52	
교육과학기술부	중견연구자 지원사업	신 모델링 기법에 의한 미세조직 및 물성예측기술 개발 (2007년 ~ 2012년)	10.12	
과학기술부	21C 프론티어연구개발사업	50nm급 나노 공정 측정 및 평가기술개발 (2005년 ~ 2008년)	6.58	
과학기술부	핵심연구개발사업	MEMS 엑츄에이터 신뢰성 설계기술 (2004년 ~ 2007년)	6.65	

- 본 과제와 관련하여 국토교통부 소관 연구개발사업 및 타 부처 연구개발사업으로 기수행되었거나 수행 중인 유사과제와의 중복 여부 조사 및 검토 결과, 유사하거나 중복되는 과제가 전혀 없는 것으로 나타났음. 나노기술의 적용이 세계적으로 확대되고 심도 있게 진행되고 있는 현실을 고려할 때, 건설 분야에도 나노 기술과 관련된 원천기술의 확보가 시급한 실정임

나. 연구개발과제의 차별화 방안

- 본 연구의 중복방지를 위한 조사 및 검토결과 유사하거나 중복되는 과제가 전혀 없는 것으로 확인하였음

2. 관련분야의 국내외 연구동향 및 학술적 흐름 분석

- 나노기술은 물질을 나노미터 크기의 범주에서 조작·분석하고 이를 제어함으로써 새롭거나 개선된 물리·화학·소자 또는 시스템을 창출하는 과학기술임
- 미국 및 유럽에서 에너지 관련 나노기술분야 정부 투자가 지속적으로 확대되고 있으며 중국, 러시아 등의 신흥국에서도 국가차원의 나노기술전략을 수립하고 동 분야 정부 투자를 지속적으로 확대하고 있음
- 특히 미국의 경우 측정/장비/표준을 포함하는 나노 응용 연구 분야에 대부분의 연구가 집중되어 있음
- 중국의 경우 '09년 국가자연과학기금위원회(NSFC)는 나노제조 기초연구분야에 육성항목 36개과제, 중점지원분야 6개 과제에 대해 총 3,396만 위안을 집중투자하고 있음
- 한국의 경우 교과부는 '09년 1,246억 원에서 매년 10% 증액을 추진하였으며, 지경부는 '09년 100억 원, 환경부는 '10년부터 5년간 200억 원을 투자 중에 있음
- 나노압입에 대한 연구분야는 주로 신소재 개발과 장비개발 위주로 진행되고 있으며, 향후 보다 사용이 편리한 소형화된 나노압입 장비의 개발이 실현될 것임
- 향후 강재 연결부의 비파괴 검사 기법의 일환으로 나노압입을 사용할 경우 본 연구의 결과가 매우 중요한 원천기술로 사용될 것임

2절. 국내외 관련 기술 특허 동향

- 강재 용접부의 나노압입에 관련된 국내 및 국외특허는 없음
- 기타 나노압입에 관련된 국내특허는 6건으로 집계되었으며 아래 표에 정리하였음

특허제목	출원년도
시험체의 잔류 응력 도입장치	2015
나노경도 기준시편을 이용한 나노압입시스템 분석방법, 이를 이용한 나노압입시스템 교정방법, 나노압입시스템 및 기록매체	2014
나노인덴터	2008
나노 압입 시험 기능을 갖는 AFM 캔틸레버	2004
압입시험을 통한 나노박막의 두께측정방법	2003
외부하중이 인가된 시편의 나노인덴테이션용 실험 치구	2003

- 미국 및 유럽에서 에너지 관련 나노기술분야 정부 투자가 지속적으로 확대되고 있으며 중국, 러시아 등의 신흥국에서도 국가차원의 나노기술전략을 수립하고 동 분야 정부 투자를 지속적으로 확대하고 있음
- 특히 미국의 경우 측정/장비/표준을 포함하는 나노 응용 연구 분야에 대부분의 연구가 집중되어 있음
- 중국의 경우 '09년 국가자연과학기금위원회(NSFC)는 나노제조 기초연구분야에 육성항목 36개 과제, 중점지원분야 6개 과제에 대해 총 3,396만 위안을 집중투자하고 있음
- 나노압입에 대한 연구분야는 주로 신소재 개발과 장비개발 위주로 진행되고 있으며, 향후 보다 사용이 편리한 소형화된 나노압입 장비의 개발이 실현될 것임
- 향후 강구조의 취약도 진단을 위한 비파괴 검사 기법의 일환으로 나노압입을 사용할 경우 본 연구의 결과가 매우 중요한 원천기술로 사용될 것임

- 나노압입을 활용한 구조용 강의 변형률 속도효과 도출 및 지진에 대한 취약도 진단 관련 국외 특허는 없는 것으로 조사되었음
- 기타 나노압입에 관련된 국외특허는 미국 9건, 중국 5건, 대만 4건으로 집계되었으며 아래 표에 정리하였음

출원국	특허제목	출원년도
미국	Hard aluminum oxide coating for various applications	2015
	Actuatable capacitive transducer for quantitative nanoindentation combined with transmission electron microscopy	2010
	Nanoindenter	2010
	Micromachined comb drive for quantitative nanoindentation	2009
	Device and method for optical nanoindentation measurement	2008
	Nanoindentation surface analysis method	2008
	Nanoindenter tip for uniaxial tension and compression testing	2007
	Nanoindentation surface analysis tool and method	2006
	MEMS nanoindenter	2005
중국	Power law creep stress index testing method based on nanoindentation steady-state process	2014
	Nanoindentation test desk and experimental method for interfacial shear force of carbon fiber composite	2012
	Precise nanoindentation test device	2011
	Nanoindentation/cutting test device	2011
	AFM (Atomic Force Microscope)-based device for performing nanoindentation measurement on surface of microparticle	2010
대만	Improvement method for measurement error caused by sink-in phenomenon of nanoindentation	2014
	Process for determining viscous, elastic, plastic, and adhesive (VEPA) properties of materials using AFM-based or conventional nano-indentation	2008
	Improved device for nanoindentation system	2007
	Auxiliary apparatus of specimen carriage for nanoindenter	2007

3절. 국내외 시장분석 및 산업동향

- 영국 Cientifica Ltd.의 조사에 따르면, 2011년 나노기술에 대한 전 세계의 정부투자액은 650억 달러였으며 2014년에 1000억 달러까지 증가할 것으로 예상함

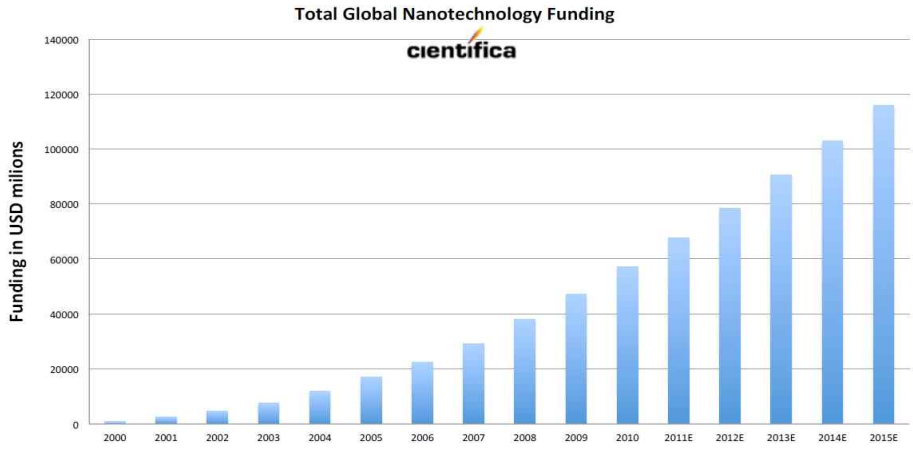


그림 23. 나노기술에 대한 전 세계의 투자액 (Cientifica Ltd 2011)

- 미국의 경우, NNI Signature Initiative 발표를 통해 나노기술 분야의 글로벌 리더십 확보 및 산업화 연계 촉진을 위한 원천연구 투자가 증가하는 추세이며, 2013년 나노기술에 대한 미국 정부의 투자액 17.6억 달러 중 나노스케일 장비 및 시스템 분야가 23%를 차지하였음

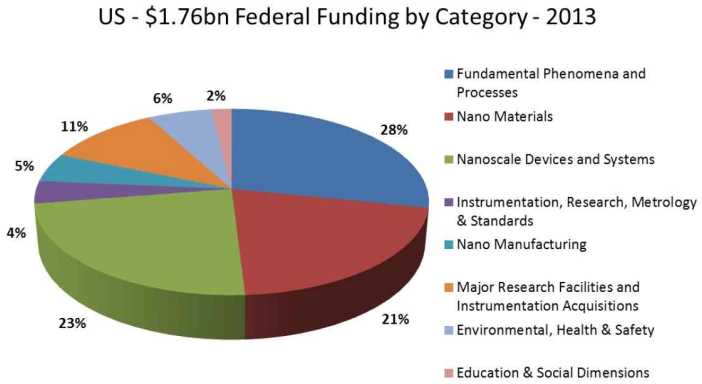


그림 24. 미국 정부의 나노기술 분야별 투자비중 [NNI (Nano.Gov Web Site)]

- 일본에서는 지난 2001년부터 제2기 과학기술기본계획 (2001~2005년)에 이어 제3기 과학기술기본계획 (2006~2010)의 중점 분야 중 하나로 나노기술을 선정하고 전략적인 국가투자를 실시하고 있음. 일본 정부의 나노기술 투자 예산은 2006년 762억 엔에서 2010년 1,128억 엔으로 연평균 10%씩 증가하였으며, 이는 동기간 중 미국 (8.1%)의 예산 증가율보다 높은 수치임
- 국내의 경우, 2012년도 나노기술 분야에 대한 정부투자액 총 2,834억 원 중 기술 분류별 비중은 나노소재 29%, 나노소자 21%, 에너지·환경 15%, 나노바이오 11%를 차지하였으며, 본 연구에서 개발할 기술을 포함하는 나노공정·장비·측정 분야는 24%의 비중을 차지하였음

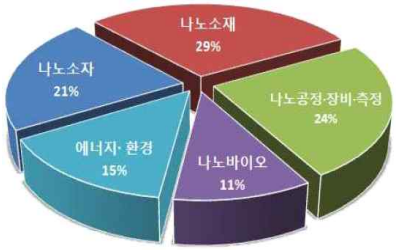


그림 25. 2012년 나노기술 분야별 정부투자 비중 (2013년도 나노기술발전시행계획)

- 2013년 1월 기준, 국내 230개의 나노관련기업을 대상으로 조사·분석한 결과 나노소재 기업이 59.1%로 가장 많았으며, 나노공정·측정·장비 기업은 27%의 비중을 차지하였음. 그 외 나노바이오 6.5%, 나노소자 3.9%, 나노에너지·환경 3.5% 순으로 확인되었음

4절. 종합결론

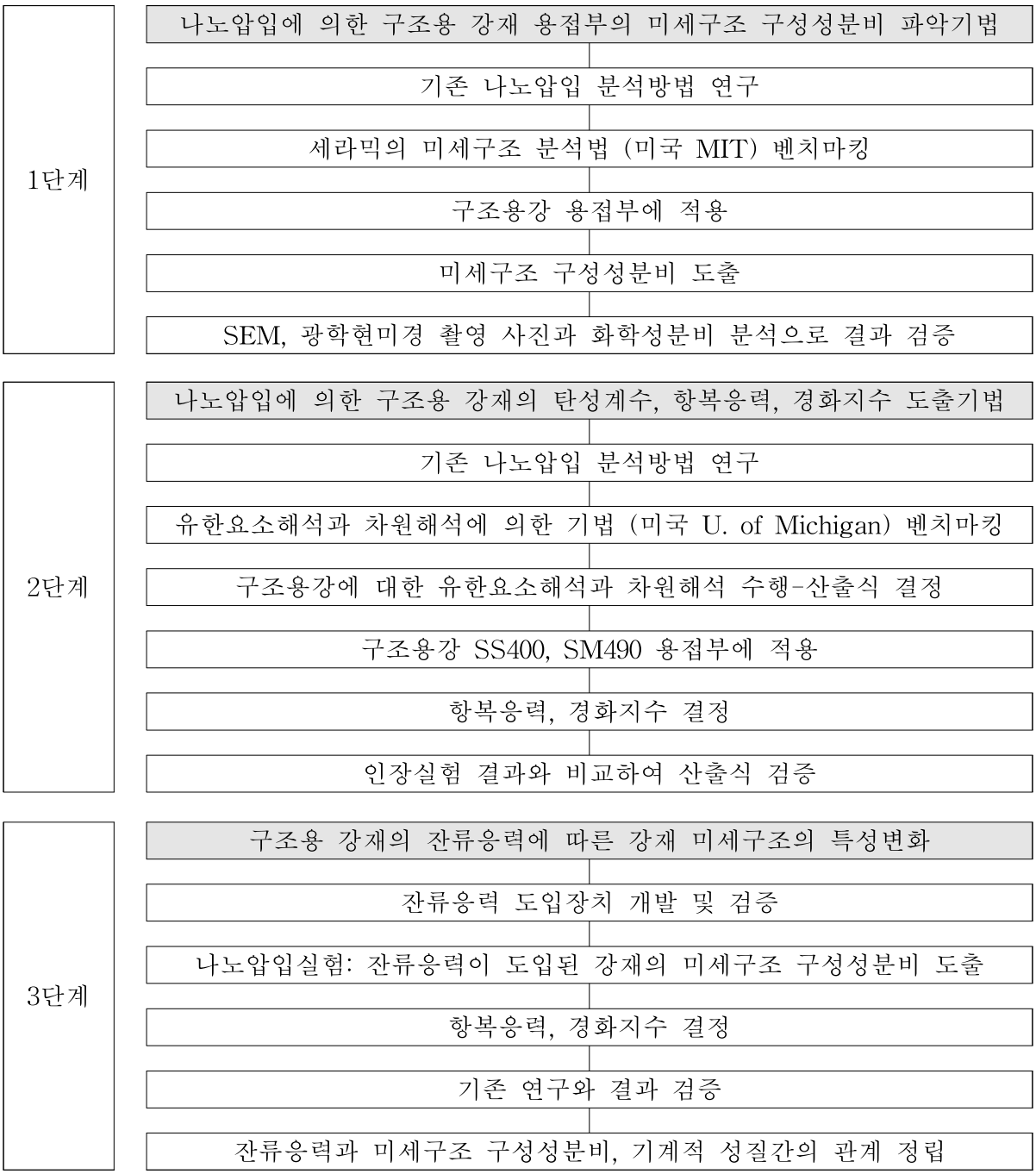
- 다양한 공학 분야에서 나노기술의 필요성이 대두되고 있으며, 국내뿐만 아니라 세계적으로도 나노기술에 대한 투자와 관심이 지속적으로 확대되고 있음
- 나노기술에 의해서 기존에는 수행할 수 없었던 다양한 형태의 실험들이 마이크로 단위에서 수행되고 있음
- 건설 분야에도 나노압입과 나노스크래치등의 나노기술의 사용과 카본나노튜브, 나노실리카등의 나노소재를 이용하려는 노력이 급증하고 있음
- 건설 분야에 적용 가능한 나노기술 관련 원천기술의 확보가 시급한 실정임

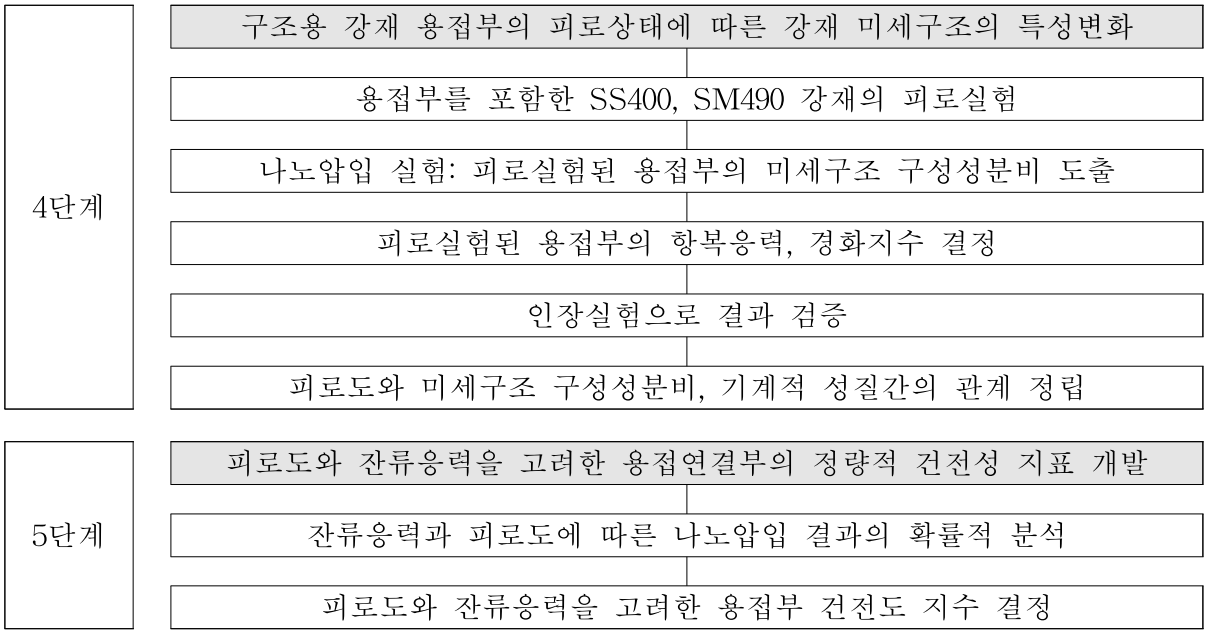
제3장. 연구 수행 내용 및 성과

1절. 연구성과별 세부추진내용

1. 연구개발 흐름도

- 본 연구는 실험적 증명 단계로써, 연구개발 흐름도는 아래와 같음





2. 연구개발 단계에 따른 세부연구내용

기간	단계별 주요 연구활동	세부추진내용
1단계 ('15.06 -'15.11)	기존 나노압입 분석방법 연구	• 나노압입에 의한 분석기법 정리 • 재료의 특성에 따른 나노압입 하중 결정 • 나노압입으로 추출이 가능한 물성치 조사
	세라믹의 미세구조 분석법 (미국 MIT) 벤치마킹	• 세라믹과 시멘트계 재료에 사용된 기법 연구 • 강재 미세구조별 특성 및 성질 파악 • 미세구조를 특정지을 수 있는 물성치 파악
	구조용강 용접부에 적용	• 용접재, 열영향지역, 모재에 대한 특성 연구 • SS400, SM490 강재 구입 • 용접부 도입 • 나노압입 시편제작 (수압절단) • 용접부 각 영역에 나노압입 수행
	미세구조 구성성분비 도출	• 확률적 deconvolution 기법 적용 • 미세구조 탄성계수의 빈도 함수 도출 • 미세구조 경도의 빈도 함수 도출
	SEM, 광학현미경 촬영 사진과 화학성분비 분석으로 결과 검증	• 광학현미경 촬영 • SEM 촬영 • 화학성분비 분석 • 미세구조 구성성분비 검증

2단계 ('15.12 -'16.05)	기존 나노압입 분석방법 연구	• 재료의 소성 성질 산정 기법 연구 • 재료의 소성 특성에 따른 나노압입 하중 결정 • 나노압입으로 추출이 가능한 소성특성 조사
	유한요소해석과 차원해석에 의한 기법 (미국 U. of Michigan) 벤치마킹	• 기존 나노압입 유한요소 모델 연구 • 나노압입 결과의 활용법 연구 • 기존의 차원해석 방법 연구
	구조용강에 대한 유한요소해석과 차원해석 수행 - 산출식 결정	• 나노압입 유한요소 모델 개발 및 검증 • 해석수행 • 차원해석에 의한 제안식 결정
	구조용강 SS400, SM490 용접부에 적용	• 용접재, 열영향지역, 모재에 대한 특성 연구 • SS400, SM490 강재 구입 • 용접부 도입 • 나노압입 시편제작 (수압절단) • 용접부 각 영역에 나노압입 수행
	항복응력, 경화지수 결정	• 차원해석에 의한 제안식 사용 • 항복응력, 경화지수 결정 • 소성특성에 따른 미세구조 구성성분비 도출
	인장실험 결과와 비교하여 산출식 검증	• 용접부 포함 인장실험 시편제작 (수압절단) • 제안식 검증
3단계 ('16.06 -'16.08)	잔류응력 도입장치 개발 및 검증	• 잔류응력 도입장치 제작 • SS400, SM490 강재 시편 제작 • 스트레인 게이지 부착 • 시편 설치 시 원하는 응력이 도입되는지 검증
	나노압입실험: 잔류응력이 도입된 강재의 미세구조 구성성분비 도출	• 다섯가지 레벨의 잔류응력 상태에서 나노압입 수행 • 탄성계수, 경도 산정후 빈도함수 작성 • 미세구조 구성성분비 도출
	항복응력, 경화지수 결정	• 제안식 사용하여 소성특성 결정 • 빈도함수 작성 • 미세구조 구성성분비 도출
	기존 연구와 결과 검증	• 잔류응력에 대한 특성변화 연구자료 참조 • 기존 연구와 결과 검증
	잔류응력과 미세구조 구성성분비, 기계적 성질간의 관계 정립	• 다섯가지 레벨의 잔류응력 상태에 대한 미세구조의 구성성분비, 기계적 성질간의 관계 정립

4단계 ('16.09 -'17.02)	용접부를 포함한 SS400, SM490 강재의 피로실험	• SS400, SM490 강재 구입 • 용접부 도입 • 피로실험 시편제작 (수압절단) • 세가지 레벨의 피로실험 수행
	나노압입 실험: 피로실험된 용접부의 미세구조 구성성분비 도출	• 세가지 레벨의 피로도에 의한 강재 용접부의 나노압입 수행 • 탄성계수, 경도 산정후 빈도함수 작성 • 미세구조 구성성분비 도출
	피로실험된 용접부의 항복응력, 경화지수 결정	• 제안식 사용하여 용접부의 소성특성 결정 • 빈도함수 작성 • 미세구조 구성성분비 도출
	인장실험으로 결과 검증	• 용접부 포함 인장실험 시편제작 (수압절단) • 제안식 검증
	피로도와 미세구조 구성성분비, 기계적 성질간의 관계 정립	• 세가지 레벨의 피로 상태에 대한 미세구조의 구성성분비, 기계적 성질간의 관계 정립
5단계 ('17.03 -'17.05)	잔류응력과 피로도에 따른 나노압입 결과의 확률적 분석	• 기존의 통계적 기법으로 실험결과 데이터화 • 잔류응력 정도에 따른 강재 미세구조별 특성치 관계 수립 • 피로 정도에 따른 용접부 (WM, HAZ, BM) 미세구조별 특성치 관계 수립
	피로도와 잔류응력을 고려한 용접부 건전도 지수 결정	• 건전도 지수 결정 • 프로그램 작성 • 용접부 미세구조 특성치에 대한 건전도지수 도출 프로그램 작성

2절. 단계별 연구수행 내용

1. 주요 연구내용

가. 나노압입에 의한 구조용 강재 용접부의 미세구조 구성성분비 파악기법 개발

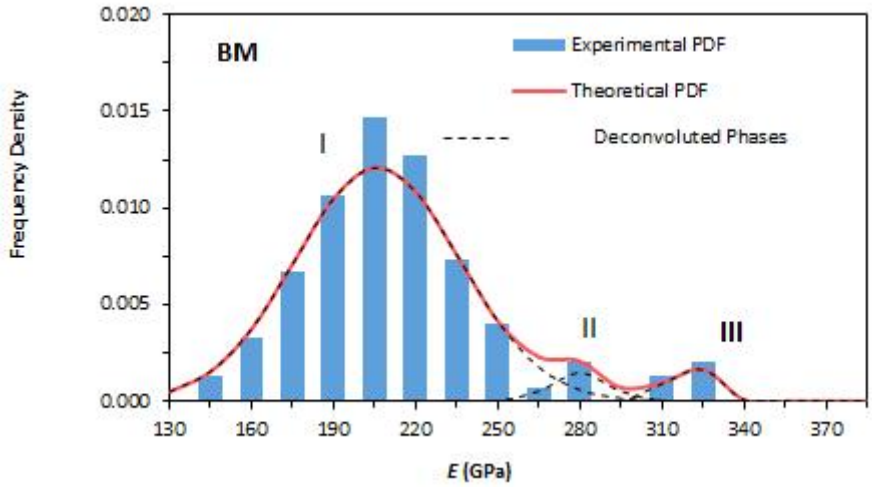
(1) 실험체 제작

■ SS400, SM490 구조용 강재의 용접부의 미세구조 구성성분비를 파악하기 위해 실험체 제작은 다음과 같이 이루어짐

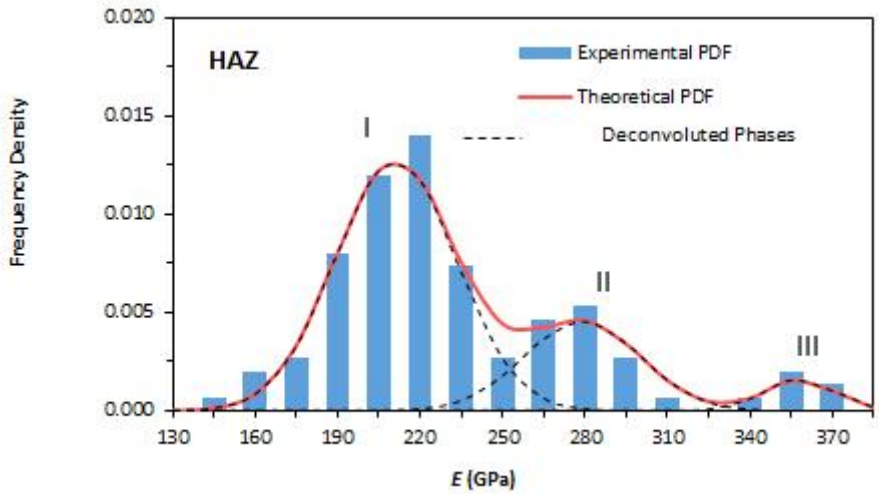
- SS400, SM490 구조용 강재에 대하여 수동 아크 용접 (Manual Metal Arc Welding) 방법을 활용하여 맞대기 용접 (Butt Welding)에 의해 용접부를 생산
- 추가적인 열의 영향을 제거하기 위해 수압절단을 이용하여 나노압입에 필요한 용접부를 포함한 시험체 제작
- 시험체는 일반강재 (Base Metal), 열영향부 (Heat Affected Zone), 용접재 (Weld Metal)을 모두 포함

(2) 나노압입 분석

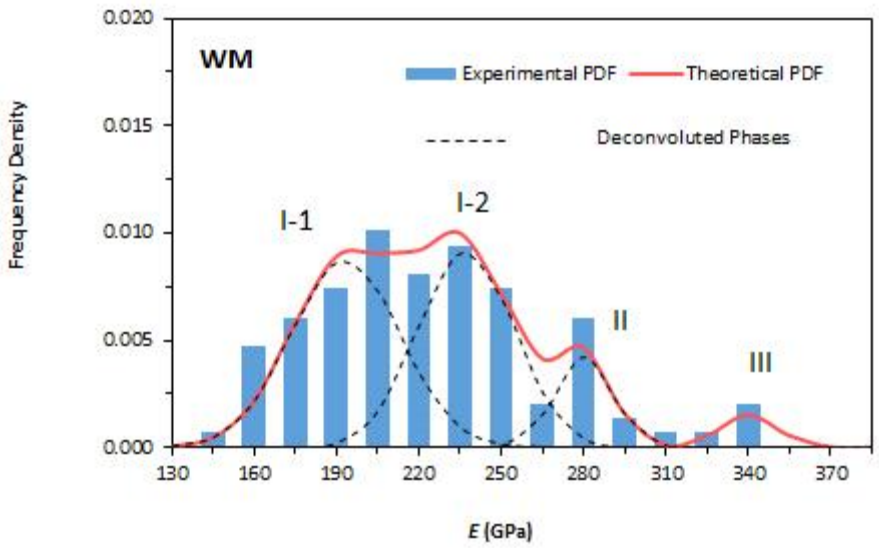
- 일반강재 (Base Metal), 열영향부 (Heat Affected Zone), 용접재 (Weld Metal) 영역에 나노압입을 수행하여 탄성계수와 경도의 빈도함수로부터 미세구조의 구성성분비를 결정
- SS400과 SM490 구조용 강재 용접부를 사용하여 100회의 나노압입을 수행하여 100개의 미세구조 구성성분비 파악



(a) BM

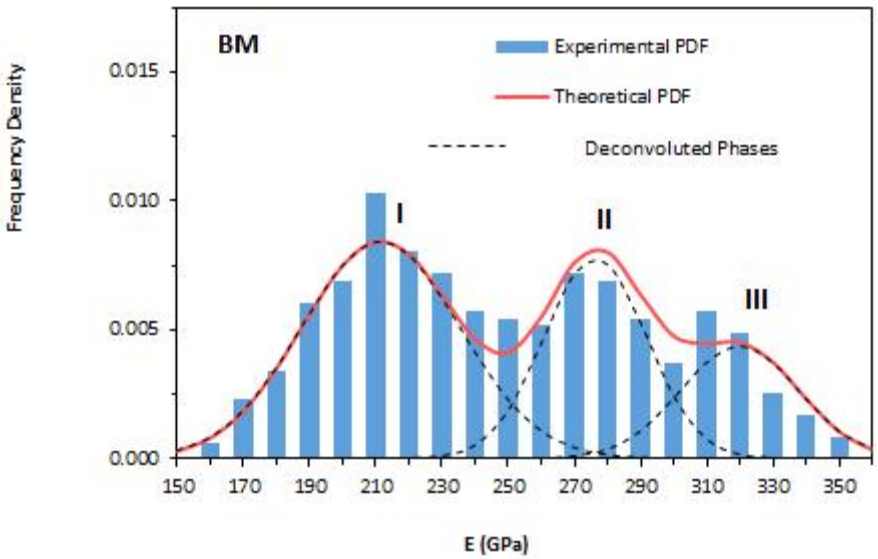


(b) HAZ

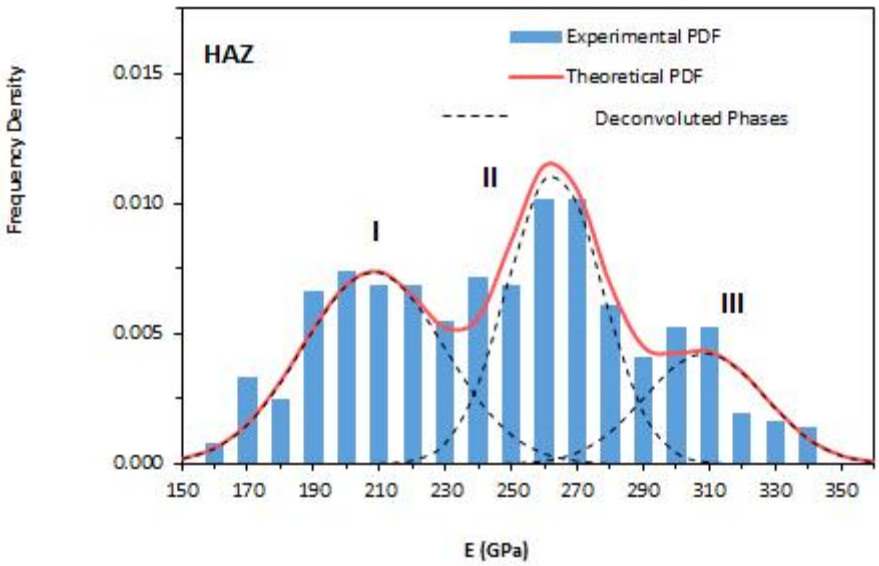


(c) WM

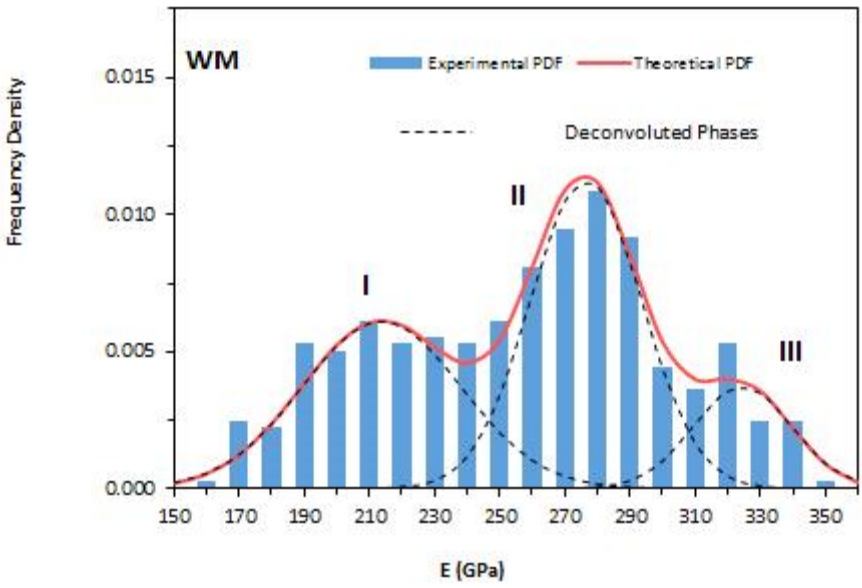
그림 26. SS400 구조용 강재 용접부 나노압입 결과



(a) BM



(b) HAZ

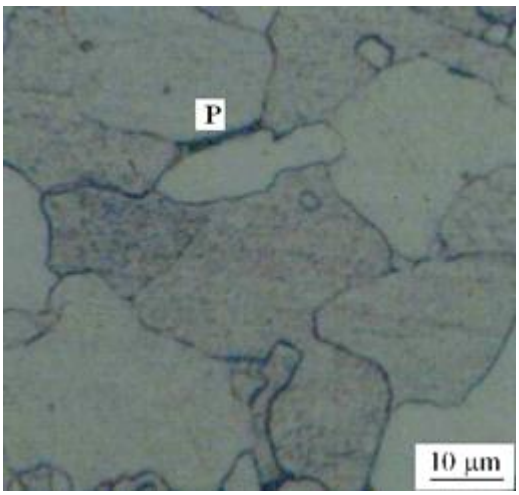


(c) WM

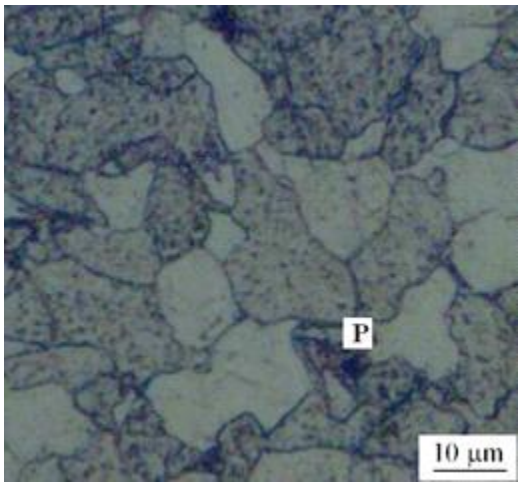
그림 27. SM490 구조용 강재 용접부 나노압입 결과

(3) 구성성분비 파악

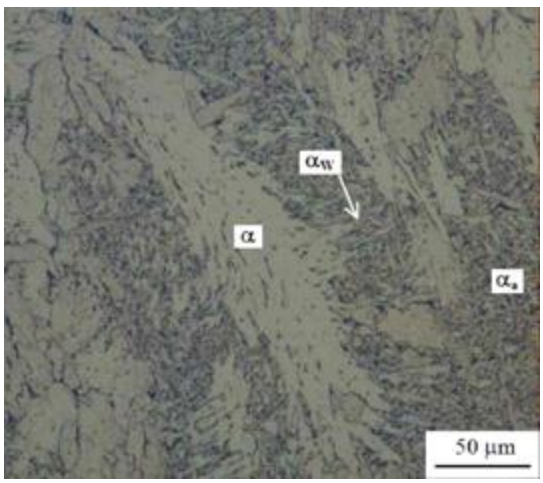
■ 나노압입 결과를 광학현미경, SEM촬영, 화학 성분검사로부터 검증



(a) BM의 미세구조

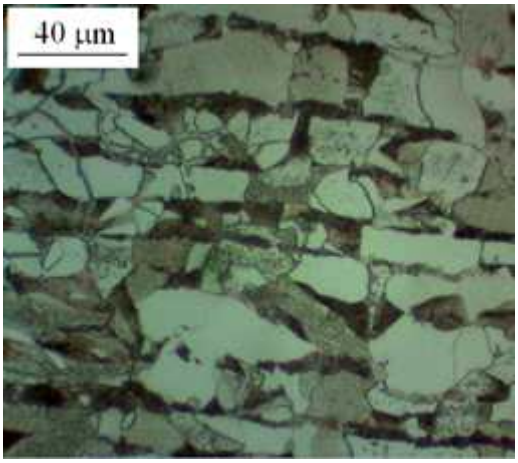


(b) HAZ의 미세구조

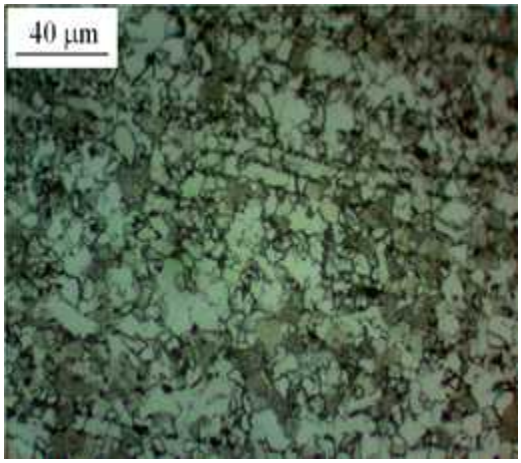


(c) WM의 미세구조

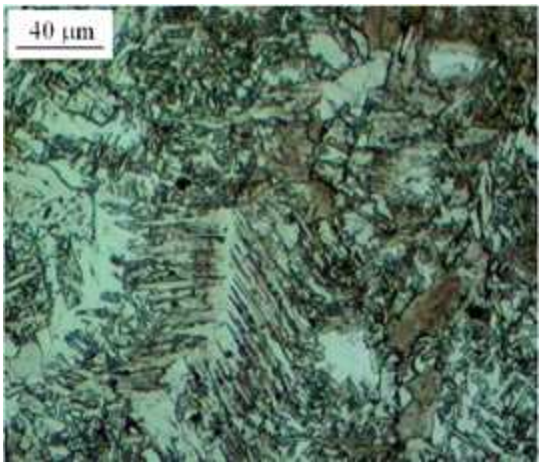
그림 28. SEM, 광학현미경에서의 용접열 영향에 의한 SS400 구조용 강재 용접부의 미세구조 변화모습



(a) BM의 미세구조



(b) HAZ의 미세구조



(c) WM의 미세구조

그림 29. SEM, 광학현미경에서의 용접열 영향에 의한 SM490 구조용 강재 용접부의 미세구조 변화모습

- 탄성계수에 따른 구성성분비의 오차는 0-1%이며, 경도에 따른 구성성분비의 오차는 BM, HAZ, WM이 각각 1-2%, 0-1%, 1-2%임

Location	화학성분분석, %		나노압입-탄성계수		나노압입-경도	
	Ferrite	Pearlite	Ferrite	Pearlite	Ferrite	Pearlite
BM	94-95	5-6	94	6	96	4
HAZ	94-95	5-6	94	6	94	6
WM	95-96	4-5	96	4	97	3

표 7. SS400 구조용 강재 화학 성분 분석에 의한 구성성분비와 비교 검증

- 탄성계수에 따른 구성성분비의 오차는 0.2-0.8%이내 이며, 경도에 따른 구성성분비의 오차는 BM, HAZ, WM이 각각 0-1%, 2-3%, 1-2%임

Location	화학성분분석, %		나노압입-탄성계수		나노압입-경도	
	Ferrite	Pearlite	Ferrite	Pearlite	Ferrite	Pearlite
BM	94-95	5-6	94	6	96	4
HAZ	94-95	5-6	94	6	94	6
WM	95-96	4-5	96	4	97	3

표 8. SM490 구조용 강재 화학 성분 분석에 의한 구성성분비와 비교 검증

나. 나노압입에 의한 구조용 강재의 탄성계수, 항복응력, 경화지수 도출기법

(1) 나노압입 결과로 상관 관계식 유도

■ 나노압입 하중-압입 곡선과 응력-변형률 선도간의 2개의 상관 관계식 유도

- 나노압입으로 하중-압입 곡선으로부터 하중 곡선식, 하중제거 곡선 초기강성, 접촉면적 등을 알 수 있음

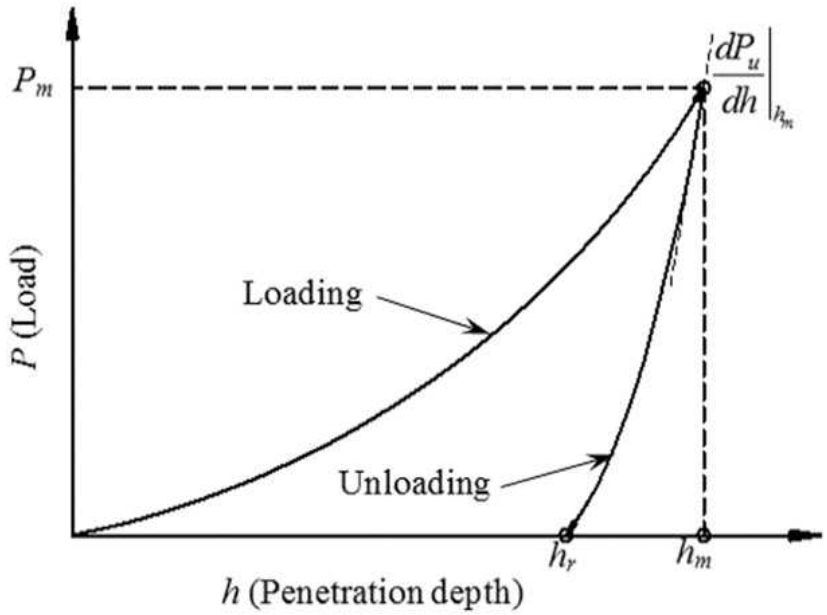


그림 30. 나노압입 하중-압밀 곡선

- 나노압입에 의한 하중 재하시 탄성과 소성변형이 함께 일어나므로, 나노압입의 가력(loading)곡선은 재료의 탄성계수, 항복응력, 경화지수의 함수로 가정할 수 있음. 이들의 관계를 차원해석에 의해 상관 관계식을 유도 할 수 있음

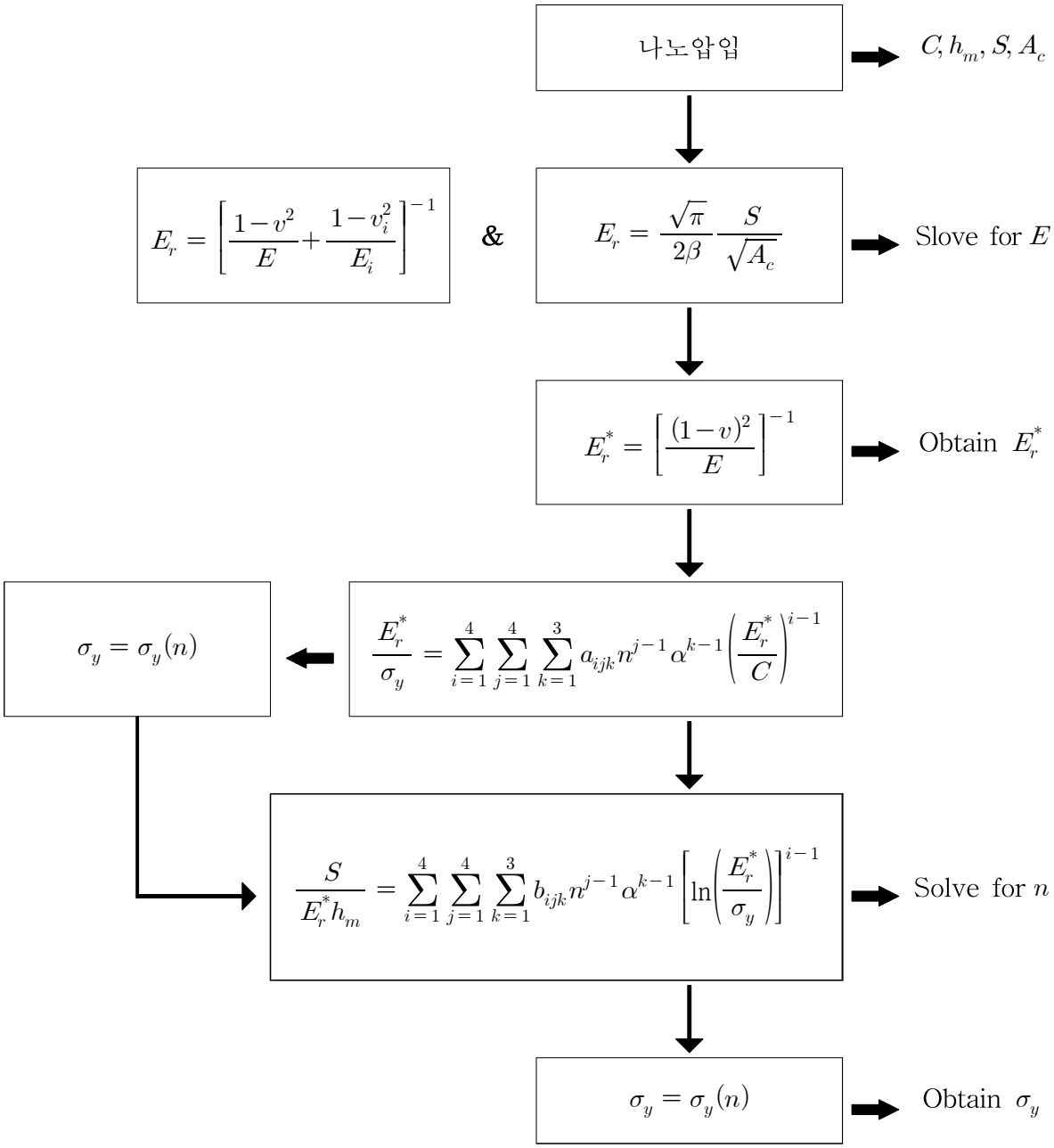
$$\text{하중 곡선식 : } C = \frac{P_m}{h_m^2}$$

- 제력(unloading)곡선의 초기 접촉강성은 재료의 탄성계수와 압입기와 강재가 접촉하는 면적의 넓이의 함수이며 접촉면적은 재료의 소성 성질과 관련이 있음. 이들의 관계는 차원해석에 의해 상관 관계식으로 유도 할 수 있음

$$\text{하중제거 곡선 초기강성 : } S = \left.\frac{dP_u}{dh}\right|_{h_m} = mB(h_m - h_r)^{m-1}$$

$$\text{접촉면적 : } A_c = 24.5h_c^2$$

- 다음은 나노압입 하중-압입 곡선과 응력 변형률 선도로부터 유도한 두 개의 상관관계식의 알고리즘을 나타냄



- 위의 알고리즘으로부터 응력에 대한 상관 관계식으로 정리 할 수 있음

$$\sigma = \begin{cases} E\varepsilon & \text{for } \varepsilon \le \varepsilon_y \\ \sigma_y & \text{for } \varepsilon \le \varepsilon_y \\ \sigma_y[1 + E(\varepsilon - \varepsilon_y)/(\alpha\sigma_y)]^n & \text{for } \varepsilon \ge \varepsilon_y \end{cases}$$

- 576개의 재료특성 조합으로 유한요소 해석 수행 후 결과를 2차원 회귀분석하여 상관 관계식의 상수를 결정함

	E(GPa)	σ_y(MPa)	n	α
576조합 $\upsilon = 0.3$	10	235	0	7
	40	285	0.1	
	110	335	0.2	16
	160	385	0.3	
	210	435	0.4	23
	260	535	0.5	

표 9. 2차원 회귀분석으로 상관 관계식의 상수 결정

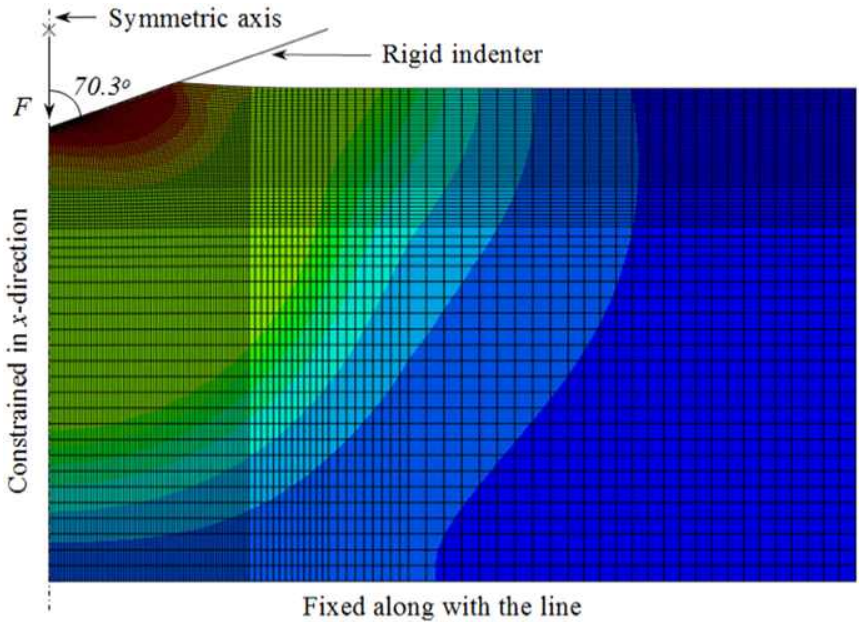


그림 31. 나노압입 실험의 유한요소 해석 모델

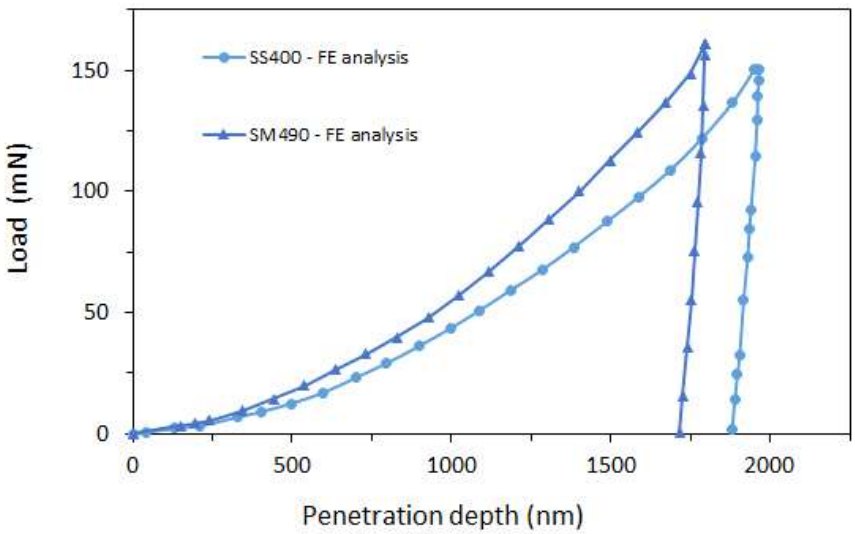


그림 32. 나노압입 실험의 유한요소 해석 그래프

- 유한요소해석 결과를 2차원 회귀분석하여 상관 관계식의 상수 결정

✓ $\frac{E_r^*}{\sigma_y} = \sum_{i=1}^{4}\sum_{j=1}^{4}\sum_{k=1}^{3} a_{ijk} n^{j-1} \alpha^{k-1} \left(\frac{E_r^*}{C}\right)^{i-1}$ 의 상관계식 상수 결정

(k, j)	a_{ijk}			
	i=4	i=3	i=2	i=1
(1, 1)	-1.710E -1	1.629E +0	1.144E +2	-4.574E +1
(2, 1)	1.395E -2	-1.195E -1	2.955E -1	-1.643E -1
(3, 1)	-4.231E -4	3.903E -3	-9.428E -3	5.243E -3
(1, 2)	9.940E +0	7.973E +0	5.240E +1	-6.190E +1
(2, 2)	-1.193E +0	2.573E +0	-5.962E +0	3.952E +0
(3, 2)	3.876E -2	-1.429E -1	1.858E -1	-5.743E -2
(1, 3)	-1.196E +2	5.892E +2	-9.072E +2	4.656E +2
(2, 3)	1.194E +1	-5.351E +1	5.441E +1	-1.804E +1
(3, 3)	-3.417E -1	1.631E +0	-1.443E +0	2.175E -1
(1, 4)	1.981E +2	-4.190E +2	4.267E +2	-2.408E +2
(2, 4)	-1.845E +1	3.178E +1	2.717E +0	-1.053E +1
(3, 4)	5.023E -1	-1.147E +0	3.126E -2	5.674E - 1
R^2	0.9717	0.9976	0.9934	0.9865

표 10. 유한요소해석 결과로부터 상관 관계식의 상수 결정

✓ $\frac{S}{E_r^* h_m} = \sum_{i=1}^{4}\sum_{j=1}^{4}\sum_{k=1}^{3} b_{ijk} n^{j-1} \alpha^{k-1} \left[\ln\left(\frac{E_r^*}{\sigma_y}\right)\right]^{i-1}$ 의 상관계식 상수 결정

(k, j)	b_{ijk}			
	i=4	i=3	i=2	i=1
(1, 1)	-6.197E -2	8.766E -1	-3.097E +0	6.085E +0
(2, 1)	2.285E -5	-7.846E -4	5.723E -3	-1.095E -2
(3, 1)	-4.241E -6	8.032E -5	-4.539E -4	7.676E -4
(1, 2)	9.840E -1	-1.477E +1	6.723E +1	-9.676E +1
(2, 2)	-6.638E -2	9.160E -1	-3.909E +0	5.367E +0
(3, 2)	1.877E -3	-2.619E -2	1.147E -1	-1.630E -1
(1, 3)	-4.036E +0	6.074E +1	-2.847E +2	4.247E +2
(2, 3)	4.241E -1	-6.122E +0	2.797E +1	-4.112E +1
(3, 3)	-1.324E -2	1.911E -1	-8.782E -1	1.301E +0
(1, 4)	4.871E +0	-7.309E +1	3.440E +2	-5.160E +2
(2, 4)	-5.777E -1	8.394E +0	-3.875E +1	5.745E +1
(3, 4)	1.875E -2	-2.718E -1	1.257E +0	-1.870E +0
R^2	0.9938	0.9945	0.9944	0.9942

표 11. 유한요소해석 결과로부터 상관 관계식의 상수 결정

- 인장강도 실험과 비교 검증 및 나노압입으로부터 도출된 응력-변형률 선도 비교

	SS400			
	E(GPa)	σ_y(MPa)	n	α
S1	210.2	306.9	0.203	17.6
S2	213.2	305.6	0.205	18.0
S3	208.4	307.2	0.205	18.7
Ave.	210.6	306.6	0.204	18.1

표 12. SS400 구조용 강재의 실험으로 도출된 응력-변형률 선도 비교

	SM490			
	E(GPa)	σ_y(MPa)	n	α
S1	212.3	353.7	0.267	13.5
S2	212.1	354.3	0.262	13.4
S3	210.8	352.6	0.268	13.4
Ave.	211.7	353.5	0.266	13.4

표 13. SM490 구조용 강재의 실험으로 도출된 응력-변형률 선도 비교

- SS400 구조용 강재의 경우, 항복강도와 경화지수의 오차율은 각각 1.6%, 3.1%임

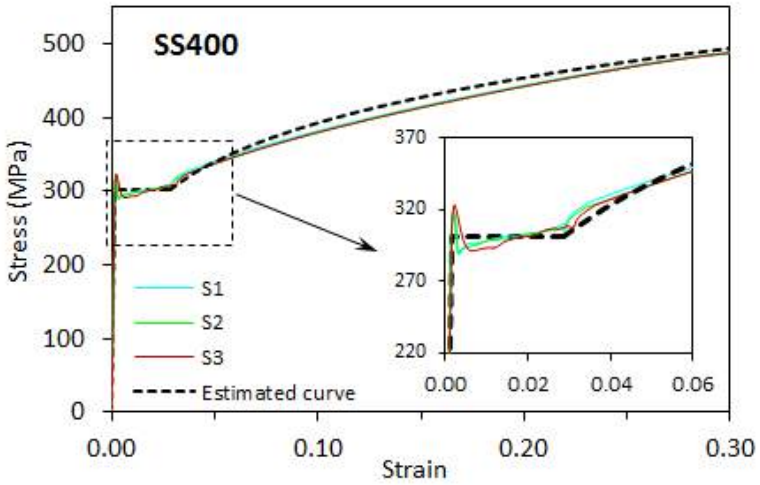


그림 33. SS400 구조용 강재의 항복강도와 경화지수 비교

- SM490 구조용 강재의 경우, 항복강도와 경화지수의 오차율은 각각 2.5%, 5.3%임

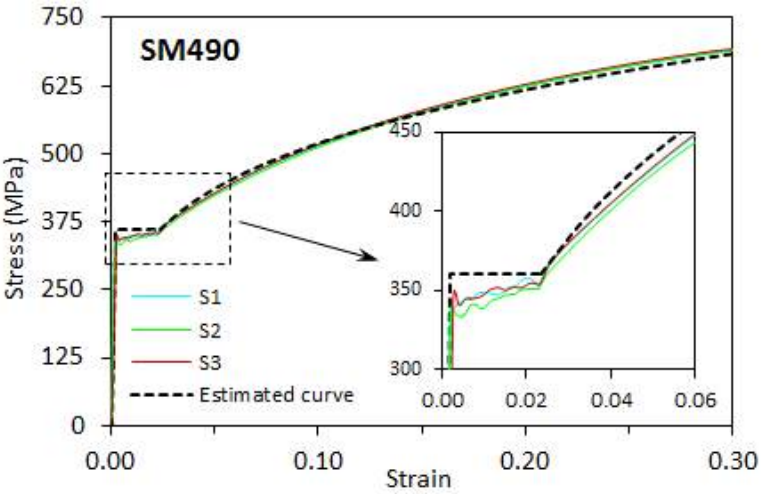


그림 34. SM490 구조용 강재의 항복강도와 경화지수 비교

다. 구조용 강재의 잔류응력에 따른 강재 미세구조의 특성변화

(1) 시험체의 잔류 응력 도입장치 개발 (등록번호 : 10-1670064)

(가) 기술분야

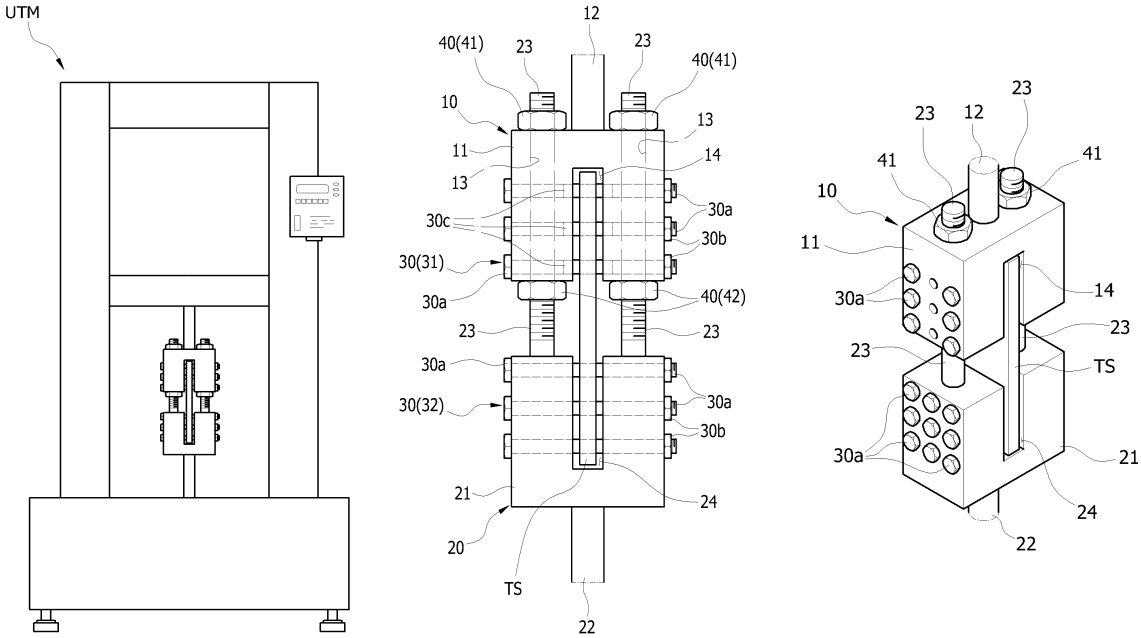
- 시험체의 잔류 응력 도입을 위하여 개발한 제품으로, 양단의 로딩바를 UTM에 체결하여 외부하중을 이가하고, 서포팅 컬럼을 고정하여 시험체에 균일한 잔류 응력을 도입함으로써, 잔류 응력에 따른 추가적인 압입실험 결과의 차이를 연구하기 위한 장치

(나) 배경기술

- 인덴테이션이란, 시험체의 기계적 성질을 분석하기 위한 방법 중 하나로서, 다양한 형상의 다이아몬드 압입자를 재료에 압입한 후 그 압입자국과 압입 시의 하중을 비교, 분석하여 시험체의 경도나 파괴인성 등을 정밀하게 측정하기 위한 방법
- 인덴테이션은 다양한 범주의 연구에 사용되고 있으며, 그 범주로서 시험체의 탄소성 거동, 잔류 응력상태의 해석, 박막의 응착력 시험, 파괴특성, 상변화 해석 등에 대한 연구기법으로도 널리 활용되고 있으며, 최근에는 공학기술의 미세화와 소형화에 따라 나노인덴테이션(nanoindentation)의 실험방법이 개발된 바 있음
- 통상적으로 잔류 응력을 도입하기 위한 기구로서 UTM(Universal Testing Machine)을 사용하나, UTM에 고정된 시험체를 바탕으로 추가적인 압입설험을 수행하는 것에는 많은 제약이 따를 수 밖에 없으므로 대한민국 실용신안공보 제20-0312482호 '외부하중이 인가된 시편의 나노인덴테이션용 실험 치구'(2003. 04. 23. 등록, 이하 '선행기술문헌'이라 한다)가 제안된 바 있음
- 선행기술문헌은 시험체에 가해지는 외부하중을 임의로 변화시키면서 이 외부하중이 유지된 상태로 나노인덴테이션 실험을 수행하고자 개발되었으나, 꺾임시험(bending test)을 통하여 외부하중을 인가하는바, 시험체의 단면 위치에 따라 선형의 인장력과 압축력 분포가 도입되어 균일한 응력분포를 확보할 수 없는 문제점이 있음
- 본 발명은 선행기술문헌의 문제점을 해결하기 위하여 안출된 것으로서, UTM을 이용하여 시험체에 외부하중을 인가하되, 추가적인 압입실험을 수행할 수 있도록 분리할 수 있으며, 시험체의 단면 위치와 무관하게 균일한 응력분포를 확보할 수 있음

(다) 발명의 효과

- 시험체의 잔류 응력 도입장치에 따르면, 양단에 로딩바가 구비되어 UTM을 체결하여 시험체에 외부하중을 인가하고, 장치를 UTM으로부터 분리하여 추가적인 압입실험을 수행할 수 있음
- 서포팅 컬럼이 컬럼홀을 관통하여 외측나사와 내측나사에 의하여 제1 몸체와 고정되어 인가된 하중이 고정될 수 있음
- 시험체의 단면 위치와 무관하게 균일한 응력분포를 확보할 수 있음



(a) (b) (c)

그림 35. 시험체의 잔류 응력 도입장치

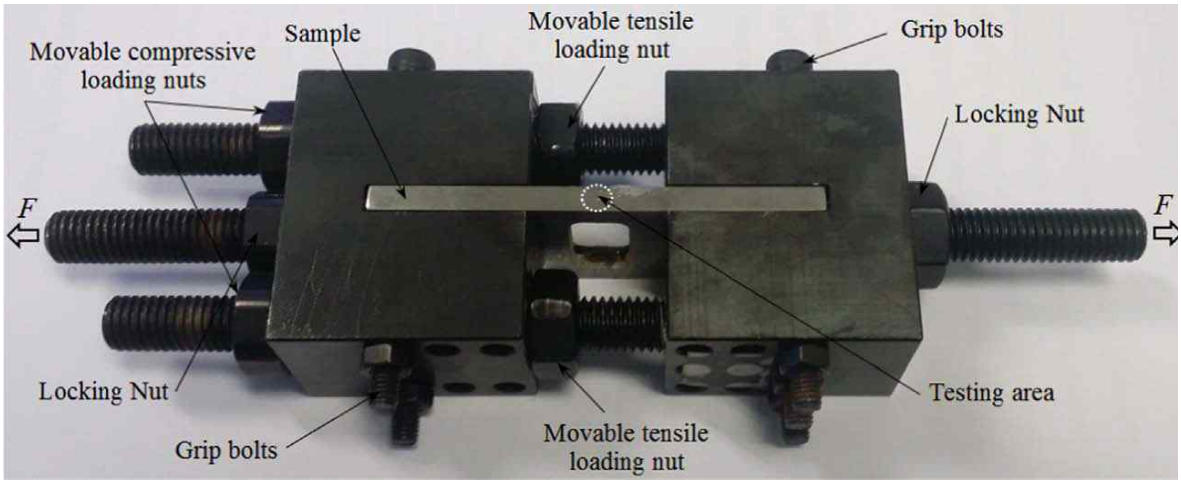


그림 36. 시험체의 잔류 응력 도입장치 실제 모습

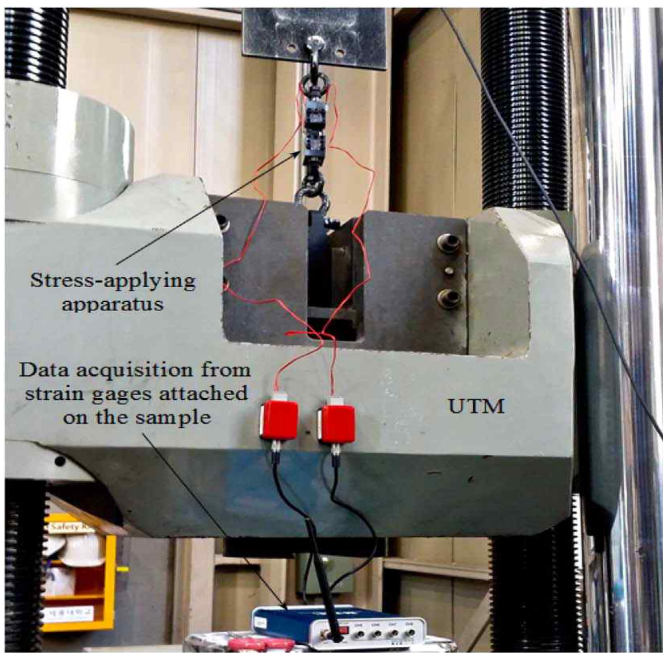


그림 37. 시험체에 잔류 응력 도입을 위한 인장 실험 모습

(2) 나노압입실험

■ 잔류응력이 도입된 강재의 미세구조 구성성분비 도출

• 잔류응력 상태에서 나노압입 실험 수행

		SS400			
		Wt (N.mm)	We (N.mm)	S (N/mm)	hm (mm)
Test	1	0.10893	0.00417	1824.6	0.002018
Test	2	0.10657	0.00393	1864.4	0.002020
Test	3	0.10721	0.00391	1863.0	0.002033
Test	4	0.11595	0.00463	1879.3	0.002018
Test	5	0.11695	0.00473	1881.2	0.002013
Test	6	0.11121	0.00415	1938.6	0.002018
Test	7	0.09955	0.00337	1898.0	0.002021
Test	8	0.10948	0.00429	1820.9	0.002003
Test	9	0.12236	0.00515	1867.4	0.002023
(a) sR = 117.3 MPa					
Test	1	0.09480	0.00312	1867.0	0.002018
Test	2	0.98250	0.00396	1879.9	0.002022
Test	3	0.09996	0.00346	1863.9	0.002021
Test	4	0.96009	0.00360	1858.8	0.002021
Test	5	0.10418	0.00375	1875.8	0.002021
Test	6	0.09991	0.00355	1814.9	0.002022
Test	7	0.90999	0.00368	1859.1	0.002029
Test	8	0.99442	0.00410	1806.0	0.002015
Test	9	0.09120	0.00289	1869.1	0.002017
(b) sR = 236.9 MPa					

표 14. SS400 구조용 강재의 잔류응력 상태에서 나노압입 실험 결과

		SM490			
		Wt (N.mm)	We (N.mm)	S (N/mm)	hm (mm)
Test	1	0.13416	0.00587	1984.8	0.002018
Test	2	0.14567	0.00692	1969.7	0.002020
Test	3	0.12530	0.00492	2041.7	0.002033
Test	4	0.13997	0.00634	1992.6	0.002018
Test	5	0.12015	0.00468	2016.4	0.002013
Test	6	0.12825	0.00523	2047.0	0.002018
Test	7	0.11923	0.00445	2080.9	0.002021
Test	8	0.12040	0.00485	1961.3	0.002003
Test	9	0.14628	0.00686	2000.0	0.002023
(a) sR = 184.6 MPa					
Test	1	0.11452	0.00423	2019.3	0.002018
Test	2	0.11083	0.00425	2041.7	0.002022
Test	3	0.11284	0.00403	2060.7	0.002021
Test	4	0.11716	0.00506	1991.8	0.002021
Test	5	0.10888	0.00381	2028.1	0.002021
Test	6	0.11899	0.00501	1953.4	0.002022
Test	7	0.11169	0.00422	2030.8	0.002029
Test	8	0.10290	0.00350	1978.3	0.002015
Test	9	0.11848	0.00452	2028.1	0.002017
(b) sR = 311.5 MPa					

표 15. SM490 구조용 강재의 잔류응력 상태에서 나노압입 실험 결과

• 잔류응력과 미세구조 구성성분비, 기계적 성질간의 관계 정립

	SS400							
	σ_y (MPa)	% err. sy	σ_R (MPa)	% err. σ_R	n	% err. n	a	% err. a
Test 1	271.3	-13.5 %	95.0	-19.0 %	0.273	12.4 %	7.8	-20.3 %
Test 2	306.5	-2.3 %	137.9	17.6 %	0.274	12.8 %	9.4	-4.0 %
Test 3	278.2	-11.3 %	102.9	-12.3 %	0.270	11.2 %	9.3	-5.0 %
Test 4	341.2	8.8 %	122.8	4.7 %	0.253	4.0 %	10.7	9.2 %
Test 5	355.9	13.5 %	113.9	-2.9 %	0.259	6.4 %	11.9	21.2 %
Test 6	347.2	10.7 %	121.5	3.6 %	0.209	-13.8 %	10.9	11.0 %
Test 7	280.5	-10.6 %	126.2	7.6 %	0.232	-4.4 %	9.5	-3.0 %
Test 8	288.7	-8.0 %	92.4	-21.3 %	0.276	13.6 %	8.6	-12.3 %
Test 9	336.6	7.3 %	131.3	11.9 %	0.238	-2.0 %	8.0	-18.0 %
Ave.	311.8	-0.6 %	116.0	-1.1 %	0.254	4.5 %	9.6	-2.4 %
STDEV	31.7		15.2		0.024		1.3	
COV*	10.1 %		13.0 %		10.0 %		13.3 %	

(a) sR = 117.3 MPa

Test 1	273.6	-12.8 %	199.7	-15.7 %	0.235	-3.2 %	9.5	-3.0 %
Test 2	363.7	16.0 %	294.6	24.4 %	0.222	-8.8 %	11.0	12.0 %
Test 3	283.7	-9.5 %	229.8	-3.0 %	0.218	-10.4 %	7.7	-21.0 %
Test 4	298.2	-4.9 %	196.8	-16.9 %	0.237	-2.4 %	8.5	-13.0 %
Test 5	316.2	0.8 %	240.3	1.5 %	0.229	-5.6 %	10.0	2.5 %
Test 6	293.8	-6.3 %	273.2	15.3 %	0.280	15.2 %	11.1	13.0 %
Test 7	323.5	3.1 %	274.9	16.1 %	0.227	-6.4 %	8.7	-11.0 %
Test 8	329.9	5.2 %	260.6	10.0 %	0.266	9.6 %	9.2	-6.0 %
Test 9	275.8	-12.0 %	220.7	-6.9 %	0.245	0.8 %	11.4	16.0 %
Ave.	306.5	-2.3 %	243.4	2.7 %	0.240	-1.2 %	9.7	-1.2 %
STDEV	28.7		33.3		0.020		1.2	
COV*	9.2 %		14.1 %		8.1 %		12.3 %	

(b) sR = 236.9 MPa

표 16. SS400 구조용 강재의 잔류응력과 미세구조 구성성분비, 기계적 성질간의 관계

	SM490							
	σ_y (MPa)	% err. sy	σ_R (MPa)	% err. σ_R	n	% err. n	a	% err. a
Test 1	442.9	12.1 %	225.9	22.4 %	0.272	18.4 %	14.6	21.0 %
Test 2	452.4	14.5 %	194.5	5.4 %	0.259	12.8 %	9.4	-22.0 %
Test 3	392.0	-0.8 %	152.9	-17.2 %	0.256	11.2 %	13.9	15.0 %
Test 4	435.6	10.2 %	183.0	-0.9 %	0.239	4.0 %	10.7	-11.6 %
Test 5	387.7	-1.9 %	193.9	5.0 %	0.245	6.4 %	12.9	7.0 %
Test 6	435.6	10.2 %	217.8	18.0 %	0.214	-6.8 %	13.2	9.0 %
Test 7	400.9	1.5 %	208.5	12.9 %	0.197	-14.4 %	12.6	4.0 %
Test 8	350.5	-11.3 %	140.2	-24.1 %	0.270	17.6 %	10.4	-14.0 %
Test 9	456.3	15.4 %	196.2	6.3 %	0.225	-2.0 %	10.0	-17.0 %
Ave.	417.1	5.5 %	190.3	3.1 %	0.242	5.2 %	12.0	-1.0 %
STDEV	40.3		33.6		0.027		1.8	
COV*	10.2 %		18.2 %		11.8 %		14.6 %	

(a) sR = 184.6 MPa

Test 1	366.3	-7.3 %	256.4	-17.7 %	0.223	-3.2 %	11.3	-7.0 %
Test 2	410.3	3.8 %	291.3	-6.5 %	0.210	-8.8 %	12.7	5.0 %
Test 3	382.1	-3.3 %	263.7	-15.4 %	0.206	-10.4 %	13.1	8.0 %
Test 4	416.7	5.4 %	333.4	7.0 %	0.224	-2.4 %	11.1	-8.0 %
Test 5	360.0	-8.9 %	302.4	-2.9 %	0.217	-5.6 %	12.2	1.0 %
Test 6	433.8	9.8 %	373.1	19.8 %	0.274	19.2 %	14.4	19.0 %
Test 7	426.8	8.0 %	371.3	19.2 %	0.215	-6.4 %	14.2	17.0 %
Test 8	328.7	-16.8 %	299.1	-4.0 %	0.252	9.6 %	12.5	3.0 %
Test 9	404.0	2.2 %	270.7	-13.1 %	0.232	0.8 %	14.3	18.0 %
Ave.	392.1	-0.8 %	306.8	-1.5 %	0.228	-0.8 %	12.9	6.2 %
STDEV	33.2		41.5		0.021		1.4	
COV*	8.4 %		13.3 %		9.0 %		11.5 %	

(b) sR = 311.5 MPa

표 17. SM490 구조용 강재의 잔류응력과 미세구조 구성성분비, 기계적 성질간의 관계

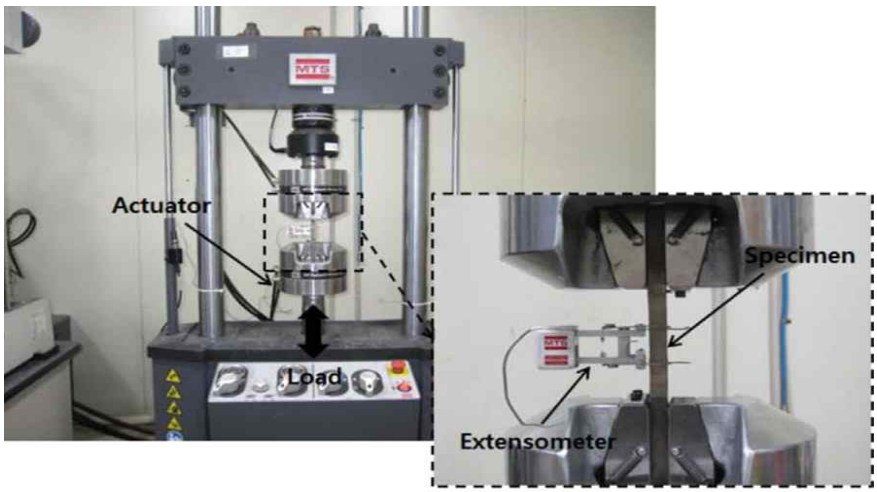
라. 구조용 강재 용접부의 피로상태에 따른 강재 미세구조의 특성변화

(1) 용접부를 포함한 SS400 강재의 피로실험

- 일반적으로 강구조물의 피로에 대한 설계는 강구조물 사용 시 부재에 작용하는 응력을 강재의 내구한계(endurance limit) 이내로 제한하는 것이며 평균응력 S에 대하여 파단이 발생하는 반복횟수를 결정하는 실험



(a) 시험체



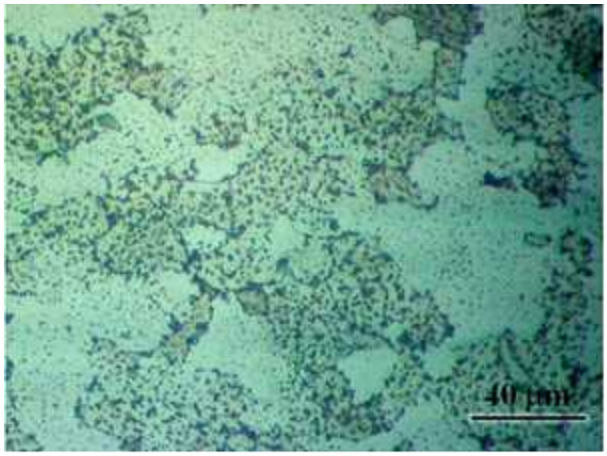
(b) 실험 장비 (Actuator)



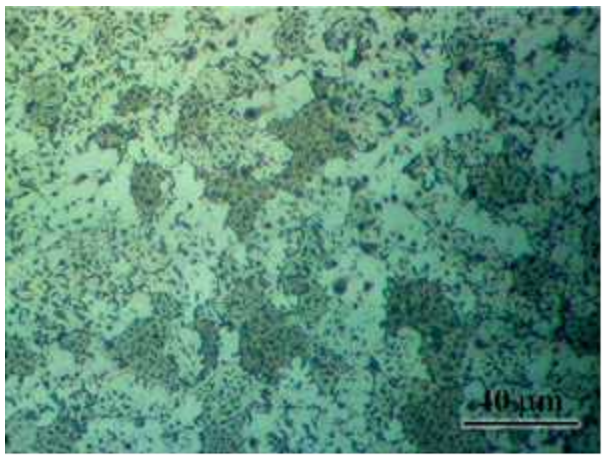
(c) 실험장비에서의 시험체 옆 모습

그림 38. 피로 실험 시험체와 장비

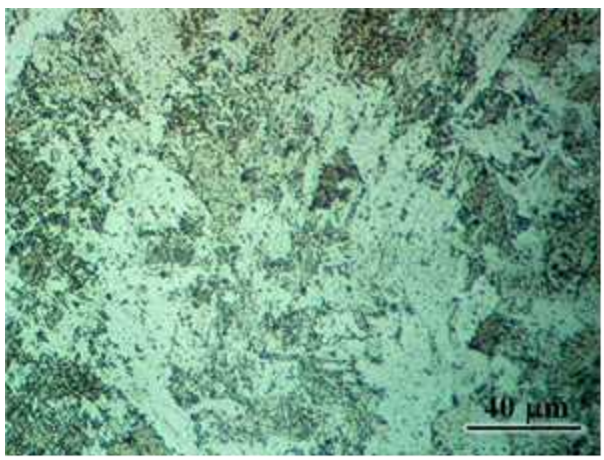
(2) SEM, 광학현미경 촬영으로 피로에 의한 강재의 미세구조 변화 검증



(a) BM의 미세구조

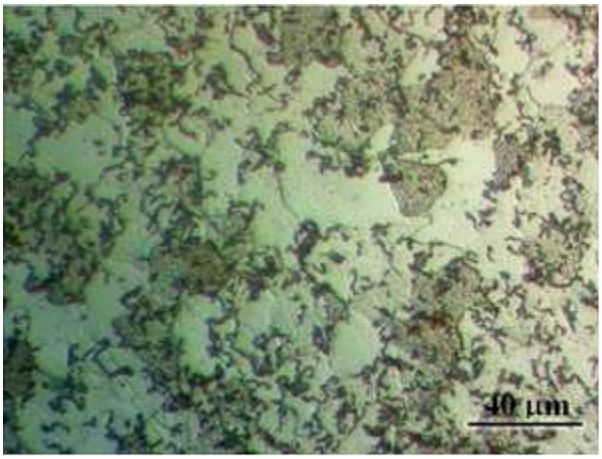


(b) HAZ의 미세구조

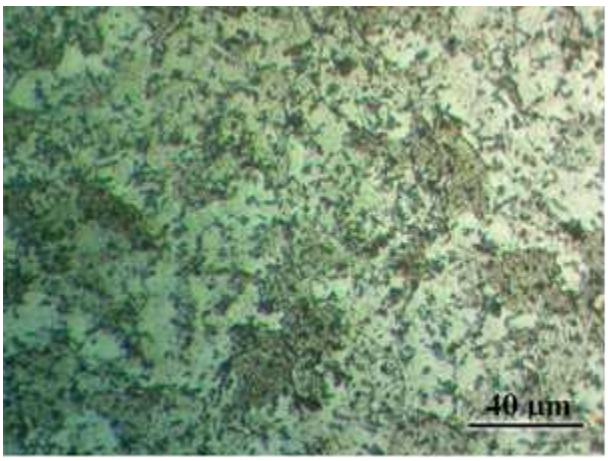


(c) WM의 미세구조

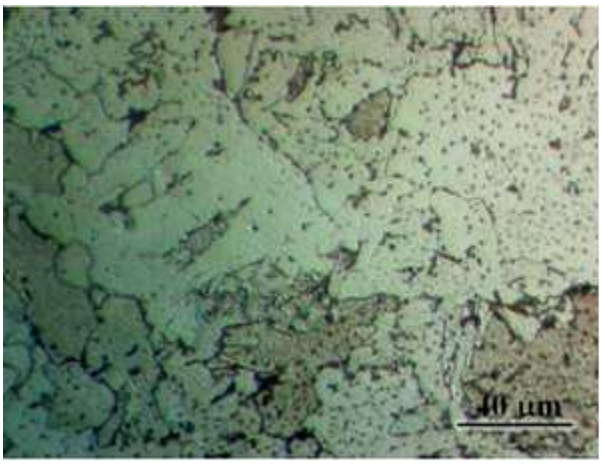
그림 39. SEM, 광학현미경에서의 피로실험 전 SS400 구조용 강재 용접부 미세구조 모습



(a) BM의 미세구조



(b) HAZ의 미세구조



(c) WM의 미세구조

그림 40. SEM, 광학현미경에서의 피로실험 후 SS400 구조용 강재 용접부 미세구조 모습

(3) 피로실험된 용접부의 항복응력, 경화지수 결정

- 5가지 평균응력에서의 용접부의 WM, HAZ, BM 값 측정

	S0 (ea = 0.0%)	S1 (ea = 0.4%)	S2 (ea = 0.6%)	S3 (ea = 0.8%)	S4 (ea = 1.0%)
WM	9.0	8.0	8.0	8.0	8.0
HAZ	15.0	12.0	12.0	10.0	9.0
BM	18.1	15.0	13.0	11.0	10.0

표 18. 5가지 평균응력에서의 용접부의 값 측정

- 나노압입 실험을 수행하여 피로실험된 용접부의 미세구조의 기계적 특성 구성성분비를 도출함

Virgin SS400	steel weld zone	Present study	Previous study	Err. (%)
E (GPa)	WM	215.9	218.2	-1.05*
	HAZ	211.1	212.4	-0.61
	BM	206.7	207.2	-0.24
sy (MPa)	WM	407.2	403.5	0.92
	HAZ	338.3	331.4	2.08
	BM	297.6	302.7	-1.68
n	WM	0.212	0.203	4.43
	HAZ	0.205	0.195	5.13
	BM	0.193	0.191	1.05

표 19. SS400 구조용 강재의 기계적 특성 구성성분비 도출

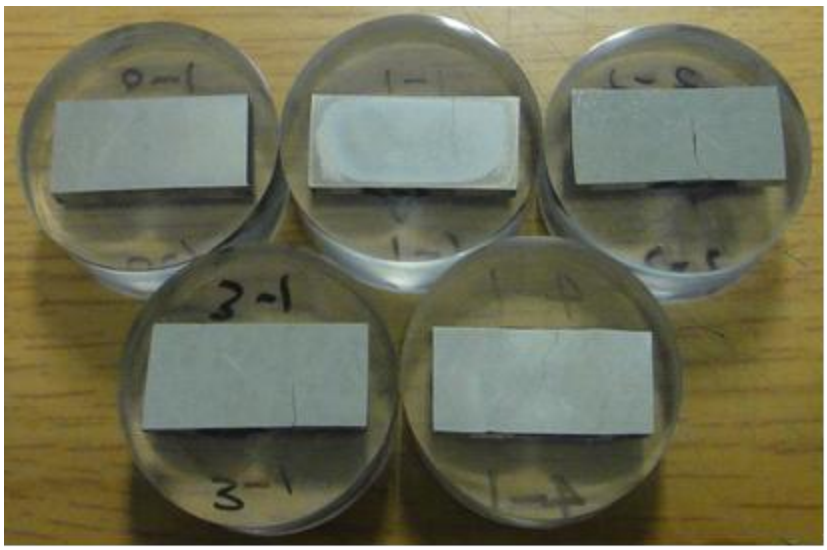


그림 42. 나노압입 실험 후의 다섯가지 샘플1

마. 피로도와 잔류응력을 고려한 용접연결부의 정량적 건전성 지표 개발

(1) 잔류응력과 피로도를 고려한 구조용 강재 용접부 건전도 지수 결정

- 잔류응력에 대한 나노압입 실험 결과와 피로에 대한 나노압입 실험 결과를 바탕으로 구조용 강재 용접부의 건전도지수를 산출하는 알고리즘 고안
- 제안된 기법들을 강재 용접부의 비파괴 검사를 위한 방안으로 발전시키기 위해 용접부의 건전성을 정량적으로 나타낼 수 있는 지표를 제안함
- 확률분포를 이용한 일반적인 통계기법이 사용되었으며, 나노압입에 의해 측정된 강재의 피로상태, 잔류응력, 항복응력을 이용하여 용접 연결부의 상태를 나타내는 지표를 제안함
- 구조용 강재의 다양한 잔류응력과 피로도에 따라 각각의 미세구조의 기계적 성질과 성분비의 분포가 결정됨

(2) 나노압입 실험을 활용하여 구조용 강재 용접부의 건전도지수를 산출하는 알고리즘

(출원번호 : 10-2017-0052870)

(가) 배경기술

- 강구조 용접부의 나노압입 결과로부터 산출된 물성치 (예, 탄성계수, 항복응력, 경화지수 등)를 사용하여 강재의 손상정도(예, 피로, 잔류응력 등)를 고려한 퍼지멤버쉽함수(Fuzzy membership function)로 이루어진 데이터베이스에 대한 유사도를 산출하고, 용접부의 건전성 지표를 결정함

(나) 구성 및 작용

- 구조용 강재는 다양한 이점으로 많은 인프라 구조물의 재료로 사용되고 있으며, 강재는 다른 재료에 비해 비강도와 비강성이 매우 크고 인성과 연성도 우수함. 강재를 이용한 구조물은 볼팅(Bolting)과 용접으로 연결이 가능하기 때문에 강구조는 보수보강 또는 증개축이 용이함. 이러한 강재의 장점에도 불구하고, 강재의 연결부는 강구조의 가장 취약한 부분으로 알려져 있으며, 특히 반복하중에 의한 피로에 취약함. 강재를 용접에 의해 연결 시 용접부는 그림 42에서 보인 것처럼 강재(Base Metal, BM), 용접모재(Weld Metal, WM), 열영향부(Heat Affected Zone, HAZ)로 구성됨

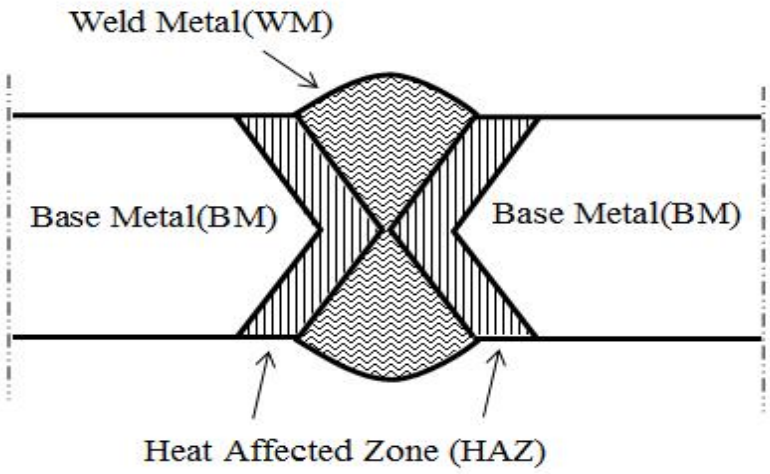
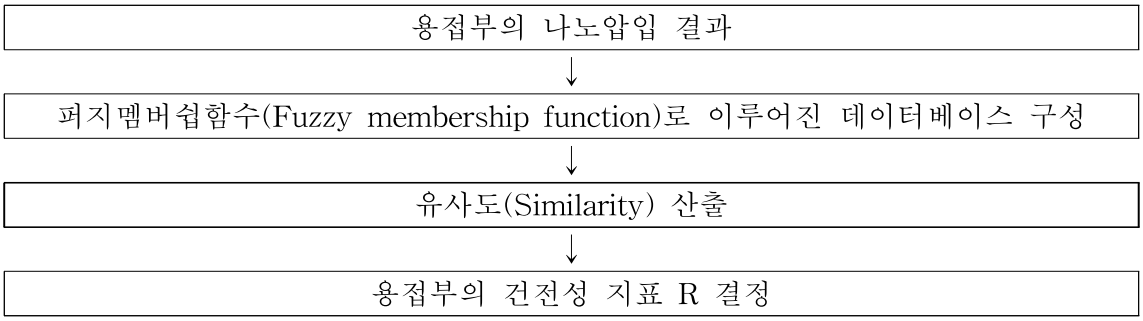


그림 42. 강재의 용접부

(다) 용접부의 건전성 지표를 결정하는 방법

- 강구조 용접부에 나노압입을 수행하고 WM, HAZ, BM에 대한 물성치 (예, 탄성계수, 항복응력, 경화지수 등)를 산출함
- 용접부의 건전성을 평가하기 위하여 피로도, 잔류응력 및 충격 중 적어도 하나의 손상대상을 선정하거나 탄성계수, 항복응력 및 경화지수 중 적어도 하나의 물성치를 선정하는 손상대상/물성치 선정부를 포함할 수 있음
- 강재의 손상정도(예, 피로, 잔류응력 등)에 따른 퍼지멤버쉽합수(Fuzzy membership function)를 작성하여 데이터베이스(Database)를 구성함
- 구조용 강재 용접부는 강재(Base Metal, BM), 용접모재(Weld Metal, WM) 및 열영향부(Heat Affected Zone, HAZ) 중 적어도 하나의 영역을 포함하고, 상기 손상정도는 없음(N), 낮음(L), 중간(ML), 약간높음(MH) 및 높음(H)의 단계를 구성함
- 실험결과와 데이터베이스에 대한 유사도(Similarity)를 산출함
- 유사도에 가중치(Weight)와 지표계수(Scaling factor)를 곱하고 0과 1사이의 값으로 맵핑(Mapping)하여 건전성지수를 결정함



① 강구조 용접부에 나노압입을 수행하고 WM, HAZ, BM에 대한 물성치 (예, 탄성계수, 항복응력, 경화지수 등)를 산출함

구분	WM	HAZ	BM
평균(GPa)	215.0	210.0	205.0
표준편차(GPa)	3.5	4.0	5.0

표 20. 나노압입에 의해 결정된 용접부 물성치의 예 (탄성계수)

② 강재의 손상정도(예, 피로, 잔류응력 등)에 따른 퍼지멤버쉽합수(Fuzzy membership function)를 작성하여 데이터베이스(Database)를 구성함

손상정도		없음	낮음	중간	약간높음	높음
기호		N	L	ML	MH	H
피로 정도		0.0	0.40%	0.60%	0.80%	1.00%
WM	평균(GPa)	215.9	211.9	210.9	207.0	203.0
	표준편차(GPa)	2.8	2.9	2.3	5.0	9.1
HAZ	평균(GPa)	211.1	202.9	202.7	188.0	187.6
	표준편차(GPa)	4.5	8.3	5.1	6.1	7.1
BM	평균(GPa)	206.7	198.0	194.9	179.8	174.9
	표준편차(GPa)	3.6	3.8	10.1	8.1	6.7

표 21. 강재의 손상정도(피로도)에 따른 용접부 물성치(탄성계수)

$$\mu = \exp\left(-\frac{(x-m)^2}{\sigma^2}\right) \qquad (1)$$

- 식(1)에서 μ는 퍼지멤버쉽, m은 평균, σ는 표준편차이다.

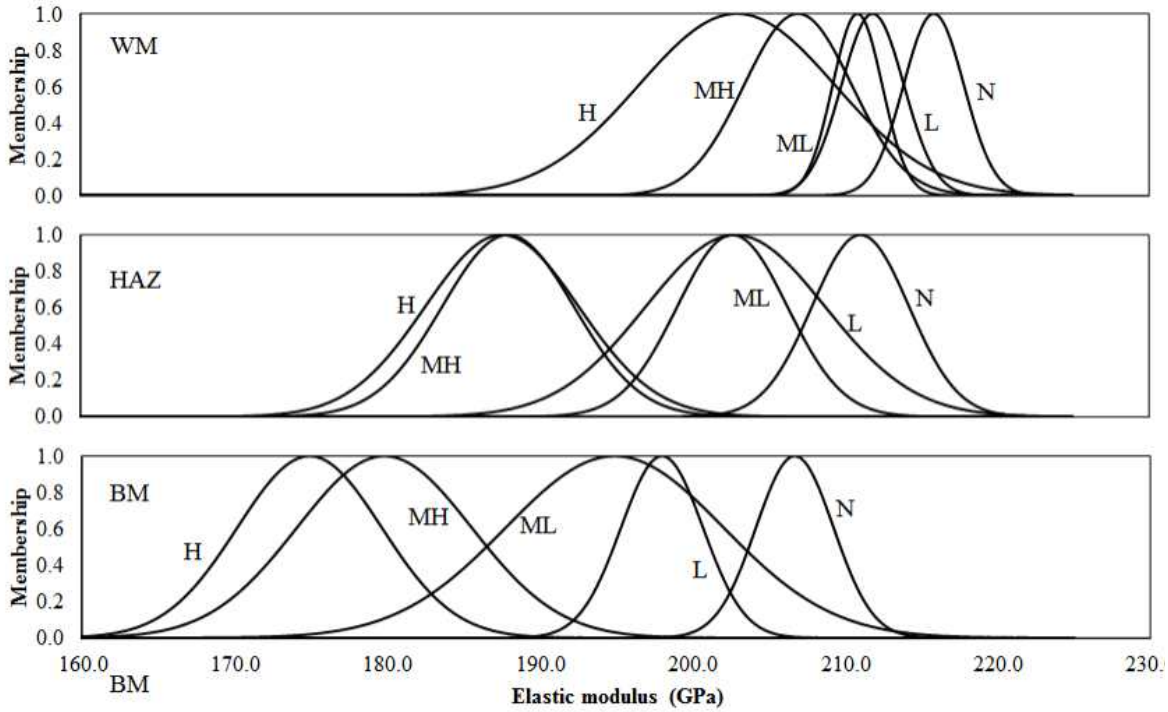


그림 43. 퍼지멤버쉽함수로 구성된 데이터베이스

③ 실험결과와 데이터베이스에 대한 유사도(Similarity)를 산출함

- 식(2)로부터 실험결과와 데이터베이스에 대한 유사도(Similarity)를 산출함

$$\lambda(A,B)=\frac{1}{2}\left\{\exp\left[-\frac{(m_A-m_B)^2}{(\sigma_A+\sigma_B)^2}\right]+1\right\} \qquad (2)$$

- 식(2)에서 m과 σ는 해당 퍼지멤버쉽함수 A(실험결과)와 B(데이터베이스)의 평균과 표준편차임
- 산출된 유사도는 강재 용접부의 영역에 따른 손상정도의 단계를 바탕으로 유사도 행렬로 산출될 수 있음. 또한, 산출된 유사도 행렬에 중요도에 따라 가중치 벡터를 부여하는 가중치 부여부를 포함할 수 있음
- 실험결과를 WM, HAZ, BM 영역(행)별로 N, L, ML, MH, H의 손상정도(열)에 따른 데이터베이스와 유사도를 결정하면, 식(3)의 행렬을 얻음

$$\Lambda=\begin{bmatrix}\lambda(E_{WM},D_{WM-N}) & \lambda(E_{WM},D_{WM-L}) & \lambda(E_{WM},D_{WM-ML}) & \lambda(E_{WM},D_{WM-MH}) & \lambda(E_{WM},D_{WM-H})\\ \lambda(E_{HAZ},D_{HAZ-N}) & \lambda(E_{HAZ},D_{HAZ-L}) & \lambda(E_{HAZ},D_{HAZ-ML}) & \lambda(E_{HAZ},D_{HAZ-MH}) & \lambda(E_{HAZ},D_{HAZ-H})\\ \lambda(E_{BM},D_{BM-N}) & \lambda(E_{BM},D_{BM-L}) & \lambda(E_{BM},D_{BM-ML}) & \lambda(E_{BM},D_{BM-MH}) & \lambda(E_{BM},D_{BM-H})\end{bmatrix} \qquad (3)$$

- 식(3)의 Λ행렬 1행 1열의 값 λ(EWM,DWM-N)는 WM영역의 실험결과(EWM)을 WM영역의 손상 없음 데이터베이스 함수(DWM-N)과 유사도를 결정한 값임

④ 유사도에 가중치(Weight)와 지표계수(Scaling factor)를 곱하고 0과 1사이의 값으로 맵핑(Mapping)하여 건전성지수를 결정함

- 유사도 행렬에 식(4)의 가중치(Weight) 행벡터와 식(5)의 지표계수 (Scaling factor) 열벡터를 곱하고 식(6)과 같이 0과 1사이의 값으로 맵핑 (Mapping) 하여 건전성지수 R을 결정함

$$w = \{w_{WM}, w_{HAZ}, w_{BM}\} \qquad (4)$$

- 식(4)의 행벡터의 값은 WM, HAZ, BM에 대한 가중치를 순서대로 쓴 것임. 가중치는 용접부 영역의 중요도에 따라 달라질 수 있음

$$f = \begin{Bmatrix} f_N \\ f_L \\ f_{ML} \\ f_{MH} \\ f_H \end{Bmatrix} \qquad (5)$$

- 식(5)의 열벡터의 값은 손상정도 N, L, ML, MH, H를 건전성 지표로 스케일링하는 값임
- 건전성지표 R은 식(6)으로 결정되며, 0과 1사이의 값을 갖음. 지표가 1에 가까울수록 용접부가 건전함을 나타냄

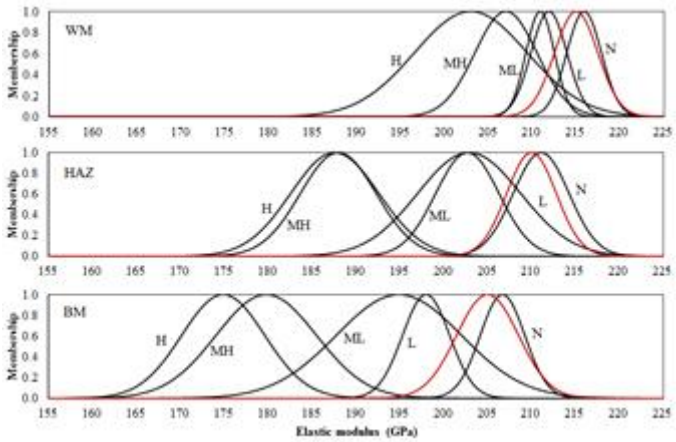
$$R = \frac{w\Lambda f - R_{\min}}{R_{\max} - R_{\min}} \qquad (6)$$

- 식(6)에서 Rmax와 Rmin은 지표를 맵핑하기 위한 wΛf값의 최대값과 최소값임

(라) 용접부의 건전도 판단 요약

- 본 발명의 구조용 강재 용접부의 건전성 지표 결정 시스템 및 방법에 의하면, 유사도 산출부가 산출된 대상 퍼지멤버쉽함수와 데이터베이스의 퍼지멤버쉽함수에 대한 유사도를 산출하므로, 측정된 물성치를 바탕으로 구조용 강재의 건전성 지표를 간편하게 결정할 수 있음
- 이때, 물성치 측정부가 나노압입 실험을 바탕으로 구조용 강재에 구조적 부담을 주지 않으면서도 대상 구조용 강재의 정확한 물성치를 측정할 수 있음
- 강재 용접부의 단순한 건전성 평가에 더 나아가 사용연한에 따른 건전성을 지속적으로 관리하여 정량적인 분석이 가능한 효과가 있으며, 손상정도/물성치 선정부가 강재 용접부의 건전성을 평가하기 위하여 피로도, 잔류응력 및 충격 중 적어도 하나의 손상대상을 선정하거나 탄성계수, 항복응력 및 경화지수 중 적어도 하나의 물성치를 선정할 수 있어 다양한 항목에 대한 정확도 높은 건전성 평가가 가능한 이점이 있음
- 가중치 부여부가 산출된 유사도 행렬에 중요도에 따라 가중치 벡터를 부여함으로써 용접부를 구성하는 강재, 용접모재 및 열영향부를 종합적으로 고려하여 용접부의 건전성을 결정할 수 있으며, 용접부의 형상에 따라서 각 영역의 중요도를 달리 고려할 수 있음
- 건전성 지표 산출부가 건전성 지표(R)를 0과 1 사이의 값으로 산출하여 강재 용접부의 건전성을 보다 직관적이고 용이하게 평가할 수 있도록하며, 건전성 지표(R)가 1에 가까울수록 구조용 강재 용접부의 건전성이 높음을 의미함
- 건전도 판단 예시는 아래와 같음

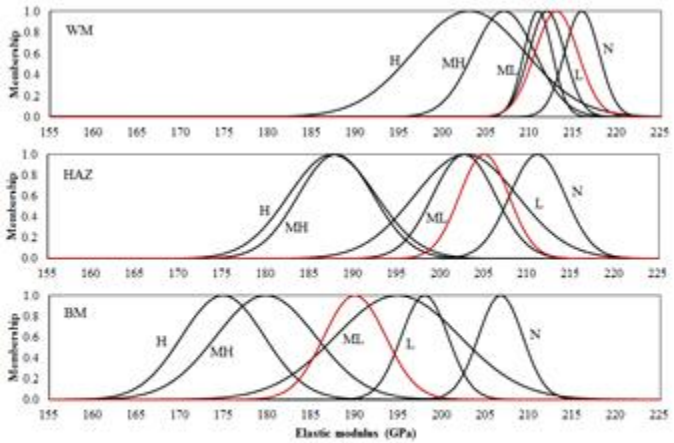
✓ 건전도 판단 예시1



건전도 지수 = 0.968

→ 건전성 지표가 N에 해당함을 의미하며, 손상정도는 없음으로 간주함

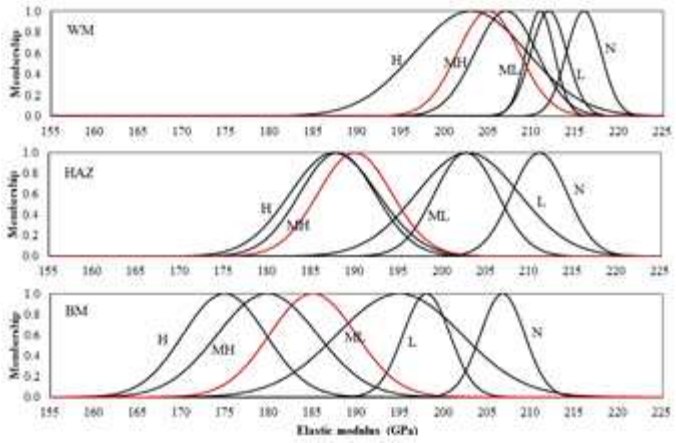
✓ 건전도 판단 예시2



건전도 지수 = 0.519

→ 건전성 지표가 ML에 해당함을 의미하며, 손상정도는 중간정도로 간주함

✓ 건전도 판단 예시3



건전도 지수 = 0.088

→ 건전성 지표가 MH에 해당함을 의미하며, 손상정도는 약간 높음정도로 간주함

제4장. 목표 달성도 및 관련 분야 기여도

1절. 목표 달성도

1. 연구 성과목표 및 성과지표

가. 총괄 성과목표 및 성과지표

구분	핵심성과 (level1)		단위성과 (level2)		최종 성과점검기준					해당 기관	예산 (백만원)	양적 성과목표
					질적 성과지표		목표치	측정방법	검증방법	가중치			
주관	A	나노압입에 의한 구조용 강재의 미세구조 및 기계적 성질 도출기법 개발	A-1	나노압입에 의한 구조용 강재 용접부의 미세구조 구성성분비 파악기법 개발	①	구성성분비 오차	±5% 이하	나노압입	광학현미경, SEM 촬영, 화학성분검사결과와 비교 검증	4	세종대학교 및 경남대학교	100	SCI(E)급 학술지: 1 건
			A-2	나노압입에 의한 구조용 강재의 탄성계수, 항복응력, 경화지수 도출기법 개발	①	나노압입에 의한 항복강도, 경화지수 측정 오차	±5% 이하	나노압입	인장강도 실험 및 FEM 결과와 비교 검증	4	세종대학교 및 경남대학교	100	SCI(E)급 학술지: 1 건
	B	피로도와 잔류응력에 따른 미세구조 파악 및 용접연결부의 정략정 건전성 지표 개발	B-1	구조용 강재의 잔류응력에 따른 강재 미세구조의 특성변화 파악	①	잔류응력 측정 오차	±10% 이하	잔류응력 도입 장치를 활용한 나노압입	잔류응력 측정	4	세종대학교 및 경남대학교	71	특허: 출원 1 건 SCI(E)급 학술지: 1 건
			B-2	구조용 강재 용접부의 피로상태에 따른 강재 미세구조의 특성변화 파악	①	피로실험을 수행한 강재의 항복응력, 경화지수 오차	±10% 이하	나노압입	피로실험을 수행한 강재의 인장강도 실험 및 FEM 결과와 비교 검증	4	세종대학교	98	특허: 출원 1 건
			B-3	피로도와 잔류응력을 고려한 용접연결부의 정량적 건전성 지표 개발	①	건전성 지표 신뢰도	95% 이상	SCI 논문 게재	논문 게재 여부	4	세종대학교 및 경남대학교	31	SCI(E)급 학술지: 1 건
계										20		400	특허: 출원 2 건 SCI(E)급 학술지: 4 건

나. 연차별 성과목표 및 성과지표

(1) 1차년도

구분	핵심연구성과 (level1)		단위 성과 (level2)		1차년도 성과점검기준						해당 기관	예산 (백만)	정량목표
						질적성과지표	목표치	측정방법	검증방법	가중치			
주관	A	나노압입에 의한 구조용 강재의 미세구조 및 기계적 성질 도출기법 개발	A-1	나노압입에 의한 구조용 강재 용접부의 미세구조 구성성분비 파악기법 개발	①	구성성분비 오차	±5% 이하	나노압입	광학현미경, SEM 촬영, 화학성분검사결과와 비교 검증	10	세종대학교 및 경남대학교	100	SCI(E)급 학술지: 1 건
			A-2	나노압입에 의한 구조용 강재의 탄성계수, 항복응력, 경화지수 도출기법 개발	①	나노압입에 의한 항복강도, 경화지수 측정 오차	±5% 이하	나노압입	인장강도 실험 및 FEM 결과와 비교 검증	10	세종대학교 및 경남대학교	100	SCI(E)급 학술지: 1 건
계										20		200	SCI(E)급 학술지: 2 건

(2) 2차년도

구분	핵심연구성과 (level1)		단위 성과 (level2)		1차년도 성과점검기준						해당 기관	예산 (백만)	정량목표
						질적성과지표	목표치	측정방법	검증방법	가중치			
주관	B	피로도와 잔류응력에 따른 미세구조 파악 및 용접연결부의 정략정 건전성 지표 개발	B-1	구조용 강재의 잔류응력에 따른 강재 미세구조의 특성변화 파악	①	잔류응력 측정 오차	±10% 이하	잔류응력 도입 장치를 활용한 나노압입	잔류응력 측정	6	세종대학교 및 경남대학교	71	특허: 출원 1 건 SCI(E)급 학술지: 1 건
			B-2	구조용 강재 용접부의 피로상태에 따른 강재 미세구조의 특성변화 파악	①	피로실험을 수행한 강재의 항복응력, 경화지수 오차	±10% 이하	나노압입	피로실험을 수행한 강재의 인장강도 실험 및 FEM 결과와 비교 검증	6	세종대학교	98	특허: 출원 1 건
			B-3	피로도와 잔류응력을 고려한 용접연결부의 정량적 건전성 지표 개발	①	건전성 지표 신뢰도	95% 이상	SCI 논문 게재	논문 게재 여부	8	세종대학교 및 경남대학교	31	SCI(E)급 학술지: 1 건
계										20		200	특허: 출원 2 건 SCI(E)급 학술지: 2 건

다. 연도별 주요 추진 일정

구분	연구과제명 (연구수행 기관)	관련 성과목표/지표			세부추진내용 (연구수행 Activity)	Activity별 산출물	소요 연구비 (백만원)	1차년도				2차년도			
		핵심성과	단위성과	질적 성과지표				1/4	2/4	3/4	4/4	1/4	2/4	3/4	4/4
총괄							400	200				200			
주관	나노압입을 이용한 구조용 강재 용접부의 미세구조 파악 및 건전성 지표 개발 연구 (세종대학교)	A	A-1	A-1-①	기존 나노압입 분석방법 연구	나노압입 분석방법	19	19							
					구조용강 용접부에 적용	-	19	19							
					미세구조 구성성분비 도출	미세구조 탄성계수 및 경도의 빈도 함수	19		19						
					SEM, 광학현미경 촬영사진과 화학성분비 분석으로 결과 검증	미세구조 구성성분비 파악 기법	19		19						
		A	A-2	A-2-①	기존 나노압입 분석방법 연구	재료의 소성 성질 산정 기법	15			15					
					구조용강에 대한 유한요소해석과 차원해석 수행-산출식 결정	나노압입 유한요소 모델 및 차원해석에 의한 제안식	15			15					
					구조용강 SS400, SM490 용접부에 적용	-	18				18				
					항복응력, 경화지수 결정	강재의 항복응력 및 경화지수	14				14				
					인장실험 결과와 비교하여 산출식 검증	구조용 강재의 항복응력, 경화지수 등을 결정하는 제안식	14				14				
		B	B-1	B-1-①	항복응력, 경화지수 결정	잔류응력이 도입된 강재의 항복응력 및 경화지수	12					12			
					기존 연구와 결과 검증	잔류응력이 도입된 강재의 기계적 성질	12					12			
					잔류응력과 미세구조 구성성분비, 기계적 성질간의 관계 정립	미세구조 구성성분비 및 기계적 성질간의 관계	12					12			
		B	B-2	B-2-①	용접부를 포함한 SS400, SM490 강재의 피로실험	피로실험을 수행한 강재	36						36		
					나노압입 실험: 피로실험된 용접부의 미세구조 구성성분비 도출	피로실험을 수행한 강재 용접부의 미세구조 구성성분비	20						20		
					피로실험된 용접부의 항복응력, 경화지수 결정	피로실험을 수행한 강재 용접부의 소성 특성	15						15		
					인장실험으로 결과 검증	피로실험을 수행한 강재 용접부의 기계적 성질	15							15	
					피로도와 미세구조 구성성분비, 기계적 성질간의 관계 정립	미세구조 구성성분비 및 기계적 성질간의 관계	12							12	
		B	B-3	B-3-①	잔류응력과 피로도에 따른 나노압입 결과의 확률적 분석	잔류응력과 피로도에 따른 미세구조별 특성치 관계	18								18
위탁	나노압입에 의한 미세구조 분석기법과 용접부의 건전도 지수 개발 (경남대학교)	A	A-1	A-1-①	세라믹의 미세구조 분석법 (MIT) 벤치마킹	미세구조를 특정 지을 수 있는 물성치 파악 방법	24	24							
		A	A-2	A-2-①	유한요소해석과 차원해석에 의한 기법 (미국 U. of Michigan) 벤치마킹	유한요소해석 및 차원해석을 활용한 나노압입 결과 분석방법	24			24					
		B	B-1	B-1-①	잔류응력 도입장치 개발 및 검증	잔류응력 도입장치	20					20			
					나노압입실험: 잔류응력이 도입된 강재의 미세구조 구성성분비 도출	잔류응력이 도입된 강재의 미세구조 구성성분비	15					15			
		B	B-3	B-3-①	피로도와 잔류응력을 고려한 용접부 건전도 지수 결정	용접 연결부의 정량적 건전성 지표	13								13
계							400	200				200			

2. 연구개발 목표 달성도

가. 핵심성과물 달성도

목 표	달 성 도 (%)	내 용
나노압입에 의한 구조용 강재 용접부의 미세구조 구성성분비 파악기법 개발	100	• 기존 나노압입 분석방법 연구 • 구조용강 용접부에 적용 • 미세구조 구성성분비 도출 • SEM, 광학현미경 촬영사진과 화학성분비 분석으로 결과 검증 • 세라믹의 미세구조 분석법 (MIT) 벤치마킹
나노압입에 의한 구조용 강재의 탄성계수, 항복응력, 경화지수 도출기법 개발	100	• 기존 나노압입 분석방법 연구 • 구조용강에 대한 유한요소해석과 차원해석 수행-산출식 결정 • 구조용강 SS400, SM490 용접부에 적용 • 항복응력, 경화지수 결정 • 인장실험 결과와 비교하여 산출식 검증 • 유한요소해석 및 차원해석을 활용한 나노압입 결과 분석방법
구조용 강재의 잔류응력에 따른 강재 미세구조의 특성변화 파악	100	• 항복응력, 경화지수 결정 • 기존 연구와 결과 검증 • 잔류응력과 미세구조 구성성분비, 기계적 성질간의 관계 정립 • 잔류응력 도입장치 개발 및 검증 • 나노압입실험: 잔류응력이 도입된 강재의 미세구조 구성성분비 도출
구조용 강재 용접부의 피로상태에 따른 강재 미세구조의 특성변화 파악	100	• 용접부를 포함한 SS400, SM490 강재의 피로실험 • 나노압입 실험: 피로실험된 용접부의 미세구조 구성성분비 도출 • 피로실험된 용접부의 항복응력, 경화지수 결정 • 인장실험으로 결과 검증 • 피로도와 미세구조 구성성분비, 기계적 성질간의 관계 정립
피로도와 잔류응력을 고려한 용접연결부의 정량적 건전성 지표 개발	100	• 잔류응력과 피로도에 따른 나노압입 결과의 확률적 분석 • 피로도와 잔류응력을 고려한 용접부 건전도 지수 결정

나. 핵심성과물별 세부 설명

(1) 나노압입에 의한 구조용 강재 용접부의 미세구조 구성성분비 파악기법 개발

정의	나노압입을 이용한 강재 미세구조의 구성비 도출	
목적	나노압입을 강재 용접부의 비파괴 검사 방법으로 활용하기 위한 원천 기술 확보	
성능목표	(기존기술 수준) 세라믹의 미세구조 구성성분비 도출에 적용 되었음 (개발기술 수준) 구조용강의 페리트와 펄라이트, 시멘타이트 구성성분비 도출을 위한 방법 제시	
성과달성 책임자 (소속기관)	김승억 (세종대학교)	
소요기간	2015.06 ~ 2015.11 (0년6개월, 1년차)	
성과달성 확인방법	SEM촬영과 화학 성분비 검사를 이용하여, 제안된 기법에서 결정된 구성성분비 확인.	
성과달성에 따른 정량적 성과	특허 출원/등록	국내 : 0건, 국외 : 0건
	논문	국내 : 0건, 국외 : 1건
	저작	0건
	S/W	0건
	신기술	0건
	기타	0건
달성도 (%)	100	

(2) 나노압입에 의한 구조용 강재의 탄성계수, 항복응력, 경화지수 도출기법 개발

정의	구조용 강재의 나노압입 결과를 분석하여 항복강도, 경화지수 결정 알고리즘 개발	
목적	나노압입을 강재 용접부의 비파괴 검사 방법으로 활용하기 위한 원천 기술 확보	
성능목표	(기존기술 수준) 기계용 강재와 폴리머에 대한 알고리듬 개발되고 있음 (개발기술 수준) 구조용강의 소성특성, 항복강도와 경화지수 산정 기법 개발	
성과달성 책임자 (소속기관)	김승억 (세종대학교)	
소요기간	2015.12 ~ 2016.05 (0년6개월, 1년차)	
성과달성 확인방법	인장강도 실험을 통하여 구조용강의 구성방정식 도출후 나노압입결과에서 산정된 항복강도, 경화지수와 비교 검증	
성과달성에 따른 정량적 성과	특허 출원/등록	국내 : 0건, 국외 : 0건
	논문	국내 : 0건, 국외 : 1건
	저작	0건
	S/W	0건
	신기술	0건
	기타	0건
달성도 (%)	100	

(3) 구조용 강재의 잔류응력에 따른 강재 미세구조의 특성변화 파악

정의	구조용 강재의 잔류응력에 따른 강재 미세구조의 특성변화 연구	
목적	나노압입을 강재의 잔류응력 산정 방법으로 활용하기 위한 원천 기술 확보	
성능목표	(기존기술 수준) 강재의 잔류응력을 비파괴로 측정하기는 매우 어려운 실정임 (개발기술 수준) 잔류응력과 미세구조 구성성분비, 기계적 성질과의 관계 수립	
성과달성 책임자 (소속기관)	김승억 (세종대학교)	
소요기간	2016.06 ~ 2016.08 (0년3개월, 2년차)	
성과달성 확인방법	잔류응력 도입 장치에 대한 검증 (스트레인 게이지 부착). 기존 잔류응력에 따른 강재의 기계적 성질과 연구결과를 비교하여 검증	
성과달성에 따른 정량적 성과	특허 출원/등록	국내 : 1건, 국외 : 0건
	논문	국내 : 0건, 국외 : 1건
	저작	0건
	S/W	0건
	신기술	0건
	기타	0건
달성도 (%)	100	

(4) 구조용 강재 용접부의 피로상태에 따른 강재 미세구조의 특성변화 파악

정의	구조용 강재 용접부의 피로도에 따른 강재 미세구조의 특성변화 연구	
목적	나노압입을 강재의 피로도 산정 방법으로 활용하기 위한 원천 기술 확보	
성능목표	(기존기술 수준) 피로에 위한 미세균열 발생후 측정가능 (개발기술 수준) 피로도와 미세구조 구성성분비, 기계적 성질과의 관계 수립	
성과달성 책임자 (소속기관)	김승억 (세종대학교)	
소요기간	2016.09 ~ 2017.02 (0년6개월, 2년차)	
성과달성 확인방법	피로실험된 강재의 인장강도 실험을 통하여 구조용강의 구성방정식 도출후 나노압입결과에서 산정된 항복강도, 경화지수와 비교 검증	
성과달성에 따른 정량적 성과	특허 출원/등록	국내 : 1건, 국외 : 0건
	논문	국내 : 0건, 국외 : 0건
	저작	0건
	S/W	0건
	신기술	0건
	기타	0건
달성도 (%)	100	

(5) 피로도와 잔류응력을 고려한 용접연결부의 정량적 건전성 지표 개발

정의	강재 용접부의 건전성을 나타내는 지표 개발	
목적	나노압입을 강재 용접부의 비파괴 검사 방법으로 활용하기 위한 원천 기술 확보	
성능목표	(기존기술 수준) 건전성 지표 사용하지 않음. (개발기술 수준) 용접부의 건전성을 쉽게 확인할 수 있는 정량적 지표 개발	
성과달성 책임자 (소속기관)	김승억 (세종대학교)	
소요기간	2017.03 ~ 2017.05 (0년3개월, 2년차)	
성과달성 확인방법	논문발표를 통하여 효율성 검증	
성과달성에 따른 정량적 성과	특허 출원/등록	국내 : 0건, 국외 : 0건
	논문	국내 : 0건, 국외 : 1건
	저작	0건
	S/W	0건
	신기술	0건
	기타	0건
달성도 (%)	100	

2절. 관련 분야 기여도

1. 연구개발 핵심성과

가. 성과 리스트

연번	핵심성과물	해당과제	유형	기여도 (%)
1	나노압입에 의한 구조용 강재 용접부의 미세구조 구성성분비 파악기법 개발	SCI논문 : 2건	공법·기법	100
2	나노압입에 의한 구조용 강재의 탄성계수, 항복응력, 경화지수 도출기법 개발		공법·기법	
3	구조용 강재의 잔류응력에 따른 강재 미세구조의 특성변화 파악	SCI논문 : 2건 특허 : 2건	공법·기법	100
4	구조용 강재 용접부의 피로상태에 따른 강재 미세구조의 특성변화 파악		공법·기법	
5	피로도와 잔류응력을 고려한 용접연결부의 정량적 건전성 지표 개발		공법·기법	

- 국내뿐만 아니라 세계적으로도 나노기술에 대한 투자와 관심이 지속적으로 확대되고 있으나, 현재까지는 연구 진행이 많이 되지 않은 상황임. 이에 본 연구는 국·내외 적으로 이전에 없던 나노압입 기술을 구조용 강재에 적용하였다는 점에서 많은 기여를 함
- 건설 분야에 적용 가능한 나노기술 관련 원천기술의 확보가 시급한 실정에 본 연구는 앞으로의 기술 발전에서 시발점 역할을 함

- 본 연구를 통하여 다양한 구조물 및 재료 특성에 대한 데이터가 나노압입 수행으로 파악 가능하며, 본 연구는 SS400과 SM490 구조용강재를 나노압입 수행하여 건전도를 측정할 수 있도록 데이터 축적을 완료 하였음
- 추후 활용시 SS400과 SM490을 제외한 구조용강재에 대해 종류별로 나노압입을 수행하여 데이터를 축적하면 건전도를 측정 할 수 있음

제5장. 연구개발성과의 활용계획

1절. 연구결과의 활용방안

- 최근 10년간 시설물 안전 및 유지관리 시장은 그림 44와 같이 점차 증가하는 추세를 보이고 있음

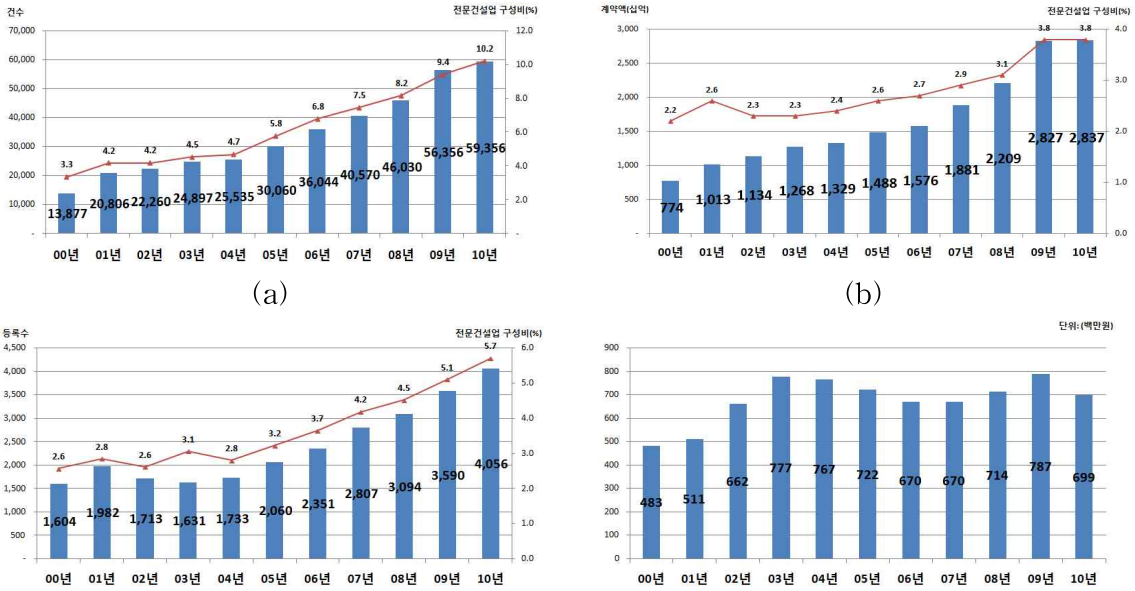


그림 44. 안전점검 및 정밀안전진단 시장 통계 (a) 정밀안전진단 건수 및 금액 (b) 정밀점검 건수 및 금액 (c) 정밀점검 및 정밀안전진단 금액 (d) 안전진단전문기관 (시설물정보관리종합시스템(FMS), '12.07 기준)

- 또한, 국토해양부의 제3차 시설물의 안전 및 유지관리 기본계획에 따르면 현재 유지관리 기술의 전문성이 낮아 이를 보완할 필요가 있고 한국의 지능형 시설물 안전 및 유지관리 기술수준이 최고 기술보유국 대비 76.2%에 불과한 것으로 나타났음

(국가 R&D 기술산업정보서비스, 2010년)

국가	미국	EU	일본	한국	중국	세계 최고국과의 기술격차
기술수준	100%	99.7%	95.9%	76.2%	63.8%	4.3년

표 22. 시설물 안전 및 유지관리 분야 지능형 기술수준 비교

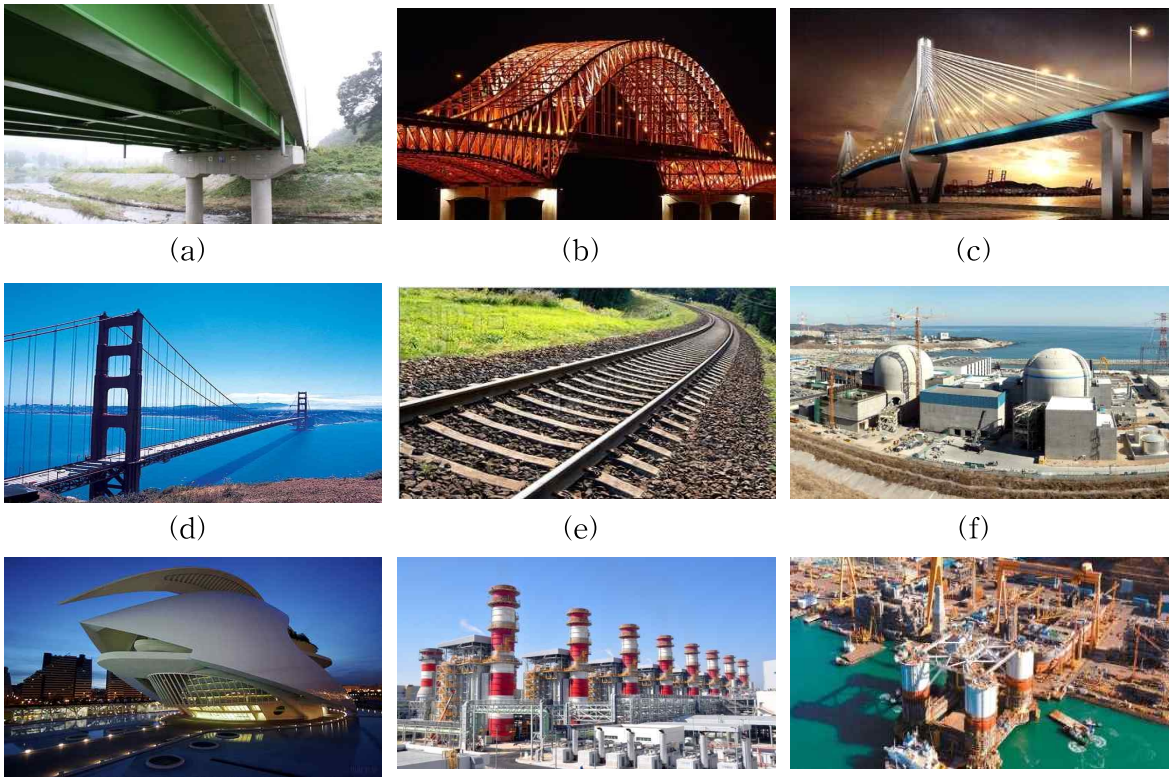
- 제안한 기술을 활용하여 향후 강구조 용접연결부의 건전성을 측정하는 비파괴 검사 장비개발이 가능하며 비파괴 검사 장비를 활용하여 용접연결부에 대한 건전성을 측정함으로써 그림 45 (b)와 같은 용접연결부의 균열로 인한 사고를 예방할 수 있음



(a) (b)

그림 45. (a) 강구조물의 붕괴, (b) 용접연결부 파괴

- 시설물 안전 및 유지관리산업에 활용 가능한 대상구조물로는 ① 교량 (거더교, 트러스교, 아치교, 사장교 및 현수교), ② 철도레일, ③ 원전구조물, ④ 건축구조물, ⑤ 플랜트 구조물, ⑥ 항만구조물 등이 있음



(a) (b) (c)

(d) (e) (f)

(g) (h) (i)

그림 46. 본 기술을 활용할 대상구조물 (a) 거더교, (b) 아치트러스교, (c) 사장교, (d) 현수교, (e) 철도레일, (f) 원전구조물, (g) 건축구조물, (h) 플랜트구조물, (i) 항만구조물

- 본 연구를 통하여 개발한 나노압입에 의한 구조용 강재 용접부의 탄소성 성질을 도출하는 기법 및 피로도와 잔류응력을 고려한 용접연결부의 정량적 건전성 지표 개발 연구는 새로운 형태의 기술 개념임
- 실험과 제안식을 바탕으로 국제학술지에 연구결과를 발표하고 특허를 출원하여 원천기술을 검증받을 예정이며 검증된 기술을 바탕으로 향후 강구조 용접연결부의 건전성을 측정하는 비파괴 검사 장비개발 및 점검·진단기술로 확장하고자 함
- 구조물의 영향을 최소화하도록 드릴을 사용하여 용접부의 직경 1cm 미만의 크기의 샘플을 채취 한 후, 재용접 등을 통하여 보수를 함
- 추가적으로 실제 구조물에서 발생하는 미세 진동 및 환경 등의 외부적인 영향요소를 고려한 연구 및 검토 후, 용접 연결부의 샘플링 없이 구조물 용접부에 직접적으로 나노압입을 수행하여 잔류응력과 피로를 측정 할 수 있는 이동식 비파괴 검사 장치가 개발

된다면 사용 가능 범위가 무궁무진함

- 향후, 다양한 종류의 용접재와 용접 방식에 대하여 본 연구에서 제안된 기법과 연구결과를 바탕으로 나노압입을 수행 할 수 있음. 이렇게 조사된 용접부의 상태변화 데이터를 축적할 경우, 본 연구의 활용도를 더욱 높일 수 있음

2절. 기대효과

1. 기술적 측면

- 나노기술을 활용하여 용접부의 탄소성 성질을 산정하는 방법을 결정
- 구조용 강재의 잔류응력에 따른 미세구조의 특성변화를 파악하여, 잔류응력 측정기술 확보
- 구조용 강재 용접연결부의 피로도에 따른 미세구조의 특성변화를 파악하여, 용접부 피로도 측정기술 확보
- 강구조 용접부의 응력집중 현상과 연계하여 용접 연결부의 건전성을 확인할 수 있는 비파괴 검사 기술 개발
- 강구조 용접부의 건전성 평가에 대해 기존 선진국 기술과 대등한 위치를 확보하여 보다 정확하고 합리적인 안전 및 유지관리 기술 확보

2. 경제적·산업적 측면

- 비파괴 검사 장비를 개발하여 저렴하게 용접연결부의 안전성 평가
- 효율적인 용접연결부의 건전성 평가를 통해 강구조물의 재해 및 붕괴에 따른 인명과 경제적 손실 예방
- 나노기술을 이용한 강구조 용접부의 비파괴 검사 장비를 개발하여 수출 가능

3. 사회적 측면

- 지진에 의해 피해를 입은 강구조의 진단으로 심리적 안정감
- 연구결과를 활용하여 추후 비파괴 검사 장비개발 및 점검·진단기술로 확장할 것으로써 관련 기업에서 활용 가능

제6장. 연구 과정에서 수집한 해외 과학기술 정보

1절. 나노압입 자료 분석

1. 나노압입 해외 학술지 자료 분석

- 국외에서 나노압입에 관한 학술 자료로는 논문 3건으로써 다음 표에 요약하였음

연구기관 (년도)	논문 제목	연구방법	논문 요약
중국 Beijing 대학 (2010)	Measurement of residual stress in quenched 1045 steel by the nanoindentation method	실험	• 급냉된 AISI 1045강의 잔류응력을 나노입입기술로 측정함 • 나노압입에 의해 측정된 잔류응력의 값은 XRD(X선 회절방법)법과 일치하였음
스위스 EMPA 연구소 (2015)	High temperature nanoindentation: The state of the art and future challenges	실험, 시뮬레이션	• 고온나노압입의 기술적 진보에 대한 상세 검토 • 고온에서의 진공 및 그 위치에서의 나노압입 기술을 논의함 • 다수의 새로운 고온나노압입 기술을 설명함
중국 Zhejiang 대학 (2017)	Hydrogen effect on the deformation evolution process in situ detected by nanoindentation continuous stiffness measurement	실험	• 나노압입 연속 강성측정을 통해 스테인리스강의 변형에 대한 수소 효과를 연구함 • 수소는 소성변형의 초기단계에서 탄성계수를 감소시키고 경도를 증가시킴 • 수소 효과는 소성변형이 약해짐에따라 약해짐

2. 나노압입 개발 현황 분석

- 국외 나노압입 기술을 사용하여 제품을 생산하고 있는 업체는 미국의 Rubicon Technology 이며, 개발한 제품은 상용화가 되고 있으며 다음 표에 요약하였음

기업명 (국가)	개요	사진
Rubicon Technology (미국)	• 다양한 응용을 위한 단단한 알루미늄 산화물 코팅 개발 • 2013년 4″및 6″패턴화 사파이어 기판 (PSS)을 출시	• 기판에 쓰이는 사파이어 

가. Rubicon Technology사 (미국)

- 미국의 Rubicon Technology는 산화알루미늄 막을 코팅하고 나노압입 측정기법으로 강도를 측정함
- 산화알루미늄 필름은 나노압입으로 측정한 경도가 10Gpa이상으로 측정되며, 알루미늄 옥사이드 막으로 코팅된 기판은 다양한 제품에 적용되고 있음

제7장. 연구개발성과의 보안등급

1절. 보안등급의 분류

보안	일반
	○

2절. 결정사유

‘국토교통부소관 연구개발사업 운영규정’ 제47조의 4 (보안등급 분류기준)의 보안과제 기준에 해당하지 않음

제8장. 국가과학기술종합정보시스템에 등록한 연구시설·장비 현황

- 해당사항 없음

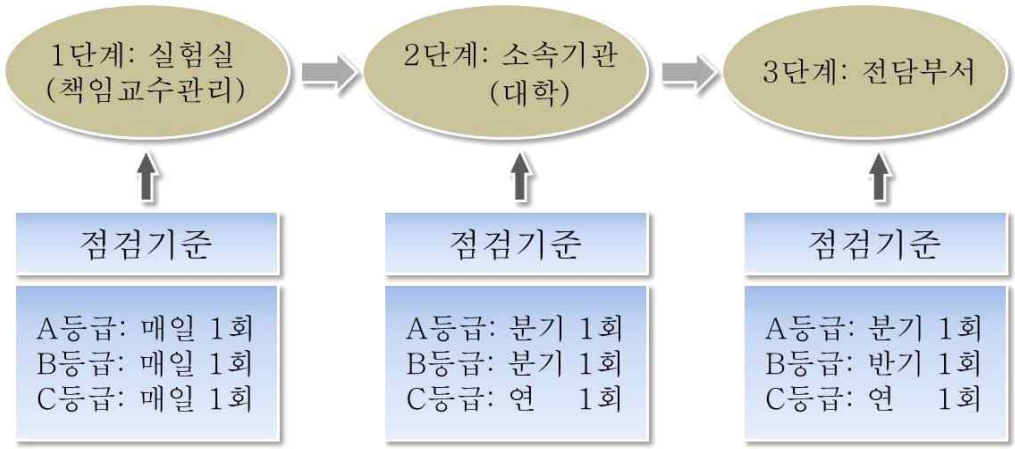
구입 기관	연구시설/ 연구장비명	규격 (모델명)	수량	구입 연월일	구입 가격 (천원)	구입처 (전화번호)	비고 (설치 장소)	NTIS장비 등록 번호

제9장. 연구개발과제 수행에 따른 연구실 등의 안전조치 이행 실적

1절. 연구실 안전조치 이행계획

1. 연구실 안전 점검 체계 및 실시

가. 실험실 안전 점검 체계



※ 위험등급별로 환경안전점검을 단계별로 체계화하여 관리

※ 관리위험등급의 지정

- A등급: 가연성가스, 인화성 시약, 유해화학물질, 다량의 폐액배출, 독극물, 생물 및 동물, 방사성 동위원소, 위험성이 높은 기계장비가 설치된 실험실
- B등급: 일반시약, 소규모 인화성 시약, 불연성가스, 소량의 폐수발생실험실
- C등급: 이화학실험을 수행하지 않는 전기, 설계, 컴퓨터 관련 실험실

나. 실험실 정밀안전진단 실시

- 대상: 연구실 안전환경 조성에 관한 법률 제15조(미래창조과학부), 연구개발활동에 유해화학물질 관리법 제2조 7호에 따른 유해화학물질을 취급하는 연구실, 산업안전보건법 제39조에 따른 유해인자를 취급하는 연구실, 과학기술부령이 정하는 독성가스를 취급하는 연구실
- 실험실 정밀안전진단 실시: 2년마다 1회 실시하여 미래창조과학부에 보고

다. 실험실 정기점검 실시

- 실험실 정기점검 실시: 1년마다 1회 실시하여 미래창조과학부에 보고

2. 교육 훈련

가. 개요

- 실험실의 안전을 확보하고 종사자의 건강을 보호하여 실험 및 연구활동에 기여하고, 또한 연구실 안전환경조성에 관한 법률에 의거하여 실험실의 환경안전교육이 의무화됨에 따라 이공계열 대학원생 및 연구원 등 관련자 전원은 연구실 안전교육을 의무적으로 수강

나. 교육대상

- 교수, 대학원생, 실험조교, 전문직원, 소속연구원, 실험참여 학부생 및 업체직원 등

다. 단계별 교육 이수과정

- 1단계: 공통이수과목 (등록실험실전체)
- 2단계: 특수실험실

라. 교육구분

- 정기교육: 온라인 안전교육 또는 집체 안전교육(6시간) 실시, 신규 등록 시(8시간)
- 비정기 임시교육
  - ✓ 대상: 새로운 실험과정의 신설시, 연구소의 신설시, 교육 미 이수자(신입 대학원생, 전담직원, 연구원, 업체직원, 유해물질 취급자 등)
  - ✓ 방법: 사이버 교육 환경안전교육 등(홈페이지 개설 동영상교육), 자료/유인물, 외부 온라인상, 외부강사, 전문교육기관의뢰 등
- 특별교육: 해당기관에서 자체 또는 외부의 전문기관에 의뢰하여 위탁교육 실시

2절. 연구시설 및 수입신고 현황 - 해당사항 없음

제10장. 연구개발과제의 대표적 연구 실적

번호	구분 (논문/특허/기타)	논문명/특허명/기타	소속 기관명	역할	논문 게재지/특허 등록 국가	영향력 지수	논문 게재일/특허 등록일	사사 여부 (단독사사 또는 중복사사)	특기 사항 (SCI 여부/인용 횟수 등)
1	논문	Instrumented indentation testing and FE analysis for investigation of mechanical properties in structural steel weld zone	경남 대학교 세종 대학교	제1저자 (김정중) 교신저자 (김승억)	International Journal of Mechanical Sciences	2.481	201511	O (단독)	SCI 논문 인용 횟수(5회) JCR기준 상위 11.28% (Category : MECHANICS)
2	논문	Determination of mechanical properties in SM490 steel weld zone using nanoindentation and FE analysis	세종 대학교	제1저자 (Pham, Thai-Hoan) 교신저자 (김승억)	Journal of Constructional Steel Research	1.702	201511	O (단독)	SCI 논문
3	논문	Microstructure evolution and mechanical properties changes in the weld zone of a structural steel during low-cycle fatigue studied using instrumented indentation testing	세종 대학교	제1저자 (Pham, Thai-Hoan) 교신저자 (김승억)	International Journal of Mechanical Sciences	2.481	201608	O (단독)	SCI 논문 JCR기준 상위 11.28% (Category : MECHANICS)

4	논문	Determination of equi-biaxial residual stress and plastic properties in structural steel using instrumented indentation	세종대학교	제1저자 (Pham, Thai-Hoan) 교신저자 (김승억)	Materials Science and Engineering A-Structural Materials Properties Microstructure and Processing	2.647	201703	O (단독)	SCI 논문 JCR기준 상위 8.11% (Category : METALLURGY & METALLURGICAL ENGINEERING)
5	특허	시험체의 잔류 응력 도입장치	세종대학교 산학협력단, 경남대학교 산학협력단	발명자 (김승억, 김정중)	대한민국		2016.10.21	O (단독)	

제11장. 기타 사항 - 해당사항 없음

제12장. 참고 문헌

[1] Easterling K.E., Introduction to the physical metallurgy of welding. Butterworth-Heinemann, London; 1992.

[2] Oliver W.C., Pharr G.M., An improved technique for determining hardness and elastic-modulus using load and displacement sensing indentation experiments. J Mater Res 1992; 7(4): 1564-1583.

[3] Wang X., Yang X., Guo Z., Zhou Y., Song H., Nanoindentation characterization of mechanical properties of ferrite and austenite in duplex stainless steel. Advanced Mater Res 2007; 26-28: 1165-1170.

[4] Ulm F-J., Vandamme M., Bobko C., Ortega J.A., Tai K., Ortiz C., Statistical indentation techniques for hydrated nanocomposites: concrete, bone, shale. J of the Am Ceram Soc 2007; 90(9): 2677 - 2692.

[5] Dao M., Chollacoop N., Vliet K.J.V., Venkatesh T.A., Suresh S., Computational modeling of the forward and reverse problem in instrumented sharp indentation. Acta Mater 2001; 49: 3899-3918.

[6] ASTM A36 (American Society for Testing and Materials): Standard Specification for Carbon Structural Steel, Chicago, IL, 1997.

[7] Jang J., Estimation of residual stress by instrumented indentation: A review. J Cer Process Res 2009; 10(3): 391-400.

[8] Ye D., Xu Y., Xiao L., Cha H., Effects of low-cycle fatigue on static mechanical properties, microstructures and fracture behavior of 304 stainless steel. Mater Sci Eng A 2010; 527: 4092-4102.

[9] Jalalpour M., Kim J.J., Taha M.M.R., Monitoring of L-shape bolted joint tightness using thermal contact resistance. Experimental Mechanics 2013; 53: 1531-1543.

[10] W. F. Chen, S. E. Kim , LRFD Steel Design Using Advanced Analysis, CRC Press, 1997.

부록

1. 품질시험·검사성적서

2. 논문게재 성과

3. 논문발표 성과

4. 특허 성과

5. 인력양성

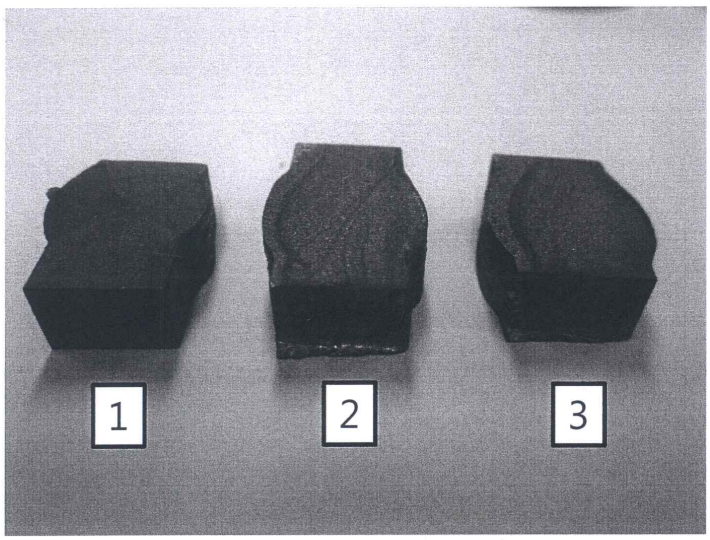
부록 1.

품질시험·검사성적서

01
Objective

- Nano Indentation 측정용 시편 전처리

02
Sample Description



- 재질 : 시멘트 + 금속 와이어
- 작업내용 : Mounting, Grinding, Polishing

시편 전처리 기술 지원 센터

03
Process

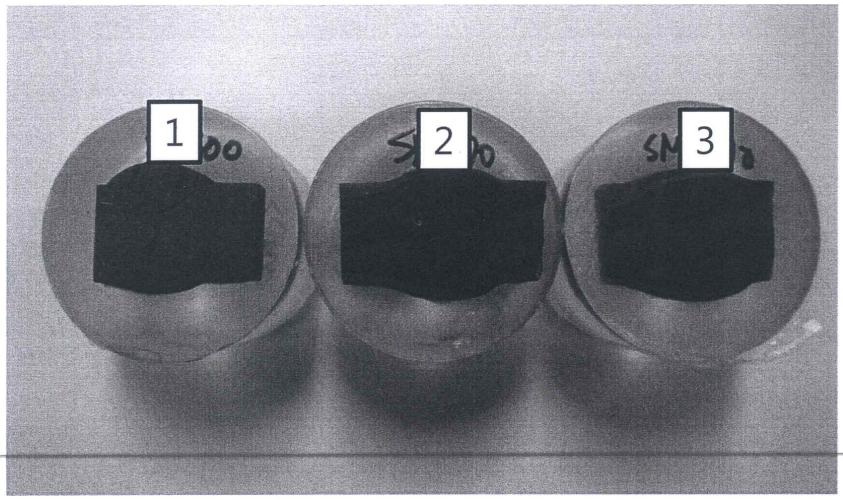
- 1-1. Cold Mounting

Consumables	Item	EpoxySet, Resin	EpoxySet, Hardener	32㎜ Diameter, 2-Part Mounting Cups
	Item Number	145-20005	145-20010	197-10005

→ 장비 및 소모품 사진 별도 (7 page)

- 1-2. Mixing & Cure Time

Mixing	EpoxySet Resin 100 : 12 EpoxySet Hardener Ratio (by WEIGHT)
Cure Time	8 hours / 480 minutes



Mounting 완료

03
Process

- 2-1. Grinding & Polishing by MetPrep3/PH-3™ Individual Pressure Polishing

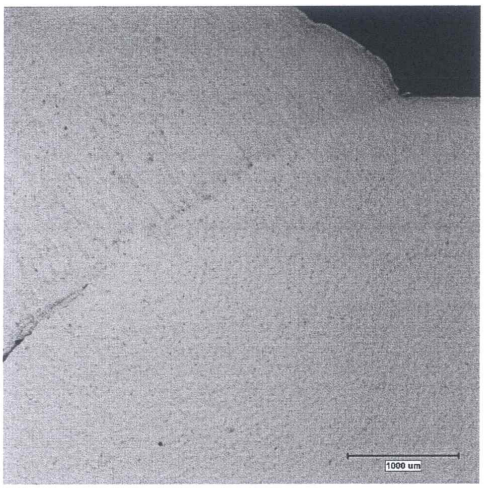
	Grinding				Polishing	
Step	**1**	**2**	**3**	**4**	**5**	**6**
Abrasive	320Grit	600Grit (P-1200)	800 Grit (P-2400)	1200Grit (P-4000)	3 μm	0.04 μm
Type	SiC	SiC	SiC	SiC	Diamond	Colloidal Silica
Carrier	Abrasive Disc	Abrasive Disc	Abrasive Disc	Abrasive Disc	Suspension	Suspension
Item No.	**50-10065**	**50-10075**	**50-10076**	**50-10077**	**90-30020**	**180-25015**
Polishing Cloth	-	-	-	-	DiaMat	Final A
Item No.	-	-	-	-	**90-150-550**	**180-10705**
Coolant	Water	Water	Water	Water	GreenLube	-
Item No.	-	-	-	-	**90-209010**	-
Platen peed(RPM) / Direction	100 /Comp	100 /Comp	100 /Comp	100 /Comp	100 / Contra	100 / Contra
Sample Speed (RPM)	90	90	90	90	90	90
Force (lbF)	3	3	4	4	3	3
Time (min)	Until Target	2'30"	3'00"	3'00"	2'30"	20'00"

→ 장비 및 소모품 사진 별도 (8 page)

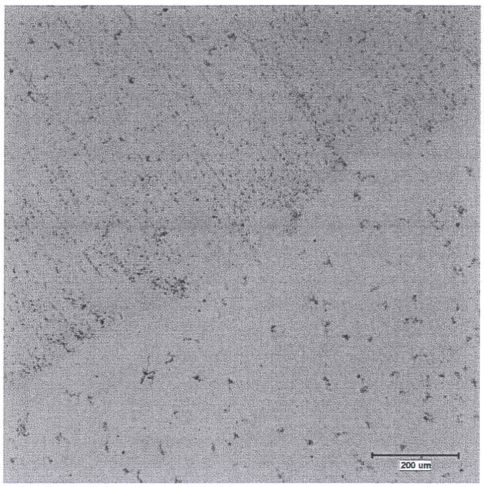
- 2-2. AD-5™ Dispensing Parameters

Step	**5**
Type	Diamond Suspension & GreenLube™
Pulses / Min	5
Pulse Length	0.5 sec.
Water Flush	Off

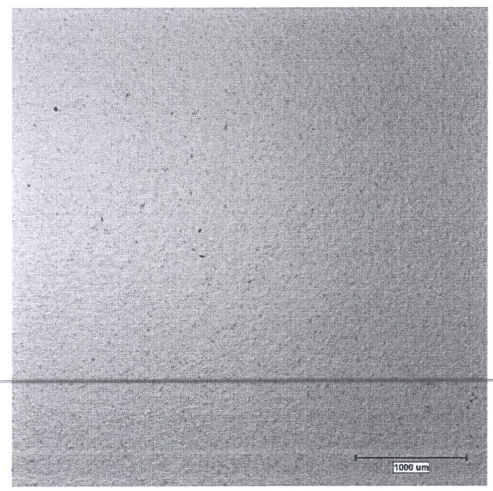
04
결과



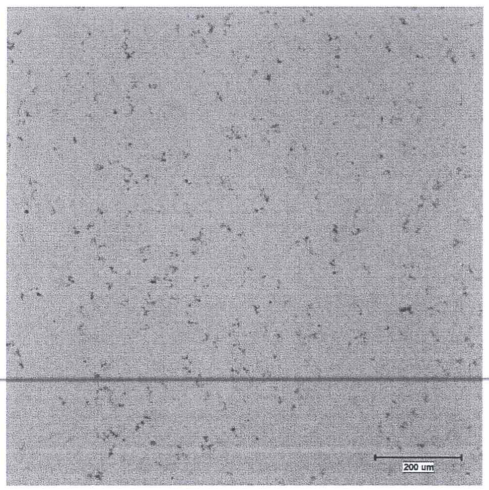
1 - x 25(1)



1 - x 100(1)

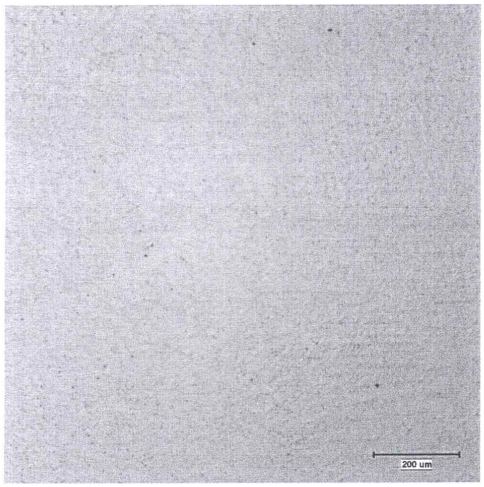


1 - x 25(2)

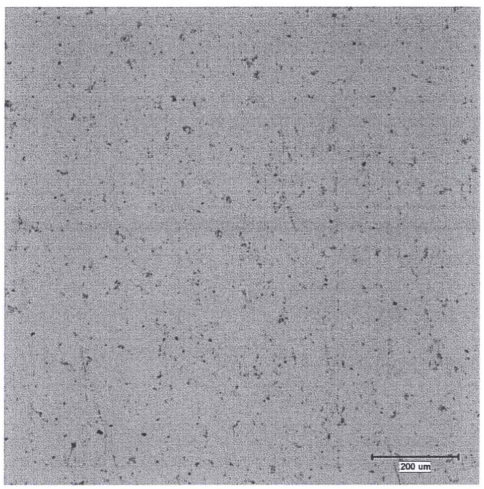


1 - x 100(2)

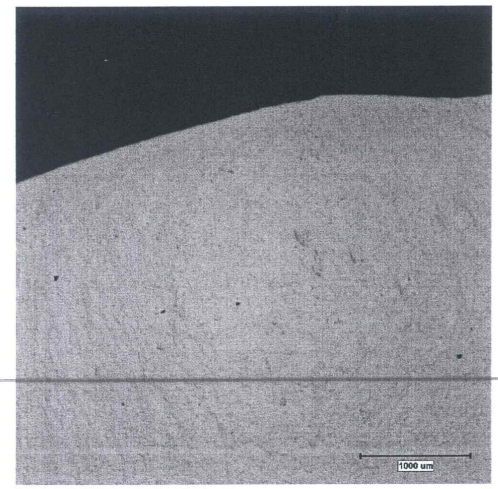
04
결과



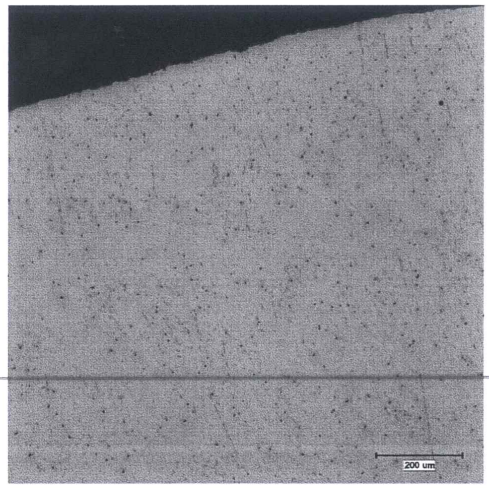
2 - x 25(1)



2 - x 100(1)

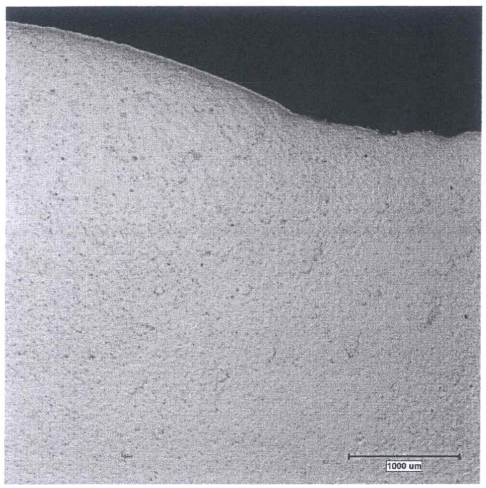


2 - x 25(2)

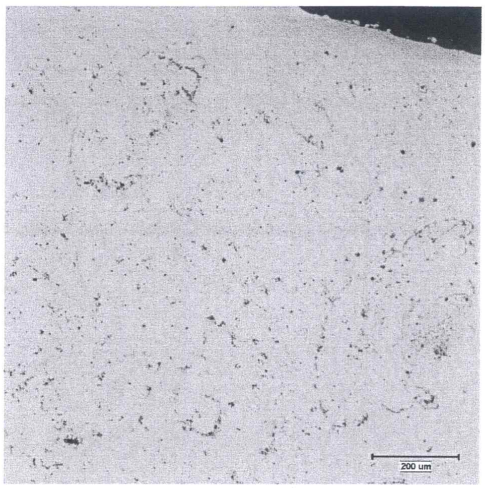


2 - x 100(2)

04
결과



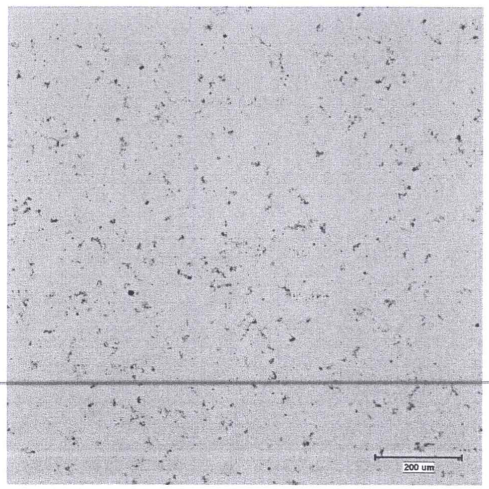
3 - x 25(1)



3 - x 100(1)



3 - x 25(2)



3 - x 100(2)

결과보고서

YOUR PARTNER FOR THE BEST QUALITY

TEST REPORT

우 13810 경기도 과천시 교육원로 98 (중앙동) TEL (02)2164-0011 FAX (02)2634-1008

성적서번호 : TAK-027007
대 표 자 : 의뢰인 박호훈
업 체 명 : 세종대학교산학협력단
주 소 : 서울특별시 광진구 군자동 98 세종대학교 충무관 707호

접 수 일 자 : 2015년 12월 24일
시험완료일자 : 2016년 01월 07일

시 료 명 : 일반 구조용 압연 강재(SM520) - W4

시 험 결 과

시험항목	단위	시료구분	결과치	시험방법
C	%	Location #1	0.17	KS D ISO 14707 : 2003
C	%	Location #2	0.12	KS D ISO 14707 : 2003
C	%	Location #3	0.15	KS D ISO 14707 : 2003
Si	%	Location #1	0.41	KS D ISO 14707 : 2003
Si	%	Location #2	0.35	KS D ISO 14707 : 2003
Si	%	Location #3	0.40	KS D ISO 14707 : 2003
Mn	%	Location #1	1.39	KS D ISO 14707 : 2003
Mn	%	Location #2	1.44	KS D ISO 14707 : 2003
Mn	%	Location #3	1.37	KS D ISO 14707 : 2003
P	%	Location #1	0.017	KS D ISO 14707 : 2003
P	%	Location #2	0.017	KS D ISO 14707 : 2003
P	%	Location #3	0.016	KS D ISO 14707 : 2003

- 다음 페이지 -

An Chi-young
작성자 : 안치영
E-mail: anchi1@ktr.or.kr

Kim Sun-il
기술책임자 : 김선일
Tel : 1577-0091(ARS ①→④)

2016년 01월 07일

KTR 한국화학융합시험연구원장

위변조 확인용 QR code

KOREA TESTING & RESEARCH INSTITUTE

TEST REPORT

우 13810 경기도 과천시 교육원로 98 (중앙동) TEL (02)2164-0011 FAX (02)2634-1008

성적서번호 : TAK-027007
대 표 자 : 의뢰인 박호훈
업 체 명 : 세종대학교산학협력단
주 소 : 서울특별시 광진구 군자동 98 세종대학교 충무관 707호

접 수 일 자 : 2015년 12월 24일
시험완료일자 : 2016년 01월 07일

시 료 명 : 일반 구조용 압연 강재(SM520) - W4

시 험 결 과

시험항목	단위	시료구분	결과치	시험방법
S	%	Location #1	0.001	KS D ISO 14707 : 2003
S	%	Location #2	0.001	KS D ISO 14707 : 2003
S	%	Location #3	0.001	KS D ISO 14707 : 2003
Al	%	Location #1	0.04	KS D ISO 14707 : 2003
Al	%	Location #2	0.04	KS D ISO 14707 : 2003
Al	%	Location #3	0.04	KS D ISO 14707 : 2003
Cu	%	Location #1	0.02	KS D ISO 14707 : 2003
Cu	%	Location #2	0.02	KS D ISO 14707 : 2003
Cu	%	Location #3	0.02	KS D ISO 14707 : 2003

* 12.5 mm Wide Sheet Type Specimen

* 용 도 : 품질관리용

비 고 : 1. 이 성적서는 의뢰자가 제시한 시료 및 시료명으로 시험한 결과로써 전체 제품에 대한 품질을 보증하지 않으며, 성적서의 진위확인은 홈페이지(www.ktr.or.kr) 또는 QR code로 확인 가능합니다.
2. 이 성적서는 홍보, 선전, 광고 및 소송용 등으로 사용될 수 없으며, 용도 이외의 사용을 금합니다.
3. 이 성적서는 원본(등본 포함)만 유효하며, 사본 및 전자 인쇄본/파일본은 결과치 참고용입니다.

An Chi-young
작성자 : 안치영
E-mail: anchi1@ktr.or.kr

Kim Sun-il
기술책임자 : 김선일
Tel : 1577-0091(ARS ①→④)

2016년 01월 07일

KTR 한국화학융합시험연구원

위변조 확인용 QR code

YOUR PARTNER FOR THE BEST QUALITY

TEST REPORT

우 13810 경기도 과천시 교육원로 98 (중앙동) TEL (02)2164-0011 FAX (02)2634-1008

성적서번호 : TAK-027006
대 표 자 : 의뢰인 박호훈
업 체 명 : 세종대학교산학협력단
주 소 : 서울특별시 광진구 군자동 98 세종대학교 충무관 707호

접 수 일 자 : 2015년 12월 24일
시험완료일자 : 2016년 01월 13일

시 료 명 : 일반 구조용 압연 강재(SM520)

시 험 결 과

시험항목	단위	시료구분	결과치	시험방법
치수(좌측)	㎜	N1	11.88	KS B 5202 : 2008
치수(좌측)	㎜	N2	11.88	KS B 5202 : 2008
치수(좌측)	㎜	N3	11.91	KS B 5202 : 2008
치수(좌측)	㎜	W1	12.10	KS B 5202 : 2008
치수(좌측)	㎜	W2	12.10	KS B 5202 : 2008
치수(좌측)	㎜	W3	12.11	KS B 5202 : 2008
치수(중앙)	㎜	N1	11.88	KS B 5202 : 2008
치수(중앙)	㎜	N2	11.88	KS B 5202 : 2008
치수(중앙)	㎜	N3	11.88	KS B 5202 : 2008
치수(중앙)	㎜	W1	12.23	KS B 5202 : 2008
치수(중앙)	㎜	W2	12.25	KS B 5202 : 2008
치수(중앙)	㎜	W3	12.25	KS B 5202 : 2008
치수(우측)	㎜	N1	11.88	KS B 5202 : 2008
치수(우측)	㎜	N2	11.91	KS B 5202 : 2008
치수(우측)	㎜	N3	11.89	KS B 5202 : 2008
치수(우측)	㎜	W1	12.07	KS B 5202 : 2008
치수(우측)	㎜	W2	12.05	KS B 5202 : 2008
치수(우측)	㎜	W3	12.05	KS B 5202 : 2008
인장강도	N/㎟	N1	587	ASTM A370-15(*)

- 다음 페이지 -

Lee Seungho
작성자 : 이승호
E-mail: peter@ktr.or.kr

Ham Jong-oh
기술책임자 : 함종오
Tel : 1577-0091(ARS ①→④)

2016년 01월 13일

KTR 한국화학융합시험연구원장

위변조 확인용 QR code

KTR KOREA TESTING & RESEARCH INSTITUTE

첨부보고서

YOUR PARTNER FOR THE BEST QUALITY

TEST REPORT

우 13810 경기도 과천시 교육원로 98 (중앙동) TEL (02)2164-0011 FAX (02)2634-1008

성적서번호 : TAK-027006
대 표 자 : 의뢰인 박호훈
업 체 명 : 세종대학교산학협력단
주 소 : 서울특별시 광진구 군자동 98 세종대학교 충무관 707호

접 수 일 자 : 2015년 12월 24일
시험완료일자 : 2016년 01월 13일

시 료 명 : 일반 구조용 압연 강재(SM520)

시 험 결 과

시험항목	단위	시료구분	결과치	시험방법
인장강도	N/㎟	N2	582	ASTM A370-15(*)
인장강도	N/㎟	N3	587	ASTM A370-15(*)
인장강도	N/㎟	W1	584	ASTM A370-15(*)
인장강도	N/㎟	W2	587	ASTM A370-15(*)
인장강도	N/㎟	W3	584	ASTM A370-15(*)
Raw Data	-	N1	첨부참조	ASTM A370-15(*)
Raw Data	-	N2	첨부참조	ASTM A370-15(*)
Raw Data	-	N3	첨부참조	ASTM A370-15(*)
Raw Data	-	W1	첨부참조	ASTM A370-15(*)
Raw Data	-	W2	첨부참조	ASTM A370-15(*)
Raw Data	-	W3	첨부참조	ASTM A370-15(*)

* 12.5 mm Wide Sheet Type Specimen

* 용 도 : 품질관리용

비 고 : 1. 이 성적서는 의뢰자가 제시한 시료 및 시료명으로 시험한 결과로써 전체 제품에 대한 품질을 보증하지 않으며, 성적서의 진위확인은 홈페이지(www.ktr.or.kr) 또는 QR code로 확인 가능합니다.
2. 이 성적서는 홍보, 선전, 광고 및 소송용 등으로 사용될 수 없으며, 용도 이외의 사용을 금합니다.
3. 이 성적서는 원본(등본 포함)만 유효하며, 사본 및 전자 인쇄본/파일본은 결과치 참고용입니다.

Lee Seungho
작성자 : 이승호
E-mail: peter@ktr.or.kr

Ham Jong-oh
기술책임자 : 함종오
Tel : 1577-0091(ARS ①→④)

2016년 01월 13일

KTR 한국화학융합시험연구원장

위변조 확인용 QR code

TEST REPORT

우 13810 경기도 과천시 교육원로 98 (중앙동) TEL (02)2164-0011 FAX (02)2634-1008

성적서번호 : TAK-030835
대 표 자 : 의뢰인 박호훈
업 체 명 : 세종대학교산학협력단
주 소 : 서울특별시 광진구 군자동 98 세종대학교 충무관 707호

접 수 일 자 : 2016년 10월 27일
시험완료일자 : 2016년 11월 07일

시 료 명 : 구조용 강재(SM490)

시 험 결 과

시험항목	단위	시료구분	결과치	시험방법
인장강도	N/㎟	n1	546	KS B 0802 : 2003(13B호 시험편)
인장강도	N/㎟	n2	549	KS B 0802 : 2003(13B호 시험편)
인장강도	N/㎟	n3	544	KS B 0802 : 2003(13B호 시험편)

* 용 도 : 품질관리용

비 고 : 1. 이 성적서는 의뢰자가 제시한 시료 및 시료명으로 시험한 결과로써 전체 제품에 대한 품질을 보증하지 않으며, 성적서의 진위확인은 홈페이지(www.ktr.or.kr) 또는 QR code로 확인 가능합니다.
2. 이 성적서는 홍보, 선전, 광고 및 소송용 등으로 사용될 수 없으며, 용도 이외의 사용을 금합니다.
3. 이 성적서는 원본(등본 포함)만 유효하며, 사본 및 전자 인쇄본/파일본은 결과치 참고용입니다.

Park Ki Woong
작성자 : 박기웅
E-mail: impact@ktr.or.kr

Ham Jong-oh
기술책임자 : 함종오
Tel : 1577-0091(ARS ①→④)

2016년 11월 07일

KTR 한국화학융합시험연구원장

위변조 확인용 QR code

전자문서본은 시험결과에 대한 참고용입니다.

전자문서본(Electronic Copy)

TEST REPORT

우 13810 경기도 과천시 교육원로 98 (중앙동) TEL (02)2164-0011 FAX (02)2634-1008

성적서번호 : TAK-030834
대 표 자 : 의뢰인 박호훈
업 체 명 : 세종대학교산학협력단
주 소 : 서울특별시 광진구 군자동 98 세종대학교 충무관 707호

접 수 일 자 : 2016년 10월 27일
시험완료일자 : 2016년 11월 07일

시 료 명 : 구조용 강재(SS400)

시 험 결 과

시험항목	단위	시료구분	결과치	시험방법
인장강도	N/㎟	n1	459	KS B 0802 : 2003(13B호 시험편)
인장강도	N/㎟	n2	474	KS B 0802 : 2003(13B호 시험편)
인장강도	N/㎟	n3	465	KS B 0802 : 2003(13B호 시험편)

* 용 도 : 품질관리용

비 고 : 1. 이 성적서는 의뢰자가 제시한 시료 및 시료명으로 시험한 결과로써 전체 제품에 대한 품질을 보증하지 않으며, 성적서의 진위확인은 홈페이지(www.ktr.or.kr) 또는 QR code로 확인 가능합니다.
2. 이 성적서는 홍보, 선전, 광고 및 소송용 등으로 사용될 수 없으며, 용도 이외의 사용을 금합니다.
3. 이 성적서는 원본(등본 포함)만 유효하며, 사본 및 전자 인쇄본/파일본은 결과치 참고용입니다.

Park Ki Woong

작성자 : 박기웅
E-mail: impact@ktr.or.kr

Ham Jong-oh

기술책임자 : 함종오
Tel : 1577-0091(ARS ①→④)

2016년 11월 07일

KTR 한국화학융합시험연구원장

위변조 확인용 QR code

전자문서본은 시험결과에 대한 참고용입니다.

전자문서본(Electronic Copy)

부록 2.

논문게재 성과

1. Instrumented indentation testing and FE analysis for investigation of mechanical properties in structural steel weld zone(2015)

International Journal of Mechanical Sciences 103 (2015) 265–274

Contents lists available at ScienceDirect

International Journal of Mechanical Sciences

journal homepage: www.elsevier.com/locate/ijmecsci

Instrumented indentation testing and FE analysis for investigation of mechanical properties in structural steel weld zone

Jung J. Kim [a], Thai-Hoan Pham [b], Seung-Eock Kim [c,*]

[a] Dept. of Civil Engineering, Kyungnam University, Changwon-si, South Korea
[b] Dept. of Civil and Environmental Engineering, Sejong University, Seoul, South Korea
[c] Dept. of Civil and Environmental Engineering, Sejong University, 98 Gunja-dong, Gwangjin-ku, Seoul 143-747, South Korea

ARTICLE INFO

Article history:
Received 17 May 2015
Received in revised form
14 September 2015
Accepted 25 September 2015
Available online 9 October 2015

Keywords:
Mechanical properties
Structural steel
Weld zone
Instrumented indentation
FE analysis

ABSTRACT

In this paper, a procedure for determining mechanical properties in structural steel weld zone using indentation test and finite element (FE) analysis was established and applied for investigating mechanical properties in an SS400 steel weld zone. Instrumented indentation tests were performed across the weld zone and the mechanical properties (E, H, σ_y, and n) were then determined from their load–depth data with the aid of FE analysis. The obtained mechanical properties in the weld zone were verified to be reliable by comparing with the results from tensile tests and their FE simulations of both steel and welded specimens. It is shown that in the investigated weld zone, base metal has lower values of mechanical properties (E, H, σ_y, and n) than does the weld metal, and mechanical properties within heat affected zone (HAZ) gradually increase from the base metal to weld metal regions. Based on the optical microscopy examination results, the gradient of mechanical within HAZ is found to be associated with the change of grain sizes from base metal to weld metal regions.

© 2015 Elsevier Ltd. All rights reserved.

1. Introduction

Structural steels are one of the most prevalent and commonly used materials in civil and industrial building construction due to several of advantages, such as their low cost and excellence in machinability and weldability. In many applications of structural steel, it is essential to form strong joints that allow transferring load between components. Generally, welding is considered as the preferred joining method due to such advantages as continuous joint forming, design simplicity, and high rigidity compared to others [1]. However, the weld joints in welded components are generally considered as potential "weakest link" due to the microstructural inhomogeneity or weld defects [2]. Since the performance of weld joint is governed by its components: base metal (BM), heat affected zone (HAZ), and weld metal (WM), a comprehensive understanding of the mechanical properties including elastic modulus, hardness, yield strength, and strain hardening exponent in these components is essential for the integrity assessment of structural steel members that have a weld zone.

Instrumented indentation testing has been used in many engineering fields including biomedical, civil, mechanical, and material engineering [3]. Many researchers have developed analytical methods for characterization of basic mechanical properties (elastic modulus, yield stress, strain hardening exponents, etc.) from the load–penetration depth data of indentation tests [4–9]. Since instrumented indentation testing has various advantages in practical applications and provides access to the local material properties in the indented region, it has been extensively used in characterizing mechanical properties of inhomogeneous materials such as weld zone [2,10–13]. For example, Ye et al. [2] conducted a series of experiments including indentation tests, low-cycle fatigue tests, and optical microscopy examinations to study the local mechanical properties and microstructures in individual zone of 304L SS welded joint in both as-welded and cyclic loading conditions. Chung et al. [10] used indentation tests and finite element (FE) analysis to investigate the mechanical properties of DP590 steel weld zone, of which isotropic hardening law along with the non-quadratic anisotropic yield function Yld2000-2d was assumed as material property model. Yonezu et al. [12] utilized spherical indentation to measure local mechanical properties of welded stainless steel SUS316L at high temperature by using FE method to establish functional relationship between indentation response and plastic property of material. Recently, Sun et al. [13] applied micro-indentation and inverse modeling to determine mechanical properties of the weld line of two typical dual phase high strength steels DP600/DP980. In the research, the FE model was constructed based on the power law constitutive model to simulate the elastoplastic response of each

* Corresponding author. Tel.: +82 2 3408 3291; fax: +82 2 3408 3332.
E-mail address: sekim@sejong.ac.kr (S.-E. Kim).

http://dx.doi.org/10.1016/j.ijmecsci.2015.09.015
0020-7403/© 2015 Elsevier Ltd. All rights reserved.

Table 1
Chemical compositions SS400 steel and ER70S-6 weld material (in wt%).

Material	C	Si	Mn	P	S	Al	Ca	Cu
SS400	0.05	0.037	0.46	0.013	0.002	0.044	0.0017	–
ER70S-6	0.04	0.92	0.45	0.011	0.015	–	–	0.2

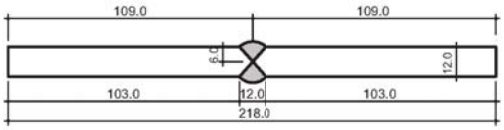


Fig. 1. Dimensions for the double V butt welding plate.

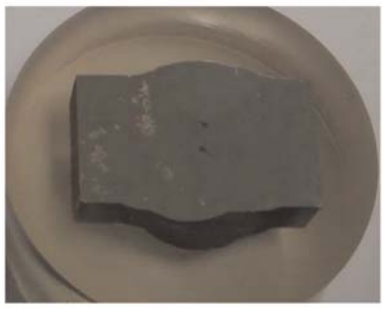


Fig. 2. Sample for indentation tests.

individual weld zone and the mechanical properties in the different zones were identified by comparing the experimental data and simulation results. However, the materials used in above studies could be accurately assumed as isotropic hardening law or power law formulation while materials with plastic plateau in their constitutive equations such as structural steel were not covered.

The aim of this study is to investigate the mechanical properties in the weld zone of a structural steel, SS400, by further extending the proposed method [9] in application for estimating the mechanical properties (yield strength σ_y and strain hardening exponent n) in structural steel weld zone from indentation results with the aid of FE analysis. Instrumented indentation, tensile tests, FE analyses, and optical microscopy examinations were conducted. The mechanical properties in the weld zone were extracted from indentation load–depth data and the correlation between microstructures and mechanical properties in the weld zone was investigated.

2. Experimental procedure

A welded plate of SS400 steel was chosen for investigation. The manual metal arc welding with electrode ER 70S-6 was used. The major chemical composition in percentage weight of SS400 and weld metal are listed in Table 1. The weld was completed with a voltage of 22 V and a current of 100 A. The dimensions for the double V groove butt welding plate are shown Fig. 1.

For instrumented indentation test, one slice of $8 \times 20\ mm^2$ containing BM, HAZ, and WM regions was cut out from the welded plate by water-jet. This slice was then mounted in epoxy and polished with different silicon carbide papers, poly diamond particles, and colloidal silica in order to obtain a flat and smooth surface. This procedure was achieved in seven stages of increasing fineness, with the last in the range of 40 nm. Fig. 2 shows the sample after being mounted and polished. A series of instrumented indentation tests consisting of 5×25 indenting points across the weld zone were performed at room temperature using a Nano Hardness Tester with an Berkovich indenter made of industrial diamond (elastic modulus $E_i = 1141$ GPa and Poisson's ratio $\upsilon_i = 0.07$). A fixed maximum load of 150 mN at a constant loading and unloading rate of 300 mN/min was applied for all indentation tests. The indenting series covered portions of base metal, heat-affected zone, and weld metal. In order to look for the correlation between microstructures and mechanical properties in the weld zone, the microstructural examinations were carried out. To reveal the microstructure, the polished specimen was etched for 30 s with 2% nital, and the microstructures were observed by optical microscopy.

Tensile tests were conducted on three specimens of SS400 (labeled N1, N2, and N3) and three welded specimens (labeled W1, W2, and W3) using an Instron tensile testing machine and tested according to ASTM standard [14]. Note that the welded specimens were directly cut from the welded plate and specimens of SS400 steel have the same thickness of 12 mm as welded plate. Fig. 3 shows the dimensions of specimens and representative specimens for tensile tests.

3. The procedure for determining mechanical properties from indentation and FE analysis results

Fig. 4 presents a load–penetration depth (P–h) curve of an elasto-plastic material to sharp indentation. From this curve,

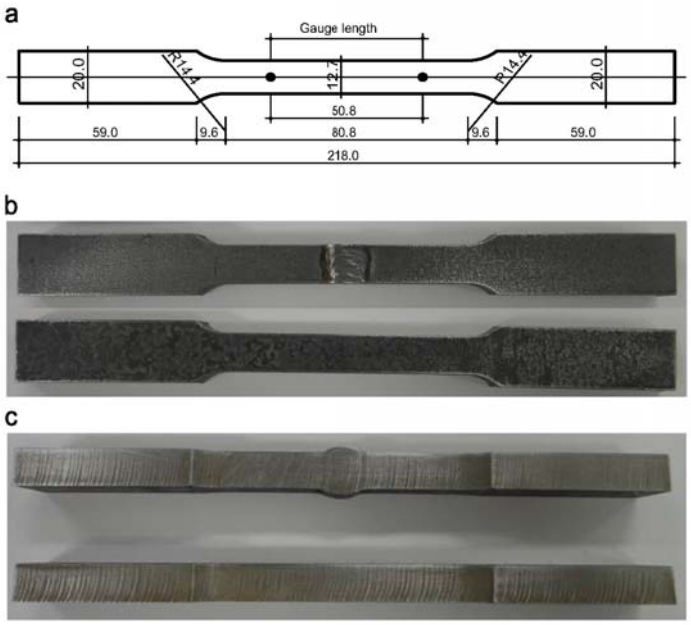


Fig. 3. Specimens for tensile tests. (a) Dimenions of specimens. (b) Top view of specimens. (c) Front view of specimens.

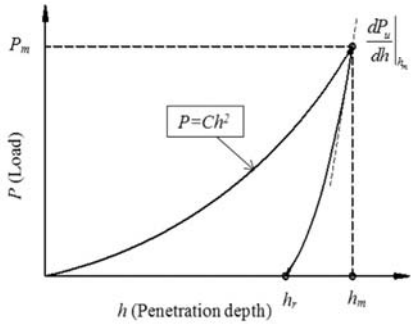


Fig. 4. Load–penetration depth curve (P–h).

various characteristic parameters of indentation, including those related with the loading (the loading curvature C and the maximum penetration depth h_m) and those related with the unloading (the initial unloading contact stiffness S and the residual impression depth after complete unloading h_r). As indicated [15], C is measurement of the resistance of the material to indentation, S characterizes the stiffness property of the indented material, h_r represents the ability of material to change its shape. The elasto-plastic properties of the indented material can thus be evaluated from the above indentation characteristic parameters.

As seen in Fig. 4, h_m and h_r can be obtained directly from the P–h curve, whereas C and S need to further provide the description of the loading and unloading curves. For sharp indenters (Berkovich, Vickers), the loading curve can be expressed using Kick's law [4], $P=Ch^2$, while the unloading curve is usually described by a power-law relation suggested by Oliver and Pharr [4]: $P_u = B(h-h_r)^m$, where B and m are the fitting parameters. Thus, C and S can be expressed, respectively, in the following forms:

$$C = \frac{P_m}{h_m^2} \tag{1}$$

$$S = \left.\frac{dP}{dh}\right|_{h_m} = mB(h_m - h_r)^{m-1} \tag{2}$$

Owing to the effects of elastic deformation of the indenter, the reduced modulus E_r can then be extracted as follows [4]:

$$E_r = \frac{\sqrt{\pi}}{2\beta}\frac{S}{\sqrt{A_c}} \tag{3}$$

where β is a correction factor for indenter shape ($\beta=1.034$ for a Berkovich indenter) and the projected contact area A_c can be determined from the contact depth h_c. For a perfect Berkovich indenter, the projected contact area is calculated by $A_c = 24.5h_c^2$, where $h_c = h_m - \varepsilon^* P_m/S$ and $\varepsilon^* = 0.75$ for sharp indenters [4].

The elastic modulus E can now be determined as

$$E_r = \left[\frac{1-\nu^2}{E} + \frac{1-\nu_i^2}{E_i}\right]^{-1} \tag{4}$$

where E, υ, E_i, and υ_i are the elastic modulus and Poisson's ratio of the indented material and indenter, respectively.

From the P–h curve, the hardness H can also be determined in terms of the indentation depth using the following equation [4]:

$$H = \frac{P_m}{A_c} \tag{5}$$

Since C, S, and $E_r^* = \left[(1-\nu^2)/E\right]^{-1}$ are obtained from the P–h curve of indentation test using Eqs. (1)–(4), the yield strength σ_y and strain hardening exponent n of structural steel can be determined with respect to α using following polynomial equations [9]:

$$\frac{E_r^*}{\sigma_y} = \sum_{i=1}^{4}\sum_{j=1}^{4}\sum_{k=1}^{3} a_{ijk} n^{j-1}\alpha^{k-1}\left(\frac{E_r^*}{C}\right)^{i-1} \tag{6}$$

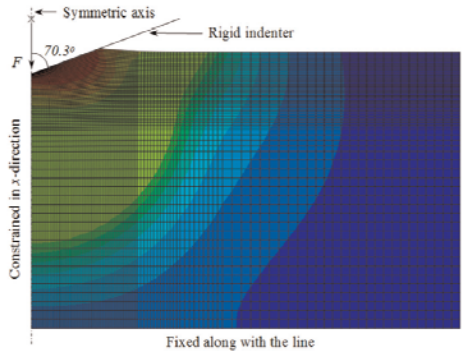


Fig. 5. Axisymmetric FE model of indentation test.

$$\frac{S}{E_r^* h_m} = \sum_{i=1}^{4}\sum_{j=1}^{4}\sum_{k=1}^{3} h_{ijk} n^{j-1} \alpha^{k-1} \left[\ln\left(\frac{E_r^*}{\sigma_y}\right)\right]^{i-1} \tag{7}$$

where a_{ijk} and h_{ijk} are coefficients (Appendix A), and α is defined as strain at the starting-point of strain hardening ε_{st} divided by the initial yield strain ε_y. It is noted that coefficients a_{ijk} and h_{ijk} are fitting parameters obtained from finite element analysis results of indentation simulations, while α can be directly determined from stress–strain curve of tensile test. With the high stiffness and the narrow ranges of structural steel property parameters, the uniqueness of inverse identification of yield strength σ_y and strain hardening exponent n from indentation data can be ensured and the further methodology details to extract σ_y and n can be found elsewhere [9].

Yield strength and strain hardening exponent of structural steel can be determined with respect to α using Eqs. (6) and (7). However, the α value of HAZ and WM regions in the weld zone could not be measured from tensile test of the welded specimens. Since preparing mini or micro specimens from the weld zone that allows determining α value of the weld zones is a rather difficult task due to the small-size of the zones [2,10], finite element (FE) analysis is now currently considered an appropriate approach. To obtain the α value of HAZ and WM, the FE analyses of indentation were performed using the nonlinear finite element analysis program ABAQUS [16] for correlating the experimental with the simulated load–penetration depth curves. The material model for structural steel that was used in the previous work was applied in this study, as follows [9]:

$$\sigma = \begin{cases} E\varepsilon & (\varepsilon \le \varepsilon_y) \\ \sigma_y & (\varepsilon_y < \varepsilon < \varepsilon_{st}) \\ \sigma_y\left[1 + E(\varepsilon - \varepsilon_{st})/(\alpha\sigma_y)\right]^n & (\varepsilon \ge \varepsilon_{st}) \end{cases} \tag{8}$$

Due to the fact that a conical indenter with a semi-apical angle of θ=70.3° has the same projected area-depth functions as the Berkovich indenter used in the indentation tests and the P–h responses of the conical and Berkovich indentations obtained from finite element analysis using ABAQUS were demonstrated to be virtually identical for micro- or nano-scale [7,17], a conical indenter was simulated instead of a Berkovich indenter in order to reduce the complexity and analysis time. Considering symmetric conditions, an axisymmetric two-dimensional FE model was developed to simulate the indentation process. The sample was modeled using 8576 four-node bilinear axisymmetric quadrilateral elements, as shown in Fig. 5. The developed FE model was also demonstrated to be accurately simulated by verifying with the experimental result [9]. The further details for the FE model can also be found in the previous work [9].

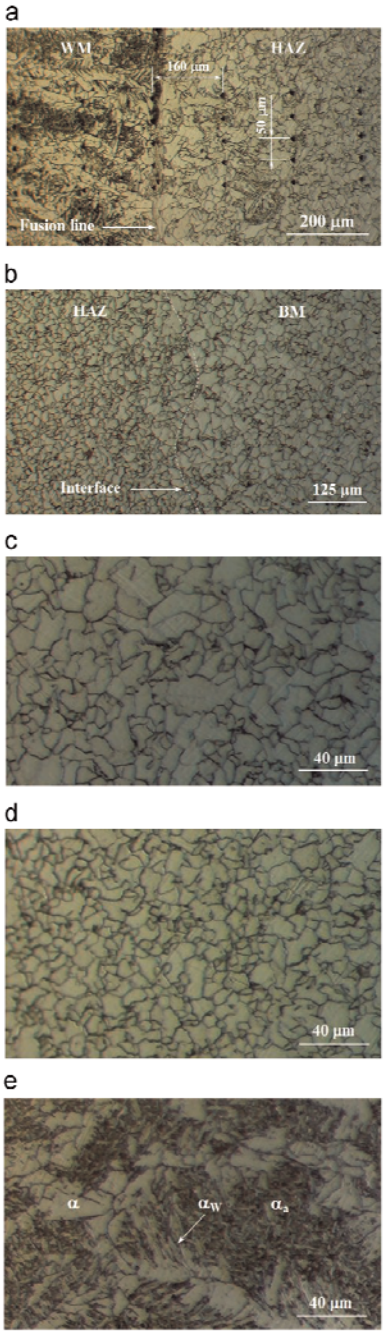


Fig. 6. Optical microstructures in the weld zone: (a) interface of WM and HAZ, (b) interface of HAZ and WM, (c) BM, (d) HAZ, and (e) WM.

Since elastic modulus of HAZ and WM could be directly obtained from indentation test results and Poisson's ratio was fixed at 0.3, a set of simulated load–penetration depth curves was prepared with various values of α, σ_y, and n as the input data for FE simulations. The representative value of α for HAZ and WM was

then determined by comparing the experimental load–penetration depth curves with the set of simulated curves. Once α value of HAZ and WM was estimated, the yield strength and strain hardening exponent distributed in HAZ and WM could be determined using Eqs. (6) and (7).

4. Results and discussion

4.1. Microstructures

The optical microstructures at the interface of WM and HAZ (including apart of indentation impressions across the weld zones), at the interface of the HAZ and BM, and in BM, HAZ, and WM regions are presented in Fig. 6. From this figure, the fusion line between WM and HAZ (Fig. 6a) and the interfacial line between HAZ and BM (Fig. 6b) were clearly observed. These observations allowed identifying the BM, HAZ, and WM regions and their approximate dimensions. The identification showed that the indenting region consisting of 5×25 points covered a length of 3.84 mm across the weld zone including approximately 2 mm of the HAZ region.

As shown in Fig. 6c, BM is composed of ferrite and small regions of pearlite. It can be seen that small amounts of pearlites are located at the grain boundary edges and the corners of the ferrite grains. These grains have various sizes with the majority of the sizes in the range of 15–20 μm, while the biggest is around 40 μm. Fig. 6d shows that the microstructure of HAZ consists of grain polygonal ferrite and some regions of pearlite also located at the corners of grains but more in amount when compared with BM. Note in Fig. 6c and d, and especially in Fig. 6b that ferrite grains in HAZ are more regular and relatively smaller in size when compared with that in BM. These observations are agree well with the results obtained from HAZ region of a similar low carbon steel weld zone with 0.053% C [18,19]. Due to the various peak heated temperatures during the welding, the microstructures in the HAZ can be well defined based on the distance from the fusion boundary [20–22]. The regions immediately to the fusion boundary are heated to very high temperatures and hence transform completely to austenite at the upper critical temperature (Ac_3) by about 100 °C. The austenite that forms is annealed during heating beyond Ac_3, giving rise to a very coarse-grain austenite zone. The austenite grain size decreases sharply with distance from the fusion boundary. These austenite grains lead to the formation of the coarse grained zone (CGZ) and fine grained zone (FGZ) of the final microstructures, which is adjacent to the weld fusion zone and slightly further away from the fusion boundary, respectively, as can be seen in Fig. 6a. As the peak temperature decreases, regions of the HAZ further away from the fusion boundary become only partially austenite during the heating part of the thermal cycle. The part that does not transform into austenite becomes tempered [20]. This causes the ferrite grains in the final microstructure of HAZ region, which is further away from fusion boundary and near the base metal, to be more regular and smaller in size when compared with those in BM, as shown in Fig. 6b.

Concerning the WM of a low carbon steel, during the welding process, the peak temperature in this zone is much higher than the upper limit of phase balance between δ-ferrite and γ-austenite [2,20], leading all ferrite and pearlite transformation to austenite. According to Easterling et al. [21], the austenite grains then can form into many different phases of microstructure such as allotriomorphic ferrite (α), Widmanstatten ferrite (α_W), cementite, pearlite, and acicular ferrite (α_a) depending on the cooling rate, detailed shape, and the size of the austenite grains. As can be seen in Fig. 6e, the microstructure of WM in the present SS400 steel weld zone mainly contains ferrite with different types of grains and certain small amounts of pearlite that are surrounded by ferrite grains. The ferrite grains are α, α_W, and α_a, where the sizes of allotriomorphic ferrite are larger than others. This result is totally consistent with the results reported above [20–22].

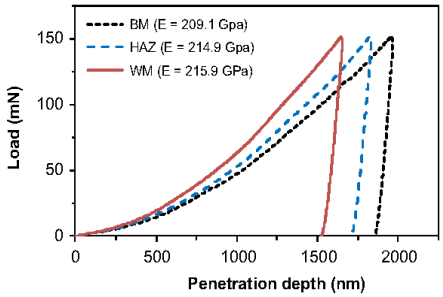


Fig. 7. Typical indentation P–h curves in the weld zone.

Table 2
Average values of mechanical properties in the weld zone.

	WM	HAZ	BM
E (GPa)	218.2	212.4	207.2
H (GPa)	2.7	2.2	2.0
σ_y (MPa)	403.5	331.4	302.7
n	0.203	0.195	0.191

4.2. Mechanical properties

It can be seen from the Fig. 6a that the size of indents is much smaller when compared to the dimension of the individual weld zone but not much smaller than the ferrite grain size in HAZ and WM. Considering that the size of plastic zone created by a Berkovich indenter is about 2 times as larger as the indentation size or indentation with a Berkovich tip 'feels" a volume with radius of 5–9 times maximum penetration depth [15], a composite behavior is always measured instead of the grain in HAZ and WM regions (Fig. 6a). However, the size of some ferrite grains in BM is quite larger than the size of plastic zone created by the indenter, and then a grain behavior could be measured instead of a composite behavior if the indentation lands on the center of a larger ferrite grain. In this study, a special attention was paid to all indentation positions in the BM region. It was found that all of indentations were landed on or near the grain boundaries. These observations indicate that the indentation load–penetration depth (P–h) curve measured in this study is an exact indication of the local elastic–plastic response of the weld zone materials.

Fig. 7 presents typical P–h curves measured in the BM, HAZ, and WM regions. In this figure, only a representative curve at the middle of each weld zone was presented for the purpose of clarity. As shown in Fig. 7, with the same maximum load, the maximum penetration depth and the shape of P–h curve at three regions are significantly different. This indicates that for the present weld zone, the indentation response is highly distinguishable from individual weld zone.

In regard to 125 experimental P–h curves, the elastic modulus E and hardness H at each indenting point were determined using Eqs. (3)–(5). The yield strength σ_y and strain hardening exponent n in BM region were extracted based on the α value of 18 obtained from the tensile tests by using Eqs. (6) and (7). To estimate σ_y and n in HAZ and WM, the representative α value of these regions was characterized with the help of FE analysis results as presented in

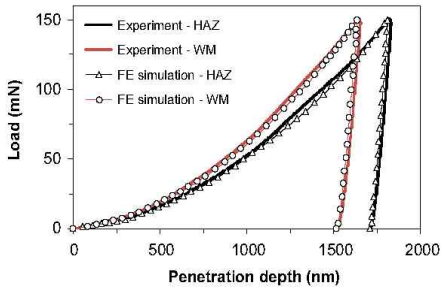


Fig. 8. Comparison of the simulated and experimental P–h curves of HAZ and WM.

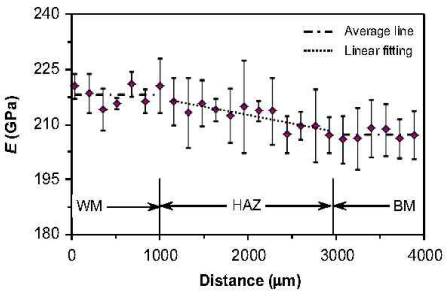


Fig. 9. Elastic modulus distribution across the weld zone.

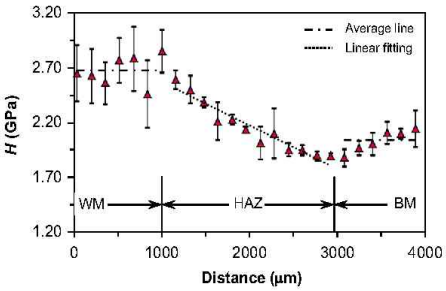


Fig. 10. Hardness distribution across the weld zone.

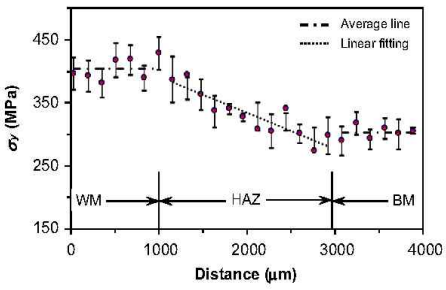


Fig. 11. Yield strength distribution across the weld zone.

Section 3. For the set of simulated load–penetration depth curves, FE analyses were carried out for the total of 576 combinations of the material parameters, in which α varied from 7 to 23 (for every 2), σ_y varied from 275 to 450 (for every 25 MPa), and n varied from 0.17 to 0.24 (for every 0.01). While Poisson's ratio was fixed for all analyses, the average value of E=215.3 GPa of all obtained E values

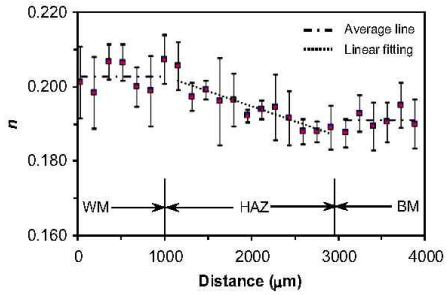


Fig. 12. Strain hardening exponent distribution across the weld zone.

Table 3
Mechanical properties of SS400 obtained from indentation and tensile tests.

	Indentation test	Tensile test				Err. (%)
		N1	N2	N3	Average	
E (GPa)	207.2	213.2	208.4	210.2	210.6	−1.6
σ_y (MPa)	302.7	305.6	307.2	306.9	306.6	−1.3
n	0.191	0.205	0.205	0.203	0.204	−6.4

in HAZ and WM was used as the representative E value for all FE analyses due to the fact that the average values of E in HAZ and WM were similar with the relative error within ±3% (Table 2) and such this small relative error would not affect much on the estimated value of α. Note that the above ranges of α, σ_y, and n were chosen after a special attention to α, σ_y, and n values in BM was paid and some prior analyses were performed in order to minimize the necessary number of FE analyses. The loading part of load–penetration depth curve, calculated up to 150 mN of applied load, was compared with the experimental ones to determine the α value of HAZ and WM. To reduce the complexity, only the load–penetration depth curves at the middle indenting column of HAZ and WM regions were used for comparison, as illustrated in Fig. 8, and the obtained value of α=15 and α=9 was considered as the representative value for HAZ and WM region, respectively. The obtained value of α=15 for HAZ indicates that the change of microstructure in HAZ during welding process influences much on the α value. This effect could be varied with different position along the HAZ region, however, the usage of α=15 as representative value for determining σ_y and n at all indenting positions along the HAZ region would be acceptable due to the fact that the estimated σ_y and n just changes around 11% and 23% when α value of SS400 steel increases from 7 to 23, respectively [9].

Since α=15 and α=9 were obtained for HAZ and WM regions, respectively, the yield strength σ_y and strain hardening exponent n at each indenting point in the HAZ and WM regions were then determined using Eqs. (6) and (7). Figs. 9–12 present the elastic modulus E, hardness H, yield strength σ_y, and strain hardening exponent n plotted as a function of the measured positions across the weld zone, respectively, where each data point represents an average of 5 values at each column of indents, together with an error bar of a standard deviation. In these figures, the dashed lines in the WM and BM regions represent the average values of all data points, while the dotted line in HAZ regions is the linear fitting of all values in this zone. As can be seen in these figures, various mechanical properties (E, H, σ_y, and n) exhibit relatively little variation in BM and WM regions, whereas a significant variation and a gradient-distribution of the mechanical properties are found in HAZ. The average values of all mechanical properties in WM region, E=218.2 GPa, H=2.7 GPa, σ_y=403.5 MPa, and n=0.203,

are highest, while the BM region has the lowest mechanical property values with E=207.2 GPa, H=2.0 GPa, σ_y=302.7 MPa, and n=0.191 as shown in Table 2, even though the hardness H, yield strength σ_y, and strain hardening exponent n in the HAZ area, which is adjacent to the BM region, are slightly smaller than those in BM (Figs. 10–12).

4.3. Verifications

Since the mechanical properties of the weld zone were indirectly measured using instrumented indentation testing and its FE analysis results, the tensile tests were performed on the SS400 steel and welded specimens to validate some of those values. Table 3 presents comparisons of E, σ_y, and n in BM with those observed from the tensile tests of three specimens, N1, N2, and N3.

It can be seen from this table that E, σ_y, and n in BM determined from indentation are in good agreement with those obtained from the tensile tests of three SS400 specimens, although the former is slightly smaller than the latter, which may be attributed to experimental errors of the indentation test [4,9] or the size-dependence of the present indentation measurements [15].

To verify the results of E in HAZ and WM regions determined from indentation test, the welded specimen of the tension test is considered as a composite made of three materials, BM, HAZ, and BM, in series with the corresponding modulus value of E_{BM}, E_{HAZ}, and E_{WM}, respectively. The equivalent modulus of the weld zone (E_{eq}) can be computed as follows:

$$E_{eq}=\frac{\lambda L E_{BM}E_{HAZ}E_{WM}}{\lambda(L_{BM}E_{HAZ}E_{WM}+L_{HAZ}E_{BM}E_{WM})+L_{WM}E_{BM}E_{HAZ}} \quad (9)$$

where λ is the ratio of section area of WM to section area of BM (or HAZ), L_{BM}, L_{HAZ}, and L_{WM} is the length of BM, HAZ, and WM, respectively, and$L=L_{BM}+L_{HAZ}+L_{WM}$ is the length between two gauges in the tension tests of the welded specimen. The equivalent modulus value of composite computed from Eq. (9) and elastic modulus of three welded specimens from the tension tests, together with their average value, are listed in Table 4. It can be seen that the equivalent elastic modulus value obtained using Eq. (9) based on the indentation test results is very close to the average value of elastic modulus obtained from the tension tests of three welded specimens, with a relative error of −1.5%.

To verify the results of yield strength σ_y and strain hardening n in HAZ and WM regions obtained from indentation tests, FE simulation of tensile test was developed using ABAQUS program [16]. The eight-node solid element C3D8R was used for all specimens. The material model illustrated in Eq. (8) was used to define the material properties of SS400 steel, HAZ, and WM regions. In order to validate the accuracy of the developed model, the FE simulation of tensile test of SS400 steel was first carried out. In this simulation, the mechanical properties (E, σ_y, and n) of SS400 steel obtained from tensile test were used as the input data. Fig. 13 shows the failure mode and locations of SS400 steel specimen from experiment and simulation. Good agreement can be observed between the simulated and experimental failure mode, whereas the failure locations show a little difference between experimental and simulated results. It might be related to the imperfection of the prepared steel specimen in the tensile test. Although the failure locations are little different, the simulated load–engineering strain curve agrees well with the experimental curve, as shown in Fig. 14. These results indicate that the developed FE model is accurately simulated the tensile test.

The developed FE model was then used to simulate the tensile test of welded specimen. The mechanical property values summarized in Table 2 were used as input properties of HAZ and WM regions in FE simulation. Fig. 15 shows the good agreement between simulated and experimental failure mode and locations for welded specimen. The load–engineering strain curves obtained from experiment of welded specimen and FE analysis of welded specimen with weld properties are presented in Fig. 16.

It can be seen from this figure that the FE analysis curve of welded specimen with weld properties closely matches the experimental curve with a little difference. The difference might be due to some certain reasons as follows: (i) the imperfection of the welded specimen in the test, especially the dimensions and the shape of the weld region; (ii) the properties used in the FE model are just the averaged properties of the WM and HAZ instead of the properties distributed across the weld zone; (iii) the change of microstructure across the weld zone are not considered in the FE model. However, the quite good agreement between these curves and the large difference between the curve from FE analysis

Table 4
Equivalent elastic modulus of SS400 steel weld zone.

	Equivalent elastic modulus value	Tension tests (welded specimens)				Err. (%)
		W1	W2	W3	Average	
E (GPa)	213.3	219.8	214.0	216.1	216.6	−1.5

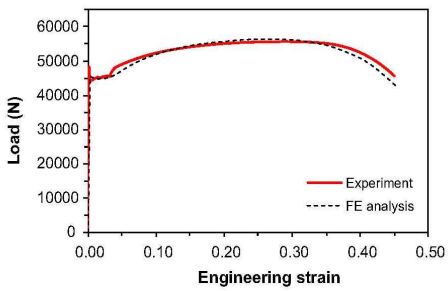


Fig. 14. Load–engineering strain curves from tensile test of steel specimen.

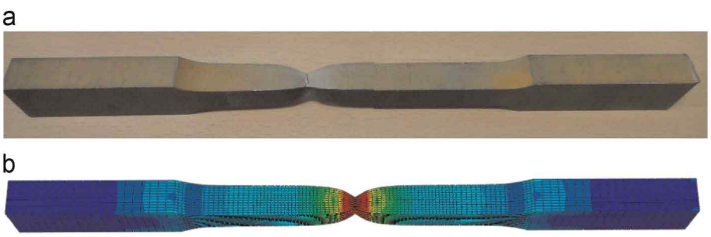


Fig. 13. Failure mode and locations of steel specimen. (a) Experiment. (b) FE simulation.

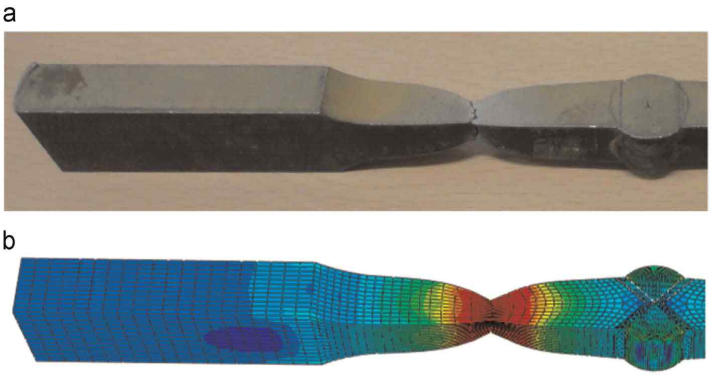


Fig. 15. Failure mode and locations of welded specimen. (a) Experiment. (b) Simulation.

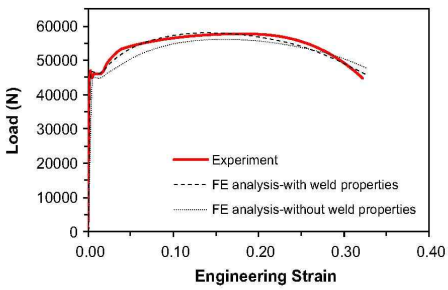


Fig. 16. Load–engineering strain curves from tensile test of welded specimen.

without welded properties and experiment, as also presented in Fig. 16, demonstrate that the indirectly measured weld zone properties are valid. Concerning the hardness, the values of H=2.7 GPa, H=2.2 GPa, and H=2.0 GPa (Table 2), corresponding to H=247.8 HV, H=198.8 HV, and H=188.6 HV, are representative of the hardness of WM, HAZ, and BM, respectively. These values and the distribution of hardness in the present weld zone are in good agreement with the results obtained from a similar low carbon steel weld zone (0.053% C) reported in the related literatures [18,23,24]. The above comparisons and results indicate that the mechanical properties of the present SS400 steel weld zone measured from instrumented indentation test are reliable.

4.4. Microstructures relevant to mechanical properties in the weld zone

The dependence of mechanical properties on the microstructure of materials has been indicated [20–22], and the variation of the mechanical properties in the present SS400 steel weld zone is essentially resulted from the changes of the microstructures during the welding. The formation of δ-ferrite is known as an important aspect among many aspects of microstructures that influence on the mechanical behavior of weldements [2,22], and the forming capacity of the δ-ferrite is governed by the α-ferrite amount in the material, the peak temperature in heating, and the cooling rate during the welding [20,21]. For present SS400 steel weld zone, the lower wt% C content of 0.04% leads to a higher amount of α-ferrite in weld metal than that in base metal, which has the higher wt% C content of 0.05% (Table 1). During the welding, all α-ferrite in the weld metal form of δ-ferrite due to the occurrence of the peak temperature this zone. Even the transformation of δ-ferrite to α-ferrite occurs during welding, it is believed that the remaining δ-ferrite in weld metal is still higher than that in base metal. The higher amount of δ-ferrite and its abundant transformed phase boundaries may be responsible for the greater strength, strain hardening exponent, and hardness in the weld metal than those in the base metal, while the slight higher elastic modulus in weld metal may be attributed to the "high stiffness ferrite" phase, which was discussed in the previous works [25,26].

The grain size and grain shape of the microstructure were demonstrated to have significant influence on the mechanical properties of structural steel [20–24,27,28]. Ding et al. [28] reported that the improvement of the mechanical properties in SS400 steel during thermomechanical control process attributed mainly to the ferrite-grain refinement. Khodabakhshi et al. [23,24] pointed out that hardness improvement in HAZ region of a low carbon steel weld zone with 0.053% C contents were due to finer microstructure. Hence, the higher mechanical properties (E, H, σ_y and n) of HAZ region when compared to base metal in present weld zone might be mainly due to the smaller and more regular sizes of ferrite grains in this region than in base metal even though other aspects such as dislocation density, etc. also have influence on. Since indentations were not indented to coarse grained zone, which is adjacent to the fusion zone, as illustrated in Fig. 6a, the decrease of mechanical properties (E, H, σ_y and n) within HAZ (Figs. 9 and 12) is associated with the increase of grain sizes from the fine grained zone to the interfacial region between the HAZ and BM. In other words, the microstructure gradient resulting from the metallurgical changes during the welding process leads to a gradient of mechanical properties within the HAZ. The severe property gradient in HAZ indicates that the other approach for determining mechanical properties, such as tensile test using mini- or micro-specimens extracted from the weld zone, can only provide an averaged mechanical measurement of the entire HAZ due to the fact that the dimension of the micro-tensile specimen is usually much larger than the size of microstructure. Thus, the instrumented indentation test would provide an appropriate approach for investigating the mechanical properties of the structural steel weld zone.

5. Conclusion

In this study, instrumented indentation, tensile tests, finite element (FE) analysis, and optical microscopy observation were carried out for the investigation of mechanical properties in the weld zone of SS400 steel. The results support the following conclusions.

Instrumented indentation test provides an appropriate approach for investigating the mechanical properties of the structural steel weld zone by combining the proposed method and FE analysis. The procedure for determining mechanical properties of structural steel weld zone from indentation test is as follows: (i) extract E and H by using conventional method [4]; (ii) determine σ_y and n in BM region by using proposed method with α value obtained from the tensile test of steel specimen; (iii) estimate the representative α value of HAZ and WM regions by correlating the experimental with the simulated load–penetration depth curves, which are obtained from various FE analyses of indentation test; (iv) determine σ_y and n in HAZ and WM regions by using proposed method with obtained α values.

For the present SS400 steel weld zone, the base metal has lower values of mechanical properties (E, H, σ_y and n) than does the weld metal, and the mechanical properties within heat affected zone gradually increase from the base metal to weld metal regions.

The microstructure of the BM is composed of ferrite and small regions of pearlite. The ferrite grain has various sizes, with the majority of the sizes in the range of 15–20 μm, while the biggest is around 40 μm. The microstructure of HAZ consists of grain polygonal ferrite with different grain sizes and some regions of pearlite that are also located at the corners of the grains. The grain size in the HAZ region is smaller and more regular than those in the BM. The microstructure of WM contains α, α_W, α_a, and certain small amounts of pearlite. These microstructures strongly influence on the mechanical properties in the weld zone.

The higher amount of δ-ferrite and its abundant transformed phase boundaries may be responsible for the higher mechanical properties values in weld metal when compared to those in base metal, while the smaller and more regular sizes of ferrite grains in HAZ may be mainly responsible for the higher mechanical properties values in HAZ when compared to those in base metal.

Acknowledgments

This research was supported by a grant (15CTAP-C098306-01) from Technology Advancement Research Program funded by Ministry of Land, Infrastructure and Transport of Korean.

Appendix A

See Appendix Table A1 and A2

Table A1
Coefficient a_{ijk}.

(k, j)	a_{ijk}			
	$i=4$	$i=3$	$i=2$	$i=1$
(1, 1)	−1.710E−1	1.629E+0	1.144E+2	−4.574E+1
(2, 1)	1.395E−2	−1.195E−1	2.955E−1	−1.643E−1
(3, 1)	−4.231E−4	3.903E−3	−9.428E−3	5.243E−3
(1, 2)	9.940E+0	7.973E+0	5.240E+1	−6.190E+1
(2, 2)	−1.193E+0	2.573E+0	−5.962E+0	3.952E+0
(3, 2)	3.876E−2	−1.429E−1	1.858E−1	−5.743E−2
(1, 3)	−1.196E+2	5.892E+2	−9.072E+2	4.656E+2
(2, 3)	1.194E+1	−5.351E+1	5.441E+1	−1.804E+1
(3, 3)	−3.417E−1	1.631E+0	−1.443E+0	2.175E−1
(1, 4)	1.981E+2	−4.190E+2	4.267E+2	−2.408E+2
(2, 4)	−1.845E+1	3.178E+1	2.717E+0	−1.053E+1
(3, 4)	5.023E−1	−1.147E+0	3.126E−2	5.674E−1

Table A2
Coefficient b_{ijk}.

(k, j)	b_{ijk}			
	$i=4$	$i=3$	$i=2$	$i=1$
(1, 1)	−6.197E−2	8.766E−1	−3.097E+0	6.085E+0
(2, 1)	2.285E−5	−7.846E−4	5.723E−3	−1.095E−2
(3, 1)	−4.241E−6	8.032E−5	−4.539E−4	7.676E−4
(1, 2)	9.840E−1	−1.477E+1	6.723E+1	−9.676E+1
(2, 2)	−6.638E−2	9.160E−1	−3.909E+0	5.367E+0
(3, 2)	1.877E−3	−2.619E−2	1.147E−1	−1.630E −1
(1, 3)	−4.036E+0	6.074E+1	−2.847E+2	4.247E+2
(2, 3)	4.241E−1	−6.122E+0	2.797E+1	−4.112E+1
(3, 3)	−1.324E−2	1.911E−1	−8.782E−1	1.301E+0
(1, 4)	4.871E+0	−7.309E+1	3.440E+2	−5.160E+2
(2, 4)	−5.777E−1	8.394E+0	−3.875E+1	5.745E+1
(3, 4)	1.875E−2	−2.718E−1	1.257E+0	−1.870E+0

References

[1] Tamboli AR. Handbook of structural steel connection design and details. NY, USA: McGraw-Hill; 1999.
[2] Ye D, Mi F, Liu J, Xu Y, Chen Y, Xiao L. Use of instrumented indentation testing to study local mechanical properties of 304L SS welded joints subjected to low-cycle fatigue loadings. Mater Sci Eng A 2013;564:76–84.
[3] Bhushan B. In: Handbook of nanotechnology. Berlin: Springer; 2007.
[4] Oliver WC, Pharr GM. An improved technique for determining hardness and elastic-modulus using load and displacement sensing indentation experiments. J Mater Res 1992;7(4):1564–83.
[5] Kucharski S. Identification of yield stress and plastic hardening parameters from a spherical indentation test. Int J Mech Sci 2007;49:1238–50.
[6] N'Jock MY, Chicot D, Decoopman X, Lesage J, Ndjaka JM, Pertuz A. Mechanical tensile properties by spherical macroindentation using an indentation strain-hardening exponent. Int J Mech Sci 2013;75:257–64.
[7] Dao M, Chollacoop N, Vliet KJV, Venkatesh TA, Suresh S. Computational modeling of the forward and reverse problem in instrumented sharp indentation. Acta Mater 2001;49:3899–918.
[8] Kang JJ, Becker AA, Sun W. Determining elastic-plastic properties from indentation data obtained from finite element simulations and experimental results. Int J Mech Sci 2012;62:34–46.
[9] Pham TH, Kim JJ, Kim SE. Estimating constitutive equation of structural steel using indentation. Int J Mech Sci 2015;90:151–61.
[10] Chung KH, Lee W, Kim JH, Kim C, Park SH, Kwon D, Chung K. Characterization of mechanical properties by indentation tests and FE analysis – validation by application to a weld zone of DP590 steel. Int J Solids Struct 2009;46 (2):344–63.
[11] Zhan M, Du H, Liu J, Ren N, Yang H, Jiang H, Diao K, Chen X. A method for establishing the plastic constitutive relationship of the weld bead and heat-affected zone of welded tubes based on the rule of mixtures and a micro-hardness test. Mater Sci Eng A 2010;527(12):2864–74.
[12] Yonezu A, Akimoto H, Fujisawa S, Chen X. Spherical indentation method for measuring local mechanical properties of welded stainless steel at high temperature. Mater Des 2013;52:812–20.
[13] Sun G, Xu F, Li G, Huang X, Li Q. Determination of mechanical properties of the weld line by combining micro-indentation with inverse modeling. Comput Mater Sci 2014;85:347–62.
[14] ASTM E8/E8M-13a. Standard test methods for tension testing of metallic. West Conshohocken, PA: ASTM International; 2013.
[15] Ye D, Matsuoka S, Nagashima N. Determination of fatigue mesoscopic mechanical properties of an austenitic stailess steel using depth-sensing indentation (DSI) technique. Mater Sci Eng A 2007;456:120–9.
[16] Hibbitt, Karlsson, Sorensen, ABAQUS Standard User's Manual, version 6.6 (2006), Inc.
[17] Lichinchi M, Lenardi C, Haupt J, Vitali R. Simualtion of Berkovich Instrumented indentation experiments on thin films using finite element method. Thin Solid Films 1998;312:240–8.
[18] Khodabakhshi F, Kazeminezhad M, Kokobi AH. Mechanical properties and microstructure of resistance spot welded severely deformed low carbon steel. Mater Sci Eng A 2011;529:237–45.
[19] Khodabakhshi F, Kazeminezhad M, Kokobi AH. On the failure behavior of highly cold worked low carbon steel resistance spot welds. Metall Mater Trans A 2014;45A:1376–89.
[20] Bhadeshia HKDH, Honeycombe R. Steels: microstructure and properties. London: Butterworth-Heinemann; 2006.
[21] Easterling KE. Introduction of the physical metallurgy of welding. 2nd ed. London: Butterworth-Heinemann; 1992.
[22] Kou S. Welding metallurgy. 2nd ed. . Hoboken, New Jersey: John Wiley & Sons, Inc.; 2003.

[23] Khodabakhshi F, Kazeminezhad M, Kokobi AH. Resistance spot welding of ultra-fine grained sheets produced by constrained groove pressing: optimization and characterization. Mater Charact, 69; 2012. p. 71–83.
[24] Khodabakhshi F, Kazeminezhad M, Kokobi AH. Metallurgical characteristics and failure mode transition for dissimilar resistance spot welded between ultra-fine and coarse-grained low carbon steel sheets. Mater Sci Eng A 2015;637:12–22.
[25] Pham TH, Kim JJ, Kim SE. Estimation of microstructural compositions in the weld zone of structural steel using instrumented indentation. J Constr Steel Res 2014;99:121–8.
[26] Pham TH, Kim SE. Nanoindentation for investigation of microstructural compositions in SM490 steel weld zone. J Constr Steel Res 2015;110:40–7.
[27] Lehto P, Remes H, Saukkonen T, Hanninen H, Romanoff J. Influence of grain size distribution on the Hall–Petch relationship of welded structural steel. Mater Sci Eng A 2014;592:28–39.
[28] Ding H, Li L, Yang C, Song D, Du L. Microstructures of an ultrafine grained SS400 steel in an industrial scale. J Mater Sci Technol 2006;22(2):145–8.

2. Determination of mechanical properties in SM490 steel weld zone using nanoindentation and FE analysis(2015)

Journal of Constructional Steel Research 114 (2015) 314–324

Contents lists available at ScienceDirect

Journal of Constructional Steel Research

Determination of mechanical properties in SM490 steel weld zone using nanoindentation and FE analysis

Thai-Hoan Pham [a], Seung-Eock Kim [b,*]

[a] Dept. of Civil and Environmental Engineering, Sejong University, Seoul, South Korea
[b] Dept. of Civil and Environmental Engineering, Sejong University, 98 Gunja-dong, Gwangjin-ku, Seoul 143-747, South Korea

ARTICLE INFO

Article history:
Received 12 April 2015
Received in revised form 1 August 2015
Accepted 4 August 2015
Available online 15 August 2015

Keywords:
Mechanical properties
Nanoindentation
SM490 steel
Weld zone
FE analysis

ABSTRACT

Nanoindentation, tensile test, finite element (FE) analysis, and optical microscopy examination were carried out to investigate the mechanical properties in an SM490 steel weld zone. Three indentation series were performed across the weld zone including the base metal (BM), heat-affected zone (HAZ), and weld metal (WM). The mechanical properties (E, H, σ_y, and n) were then estimated from the load–penetration depth data of nanoindentation and FE analysis results. The tensile tests of SM490 and welded specimens were conducted and the equivalent modulus of the weld zone was interpreted from the composite action of BM, HAZ, and WM. The results from nanoindentation showed that WM has the highest values of mechanical properties (E, H, σ_y, and n), BM has the lowest mechanical properties values, while the mechanical properties within HAZ gradually decrease from the WM to BM region. The effect of microstructural changes due to the weld on the mechanical properties in the weld zone was also discussed.

© 2015 Elsevier Ltd. All rights reserved.

1. Introduction

SM490 steel is a very commonly used hot rolled structural steel in Korea. One of the important factors contributing to the use of steel is its low cost and excellence in machinability and weldability [1]. In current usage of SM490, welding has been widely used to connect steel members due to such advantages as design simplicity and high rigidity [2]. However, the inhomogeneity of microstructures in the weld zone could lead to the changes in the mechanical properties and generate a local stress concentration, which could extensively initiate crack propagation [3]. It has been reported that during the welding, the solid-state phase transformations have a strong influence on the final microstructure and affect mechanical properties such as hardness and toughness in the weld zone of the structural steel [4–9]. However, these effects on the basic mechanical properties in SM490 steel weld zone, such as elastic modulus E, yield strength σ_y, and strain hardening exponent n, have rarely been reported so far. Thus, it is quite significant to have a comprehensive study of the mechanical properties including elastic modulus, yield strength, and strain hardening exponent in weld zone of SM490 steel.

Nanoindentation has been used in many engineering fields including biomedical, civil, mechanical, and material engineering [10–13]. Recently, numerous analytical methods have been developed for characterization of basic mechanical properties (elastic modulus, yield stress, strain hardening exponents, etc.) from the load–penetration depth data of indentation tests [14–17]. Unlike conventional tests, the indentation test allows determining the local material properties in the indented region. Due to this feature, indentation has been extensively used in characterizing mechanical properties of inhomogeneous materials such as weld zone [18–23]. Chung et al. [18] applied indentation tests and finite element (FE) analysis to obtain mechanical properties of DP590 steel weld zone, of which the isotropic hardening law was assumed along with the non-quadratic anisotropic yield function Yld2000-2d. Ambriz et al. [20] used micro-traction and instrumented indentation to investigate mechanical properties of the 6061-T6 aluminum weld and it was found that the property values in heat affected zone were smaller than those in base metal. Charitidis and Dragatogiannis [21] extracted equivalent stress–strain curves for base metal and welded zone of a friction stir welded aluminum alloy by using Berkovich nanoindentation. Ye et al. [22] conducted a series of experiments including indentation tests, low-cycle fatigue tests, and optical microscopy examinations to study the local mechanical properties and microstructures in individual zone of 304 L SS welded joint in both as-welded and cyclic loading conditions. Recently, Sun et al. [23] successfully determined mechanical properties of the weld line of two typical dual phase high strength steels DP600/DP980 by combining micro-indentation with inverse modeling. In this research [23], the FE model was constructed based on the power law constitutive model to simulate the elastoplastic response of each individual weld zone and then the

* Corresponding author.
E-mail address: sekim@sejong.ac.kr (S.-E. Kim).

http://dx.doi.org/10.1016/j.jcsr.2015.08.014
0143-974X/© 2015 Elsevier Ltd. All rights reserved.

mechanical properties in the different zone were identified by comparing the experimental data and simulation results. However, these above studies are focused on the materials of which the constitutive model could be accurately assumed as isotropic hardening law or power law formulation and do not cover materials with plastic plateau in their constitutive equations such as structural steel SM490.

This study aims to investigate the mechanical properties in the weld zone of structural steel SM490 by combining the proposed method [17], which allows estimating the mechanical properties (yield strength σ_y and strain hardening exponent n) of structural steel from indentation results, and FE analysis. For this purpose, manual metal arc welding was used for a double V groove butt welding of two SM490 steel plates. Nanoindentation, tensile test, FE analysis, and optical microscopy examination were carried out. The distributions of mechanical properties (E, H, σ_y, and n) across the weld zone were determined and the effect of microstructural changes due to the weld on the mechanical properties in the weld zone was discussed.

2. Experimental details

A SM490 steel plate thickness of 12 mm was chosen to be the welded plate for the investigation. The manual metal arc welding with electrode ER 70S-6 was used for the double V groove butt welding. The major chemical composition in percentage weight of SM490 and weld metal are listed in Table 1. The weld was completed with a voltage of 22 V and a current of 100 A. The dimensions of the weld portion are 12 mm in width, without a root gap.

For nanoindentation, one slice of 8 × 20 mm including the weld zone was cut out from the welded plate by water-jet. This slice containing BM, HAZ, and WM regions was then mounted in epoxy and polished with different silicon carbide papers, poly diamond particles, and colloidal silica in order to obtain a flat, smooth surface. This procedure was achieved in seven stages of increasing fineness, with the last in the range of 40 nm according to ASTM E3-01 standard [24]. Nanoindentation was performed at room temperature using a Nano Hardness Tester machine made by the Swiss Center for Electronics and Microtechnology. The machine operation conforms to the ISO 14577 and ASTM E2546-07 standards [25,26]. The Berkovich indenter made of industrial diamond with an elastic modulus of 1141 GPa and Poisson's ratio of 0.07 was employed. In all indentation tests, a fixed maximum load of 150 mN at a constant loading and unloading rate of 300 mN/min was applied. Taking into account the inhomogeneity of the local mechanical response in the weld zone, three nanoindentation series (labeled S1, S2, and S3) consisting of 5 × 26 indenting points across the SM490 steel weld zone were performed. The indenting regions of each series contained portions of base metal, heat-affected zone, and weld metal. To reveal the microstructure, the polished specimen was etched for 40s with 2% nital, and the microstructures were observed by optical microscopy (OM). Fig. 1 shows indenting locations on the surface of nanoindentation sample after being etched.

For tensile test, six specimens including three specimens of SM490 (labeled N1, N2, and N3) and three welded specimens (labeled W1, W2, and W3), which were taken directly from the welded plate, were prepared according to ASTM standard [27]. Specimens of SM490 have the same thickness of 12 mm as welded specimens. Fig. 2 shows (a) the dimensions of the specimens, (b) SM490 steel specimens, and (c) welded specimens for tensile tests. The tests were carried out using an Instron tensile testing machine and tested according to ASTM standard [27].

Table 1
Chemical compositions of SM490 and ER70S-6 (in wt.%).

Material	C	Si	Mn	P	S	Ni	Cu
SM490	0.16	0.40	1.45	0.010	0.003	N/A	N/A
ER70S-6	0.12	0.91	1.43	0.012	0.005	0.13	0.22

3. Determination of mechanical properties from the indentation load-penetration depth curve and FE analysis

3.1. Determination of elastic modulus and hardness

Fig. 3 schematically shows the typical load-penetration depth curve (P–h) of an elasto-plastic material to sharp indentation. While the unloading part of the load-penetration depth curve contains information related to the elastic modulus E of the indentation material, the loading part contains the plastic characteristic of the indented domain. The straightforward quantity to estimate this is to relate the material plasticity to the domain hardness H.

The indentation elastic modulus E and hardness H can be extracted from the following relations [14]:

$$E_r = \frac{\sqrt{\pi}}{2\beta}\frac{S}{\sqrt{A_c}} \tag{1}$$

$$E_r = \left[\frac{1-\upsilon^2}{E} + \frac{1-\upsilon_i^2}{E_i}\right]^{-1} \tag{2}$$

$$H = P_m / A_c^{\,c} \tag{3}$$

where A_c is the projected area of contact between the indenter and the sample, S is the contact stiffness, E_r is the reduced modulus owing to the effects of elastic deformation of the indenter, β is the correlation factor for indenter shape ($\beta = 1.034$ for a Berkovich indenter), P_m is the maximum load applied during the indentation, and E, υ, E_i and υ_i are the elastic modulus and Poisson's ratio of the sample and indenter, respectively. The contact stiffness S is the initial unloading slope defined as $S = (dP_u/dh)|_{h_m}$, where P_u is the unloading force. In this study, Eqs. (1)–(3) were used to determine the elastic modulus and hardness of all individual regions (BM, HAZ, and WM) in the SM490 steel weld zone.

3.2. Determination of yield strength and strain hardening exponent in BM

Concerning the yield strength σ_y and hardening coefficient n of structural steel, a method allows estimating these parameters from the P–h curve of nanoindentation was used [17]. In this method the plastic parameters (σ_y, n) can be determined with respect to α following the algorithm in Fig. 4, where α is defined as strain at the starting-point of strain hardening ε_{st} divided by the initial yield strain ε_y. It is noted that a range from 7 to 23 of α was obtained from the tensile tests of the most popular structural steels, SS41 and SM50A [28], and this was considered the representative range for structural steel. In Fig. 4, a_{ijk} and b_{ijk} are coefficients (Appendix A), and C is loading curvature that can be computed as $C = P_m/h_m^2$, where h_m is the maximum penetration depth. The method was demonstrated to be relatively accurate in estimating the plastic properties of structural steel. Since α value of BM can be obtained from the tensile test of SM490 steel, the proposed method was directly used for the determination of plastic parameters (σ_y, n) in BM of the weld zone.

3.3. Determination of yield strength and strain hardening exponent in HAZ and WM

The proposed method allows determining yield strength and strain hardening exponent of structural steel with respect to α. However, the α value of HAZ and WM could not be obtained from tensile test of the

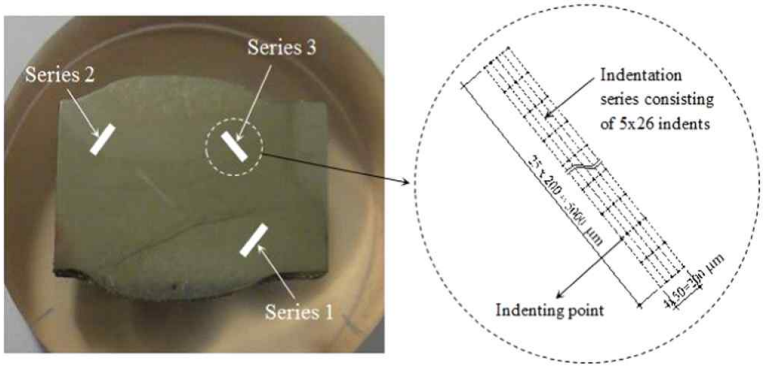
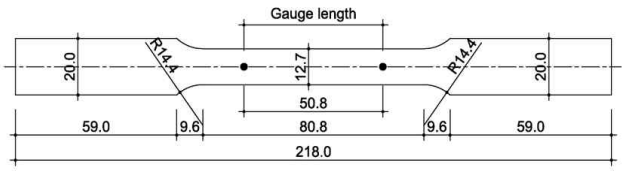


Fig. 1. Indentation sample surface after being etched and indenting locations.

welded specimens, while preparing mini- or micro-specimens from the weld zone that allows determining α value of the weld zones is a rather difficult task due to the small-size of the zones [18,22]. To overcome this challenge, the FE analyses of conical indentation were performed using the nonlinear finite element analysis program ABAQUS for correlating the experimental with the simulated load-penetration depth curves in order to obtain the α value of HAZ and WM. The conical indenter with a semi-apical angle of $\theta = 70.3°$ has the same projected area–depth



(a) Dimensions of specimens



(b) SM490 steel specimens



(c) Welded specimens

Fig. 2. Specimens for tensile tests.

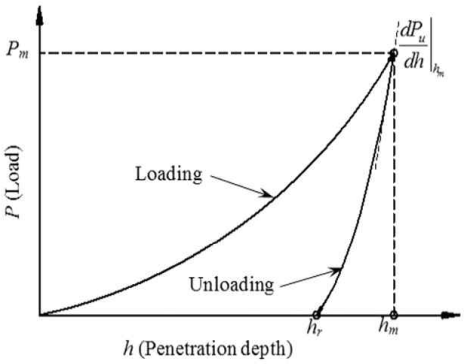


Fig. 3. Typical load–penetration depth curve (P–h).

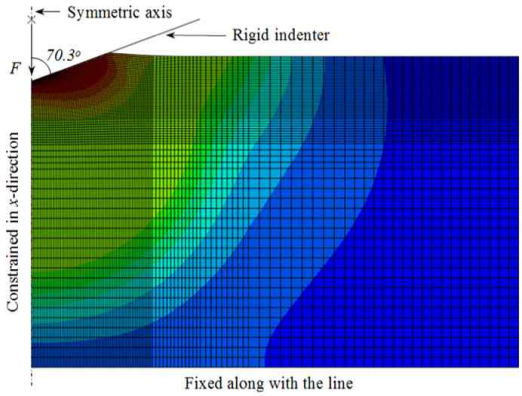


Fig. 5. FE simulation of indentation test.

functions as the standard Berkovich indenter used in the indentation tests. The P–h responses of the conical and Berkovich indentations obtained from finite element analysis using ABAQUS were demonstrated to be virtually identical for micro- or nano-scale [16,29]. Considering symmetric conditions, an axisymmetric two-dimensional FE model was developed to simulate the indentation procedure. The matrix was modeled using 8576 four-node bilinear axisymmetric quadrilateral elements. A fine mesh near the contact region and a gradually coarser mesh further from the contact region were designed to ensure numerical accuracy and save computational time. At the maximum load, the minimum number of contact elements in the contact zone was ensured to have no less than 16 elements in each FE analysis. Fig. 5 shows the axisymmetric FE simulation of indentation test. The geometric boundary conditions were applied as follows: the nodes along y axis (the axis of rotation) can move only along the axis itself, and all the nodes on the bottom of the mesh were fixed. The indenter was modeled as a rigid movable surface and the contact between the indenter and the matrix surface was assumed to be frictionless based on Bucaille's study [30]. They reported that the influence of friction on the P–h curves in cases of Berkovich and Vickers indentations can be neglected. The indentation process was simulated by two subsequent steps: loading and unloading steps. While the rigid indenter surface moved along the y direction and penetrated the matrix up to the maximum penetration depth during the loading step, the indenter returned to the initial position during the unloading step. The material model for structural steel that was used in the previous work was also applied in this study, as follows:

$$\sigma = \begin{cases} E\varepsilon & (\varepsilon \le \varepsilon_y) \\ \sigma_y & (\varepsilon_y < \varepsilon < \varepsilon_{st}) \\ \sigma_y\left[1 + E(\varepsilon - \varepsilon_{st})/(\alpha\sigma_y)\right]^n & (\varepsilon \ge \varepsilon_{st}) \end{cases}. \tag{4}$$

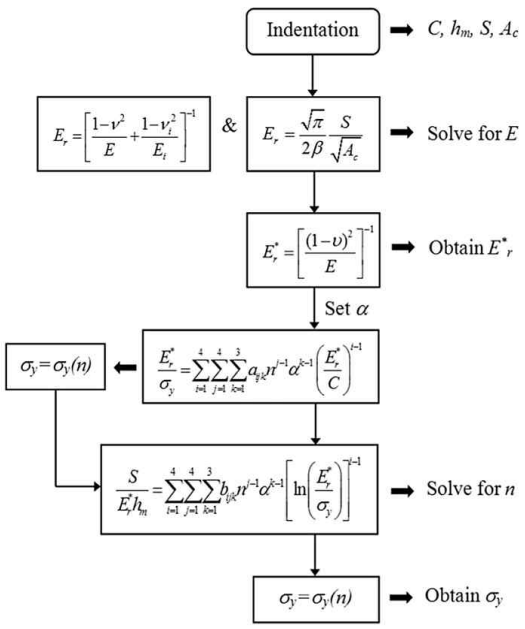


Fig. 4. Algorithm for determining yield strength and strain hardening exponent [17].

The developed FE model was demonstrated to be accurately simulated by verifying with the experimental result [17].

Since elastic modulus of HAZ and WM could be directly obtained from indentation test results and Poisson's ration was fixed at 0.3, a set of simulated load–penetration depth curves was prepared with various values of α, σ_y, and n as the input data for FE simulations. The representative value of α for HAZ and WM was then determined by comparing the experimental load–penetration depth curves with the set of simulated curves. As for the set of simulated load–penetration depth curves for SM490 steel weld zone in this study, FE analyses were carried out for the total of 576 combinations of the material parameters, in which α varied from 7 to 19 (for every 1.5), σ_y varied from 310 to 450 (for every 20 MPa), and n varied from 0.23 to 0.30 (for every 0.01). While the Poisson's ratio was fixed for all analyses, the average value of $E = 207.7$ GPa of all obtained E values in HAZ and WM was used as the representative E value for all FE analyses due to the fact that the average values of E in HAZ and WM were quite similar with the relative error within ±6% (Table 2) and such a this small

Table 2
Average values of E and H in the weld zones.

	Series	WM	HAZ	BM
E (GPa)	1	210.4	201.7	192.5
	2	213.4	204.1	201.2
	3	211.5	205.0	198.0
H (GPa)	1	2.86	2.64	2.42
	2	2.78	2.65	2.53
	3	2.84	2.65	2.50

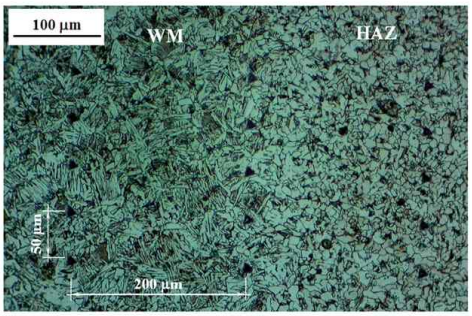
relative error would not affect much on the estimated value of α. Note that the above ranges of α, σ_y, and n were chosen after a special attention to α, σ_y, and n values in BM was paid and some prior analyses were performed in order to minimize the necessary number of FE analyses. The loading part of load–penetration depth curve, calculated up to 150 mN of applied load, were compared with the experimental ones to determine the α value of HAZ and WM. To reduce the complexity, only the load–penetration depth curves at the middle indenting column of HAZ and WM regions were used for comparison. Once α value of HAZ and WM was estimated, the yield strength and strain hardening exponent distributed in HAZ and WM could be determined using the proposed method [17].

4. Results and discussion

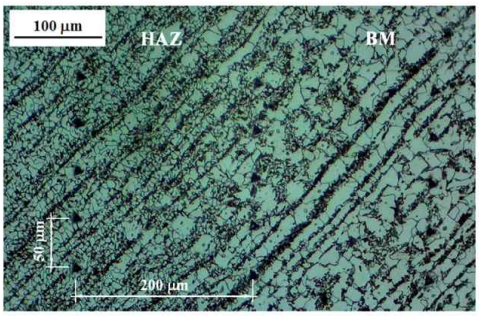
4.1. Identification of individual weld zone and indentation responses

The optical micrographs of representative parts of indentation impressions across the weld zone are presented in Fig. 6. It can be observed from this figure that the WM and HAZ regions in Fig. 6a as well as the HAZ and BM regions in Fig. 6b were clearly distinguished. This distinctness allows identifying the BM, HAZ, and WM regions as well as their approximate dimensions. The identification showed that each indenting series consisting of 5 × 26 points covered a length of 5.0 mm across the weld zone, including approximately 2.2, 2.3, and 2.2 mm of the HAZ region for series S1, S2, and S3, respectively. Fig. 7 shows high resolution optical images of the Berkovich indentation which resulted from applying a maximum load of 150 mN to the weld zone including indentation in WM, HAZ adjacent to WM, HAZ adjacent to BM, and BM. While a relatively little pile-up can be observed from the residual impression in the HAZ region adjacent to WM (Fig. 7b), the Berkovich residual impressions in other regions of the weld zone manifest virtually no pile-up or sink-in (Fig. 7a, c, and d). That means the applied methods for determining the mechanical properties work well in the case of SM490 steel weld zone [31]. Note in Figs. 6 and 7 that the size of the indents is not much smaller than the ferrite grain size in HAZ and WM. Considering that indentation with a Berkovich tip "feels" a volume with radius of 5 to 9 times maximum penetration depth or the size of plastic zone created by the indenter is about 2 times as larger as the indentation size [32], a composite behavior is always measured instead of the grain in HAZ and WM regions, as illustrated in Fig. 7a, b, and c. In contrast, the size of some ferrite grains in BM is quite larger than the size of plastic zone created by the indenter, and then a grain behavior could be measured instead of a composite behavior if the indentation lands on the center of a larger ferrite grain. In this study, a special attention was paid to all indentation positions in the BM region. It was found that all of indentations were landed on or near the grain boundaries, as illustrated in Fig. 7d. It is also noted in Fig. 6 that the size of the indents is much smaller when compared to the dimension of the individual weld zone. These observations indicate that the indentation load–penetration depth (P–h) curve measured in this study is an exact indication of the local elastic–plastic response of the weld zone materials.

The microstructure examinations and mechanical properties of the identified regions in the weld zone are detailed below.



(a) Across WM and HAZ



(b) Across HAZ and BM

Fig. 6. Optical micrograph of indenting points across the weld zone.

4.2. Microstructures in the weld zone

In order to seek for the correlation of the microstructures with the mechanical properties in different regions of the SM490 steel weld zone, microstructural examinations were performed in individual weld zones. Fig. 8 shows the microstructures of BM, HAZ, and WM. As can be seen from this figure, the microstructure of BM consists of ferrite and pearlite bands that are settled along the grain boundaries of ferrite (Fig. 8a); while HAZ is composed of grain polygonal ferrite (PF) with the majority of the sizes about 10 μm and pearlite regions located at the corners of the ferrite grains. Some pearlite bands settled along ferrite grain boundaries can also be observed from optical micrograph of HAZ (Fig. 8b). It is interesting to note in Figs. 8a, b, and 6b that both pearlite and ferrite grains in HAZ are different in shape and orientation as well as more regular and much smaller in size when compared with those in BM. The WM region in the present SM490 steel weld zone exhibits a complex microstructure (Fig. 8c), where some amounts of pearlite surrounded by different types of ferrite grain. These types of grain are allotriomorphic ferrite (α), Widmanstatten ferrite (α_W), and acicular ferrite (α_a), where the sizes of allotriomorphic ferrite are much larger than others.

As indicated [33–35], during the welding, metallurgical changes take place in weld zone. The HAZ represents regions in the close proximity of the weld where the heat input during welding changes the microstructure without melting the steel (base metal). Due to the different peak heated temperatures, a gradient of microstructure in the HAZ is well defined as a function of the distance from the fusion boundary. The regions immediately to the fusion boundary are heated to very high temperatures and hence transform completely to austenite at the upper critical temperature (Ac_3) by about 100 °C. The austenite that forms is annealed during heating beyond Ac_3, giving rise to a very coarse-grain austenite zone. The austenite grain size decreases sharply with distance from the fusion boundary. These austenite grains lead to the formation of the coarse grained zone (CGZ) and fine grained zone (FGZ) of the final microstructures, which is adjacent to the weld fusion zone and slightly further away from the fusion boundary, respectively, as can be seen in Fig. 6a. As the peak temperature decreases, regions of the HAZ further away from the fusion boundary become only partially austenite during the heating part of the thermal cycle. The part that does not transform into austenite becomes tempered [33]. This causes the ferrite grains in the final microstructure of HAZ region, which is further away from

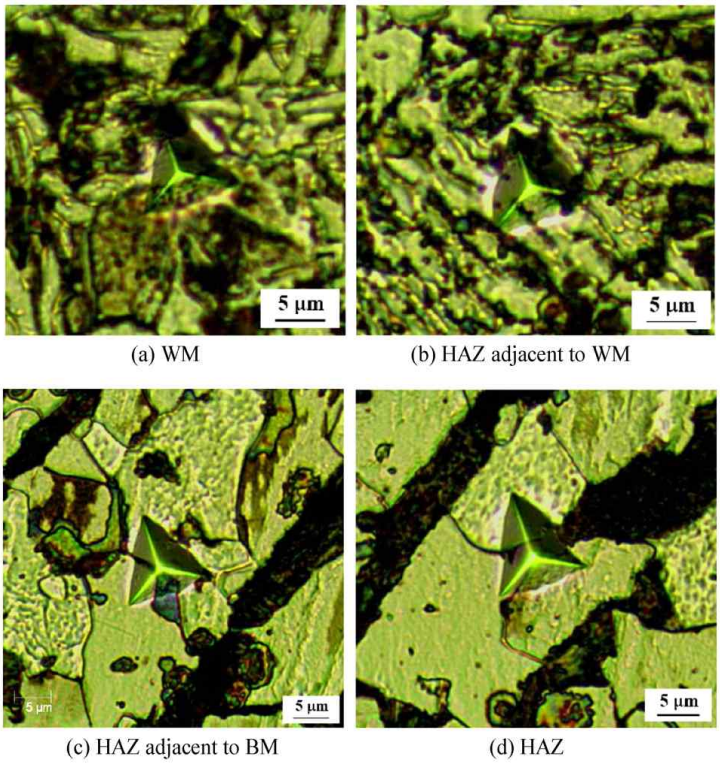


Fig. 7. Optical images of the Berkovich indentation in the weld zone.

fusion boundary and near the base metal, to be more regular and smaller in size when compared with those in BM, as shown in Fig. 6b.

The fusion zone (weld metal — WM), on the other hand, represents both the deposited metal and the parts of the steel component melted during the process, and is a solidification microstructure. During the welding process, the peak temperature in this zone is much higher than the upper limit of phase balance between δ-ferrite and γ-austenite, leading all ferrite and pearlite change to austenite. The austenite grains then can form into many different phases of microstructure depending on the cooling rate, the detailed shape, and the size of the austenite grains. During a medium-slow cooling rate as that used for the present SM490 steel weld zone, allotriomorphic ferrite (α) is the first form on cooling the austenite grains below the Ac_3 temperature. When the layers of allotriomorphic ferrite reach a limiting thickness, the remaining austenite begins to transform to Widmanstatten ferrite (α_W). On further cooling below A1 the carbon-enriched regions between the α_W grains transform to cementite or pearlite. Another reaction that can occur in the WM at undercooling near to A1 is the formation of acicular ferrite (α_a) [33,34]. The microstructure of WM in the present SM490 steel weld zone consisting of α, α_W, α_a, and pearlite is totally consistent with the above reported results.

4.3. Distributions of mechanical properties across the weld zone

The load–penetration depth curves (P–h) measured in the BM, HAZ, and WM regions are presented in Fig. 9. For clarity, only one typical curve at the middle position for each weld zone obtained from three indentation series was presented in this figure. As shown in Fig. 9, while the maximum penetration depth and the shape of P–h curves in the same region obtained from three indentation series exhibit relatively little variation, a significant variation exits between those in different regions. This indicates that for the present weld zone, the indentation response is not only reliable but also highly distinguishable from the details of the metallurgical condition that resulted from the welding process.

In terms of the experimental P–h curves obtained from the three indentation series, the elastic modulus E and hardness H at each indenting point were computed using Eqs. (1)–(3), the yield strength σ_y and strain hardening exponent n at each indenting point in the BM region were determined using the algorithm presented in Fig. 4, while σ_y and n at each indenting point in the HAZ and WM regions were estimated with the help of FE analysis results as presented in Section 3.3.

4.3.1. Distributions of elastic modulus and hardness across the weld zone

The elastic modulus E and hardness H distributions across the weld zone are illustrated in Fig. 10, where each data point is an average of 5 values at each indenting column. In this figure, the dotted lines in WM and BM represent the average values of all data points in these regions, while the dotted line in HAZ is the linear fitting of all values in this zone.

As can be seen in Fig. 10, while various E and H values exhibit relatively little variation in the BM and WM regions, a significant variation and a gradient-distribution of the E and H values are found in HAZ for all indentation series. In other words, the results obtained from all indentation series show the same trend that WM has the highest values of E and H, BM has the lowest E and H values, while the E and H values in the HAZ region gradually decrease from the WM to BM region. Table 2 presents the average values of E and H in the BM, HAZ, and WM regions obtained from three indentation series. As seen from this table, the average values of E and H obtained from three indentation

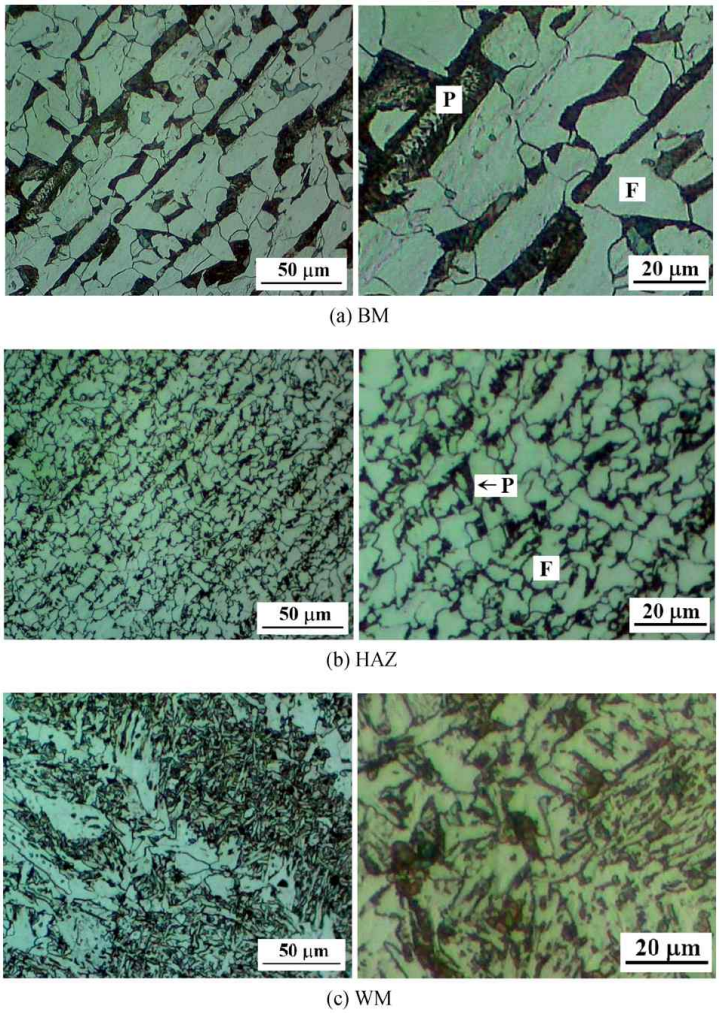


Fig. 8. Microstructures in the weld zone.

series are similar for each individual weld zone. These results and the distributions of E and H values plotted in Fig. 10 indicate that the changing trends of E and H in the weld zone obtained from nanoindentation are reliable. The variation in the E and H values across the weld zone is mainly attributed to the changes of microstructures during the welding, which will be discussed in the next subsection.

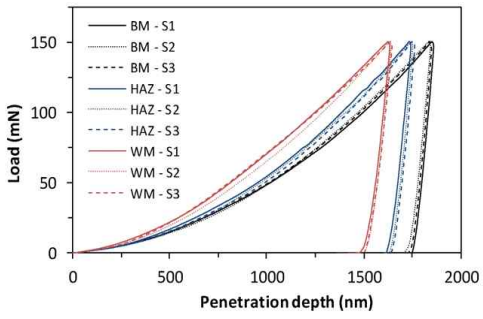


Fig. 9. Typical indentation P–h curves in the weld zones.

4.3.2. Distributions of yield strength and strain hardening exponent across the weld zone

In application of the algorithm presented in Fig. 4 for determining yield strength σ_y and strain hardening exponent n at each indenting point in the BM region, the value of $\alpha = 13.4$ obtained from the tensile tests of three SM490 steel specimens was used. The average values of $\sigma_y = 331.8$ MPa, $\sigma_y = 344.0$ MPa, and $\sigma_y = 342.4$ MPa and $n = 0.252$, $n = 0.262$, and $n = 0.258$ determined in BM region for indentation series 1, series 2, and series 3, respectively, are presented in Table 3.

Fig. 11 shows the experimental curves at the middle indenting column of HAZ and WM regions and their best fit simulated loading parts of load–penetration depth curves. Note that the best fit curves are quite easily chosen from the 576 simulated loading curves, of which the penetration depth is in the wide range of 1520 to 1960 nm at the applied load of 150 mN and the slope varies by material

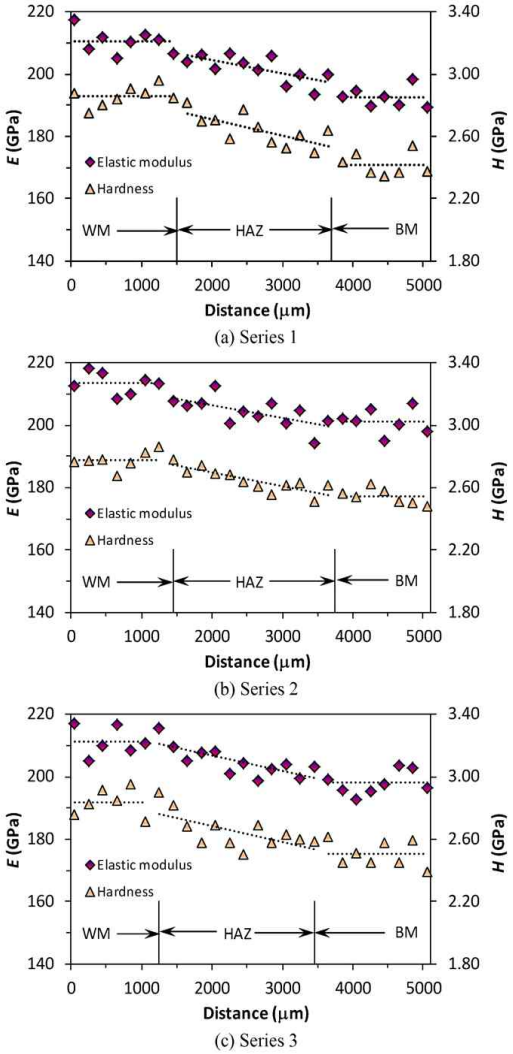


Fig. 10. Distributions of elastic modulus and hardness across the weld zone.

properties. Since the simulated curves are distinguishable from the shape and the magnitude of penetration depth and a composite behavior is always measured from each indentation test in this study, the input data (E, σ_y, n, and α) used for the best fit curves are accurately indicated the elastic–plastic properties of material at the corresponding indenting points. The α value of the best fit simulated curve of $\alpha = 10.0$

Table 3
Average values of σ_y and n in the weld zones.

	Series	WM	HAZ	BM
σ_y (MPa)	1	403.3	357.3	331.8
	2	400.1	357.5	344.0
	3	408.3	367.9	342.4
n	1	0.269	0.263	0.252
	2	0.271	0.264	0.257
	3	0.269	0.262	0.258

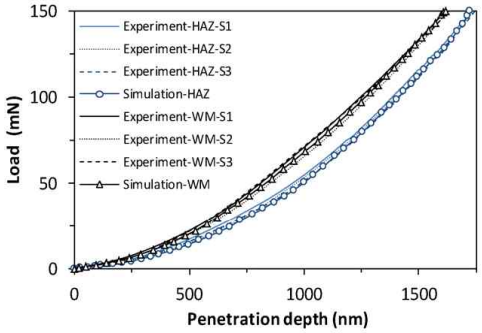


Fig. 11. Comparison of the simulated and experimental load–penetration depth curves.

and $\alpha = 8.5$ is considered as the representative α value for HAZ and WM region, respectively. The obtained value of $\alpha = 10.0$ for HAZ indicates that the change of microstructure in HAZ during welding process influences much on the α value. This effect could be varied with different position along the HAZ region, however, the usage of $\alpha = 10.0$ as representative value for determining σ_y and n at all indenting positions along the HAZ region would be acceptable due to the fact that the estimated σ_y and n just changes around 20% when α value of SM490 steel increases from 7 to 23 [17].

Since $\alpha = 10$ and $\alpha = 8.5$ are obtained for HAZ and WM regions, respectively, the yield strength σ_y and strain hardening exponent n at each indenting point in the HAZ and WM regions are then determined using the proposed algorithm. The distributions of yield strength σ_y and strain hardening exponent n across the weld zone are presented in Fig. 12 with the same illustrated way as Fig. 10. It is interesting to note in Fig. 12 that various σ_y and n values also exhibit relatively little variation in the BM and WM regions except the distribution of n obtained from indentation series 3 (Fig. 12c), and a significant variation with a gradient-distribution of the σ_y and n values are found in HAZ for all indentation series. The distributions obtained from all indentation series also show the same trend that WM has the highest values of σ_y and n, BM has the lowest σ_y and n values, while the σ_y and n values in the HAZ region gradually decrease from the WM to BM region. Note that the average values of σ_y and n determined from three indentation series are similar for each individual weld zone, as presented in Table 3. These results and the distributions of σ_y and n values plotted in Fig. 12 indicate that the changing trends of σ_y and n in the weld zone obtained from nanoindentation are reliable.

It is known that mechanical properties depend on the microstructure of materials [33–36]. Thus, the variation of the mechanical properties in the SM490 steel weld zone essentially results from the changes of the microstructures in the weld zone during the welding. There are so many aspects of microstructures that have an effect on the mechanical behavior of weldements, and the formation of δ-ferrite is one of the important elements [22,34]. The capacity of forming the δ-ferrite depends on the amount of α-ferrite on the material, the peak temperature in heating, and the cooling rate [33,35]. In the present weld zone, it is known that a lower wt.% C content of 0.12% leads to a higher amount of α-ferrite in weld metal than that in base metal, which has the higher wt.% C content of 0.16% (Table 1). On the other hand, during welding, the peak temperature occurs in the fusion zone (weld metal) and all α-ferrite form of δ-ferrite. Even though during cooling, the transformation of δ-ferrite to α-ferrite occurs, it is believed that the remaining δ-ferrite in weld metal is still higher than that in base metal. The higher amount of δ-ferrite and its many transformed phase boundaries may be responsible for the greater strength, strain hardening exponent, and hardness in the weld metal than those in the base metal, while the slight higher elastic modulus in weld metal may be attributed to

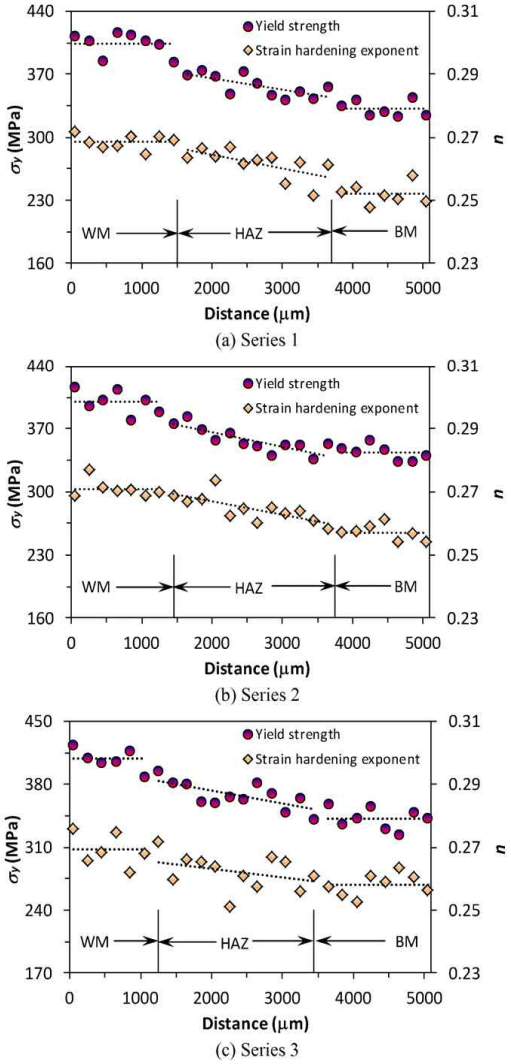


Fig. 12. Distributions of yield strength and n across the weld zone.

the "high stiffness ferrite" phase, which was discussed in the previous works [12,13].

Concerning the HAZ regions of the present weld zone, the higher mechanical properties (E, H, σy and n), when compared to base metal, might be attributed to the smaller and more regular in size of ferrite and pearlite grains in this zone than in base metal. The grain size and grain shape of the microstructure were demonstrated to have significant influence on the mechanical properties of structural steel [33–39]. Li et al. [39] also reported that the improvement of the mechanical properties in a 490 MPa grade steel (0.148 wt.% C content) during controlled rolling and the cooling process attributed mainly to the ferrite-grain refinement and pearlite morphology. In the present weld zone, the gradient of mechanical properties (E, H, σy and n) within HAZ (Figs. 10 and 12) is associated with the increase of grain sizes from the fine grained zone to the interfacial region between the HAZ and BM. In other words, the microstructure gradient resulting from the metallurgical changes during the welding process causes a gradient of mechanical properties within the HAZ. The severe property gradient in HAZ indicates that the other approach for determining mechanical properties, such as tensile test using mini- or micro-specimens extracted from the weld zone, can only provide an averaged mechanical measurement of the entire HAZ due to the fact that the dimension of the micro-tensile specimen is usually much larger than the size of microstructure. Thus, the nanoindentation test would provide an appropriate approach for investigating the mechanical properties of the structural steel weld zone.

4.4. Verification of the obtained mechanical properties in the weld zone

In order to verify the mechanical properties results estimated from nanoindentation, Table 4 provides a comparison of E, σ_y, and n in BM with those observed from the tensile tests of three specimens, N1, N2, and N3. It can be seen from this table that E, σ_y, and n in BM determined from nanoindentation are in good agreement with those obtained from the tensile tests of three SM490 specimens, although the former is slightly smaller than the latter, which may be attributed to experiment errors of the indentation test [14,17] or the size-dependence of the present indentation measurements [32].

An additional comparison was also performed in order to verify the results of elastic modulus in HAZ and WM regions estimated from nanoindentation. In this comparison, the welded specimen of the tensile test is considered as a tensile composite made of three materials, BM, HAZ, and BM, in series with the corresponding modulus value of E_{BM}, E_{HAZ}, and E_{WM}, respectively. Since the section area of BM and HAZ are identical (A), and the section area of WM in the weld zone can be approximately measured (λA), the equivalent modulus of the composite (E_{eq}) can be computed as follows:

$$E_{eq} = \frac{\lambda L E_{BM} E_{HAZ} E_{WM}}{\lambda(L_{BM} E_{HAZ} E_{WM} + L_{HAZ} E_{BM} E_{WM}) + L_{WM} E_{BM} E_{HAZ}} \quad (5)$$

where L_{BM}, L_{HAZ}, and L_{WM} is the length of BM, HAZ, and WM, respectively, while $L = L_{BM} + L_{HAZ} + L_{WM}$ is the length between two gauges in the tensile tests of the welded specimen. Since the length of WM (L_{WM}) and HAZ (L_{HAZ}) can be approximately measured, and the composite length is known, the equivalent elastic modulus of welded specimen is easy to obtain. Table 5 presents the equivalent modulus values of the composite computed from Eq. (5) using elastic modulus values of BM, HAZ, and WM obtained from three indentation series and elastic modulus obtained from the tensile test of three welded specimens, together with their average value. There it can be seen that the equivalent elastic modulus values computed using Eq. (5) based on the nanoindentation results are close to the average value of elastic modulus obtained from the tensile tests, with a relative error within ±7.5%. Concerning the yield strength in WM, it has been reported that the yield strength of a Fe–1Mn–C steel weld deposit using manual metal arc welding (1 kJ/mm) is around of 425 MPa in case of 0.12 wt.% carbon content [33–35]. The

Table 4
Mechanical properties of SM490 steel obtained from tensile tests and nanoindentation.

Mechanical properties		E (GPa)	σ_y (MPa)	n
Tensile tests	N1	212.3	353.7	0.267
	N2	210.8	352.6	0.268
	N3	212.1	354.3	0.262
	Ave.	211.7	353.5	0.266
Indentation tests	Series 1	192.5	331.8	0.252
	% err.	−9.1%[a]	−6.1%	−5.3%
	Series 2	201.2	344.0	0.257
	% err.	−5.0%	−2.7%	−3.4%
	Series 3	198.0	342.4	0.258
	% err.	−6.5%	−3.1%	−3.0%

[a] All errors were computed as $(X - X_{ave})/X_{ave}$, where X represents a variable.

Table 5
Equivalent elastic modulus in the weld zone.

		E (GPa)
Tensile tests	W1	214.9
	W2	218.6
	W3	215.1
	Ave.	216.2
Equivalent elastic modulus value	Series 1	200.1
	% err.	−7.4%[a]
	Series 2	207.4
	% err.	−4.1%
	Series 3	204.9
	% err.	−5.2%

[a] All errors were computed as $(X - X_{ave})/X_{ave}$, where X represents a variable.

yield strength values obtained from three indentation series of σ_y = 400.1–408.3 MPa in WM, which has 0.12 wt.%C (Table 1) are consistent with the reported value. In regard to hardness values listed in Table 2, the range of H = 2.78–2.86 GPa, H = 2.62–2.66 GPa, and H = 2.42–2.53 GPa, corresponding to the range of H = 222–232 HV, H = 240–244 HV, and H = 255–262 HV, are representative of the hardness of WM, HAZ, and BM, respectively. These hardness results are in good agreement with related literature [5–7]. The good comparisons and results above suggest that the mechanical properties of the present SM490 steel weld zone determined from nanoindentation are reliable.

5. Conclusion

Based on the representative methods to extract the basic mechanical properties of structural steel including elastic modulus, hardness, yield strength, and strain hardening exponent from the load–penetration depth curve of indentation test and finite element analysis, an approach for determining such mechanical parameters across SM490 steel weld zone has been proposed. Nanoindentation, tensile tests, finite element (FE) analysis, and optical microscopy observation were carried out. The experimental and analysis results support the following conclusions:

1. Nanoindentation with the aid of finite element analysis provides an appropriate approach for determining the basic mechanical properties (E, H, σ_y, and n) of structural steel weld zone. While the conventional method is used to extract E and H in the weld zone, the proposed algorithm is used to determine σ_y and n in the BM, the results of FE analysis allows obtaining the representative α value of HAZ and WM regions, which are used to estimate σ_y and n in the HAZ and WM regions of the weld zone.
2. For the present weld zone, the value α = 13.4 obtained from the tensile tests of SM490 steel is used as α value of BM region and the value α = 10.0 and α = 8.5 estimated based on FE analysis results is used as representative α value of HAZ and WM region, respectively. The distributions of mechanical properties across the weld zone are determined and the results show that the weld metal (WM) has the highest values of mechanical properties (E, H, σ_y, and n), the base metal (BM) has the lowest mechanical properties values, while the mechanical properties values in the HAZ region gradually decrease from the WM to BM regions.
3. The microstructure of BM and HAZ consist of ferrite and pearlite. Both pearlite and ferrite grains in HAZ are different in shape and orientation and much smaller in size compared with those in BM. The smaller and more regular in size of ferrite and pearlite grains in HAZ are mainly responsible for the higher mechanical properties values in HAZ when compared to those in BM, while the higher amount of δ-ferrite and its many transformed phase boundaries may be responsible for the higher mechanical properties values in WM when compared to those in BM.

Acknowledgements

This research was supported by a grant (15CTAP-C098306-01) from Technology Advancement Research Program funded by Ministry of Land, Infrastructure and Transport of Korean.

Appendix A

Table A1
Coefficient a_{ijk}.

(k, j)	a_{ijk}			
	$i = 4$	$i = 3$	$i = 2$	$i = 1$
(1, 1)	−1.710E−1	1.629E+0	1.144E+2	−4.574E+1
(2, 1)	1.395E−2	−1.195E−1	2.955E−1	−1.643E−1
(3, 1)	−4.231E−4	3.903E−3	−9.428E−3	5.243E−3
(1, 2)	9.940E+0	7.973E+0	5.240E+1	−6.190E+1
(2, 2)	−1.193E+0	2.573E+0	−5.962E+0	3.952E+0
(3, 2)	3.876E−2	−1.429E−1	1.858E−1	−5.743E−2
(1, 3)	−1.196E+2	5.892E+2	−9.072E+2	4.656E+2
(2, 3)	1.194E+1	−5.351E+1	5.441E+1	−1.804E+1
(3, 3)	−3.417E−1	1.631E+0	−1.443E+0	2.175E−1
(1, 4)	1.981E+2	−4.190E+2	4.267E+2	−2.408E+2
(2, 4)	−1.845E+1	3.178E+1	2.717E+0	−1.053E+1
(3, 4)	5.023E−1	−1.147E+0	3.126E−2	5.674E−1

Table A2
Coefficient b_{ijk}.

(k, j)	b_{ijk}			
	$i = 4$	$i = 3$	$i = 2$	$i = 1$
(1, 1)	−6.197E−2	8.766E−1	−3.097E+0	6.085E+0
(2, 1)	2.285E−5	−7.846E−4	5.723E−3	−1.095E−2
(3, 1)	−4.241E−6	8.032E−5	−4.539E−4	7.676E−4
(1, 2)	9.840E−1	−1.477E+1	6.723E+1	−9.676E+1
(2, 2)	−6.638E−2	9.160E−1	−3.909E+0	5.367E+0
(3, 2)	1.877E−3	−2.619E−2	1.147E−1	−1.630E−1
(1, 3)	−4.036E+0	6.074E+1	−2.847E+2	4.247E+2
(2, 3)	4.241E−1	−6.122E+0	2.797E+1	−4.112E+1
(3, 3)	−1.324E−2	1.911E−1	−8.782E−1	1.301E+0
(1, 4)	4.871E+0	−7.309E+1	3.440E+2	−5.160E+2
(2, 4)	−5.777E−1	8.394E+0	−3.875E+1	5.745E+1
(3, 4)	1.875E−2	−2.718E−1	1.257E+0	−1.870E+0

References

[1] I.K. Kwon, S.G. Shin, Mechanical and thermal properties of SM 490 at high temperature for fire engineering design, Met. Mater. 16 (4) (2010) 559–564.
[2] A.R. Tamboli, Handbook of Structural Steel Connection Design and Details, McGraw-Hill, NY, USA, 1999.
[3] T.L. Anderson, Fracture Mechanics: Fundamentals and Applications, 3rd ed. CRC Press, Taylor & Francis Group, FL, USA, 2005.
[4] M. Diaz, I. Madariaga, J.M. Rodriguez-Ibabe, I. Gutierrez, Improvement of mechanical properties in structural steel by development of acicular ferrite microstructures, J. Constr. Steel Res. 46 (1998) 413–414.
[5] Z. Boumerzoug, C. Derfouf, T. Baudin, Effect of welding on microstructure and mechanical properties of an industrial low carbon steel, Engineering 2 (7) (2010) 502–506.
[6] A. Gural, B. Bostan, A.T. Ozdemir, Heat treatment in two phase region and its effect on welding of a low carbon steel, Mater. Des. 28 (3) (2007) 897–903.
[7] M. Eroglu, M. Aksoy, N. Orhan, Effect of coarse initial grain size on microstructure and mechanical properties of weld metal and HAZ of a low carbon steel, Mater. Sci. Eng. A 269 (1999) 59–66.
[8] M. Eroglu, M. Aksoy, Effect of initial grain size on microstructure and toughness of intercritical heat-affected zone of a low carbon steel, Mater. Sci. Eng. A 286 (2) (2000) 289–297.
[9] C.H. Lee, H.S. Shin, K.T. Park, Evaluation of high strength TMCP steel weld for use in cold regions, J. Constr. Steel Res. 74 (2012) 134–139.
[10] B. Bhushan, Handbook of Nanotechnology, Springer, Berlin, 2007.
[11] F.-J. Ulm, M. Vandamme, C. Bobko, J.A. Ortega, K. Tai, C. Ortiz, Statistical indentation techniques for hydrated nanocomposites: concrete, bone, shale, J. Am. Ceram. Soc. 90 (9) (2007) 2677–2692.
[12] T.H. Pham, J.J. Kim, S.E. Kim, Estimation of microstructural compositions in the weld zone of structural steel using nanoindentation, J. Constr. Steel Res. 99 (2014) 121–128.

[13] T.H. Pham, S.E. Kim, Nanoindentation for investigation of microstructural compositions in SM490 steel weld zone, J. Constr. Steel Res. 110 (2015) 40–47.
[14] W.C. Oliver, G.M. Pharr, An improved technique for determining hardness and elastic-modulus using load and displacement sensing indentation experiments, J. Mater. Res. 7 (4) (1992) 1564–1583.
[15] A.E. Giannalopoulos, S. Suresh, Determination of elastoplastic properties by instrumented sharp indentation, Scr. Mater. 40 (1999) 1191–1198.
[16] M. Dao, N. Chollacoop, K.J.V. Vliet, T.A. Venkatesh, S. Suresh, Computational modeling of the forward and reverse problem in instrumented sharp indentation, Acta Mater. 49 (2001) 3899–3918.
[17] T.H. Pham, J.J. Kim, S.E. Kim, Estimating constitutive equation of structural steel using indentation, Int. J. Mech. Sci. 90 (2015) 151–161.
[18] K.H. Chung, W. Lee, J.H. Kim, C. Kim, S.H. Park, D. Kwon, K. Chung, Characterization of mechanical properties by indentation tests and FE analysis—validation by application to a weld zone of DP590 steel, Int. J. Solids Struct. 46 (2) (2009) 344–363.
[19] M. Zhan, H. Du, J. Liu, N. Ren, H. Yang, H. Jiang, K. Diao, X. Chen, A method for establishing the plastic constitutive relationship of the weld bead and heat-affected zone of welded tubes based on the rule of mixtures and a microhardness test, Mater. Sci. Eng. A 527 (12) (2010) 2864–2874.
[20] R.R. Ambriz, D. Chicot, N. Benseddiq, G. Mesmacque, S.D. Torre, Local mechanical properties of the 6061-T6 aluminium weld using micro-traction and instrumented indentation, Eur. J. Mech. A Solids 30 (2011) 307–315.
[21] C.A. Charitidis, D.A. Dragatogiannis, Finite element analysis, stress–strain distribution and size effects rise during nanoindentation of welded aluminum alloy, Int. J. Struct. Integr. 4 (1) (2013) 78–90.
[22] D. Ye, F. Mi, J. Liu, Y. Xu, Y. Chen, L. Xiao, Use of instrumented indentation testing to study local mechanical properties of 304 L SS welded joints subjected to low-cycle fatigue loadings, Mater. Sci. Eng. A 564 (2013) 76–84.
[23] G. Sun, F. Xu, G. Li, X. Huang, Q. Li, Determination of mechanical properties of the weld line by combining micro-indentation with inverse modeling, Comput. Mater. Sci. 85 (2014) 347–362.
[24] ASTM E3-01, Standard Guide for Preparation of Metallographic Specimens, ASTM International, West Conshohocken, PA, 2007.
[25] ISO 14577, Metallic Materials-Instrumented Indentation Test for Hardness and Materials Parameters, International Organization for Standarlization, Genenva, Switzerland, 2002.
[26] ASTM E2546-07, Standard Practice for Instrumented Indentation Testing, ASTM International, West Conshohocken, PA, 2007.
[27] ASTM E8/E8M-13a, Standard Test Methods for Tension Testing of Metallic, ASTM International, West Conshohocken, PA, 2013.
[28] B. Kato, H. Aoki, H. Yamanouchi, Standardized mathematical expression for stress–strain relations of structural steel under monotocic and uniaxial tensile loading, Mater. Struct. 23 (1990) 47–58.
[29] M. Lichinchi, C. Lenardi, J. Haupt, R. Vitali, Simualtion of Berkovich nanoindentation experiments on thin films using finite element method, Thin Solid Films 312 (1998) 240–248.
[30] J.L. Bucaille, S. Stauss, E. Felder, J. Michler, Determination of plastic properties of metals by instrumented indentation using different sharp indenters, Acta Mater. 51 (2003) 1663–1678.
[31] J. Hay, Introduction to instrumented indentation testing, Exp. Tech. 33 (6) (2009) 66–72.
[32] D. Ye, S. Matsuoka, N. Nagashima, Determination of fatigue mesoscopic mechanical properties of an austenitic stailess steel using depth-sensing indentation (DSI) technique, Mater. Sci. Eng. A 456 (2007) 120–129.
[33] H.K.D.H. Bhadeshia, R. Honeycombe, Steels: Microstructure and Properties, Butterworth-Heinemann, London, 2006.
[34] S. Kou, Welding Metallurgy, 2nd edition John Wiley & Sons, Inc., 2003
[35] K.E. Easterling, Introduction of the Physical Metallurgy of Welding, 2nd edition Butterworth-Heinemann, London, 1992.
[36] M.L. Zhu, F.Z. Xuan, Correlation between microstructure, hardness and strength in HAZ of dissimilar welds of rotor steels, Mater. Sci. Eng. A 527 (2010) 4035–4042.
[37] M.L. Zhu, F.Z. Zuan, Effect of microstructure on strain hardening and strength distributions along a Cr–Ni–Mo–V steel weld joint, Mater. Des. 65 (2015) 707–715.
[38] P. Lehto, H. Remes, T. Saukkonen, H. Hanninen, J. Romanoff, Influence of grain size distribution on the Hall–Petch relationship of welded structural steel, Mater. Sci. Eng. A 592 (2014) 28–39.
[39] Z. Li, Controlled processing on mechanical properties of 490 MPa grade low carbon cold heading steel, J. Iron Steel Res. Int. 16 (3) (2009) 43–48.

3. Microstructure evolution and mechanical properties changes in the weld zone of a structural steel during low-cycle fatigue studied using instrumented indentation testing(2016)

International Journal of Mechanical Sciences 114 (2016) 141–156

Contents lists available at ScienceDirect

International Journal of Mechanical Sciences

journal homepage: www.elsevier.com/locate/ijmecsci

Microstructure evolution and mechanical properties changes in the weld zone of a structural steel during low-cycle fatigue studied using instrumented indentation testing

Thai-Hoan Pham, Seung-Eock Kim *

Department of Civil and Environmental Engineering, Sejong University, 98 Gunja-dong, Gwangjin-ku, Seoul 143-747, South Korea

ARTICLE INFO

Article history:
Received 9 January 2016
Received in revised form
2 April 2016
Accepted 23 May 2016
Available online 24 May 2016

Keywords:
Instrumented indentation
Low-cycle fatigue
Mechanical properties
Microstructures
Structural steel weld zone

ABSTRACT

Room-temperature low-cycle fatigue (LCF), instrumented indentation, tensile tests, finite element (FE) analysis, and optical microscopy examinations were carried out to investigate the mechanical properties and microstructures in the weld zone of a structural steel, SS400, in cyclic loading conditions. Five indentation arrases were performed across the weld zone of five specimens, including one virgin specimen and four specimens subjected to LCF loading at different strain levels. The mechanical properties, such as elastic modulus E, yield strength σ_y, and strain hardening exponent n, were then estimated from indentation testing and FE analysis results. The obtained results and optical microscopy examinations show that the mechanical properties and microstructures in the individual region of the weld zone are not only decided by the metallurgical conditions resulting from the welding but also were highly influenced by the strain level applied during cyclic loading. In the as-welded condition, the values of elastic modulus, yield strength, and strain hardening exponent in the weld metal (WM) are higher than those in the base metal (BM), while materials in heat affected zone (HAZ) reveal a gradual decrease of elastic modulus, yield strength, and strain hardening exponent values from the WM to BM region. It is also shown that with increasing strain amplitudes during cyclic loading, the elastic modulus E displays decrease in all regions of the weld zone, both yield strength σ_y and strain hardening exponent n exhibit decreasing characteristic in WM and increasing characteristic in BM region, while the yield strength in HAZ region increases, the strain hardening exponent in this region keeps almost unchanged. The dependence of the mechanical properties on the applied strain level is also discussed in terms of microstructural changes in fatigue failure specimens.

© 2016 Elsevier Ltd. All rights reserved.

1. Introduction

Structural steels are widely used materials in civil and industrial building construction and other structural applications because of the advantageous features such as low cost and excellence in terms of machinability and weldability. In the usage of structural steel, welding has been considered to be an efficient method to form strong joints that allow transferring loads between steel components [1]. During the welding process, the microstructural changes affect mechanical properties in the fusion zone (weld metal-WM) including elastic modulus E, yield strength σ_y, strain hardening exponents n, hardness H, and lead to the difference of these properties between base metal (BM) and heat affected zone (HAZ) of the structural steel weld zone. It has also been indicated that the properties of these zones not only depend on various metallurgical factors during welding but also are intensively influenced by service conditions such as the environment, temperature, state of stress imposed, loading history [2,3]. For steel structures operating under dynamic or alternating loading conditions, the progressive deterioration with the service times of service properties, especially the mechanical properties, has been considered notable [4]. The residual fatigue life studies of existing steel structures in service conditions generally include the assessment of fatigue damage. Such assessment is frequently performed by quantitatively measuring the deterioration of material mechanical properties such as the ultimate strength, elastic modulus, toughness, hardness, and cross section area reduction [5–7]. Therefore, it is essential to investigate the mechanical properties for both the designs of the welded joints against fatigue failure and the integrity assessment of structural steel members that have a welded joint, including elastic modulus, hardness, yield strength, and strain hardening exponent in the structural steel weld zone, as well as their variation during fatigue loading.

* Corresponding author.
E-mail address: sekim@sejong.ac.kr (S.-E. Kim).

http://dx.doi.org/10.1016/j.ijmecsci.2016.05.021
0020-7403/© 2016 Elsevier Ltd. All rights reserved.

Table 1
Chemical compositions of steel and electrode (in wt%).

Material	C	Si	Mn	P	S	Al	Ca	Cu
SS400	0.05	0.037	0.46	0.013	0.002	0.044	0.0017	–
ER70S-6	0.04	0.92	0.45	0.011	0.015	–	–	0.2

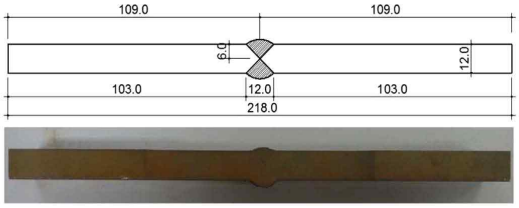
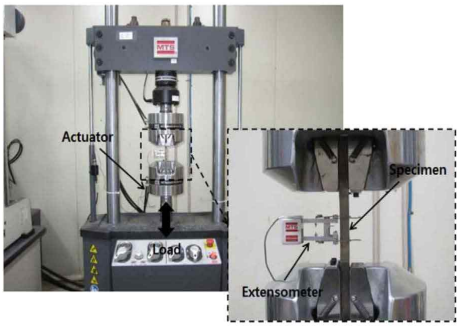


Fig. 1. Double-V groove butt welding plate.

Numerous methods for determining the mechanical properties (E, σ_y, and n) in different zones of steel welded joints have been reported [8–18]. For instance, methods to characterize the properties in welded joint using mini- or micro-tensile specimens testing were used for steel and aluminum [8–10]. However, it has been recognized that preparing mini- or micro-tensile specimens from the welded joints is a rather difficult task due to the small size of joint zones [8]. The method allowed obtaining the material properties relative to different zones of welded joints by hardness measurements using the ultrasonic contact impedance (UCI) was used for S235JR mid steel [11]. In this method, the stress-strain curves relative to different zones of welded joints can be drawn based on ultimate strength σ_u and yield strength σ_y values calculated from the corresponding measured HB hardness using approximate equations and assumptions that elastic modulus E and horizontal plastic plateau were unchanged in the joint zones. These approximated equations and assumptions may affect the accuracy of the obtained stress-strain curves. Among reported methods, instrumented indentation testing (ITT) has been considered as a promising method in practical applications due to its fast, precise and nondestructive merits, and it allows determining various mechanical properties including elastic modulus, hardness, yield strength, strain hardening exponent, facture toughness [12–18]. For example, indentation tests and finite element (FE) analysis were used to investigate the mechanical properties of DP590 steel weld zone [13], spherical indentation was utilized to measure local mechanical properties of welded stainless steel SUS316L at high temperature [15], and micro-indentation and inverse modeling were applied to determine mechanical properties of the weld line of two typical dual phase high strength steels DP600/DP980 [16]. Recently, ITT and FE analysis were conducted to investigate the mechanical properties (E, H, σ_y, and n) in the weld zone of two structural steels SM490 and SS400 [17,18]. Concerning the steel welded joints subjected to low-cycle fatigue loading, the literature on fatigue analysis was well reviewed in [19,20]. In addition, it had been found that combination of full-field techniques (digital image correlation and infrared thermography), hardness measurements using UCI method, and FE analysis can be used to analyze the welded joints under low-cycle fatigue loading [21]. However, ITT was also demonstrated to be an appropriate approach for investigation of steel welded joints under low-cycle loading by successfully applying to study the local mechanical properties and microstructures in individual zone of 304L SS welded joint in both as-welded and cyclic loading conditions [22].



(a) Welded specimens



(b) Test arrangement



(c) Side view of a specimen on the testing machnine

Fig. 2. Specimens and the installation of low-cycle fatigue tests. (a)Welded specimens. (b) Test arrangement. (c) Side view of a specimen on the testing machine.

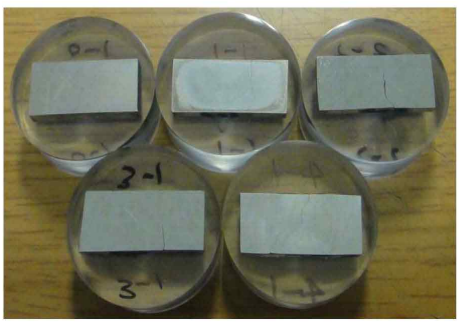


Fig. 3. Five samples for instrumented indentation tests.

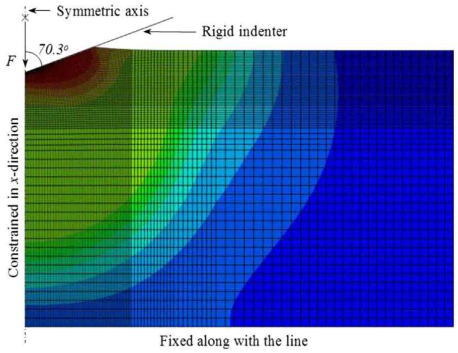


Fig. 4. FE model of indentation test.

Table 2
Elastic modulus values used for regions of weld zones in FE analyses.

	S0 (ε_a=0.0%)	S1 (ε_a=0.4%)	S2 (ε_a=0.6%)	S3 (ε_a=0.8%)	S4 (ε_a=1.0%)
WM	215	210	210	200	210
HAZ	210	200	200	190	190
BM	–	200	190	180	180

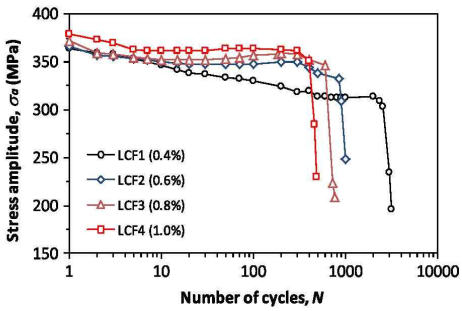


Fig. 5. Cyclic stress response curves.

The aim of this study is to investigate the effect of low-cycle fatigue loading on the microstructures and mechanical properties (E, σ_y, and n) in the weld zone of a structural steel, SS400, by using instrumented indentation testing. For this purpose, low-cycle fatigue, instrumented indentation, tensile tests, FE analyses, and optical microscopy examinations were carried out on SS400 steel double V groove butt welds. The mechanical properties in the weld zone in both as-welded and low-cycle fatigue loadings were extracted from indentation load-depth data using the proposed method [23] with the aid of FE analysis, the microstructures were observed, and the effect of low-cycle fatigue on the microstructures and mechanical properties in the weld zone was investigated.

2. Experimental details

Base plates of structural steel SS400, 12 mm in thickness, were welded by manual metal arc welding using ER 70S-6 electrode. The actual chemical composition in percentage weight of steel and electrode are listed in Table 1. The weld was completed with a voltage of 22 V and a current of 100 A in a configuration of double-V groove. The dimensions of the weld portion are 12 mm in width, without a root gap, as shown in Fig. 1.

Experiments in this study consist of constant amplitude low-cycle fatigue (LCF) tests of SS400 welded specimens, instrumented indentation tests across the weld zone of as-welded and fatigue failure specimens, optical microscopy examinations, and tensile tests of steel and welded specimens, which are described below.

For low-cycle fatigue tests, four welded specimens, labeled as LCF1, LCF2, CLF3, and LCF4, were taken directly from the middle of the welded plate in such a way that the weld zone containing base metal, heat affected zone and weld metal portions was located at the middle of 24 mm gauge length of each specimen. It is noted that these specimens taken from the middle of the welded plate may display similar residual stress variation across the weld centerline [24]. Since residual stress is not taken into account in this study, such a similar stress variation across the weld centerline of welded specimens may minimize the effect of residual stress on the investigated results, which are the evolution of microstructure and mechanical properties in the weld zone during low-cycle fatigue. Fully reversed, push-pull, total strain-controlled axial low-cycle fatigue tests were performed at room temperature on SS400 steel welded specimens using a MTS fatigue testing machine. The specimens were prepared and the tests were conducted according to ASTM standard [25]. The tests were carried out at four strain amplitudes ε_a of $\pm 0.4\%$, $\pm 0.6\%$, $\pm 0.8\%$, and $\pm 1.0\%$, corresponding to four specimens LCF1, LCF2, LCF3, and LCF4, respectively, at a constant strain rate of $1 \times 10^{-3}\ s^{-1}$. It is noted that even the strain may not be constant due to the different mechanical and microstructure across the weld zone, the changes of mechanical properties and the microstructure evolution in the weld zone under low-cycle fatigue loading can be evaluated based on the constant total strain applied over different zones of the weld [22]. In this study the fatigue life (N_f) of the welded specimens is defined as the required number of cycles to reduce the maximum stress (σ_{max}) to a value of ½ times of the maximum stress experienced in the steady-state cycle. Fig. 2 shows (a) the welded specimens, (b) test arrangement, and (c) side view of a specimen on the testing machine.

For instrumented indentation tests, five samples were cut out from the as-welded plate (labeled S0) and four fatigue failure specimens (labeled S1, S2, S3, and S4 corresponding to LCF1, LCF2, LCF3, and LCF4, respectively) by water-jet. All samples with the length of 20 mm containing BM, HAZ, and WM regions were then mounted in epoxy and polished with different silicon carbide papers, poly diamond particles, and colloidal silica in order to obtain a flat, smooth surface. This procedure was achieved in seven stages of increasing fineness, with the last in the range of 40 nm according to ASTM E3-01 standard [26]. Fig. 3 shows the samples after being mounted and polished. Instrumented indentation tests were performed at room temperature using a Nano Hardness Tester machine made by the Swiss Center for Electronics and Microtechnology. The machine operation conforms to the ASTM E2546-07 standards [27]. The Berkovich indenter made of industrial diamond with an elastic modulus of 1141 GPa and Poisson's ratio of 0.07 was employed. In all indentation tests, a trapezoidal load history was applied, defined by a maximum load of 200 mN, a loading time of 30 s, an unloading time of 30 s, and without holding time, corresponding to 400 mN/min of loading and unloading rate. On each sample, an indentation array consisting of 5 rows and 26 columns of indenting points across the weld zone was performed. The indenting regions of each indentation array contained portions of base metal, heat-affected zone, and weld metal. To reveal the microstructure, the polished samples were etched for 40 s with 2% nital in the case of as-

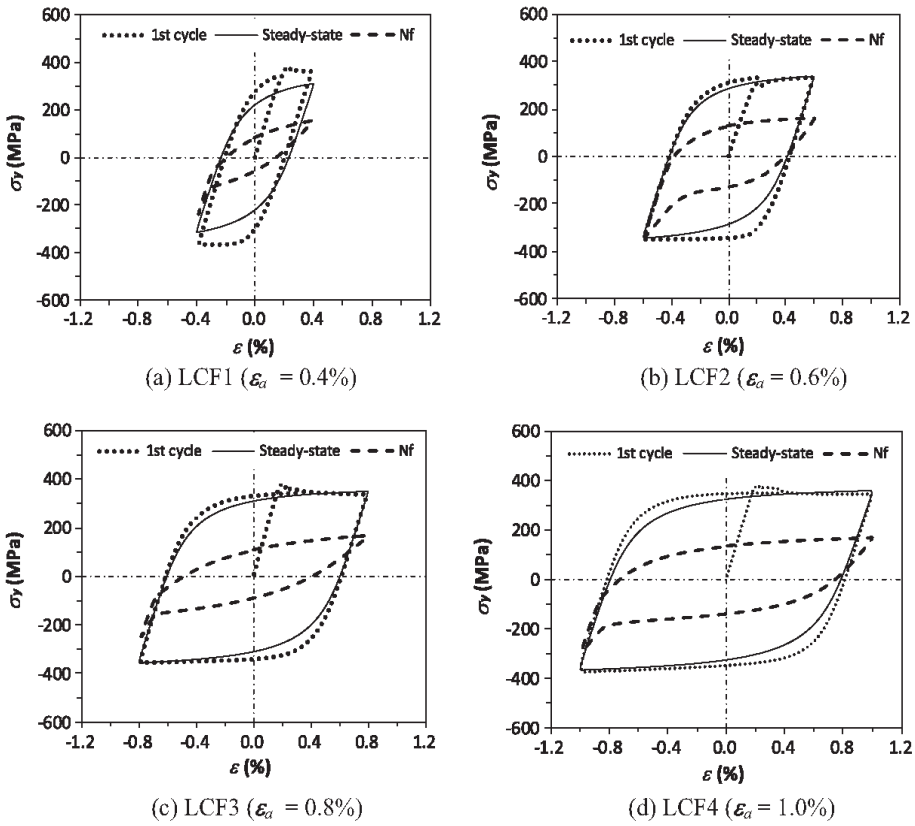


Fig. 6. Hysteresis loops at different strain amplitudes.

welded sample and for 45 s with Villela's reagent in the case of fatigue failure samples. The microstructures were then observed by optical microscopy (OM).

For tensile testing, six specimens, including three specimens of SS400 (labeled N1, N2, and N3) and three welded specimens (labeled W1, W2, and W3), which were taken directly from the welded plate, were prepared according to ASTM standard [28]. Specimens of SS400 have the same thickness of 12 mm as welded specimens. The tests were carried out using an Instron tensile testing machine and tested according to ASTM standard [28].

3. Determination of mechanical properties in the weld zone from indentation test data

The procedure for determining the mechanical properties (E, σ_y, and n) in the weld zone of structural steel, which show plastic plateau in their constitutive equations, from load-penetration depth curve of Berkovich indentation was well established and successfully applied to investigate mechanical properties in the weld zone of two common used structural steels SS490 and SS400 [17,18]. This procedure can be summarized into the following steps:

(1) Obtain the maximum applied load P_m, maximum penetration depth h_m, and residual impression depth h_r directly from P–h curve.

(2) Fit the unloading force P_u as a power-law function [29]:

$$P_u = B(h_m - h_r)^m \tag{1}$$

where B and m are fitting parameters.

(3) Calculate the contact stiffness S from the following equation [29]

$$S = \left(dP_u/dh\right)\Big|_{h_m} = mB(h_m - h_r)^{m-1} \tag{2}$$

(4) Calculate the contact depth h_c as follows [29]

$$h_c = h_m - \varepsilon^* P_m/S \tag{3}$$

where ε^*=0.75 for sharp indenters.

(5) Calculate the projected area of contact a_c as follows [29]

$$A_c = 24.5h_c^2 \tag{4}$$

(6) Extract the elastic modulus E from the following relations [29]

$$E_r = \frac{\sqrt{\pi}}{2\beta}\frac{S}{\sqrt{A_c}} \tag{5}$$

$$E_r = \left[\frac{1-\nu^2}{E} + \frac{1-\nu_i^2}{E_i}\right]^{-1} \tag{6}$$

where E_r is the reduced modulus, β is the correlation factor

for indenter shape (β=1.034 for a Berkovich indenter), E, υ, E_i and υ_i are the elastic modulus and Poisson's ratio of the sample and indenter, respectively.

(7) Calculate E_r^* from the following equation:

$$E_r^* = \left[\left(1-\upsilon^2\right)/E\right]^{-1} \tag{7}$$

(8) Obtain the α value of BM region from the tensile test of steel specimen, where α is the ratio of strain at the starting-point of strain hardening ε_{st} to the initial yield strain ε_y.

(9) Estimate the representative α value of HAZ and WM regions by correlating the representative experimental with the simulated load-penetration depth curves.

(10) Calculate σ_y and n from the following relations:

$$\frac{E_r^*}{\sigma_y} = \sum_{i=1}^{4}\sum_{j=1}^{4}\sum_{k=1}^{3} a_{ijk} n^{j-1}\alpha^{k-1}\left(\frac{E_r^*}{C}\right)^{i-1} \tag{8}$$

$$\frac{S}{E_r^* h_m} = \sum_{i=1}^{4}\sum_{j=1}^{4}\sum_{k=1}^{3} b_{ijk} n^{j-1}\alpha^{k-1}\left[\ln\left(\frac{E_r^*}{\sigma_y}\right)\right]^{i-1} \tag{9}$$

where a_{ijk} and b_{ijk} are coefficients (Appendix A).

The further details of the procedure can be found elsewhere [17,18].

In this study, due to the effect of low-cycle fatigue loading, the representative α value of BM, HAZ, and the WM regions in the weld zone of the fatigue failure samples could differ from the corresponding values in the virgin weld zone, and these values need to be estimated (step 9). For this purpose, the set of simulated load-penetration depth curves for the weld zones of SS400 steel and fatigue failure samples were prepared using the finite element (FE) analysis program ABAQUS [30], and FE analyses were conducted with various combinations of materials parameters (α, σ_y, n, υ, and E) as input data. Due to the fact that a conical indenter with a semi-apical angle of θ=70.3° has the same projected area-depth functions as the Berkovich indenter used in the indentation tests and the P–h responses of the conical and Berkovich indentations obtained from finite element analysis using ABAQUS were demonstrated to be virtually identical for micro- or nano-scale [31,32], a conical indenter was simulated instead of a Berkovich indenter in order to reduce the complexity and analysis time. Considering symmetric conditions, an axisymmetric two-dimensional FE model was developed to simulate the indentation process. The sample was modeled using 8576 four-node bilinear axisymmetric quadrilateral elements, as shown in Fig. 4. The developed FE model was also demonstrated to be accurately simulated by verifying with the experimental result [23]. The details of FE model can be found in the previous works [17,23]. After a special attention to α, σ_y, and n values in BM region of virgin weld zone and to E values in all regions of all weld zones were paid and some prior analyses were performed in order to minimize the necessary number of FE analyses, a total of 1320 combinations of appropriate material parameters were chosen to be analyzed. The ranges of α, σ_y, n, υ, and E for these combinations were as follows: α varied from 8 to 18 (for every 1.0); σ_y varied from 310 to 450 (for every 20 MPa); n varied from 0.185 to 0.205 (for every 0.01); the Poisson's ratio was fixed at 0.3 for all analyses; and five E values, which were chosen based on the obtained E value in each region of all weld zones in such a way that the number of E values was minimum and the derivation between the used and obtained E value in each region was less than 5 MPa, were used, as listed in Table 2. Noted that small derivation of 5 MPa corresponding to a relative error within ±3% would not affect much on the estimated value of α. The loading part of load-penetration depth curves, calculated up to 200 mN of applied load, was compared with the experimental one to determine the α value of each region in all weld zones. To reduce the complexity, only the load-penetration

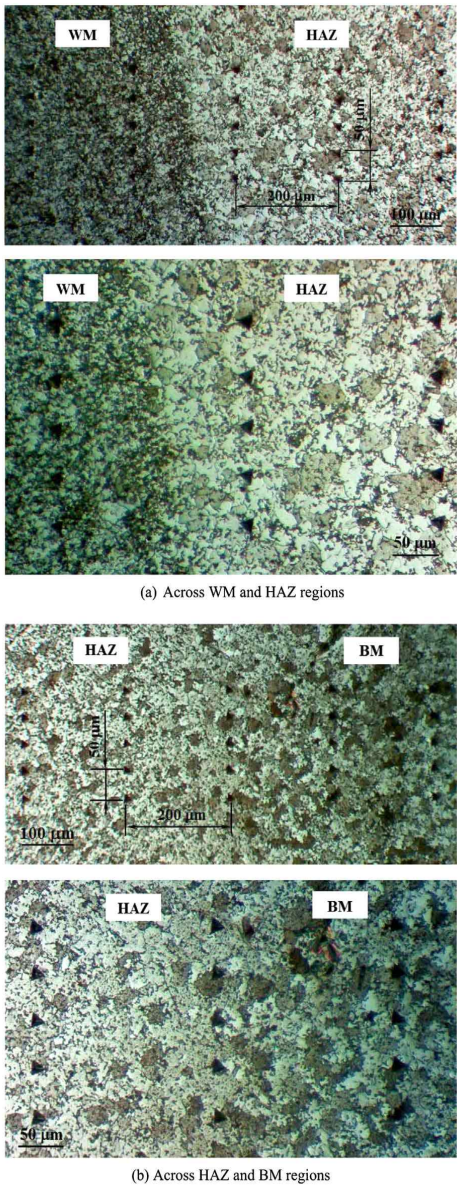


Fig. 7. Optical micrograph of indenting points across the weld zone of fatigue failure specimen S1 (ε_a=0.4%). (a) Across WM and HAZ regions. (b) Across HAZ and BM regions.

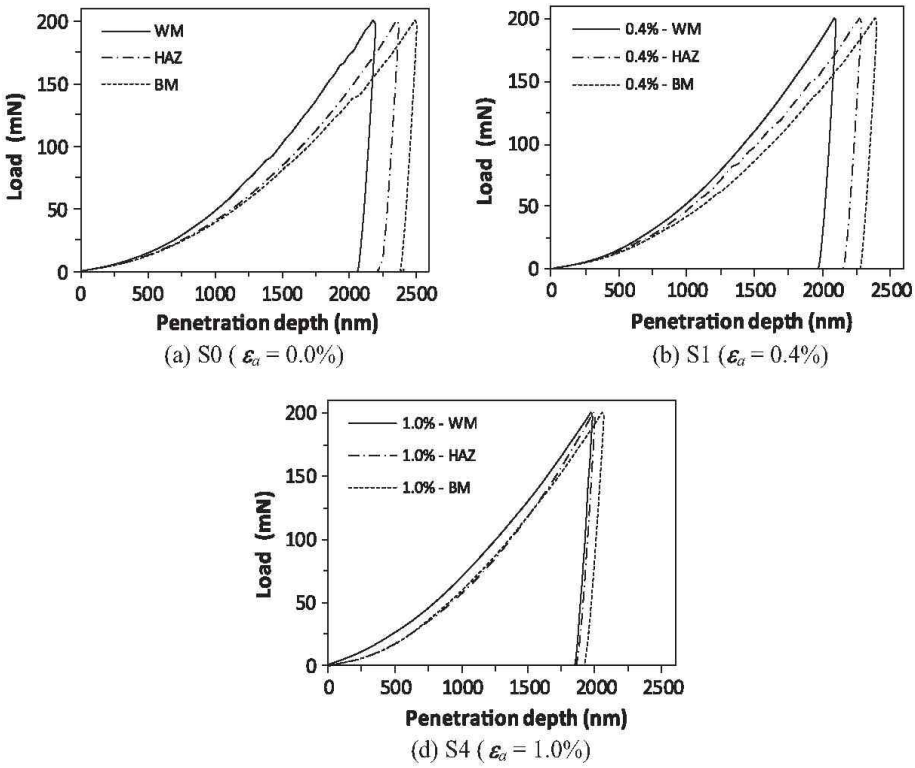


Fig. 8. Typical indentation P–h curves in the weld zone of as-welded and fatigue failure specimens (a) S0 (ε_a=0.0%). (b) S1 (ε_a=0.4%). (d) S4 (ε_a=1.0%).

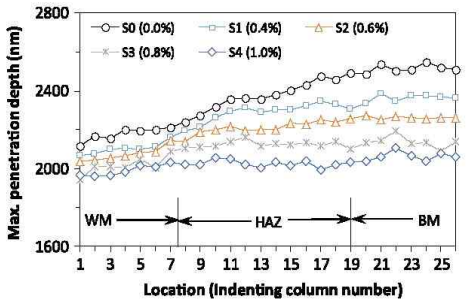


Fig. 9. Variation of maximum penetration depth across the weld zones.

depth curve at the middle indenting column of each region was used for comparison. Once α value of each region of all weld zones was estimated, the yield strength and strain hardening exponent in the weld zones could be determined following step 10.

4. Experimental results

4.1. Low-cycle fatigue tests and indentation load-penetration depth curves

The results of low-cycle fatigue tests carried out at four different total strain amplitude are presented as the cyclic stress response curves obtained by plotting the cyclic stress amplitude, which is determined by averaging the maximum tensile stress and compressive stress in a hysteresis loop, versus the number of cycles in a total strain – controlled fatigue test, as illustrated in Fig. 5. These curves illustrate the path by which the material arrives at the final cyclic flow stress level [33], represents the variation of stress response of the material during cycling, and can include regimes of hardening, softening, and saturation.

As can be seen from Fig. 5, the cyclic stress response of the present weld zones is dependent on the strain level and can be separated into two circumstances, as follows: (1) at strain amplitude of 0.4%, the material exhibited continuous and gradual softening followed by a saturation, which persisted until fracture; and

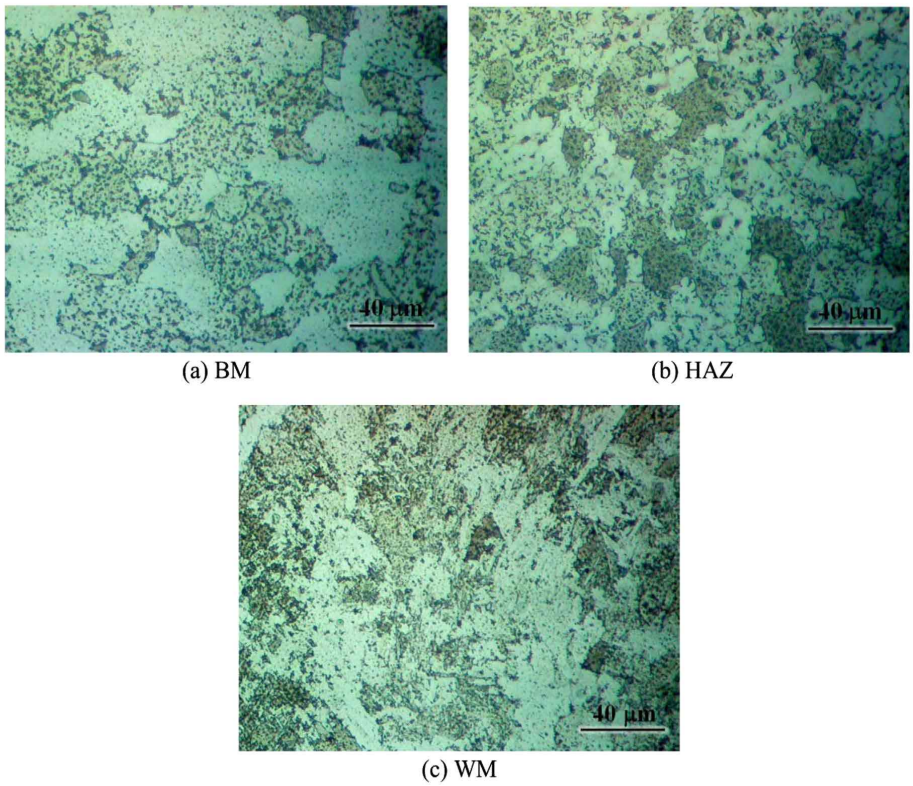


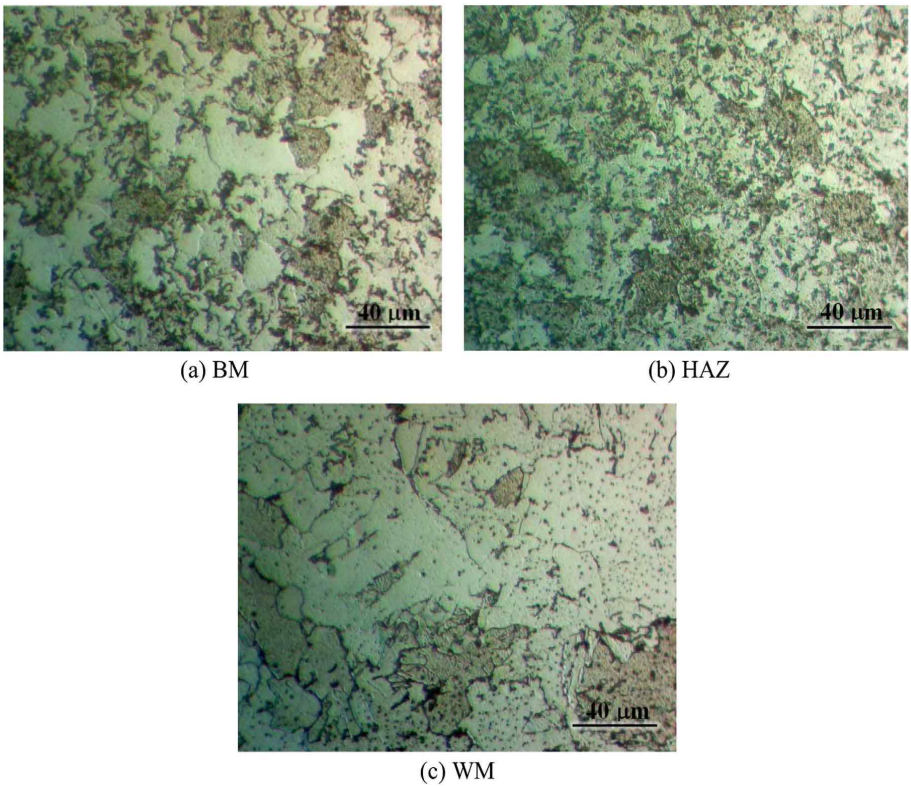
Fig. 10. Microstructures in the virgin weld zone. (a) BM. (b) HAZ. (c) WM.

(2) at strain amplitude larger than 0.6%, the initial mid softening was followed by a region of nearly stable stress response, a very small hardening, and then a slight secondary hardening up to the final failure. The relative proportion of each of above regimes is found to be dependent on the cyclic strain amplitude or in the other word, these proportions depend on the initial microstructure and also the microstructure changes took place during cycling, which are governed by strain amplitude. Fig. 6 shows the stress-total strain hysteresis loops including the first, the steady-state, and the end cycles for four different strain amplitudes.

Concerning the microstructure and mechanical properties in the weld zone of fatigue failure specimens, the region of each individual weld zone is first identified, the corresponding microstructures are examined, and the mechanical properties in each individual weld zone are then determined from the load-penetration depth curves. Fig. 7 presents the optical micrographs of representative parts of indentation impressions across the weld zone of fatigue failure specimens. This figure allows identifying the BM, HAZ, and WM regions in each weld zone as well as their approximate dimensions. The identification showed that each indenting region consisting of 5×26 points covered a length of 5.0 mm across the weld zone including approximately 2.3 mm of the HAZ region. In Fig. 7, the larger enough size of indents compared to the grain sizes and much smaller size of indents compared to the dimension of the individual weld zone ensure that a composite behavior always be measured instead of the grain in all regions of the weld zone and the indentation P–h curve exactly manifests the local elastic–plastic response of the materials in the weld zone [18].

Fig. 8 shows typical load-penetration depth curves (P–h) measured in the BM, HAZ, and WM regions of the SS400 as-welded steel and specimens cycled to failure at two representative low and high strain amplitudes of $\pm 0.4\%$ and $\pm 1.0\%$, respectively. As can be seen from this figure, the magnitudes of the P–h curves change significantly with the individual weld zone for both as-welded and fatigue failure specimens. For as-welded specimen, the maximum penetration depth in BM is larger than in HAZ, while the depth in WM is smallest. For the fatigue failure specimens, with increased strain amplitudes, maximum penetration depth as well as the residual depth tends to decrease, while the curvature of loading parts shows increasing characteristics for all regions of the weld zone. These observations signify that for the present weld zone, the indentation response is not only highly sensitive to the details of the metallurgical condition that resulted from the welding process but also sensitive to the strain amplitude applied during low-cycle fatigue loadings.

Fig. 9 presents the variation of the averaged maximum penetration depth at indenting columns across the weld zone of all specimens. The larger variation of the depth in BM due to the low-cycle fatigue loading compared to that in HAZ indicate that for the investigated weld zone, low-cycle fatigue loading has stronger influence on the BM than that on the HAZ, whereas the smallest variation of the depth in WM indicates that this region is fewest influenced by this loading. The microstructure examinations of identified regions and mechanical properties obtained from indentation P–h curves in the weld zones are detailed below.



(a) BM (b) HAZ

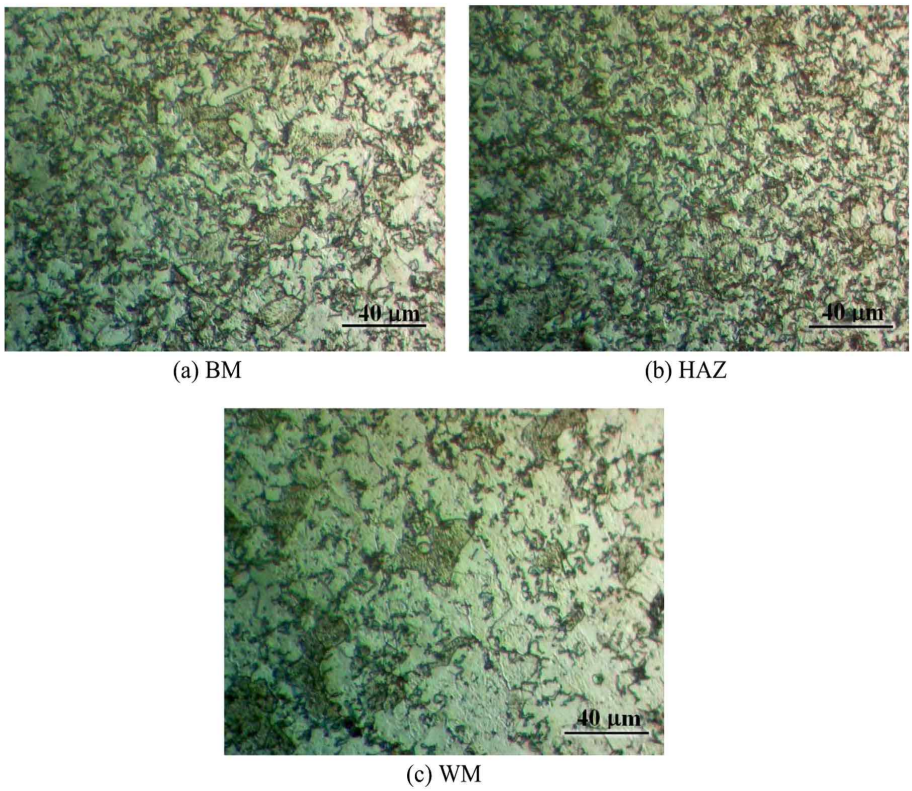
(c) WM

Fig. 11. Microstructures in the weld zone of fatigue failure specimen S1 (ε_a=0.4%). (a) BM. (b) HAZ. (c) WM.

4.2. Microstructure evolution during low-cycle fatigue

Fig. 10 shows a typical microstructure of the base metal (BM), heat affected zone (HAZ), and weld metal (WM) of S400 steel weld zone in the as-welded condition. The observed microstructures of BM and HAZ consist of approximately 6 vol% pearlite (darkest contrast) and the remainder is ferrite with different levels of reflective color brightness. It is seen in Fig. 10a that the size of ferrite grains in BM is various in the range of 20–60 μm, while the ferrite grains in HAZ (Fig. 10b) are more regular and relatively smaller when compared with that in BM. Some pearlite colonies equally distributed over the darker ferrite grains are also observed in BM and HAZ. The WM region has a more complex microstructure with different types of ferrite including allotriomorphic ferrite (α), Widmanstatten ferrite (α_W), and acicular ferrite (α_a), as shown in Fig. 10c. Few pearlite colonies at the ferrite grain boundaries can also be observed in this figure. Figs. 11 and 12 present the representative microstructures in the weld zone of fatigue failure SS400 steel tested at low and high strain amplitude of $\pm$0.4% and $\pm$1.0%, respectively. At low strain amplitude of $\pm$0.4%, the quite regular and large ferrite grains changes apparently to irregular with ragged grain boundaries in both BM (Fig. 11a) and HAZ (Fig. 11b), leading to a microstructure with smaller ferrite grain sizes in these regions compared to those in the virgin weld zone. Additionally, some carbides and oxides can be found on the grain boundaries in microstructures of BM, while few granular ferrite grains can be observed in microstructure of HAZ, as seen in Fig. 11a and b, respectively. In the WM, the equiaxed (polygonal) ferrite and few massive grains, together with some small amount of pearlites are formed (Fig. 11c). At high strain amplitude of $\pm$1.0%, the microstructures of BM and HAZ are formed in a similar morphology, in which the boundaries of granular ferrite become difficult to see and the dot-like dispersed islands appear in the matrix, as shown in Fig. 12a and b. The microstructure of WM is a complex structure of polygonal ferrite, massive ferrite, and granular ferrite, as presented in Fig. 12c.

As indicated in the previous work [18], the formation of more regular and smaller sizes of ferrite grains in HAZ when compared to that in BM as well as the formation of different types of ferrite grains in WM of SS400 steel weld zone was clearly pointed out to be completely consistent with the results reported in the literature [34–36]. In this study, the microstructure observations in the virgin weld zone are similar to the microstructure examination results obtained from the same weld zone in the previous work [18], and also agreed well with the reported results from a similar low carbon steel weld zone with 0.053% C [37]. As is pointed out in numerous investigations of steels [4,38–40], plastic deformation creates a large number of line defects (dislocations), including dislocation-dislocation interaction (working hardening) and dislocation-precipitate interaction (precipitation strengthening), and surface defects (grain boundaries) during cyclic loading. When subjected to shear forces, the dislocations travel from the one layer of atoms to another as the shear stress increase. Slipping of all the atoms simultaneously would take enormous forces, which is not explained by the much lower yield strength of metals and a dislocation may be obstructed in its movements by atoms of alloying



(a) BM (b) HAZ

(c) WM

Fig. 12. Microstructures in the weld zone of fatigue failure specimen S4 (ε_a=1.0%). (a) BM. (b) HAZ. (c) WM.

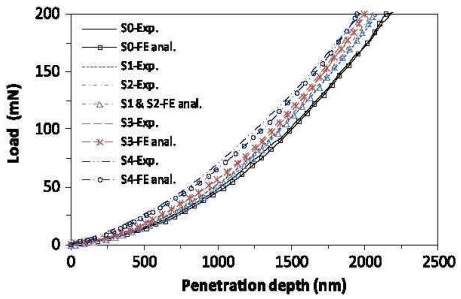
elements or point defects, by stationary dislocations and grain boundaries or by other defects. More force is then required to overcome the obstruction and with further increase in stress the dislocation may get curved inward, ultimately transforming into a ring dislocation and a new location at the initial points. Thus, this becomes a source of production of dislocations. Surface defects are the irregular arrangements of atoms at the grain boundaries. Thus, these defects lead to the formation of such microstructures in the fatigue failure weld zones described above, in which the size of grains is smaller with the increase of applied strain amplitude.

4.3. Mechanical properties changes during low-cycle fatigue

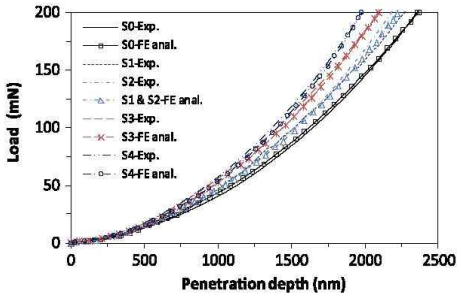
Fig. 13 shows the experimental curves at the middle indenting column of HAZ and WM regions in all weld zones and the curves at the middle indenting column of BM regions in the weld zone of fatigue failure specimens, together with their best fit simulated loading parts of load–penetration depth curves. Note that the best fit curves are quite easily identified from the 1320 simulated loading curves, of which the penetration depth is in the wide range of 1730–2640 nm at the applied load of 200 mN and the slope varies by material properties. Since the simulated curves are distinguishable from the shape and the magnitude of penetration depth and a composite behavior is always measured from each indentation test in this study, the input data (E, σ_y, n, and α) used for the best fit curves are accurately indicated the elastic–plastic properties of material at the corresponding indenting points. The α value of the best fit simulated curve for each region of the weld zones, as listed in Table 3, is considered as the representative α value for this region. As can be seen form Table 3 that α value is influenced by both welding process and low-cycle fatigue loadings.

Considering the estimated α values in Table 3 as the representative α value for each region in the weld zones, the yield strength σ_y and strain hardening exponent n at each indenting point in each region can then be determined using Eq. (9) and (10). The elastic modulus E, yield strength σ_y, and strain hardening exponent n across the weld zone in the as-welded condition (virgin weld zone) obtained from the indentation tests are presented in Fig. 14, in which an average of 5 values at each indenting column and error bar of a standard deviation are plotted as a function of the indenting columns. In this figure, the dotted lines in WM and BM represent the average values of all data points in these regions, while the dotted line in HAZ is the linear fitting of all values in this zone.

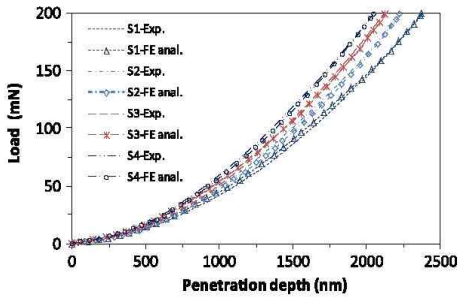
As can be seen in Fig. 14, the distribution trend of the mechanical properties across the virgin weld zone in this study is consistent with the results obtained from the same weld zone reported in the previous work [18]. The trend is that WM has the highest values of elastic modulus, yield strength, and strain



(a) In WM region of all weld zones



(b) In HAZ region of all weld zones



(c) In BM region of fatigue failure weld zones

Fig. 13. Comparison of the FE analysis and experimental *P–h* curves. (a) In WM region of all weld zones. (b) In HAZ region of all weld zones. (c) In BM region of fatigue failure weld zones.

Table 3
Estimated α values for WM, HAZ, and BM in weld zones.

	S0 (ε_a=0.0%)	S1 (ε_a=0.4%)	S2 (ε_a=0.6%)	S3 (ε_a=0.8%)	S4 (ε_a=1.0%)
WM	9.0	8.0	8.0	8.0	8.0
HAZ	15.0	12.0	12.0	10.0	9.0
BM	18.1[a]	15.0	13.0	11.0	10.0

[a] Obtained from tensile test of SS400 steel.

hardening exponent, BM has the lowest elastic modulus, yield strength, and strain hardening exponent values, while the properties values in the HAZ region gradually decrease from the WM to BM region. Concerning the average values of mechanical properties in the BM, HAZ, and WM regions obtained from indentation tests, these values are listed in Table 4, together with corresponding values reported in the previous work [18]. As seen from this table, the mechanical properties in the virgin weld zone determined in this study are also consistent with the properties obtained in the previous work with very small relative errors. Since the results in the previous work were verified to be reliable by comparing with the results from experiments and FE analysis of tensile tests of steel and welded specimens [18], the results of mechanical properties estimated from the indentation tests in this

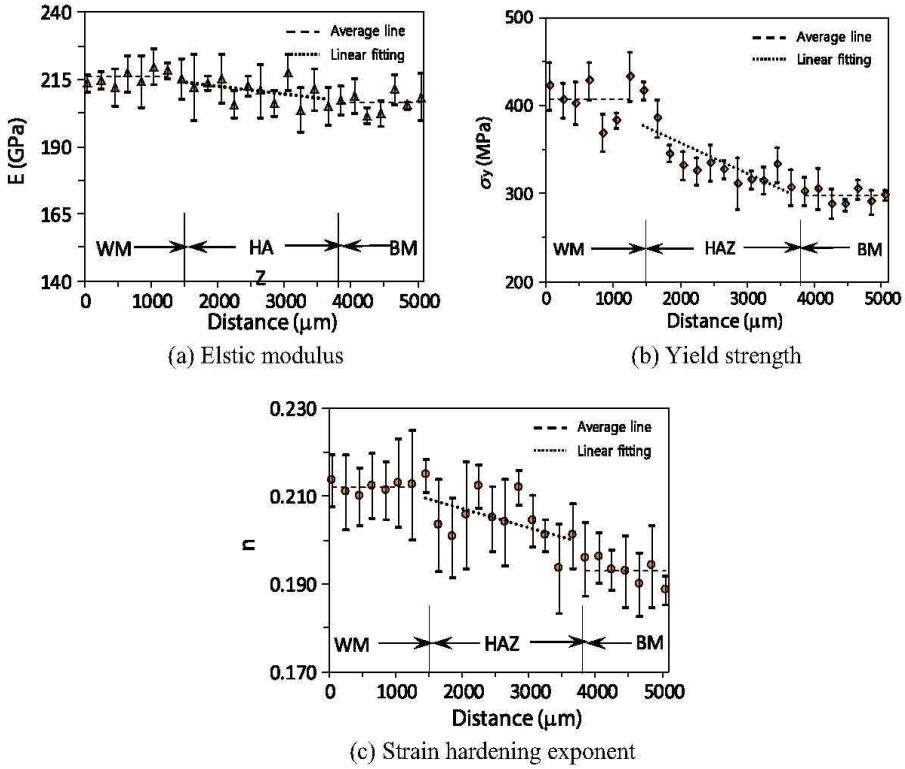


Fig. 14. Distributions of (a) elastic modulus, (b) yield strength, and (c) n across the virgin weld zone (S0).

Table 4
Average values of mechanical properties in the virgin SS400 steel weld zone.

Virgin SS400 steel weld zone		Present study	Previous study [19]	Err. (%)
E (GPa)	WM	215.9	218.2	−1.05[a]
	HAZ	211.1	212.4	−0.61
	BM	206.7	207.2	−0.24
σ_y (MPa)	WM	407.2	403.5	0.92
	HAZ	338.3	331.4	2.08
	BM	297.6	302.7	−1.68
n	WM	0.212	0.203	4.43
	HAZ	0.205	0.195	5.13
	BM	0.193	0.191	1.05

[a] Errors were computed as $(X_{Present} - X_{Previous})/X_{Previous}$, where $X_{Present}$ represents a variable.

study are acceptable for the present virgin SS400 steel weld zone. These results indicate, again, that the proposed procedure is appropriate for investigating the mechanical properties of the structural steel weld zone. In this study, the mechanical properties in fatigue failure weld zones were also estimated using the proposed procedure.

The distributions of elastic modulus E, yield strength σ_y, and strain hardening exponent n across the fatigue failure weld zones are presented in Figs. 15–17, respectively, with the same illustrated way as Fig. 14. As it is seen in Fig. 15, various elastic modulus values display a relatively little variation in the BM and WM regions and a gradient-distribution in HAZ of the fatigue failure weld zone at strain amplitude of 0.4% (Fig. 15a). In the cases of higher applied strain amplitudes, a small amount of variation and a gradient-distribution of E values is still exhibited in WM and HAZ, respectively, whereas the E values in BM are quite variant (Fig. 15b–d). However, the distribution of E values across the weld zone is found to be quite smooth for all applied strain amplitude cases. In contrast, the yield strength values exhibit a significant variation in BM and WM regions of the fatigue failure weld zone at strain amplitude of 0.4% (Fig. 16a), while these values in BM and WM regions of the weld zone tested at higher strain amplitudes are not much

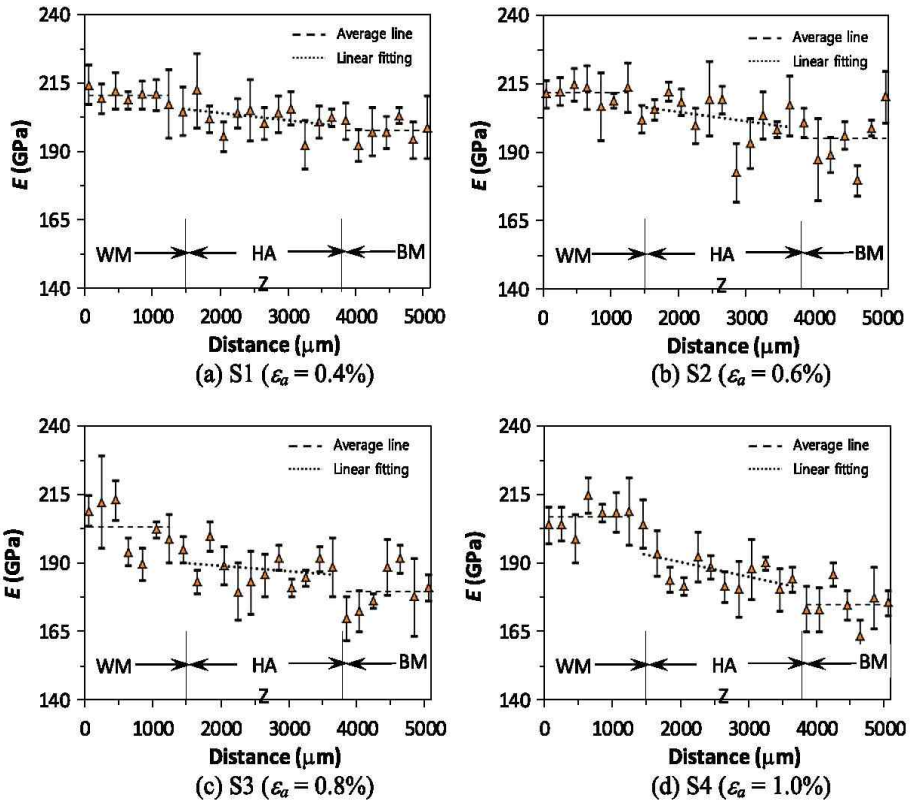


Fig. 15. Distributions of elastic modulus across the fatigue failure weld zones. (a) S1 (ε_a=0.4%). (b) S2 (ε_a=0.6%). (c) S3 (ε_a=0.8%). (d) S4 (ε_a=1.0%).

variant, as can be seen in Fig. 16b–d. Similar to elastic modulus, yield strength values in HAZ show a quite gradual decrease from WM to BM regions in all fatigue failure weld zones except the weld zone tested at the high strain amplitude of 1.0% (Fig. 16d), in which the yield strength values obtained in all regions are fairly the same. For strain hardening exponent values, the same trend that a moderate variation of these values can be observed in BM and WM regions and strain hardening exponent in HAZ decreases gradually from base metal to weld metal regions, as shown in Fig. 17.

In order to evaluate the effect of low cycle fatigue loading on the mechanical properties in the investigated weld zone, the average values of E, σ_y, and n in all regions of virgin and fatigue failure weld zones are calculated, as listed in Table 5. Fig. 18 presents these average values plotted as a function of the applied strain amplitudes (ε_a). It is visible in this figure that with increasing strain amplitudes, the elastic modulus E displays decrease in all regions of the weld zone, both yield strength σ_y and strain hardening exponent n exhibit decreasing characteristic in WM and increasing characteristic in BM region, while the yield strength in HAZ region increases, the strain hardening exponent in this region keeps almost unchanged. It is interesting to note in this figure that the increase and decrease of the mechanical properties in all regions of the weld zone with increasing strain amplitudes are nearly linear, especially in the case of yield strength. The observed slopes of these linear increase and decrease in Fig. 18 indicate that the low-cycle fatigue loading has the highest effect on the mechanical properties (E, σ_y, and n) in BM, while its influence on the E and σ_y in WM is lower than that in HAZ. LCF loading also shows quite small effect on the strain hardening exponent in WM region and there seems to be no effect of this loading on strain hardening exponent in HAZ. The effects of LCF loading on mechanical properties in the weld zone well accord with those observed in the maximum penetration depth of indentation tests presented previously.

As indicated [18], for the virgin SS400 steel weld zone, the higher amount of δ-ferrite and its abundant transformed phase boundaries may be responsible for higher mechanical properties values (E, σ_y and n) in WM when compared to those in BM, while the smaller and more regular sizes of ferrite grains in HAZ may be mainly response for the higher mechanical properties values in HAZ compared to those in BM. Concerning the changes of mechanical properties during low-cycle fatigue loading, a linear decrease of E and n, and an approximately linear increase of σ_y with the increasing strain amplitude were observed in a nickel-base superalloy [38]. Investigation of 304L SS weld zone also indicated that with the increasing strain amplitudes, the yield stress (σ_y) and strain hardening exponents (n) display increase in both BM and HAZ regions but decrease in WM regions, while elastic modulus (E) exhibits decreasing characteristic in all regions of the weld zone [22]. These strain amplitude-dependent variation in the

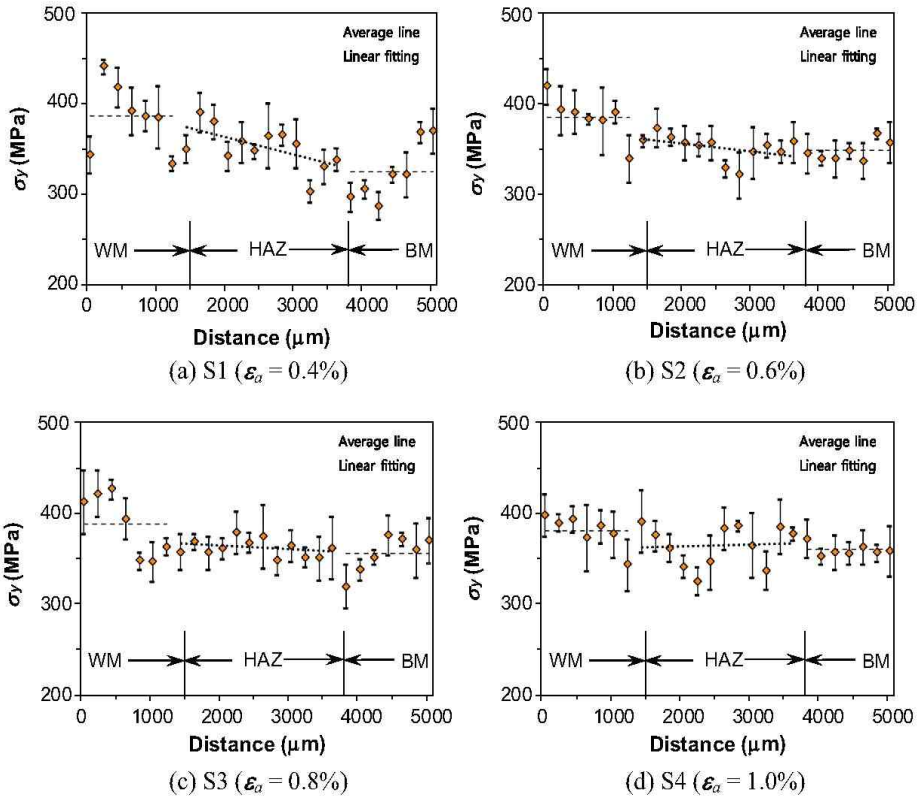


Fig. 16. Distributions of yield strength across the fatigue failure weld zones. (a) S1 (ε_a=0.4%). (b) S2 (ε_a=0.6%). (c) S3 (ε_a=0.8%). (d) S4 (ε_a=1.0%).

mechanical properties were demonstrated to be essentially resulted from the amplitude-dependent variation in the microstructures during cyclic loading [22,38]. For the present SS400 steel weld zone, even though that the strain amplitude-dependent variations in mechanical properties are different, the change trends of mechanical properties in all regions of the weld zone including BM, HAZ, and WM are completely consistent with the reported results of 304L SS weld zone [22]. The reduction of elastic modulus in all regions of the weld zone can be attributed to dislocation-precipitate interactions, the nucleation of micro cracks/microvoid at δ/γ interfaces during cyclic loading, as well as their increase in the number with increased strain amplitudes [22,38]. The strain amplitude-dependent degradation in yield strength and strain hardening exponent in WM may be attributed to the formation of polygonal ferrite with the increase of applied strain amplitude during cyclic loading, while the smaller grain size along with abundant grain boundaries due to the formation of granular ferrite, which is known as an excellent combination of strength and toughness [41–43], may be responsible for the increase in yield strength and strain hardening exponent in BM and HAZ regions of the weld zone with increased strain amplitudes.

5. Conclusion

In this study, an instrumented indentation technique was used to investigate the mechanical properties in the weld zone of SS400 steel subjected to cyclic loadings. For this purpose, low-cycle fatigue, instrumented indentation, and tensile tests, finite element (FE) analysis, and optical microscopy examinations were carried out. The experimental and analysis results support the following conclusions:

1. The indentation response is not only highly sensitive to the details of the metallurgical conditions that resulted from the welding process but also sensitive to the strain amplitude applied during low-cycle fatigue loading. For the present weld zone, low-cycle fatigue has stronger influence on indentation response in BM than that in HAZ, whereas indentation response in WM is fewest influenced by this loading.
2. In the virgin SS400 steel weld zone, the microstructure of BM and HAZ consist of a small amount of pearlite and ferrite with different levels of reflective color brightness. The ferrite grains in HAZ are more regular and relatively smaller than those in BM, leading to the higher mechanical properties values in HAZ when compared to those in BM. The WM has complex microstructure with different types of ferrite including α, α_W, α_a, and has the highest mechanical properties values in the weld zone.
3. The effect of low-cycle fatigue on mechanical properties in the weld zone was observed. The results show that with the increasing strain amplitudes, the elastic modulus E displays decrease in all regions of the weld zone, both yield strength and

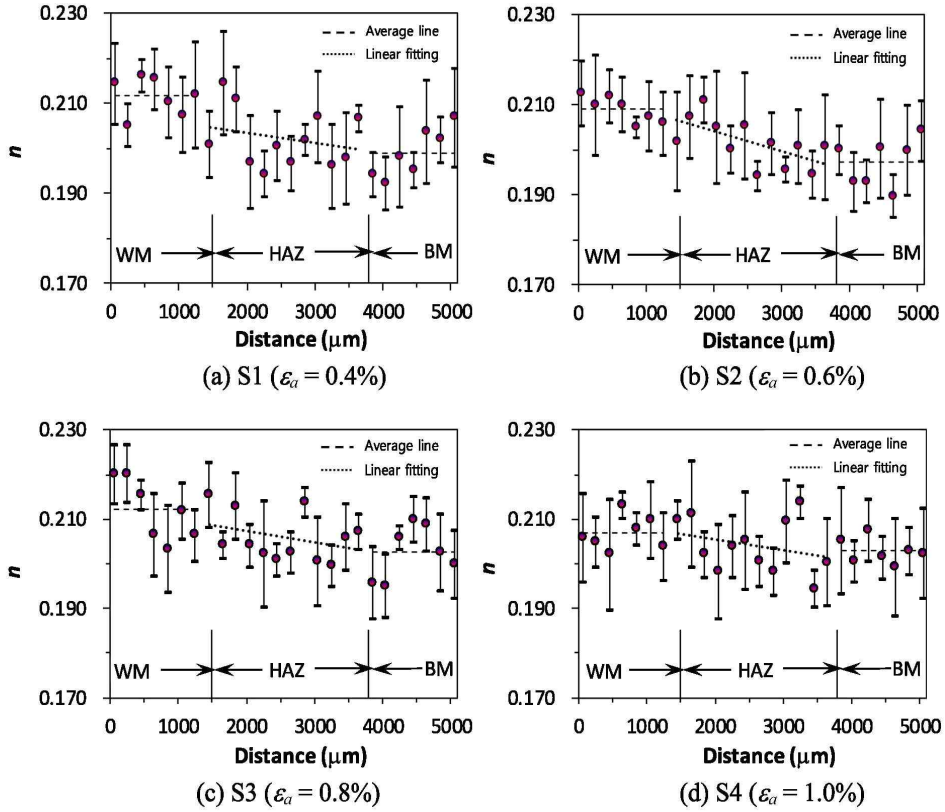


Fig. 17. Distributions of strain hardening exponent across the fatigue failure weld zones. (a) S1 (ε_a=0.4%). (b) S2 (ε_a=0.6%). (c) S3 (ε_a=0.8%). (d) S4 (ε_a=1.0%).

Table 5
Average mechanical properties in the weld zone with different strain amplitudes.

		S0 (ε_a=0.0%)	S1 (ε_a=0.4%)	S2 (ε_a=0.6%)	S3 (ε_a=0.8%)	S4 (ε_a=1.0%)
E (GPa)	WM	215.9	210.9	211.9	203.0	207.0
	HAZ	211.1	202.7	202.9	188.0	187.6
	BM	206.7	198.0	194.9	179.8	174.9
σ_y (MPa)	WM	407.2	386.3	385.8	388.0	380.4
	HAZ	338.3	352.7	352.0	362.1	364.9
	BM	297.6	325.0	348.0	355.6	359.9
n	WM	0.212	0.212	0.209	0.212	0.207
	HAZ	0.205	0.202	0.202	0.206	0.204
	BM	0.193	0.199	0.197	0.203	0.203

the strain hardening exponent exhibit decreasing characteristics in WM and increasing characteristic in BM regions, while the yield strength in HAZ region increases, the strain hardening exponent in this region remains almost unchanged. The microstructures in the weld zone are dependent on the strain amplitudes applied during low-cycle fatigue loadings, which is essentially responsible for the changes of mechanical properties in the present weld zone during cyclic loading.

4. The appropriate approach for investigation mechanical properties in the structural steel weld zone under low-cycle fatigue loading using instrumented indentation testing is provided. The changes trends of mechanical properties and the evolution trends of microstructure in the weld zone during low-cycle fatigue up to failure are obtained. The approach and the obtained results indicate that the designs of the welded joints against fatigue failure and the integrity assessment of structural steels member that have a welded joints can be performed using instrumented indentation testing.

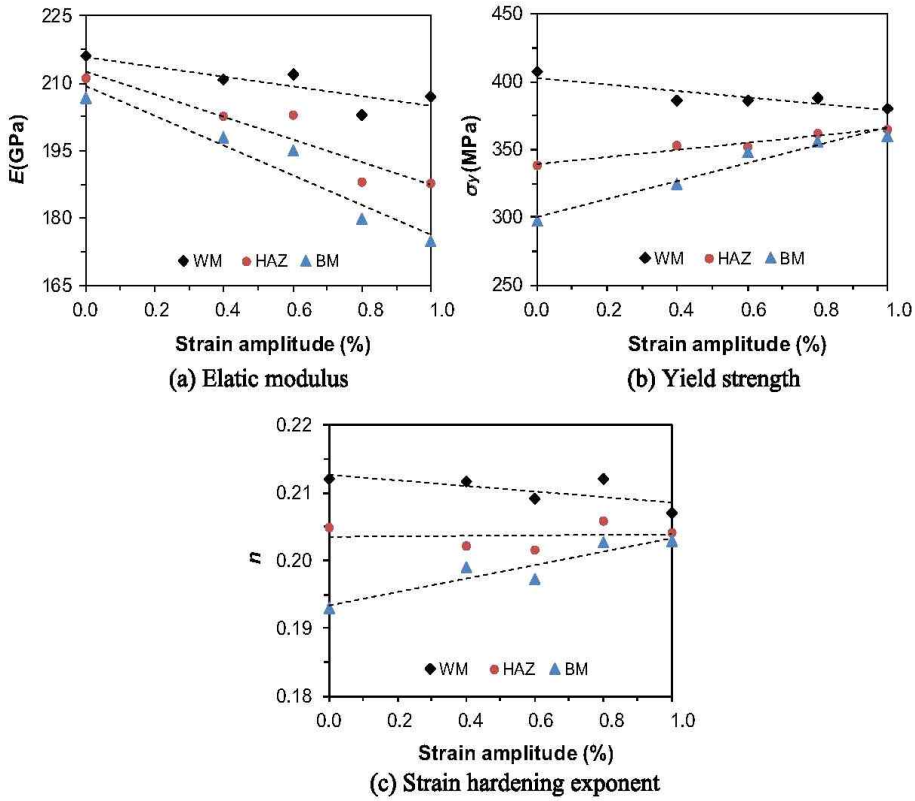


Fig. 18. Effects of strain amplitude on the mechanical properties of the weld zone (a) Elastic modulus. (b) Yield strength. (c) Strain hardening exponent.

Acknowledgments

This research was supported by a Grant (15CTAP-C098306-01) from Technology Advancement Research Program funded by Ministry of Land, Infrastructure and Transport of Korean.

Appendix A

See Table A1 and A2.

Table A1
Coefficient a_{ijk}.

(k, j)	a_{ijk}			
	$i=4$	$i=3$	$i=2$	$i=1$
(1, 1)	−1.710E −1	1.629E +0	1.144E +2	−4.574E +1
(2, 1)	1.395E −2	−1.195E −1	2.955E −1	−1.643E −1
(3, 1)	−4.231E −4	3.903E −3	−9.428E −3	5.243E −3
(1, 2)	9.940E +0	7.973E +0	5.240E +1	−6.190E +1
(2, 2)	−1.193E +0	2.573E +0	−5.962E +0	3.952E +0
(3, 2)	3.876E −2	−1.429E −1	1.858E −1	−5.743E −2
(1, 3)	−1.196E +2	5.892E +2	−9.072E +2	4.656E +2
(2, 3)	1.194E +1	−5.351E +1	5.441E +1	−1.804E +1
(3, 3)	−3.417E −1	1.631E +0	−1.443E +0	2.175E −1
(1, 4)	1.981E +2	−4.190E +2	4.267E +2	−2.408E +2
(2, 4)	−1.845E +1	3.178E +1	2.717E +0	−1.053E +1
(3, 4)	5.023E −1	−1.147E +0	3.126E −2	5.674E −1

Table A2
Coefficient b_{ijk}.

(k, j)	b_{ijk}			
	$i=4$	$i=3$	$i=2$	$i=1$
(1, 1)	−6.197E −2	8.766E −1	−3.097E +0	6.085E +0
(2, 1)	2.285E −5	−7.846E −4	5.723E −3	−1.095E −2
(3, 1)	−4.241E −6	8.032E −5	−4.539E −4	7.676E −4
(1, 2)	9.840E −1	−1.477E +1	6.723E +1	−9.676E +1
(2, 2)	−6.638E −2	9.160E −1	−3.909E +0	5.367E +0
(3, 2)	1.877E −3	−2.619E −2	1.147E −1	−1.630E −1
(1, 3)	−4.036E +0	6.074E +1	−2.847E +2	4.247E +2
(2, 3)	4.241E −1	−6.122E +0	2.797E +1	−4.112E +1
(3, 3)	−1.324E −2	1.911E −1	−8.782E −1	1.301E +0
(1, 4)	4.871E +0	−7.309E +1	3.440E +2	−5.160E +2
(2, 4)	−5.777E −1	8.394E +0	−3.875E +1	5.745E +1
(3, 4)	1.875E −2	−2.718E −1	1.257E +0	−1.870E +0

References

[1] Tamboli AR. Handbook of structural steel connection design and details. NY, USA: McGraw-Hill; 1999.
[2] Boyer HE. Atlas of stress-strain curves.Metal Park, Ohio: ASM International; 1987.
[3] Wole S. Mechanical Properties of engineered materials. New York, NY: Marcel Dekker, Inc; 2003.
[4] Ye D, Xu Y, Xiao L, Cha H. Effects of low-cycle fatigue on static mechanical properties, microstructures and fracture behavior of 304 stainless steel. Mater Sci Eng A 2010;527:4092–102.
[5] Lemaitre J, Desmorat R. Engineering damage mechanics.Berlin/Heidelberg/

New York: Springer; 2004.
[6] Ye D, Wang Z. An approach to investigate pre-nucleation fatigue damage of cyclically loaded metals using Vickers microhardness tests. Int J Fatigue 2001;23:85–91.
[7] Ye D, Wang Z. A new approach to low-cycle fatigue damage based on exhaustion of static toughness and dissiation of cyclic plastic strain energy during fatigue. Int J Fatigue 2001;23:679–87.
[8] Boronski D. Cyclic material properties distribution in laser-welded joints. Int J Fatigue 2006;28:346–54.
[9] Molak RM, Paradowski K, Brynk T, Ciupinski L, Pakiela Z, Kurzydlowski KJ. Measurement of mechanical properties in a 316L stainless steel welded joint. Int J Press Vessels Pip 2009;86:43–7.
[10] Rao D, Heerens J, pinherio GA, Santos JF, Huber N. On characterisation of local stress-strain properties in friction stir welded aluminium AA5083 sheets using micro-tensile specimen testing and instrumented indentation technique. Mater Sci Eng A 2010;527:5018–25.
[11] Corigliano P, Crupi V, Guglielmino E. FE analysis of cruciform welded joints considering different mechanical properties for base meterials, heat affected zone and weld metal. Fratt Integr Strutt 2014;30:304–10. http://dx.doi.org/10.3221/IGF-ESIS.30.37.
[12] Kang JJ, Becker AA, Sun W. Determining elastic-plastic properties from indentation data obtained from finite element simulations and experimental results. Int J Mech Sci 2012;62:34–46.
[13] Chung KH, Lee W, Kim JH, Kim C, Park SH, Kwon D, Chung K. Characterization of mechanical properties by indentation tests and FE analysis – validation by application to a weld zone of DP590 steel. Inter J Solids Struct 2009;46 (2):344–63.
[14] Zhan M, Du H, Liu J, Ren N, Yang H, Jiang H, Diao K, Chen X. A method for establishing the plastic constitutive relationship of the weld bead and heat-affected zone of welded tubes based on the rule of mixtures and a micro-hardness test. Mater Sci Eng A 2010;527(12):2864–74.
[15] Yonezu A, Akimoto H, Fujisawa S, Chen X. Spherical indentation method for measuring local mechanical properties of welded stainless steel at high temperature. Mater Des 2013;52:812–20.
[16] Sun G, Xu F, Li G, Huang X, Li Q. Determination of mechanical properties of the weld line by combining micro-indentation with inverse modeling. Comput Mater Sci 2014;85:347–62.
[17] Pham TH, Kim SE. Determination of mechanical properties in SM490 steel weld zone using nanoindentation and FE analysis. J Constr Steel Res 2015;114:314–24.
[18] Kim JJ, Pham TH, Kim SE. Instrumented indentation testing and FE analysis for investigation of mechanical properties in structural steel weld zone. Int J Mech Sci 2015;103:265–74.
[19] Radaj D, Sonsino CM, Fricke W. Recent developments in local concepts of fatigues assessment of welded joints. Int J Fatigue 2009;31:2–11.
[20] Fricke W. Recent developments and future challenges in fatigue strength assessment of welded joints. In Proc Inst Mech Eng Part C: J Mech Eng Sci 2015:1–16. http://dx.doi.org/10.1177/0954406214550015.
[21] Corigliano P, Crupi V, Fricke W, Friedrich N, Guglielmino E. Experimental and numerical analysis of fillet-welded joints under low-cycle fatigue loading by means of full-field techniques. In Proc Inst Mech Eng Part C: J Mech Eng Sci 2015;29(7):1327–38. http://dx.doi.org/10.1177/0954406215571462.
[22] Ye D, Mi F, Liu J, Xu Y, Chen Y, Xiao L. Use of instrumented indentation testing to study local mechanical properties of 304L SS welded joints subjected to low-cycle fatigue loadings. Mater Sci Eng A 2013;564:76–84.
[23] Pham TH, Kim JJ, Kim SE. Estimating constitutive equation of structural steel using indentation. Int J Mech Sci 2015;90:151–61.
[24] AWS Welding Handbook. Volume 1: welding science and technology. 9th ed.. Miami, FL: American Welding Society; 2001 33126.
[25] ASTM E606. Standard practice for strain-controlled fatigue testing.West Conshohocken, PA: ASTM International; 2013.
[26] ASTM E3-01. Standard guide for preparation of metallographic specimens. West Conshohocken, PA: ASTM International; 2007.
[27] ASTM E2546-07. Standard practice for instrumented indentation testing.West Conshohocken, PA: ASTM International; 2007.
[28] ASTM E8/E8M – 13a. Standard test methods for tension testing of metallic. West Conshohocken, PA: ASTM International; 2013.
[29] Oliver WC, Pharr GM. An improved technique for determining hardness and elastic-modulus using load and displacement sensing indentation experiments. J Mater Res 1992;7(4):1564–83.
[30] Hibbitt, Karlsson and Sorensen, ABAQUS Standard User's Manual, version 6.6 (2006), Inc.
[31] Dao M, Chollacoop N, Vliet KJV, Venkatesh TA, Suresh S. Computational modeling of the forward and reverse problem in instrumented sharp indentation. Acta Mater 2001;49:3899–918.
[32] Lichinchi M, Lenardi C, Haupt J, Vitali R. Simualtion of Berkovich Instrumented indentation experiments on thin films using finite element method. Thin Solid Films 1998;312:240–8.
[33] Srivatsan TS, Anand S, Troxell JD. Cyclic plastic strain response and fracture behavior of and oxide-dispersion-strengthened copper alloy. Int J Fatigue 1993;15(5):355–67.
[34] Bhadeshia HKDH, Honeycombe R. Steels: microstructure and properties. London: Butterworth-Heinemann; 2006.
[35] Easterling KE. Introduction of the physical metallurgy of welding. 2nd ed.. London: Butterworth-Heinemann; 1992.
[36] Kou S. Welding Metallurgy. 2nd ed.John Wiley & Sons, Inc; 2003.
[37] Khodabakhshi F, Kazeminezhad M, Kokobi AH. Mechanical properties and microstructure of resistance spot welded severely deformed low carbon steel. Mater Sci Eng A 2011;529:237–45.
[38] Ye D, Xiao L, Cha H, Xu P, Xu Y. Use of instrumented micro-indentation to study the mesoscopic elasto-plastic behavior of GH4145/SQ superalloy during high-temperature cyclic straining. Mater Sci Eng A 2011;528:6825–37.
[39] Ye D, Cha H, Xiao L, Xu Y. A study of fatigue mesoscopic elasto-plastic properties of a nickel-base superalloy by instrumented microindentation measurements. J Nucl Mater 2012;420:525–36.
[40] Plumtree A. Correlation between microstructure and cyclic behavior. In: Rie KT, editor. Low cycle fatigue and elasto-plastic behavior of materials. Netherlands: Springer; 1987.
[41] Krauss G, Thompson SW. Ferritic microstructures in continuously cooled low- and untralow- carbon steels. ISIJ Int 1995;35(8):937–45.
[42] Xiao F, Liao B, Ren D, Shan Y, Yang K. Acicular ferritic microstructure of a low-carbon Mn–Mo–Nb microalloyed pipeline steel. Mater Charact 2005;54:305–14.
[43] Wang W, Yan W, Zhu L, Hu P, Shan Y, Yang Ke. Relation among rolling parameters, microstructures and mechanical properties in an acicular ferrite pipeline steel. Mater Des 2009;30:3436–43.

4. Determination of equi-biaxial residual stress and plastic properties in structural steel using instrumented indentation(2017)

Materials Science & Engineering A 688 (2017) 352–363

Contents lists available at ScienceDirect

Materials Science & Engineering A

journal homepage: www.elsevier.com/locate/msea

Determination of equi-biaxial residual stress and plastic properties in structural steel using instrumented indentation

Thai-Hoan Pham[a], Seung-Eock Kim[a,*]

[a] Department of Civil and Environmental Engineering, Sejong University, 98 Gunja-dong, Gwangjin-ku, Seoul 143-747, South Korea

ARTICLE INFO

Keywords:
Indentation
Plastic properties
Residual stress
Structural steel

ABSTRACT

This study describes a method that allows estimation of the equi-biaxial residual stress (σ_R), yield strength (σ_y), the strain hardening exponent (n), and the ratio (α) between strain at starting-point of strain hardening (ε_{st}) and yield strain (ε_y) of structural steel from the load-depth curve of one sharp indentation test. In this method, the relationships between the structural steel properties, residual stress, and the characteristics of the indentation loading-unloading curves were established in the form of dimensionless functions via extensive finite element (FE) analyses. Based on the FE analysis results of the indentation process with a large number of different material properties combinations, the effects of residual stress and plastic parameters on the indentation response were investigated, and a reverse algorithm for estimating four unknown quantities (σ_R, σ_y, n, and α) of steel from an indentation test was proposed. A stress-applying apparatus that allows the introduction of a compressive or tensile stress to the sample by applying a compressive or tensile force and maintaining the stress after releasing the force was also developed in this study. Indentation and tensile tests of structural steels (SS400 and SM490) were carried out and the proposed algorithm was validated through both numerical analyses and experimental results.

1. Introduction

Residual stresses can exist in many engineering parts and structures made of various materials, especially structural steel, due to the thermal mismatch or thermal and mechanical processing during welding, joining, and manufacturing [1]. Since it has significant effects on the mechanical performance of materials, such as fracture, fatigue, wear, corrosion, and fraction, measurement of residual stress in materials has become important in engineering design. There are several methodologies for measuring the residual stress, including mechanical methods such as hole-drilling, saw-cutting, and layer-removing techniques [1,2], physical methods such as analysis of ultrasonic wave, X-ray and neutron diffraction, and the newly developed indentation technique [3,4]. The indentation technique has shown advantages over the others in terms of simplicity, non-destruction, applicability, and convenience at various scales [5,6].

The effect of residual stress on the load-depth (P-h) curve of indentation was first investigated by Tsui et al. [7] using experiments and by Bolshakov et al. [8] using finite element analysis. A bilinear relation between residual stress and indentation hardness was established from these investigations [7,8]. Various characteristics of the indentation load–depth curve, including contact stiffness (S), maximum indentation depth (h_m), loading curvature (C), and indentation work (W), have also been found to be in nonlinear relationships with residual stresses [9–12]. Based on the correlation between residual stress and indentation parameters from both experiments and analysis, numerous methods for the determination and measurement of residual stress from the characteristics of indentation have been proposed. For example, Suresh and Giannakopouls [9] utilized the difference in the indentation contact area between free-stress and stressed indented materials at the same indentation depth to characterize the equi-biaxial residual stress. Carlsson and Larsson [10,11] also reported the effects of residual stress on the indentation contact area, from which the residual stress can be estimated. Lee and Kwon [12] developed a new procedure to determine the residual stress based on the difference between indentation load at the same penetration depth of indented materials with and without residual stresses. One of the drawbacks of these aforementioned methods is that the indentation contact area needs to be measured accurately. Subsequently, many other methods for direct determination of residual stresses from the load-penetration depth curves of indentation without measurement of contact area have been suggested through extensive dimensional and finite element (FE) analyses [13–18]. However, these methods are only valid for either elastic, perfectly plastic materials [13,14] or materials exhibiting a

* Corresponding author.
E-mail address: sekim@sejong.ac.kr (S.-E. Kim).

http://dx.doi.org/10.1016/j.msea.2017.01.109
Received 14 January 2017; Received in revised form 27 January 2017; Accepted 30 January 2017
Available online 01 February 2017
0921-5093/ © 2017 Elsevier B.V. All rights reserved.

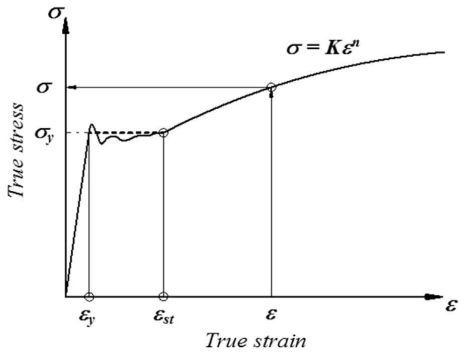


Fig. 1. Model for stress-strain behavior of structural steel (the plastic plateau is assumed perfectly plastic presented by the dotted line).

power law description in stress-strain behavior [15–17], or else need extra tests on free stress specimens for reference [18].

To our knowledge, no method has yet been established for estimating residual stress of structural steels, which exhibit a plastic plateau initiated from ε_y and ended at ε_{st} in their stress-strain curve from indentation. This study proposes a method that allows estimation of the equi-biaxial residual stress σ_R, together with yield strength σ_y, the strain hardening exponent n, and the ratio α of structural steels from the load- depth curve of indentation test. The material model for structural steels used in the previous works [19–21], which is illustrated in Fig. 1 and can be expressed as Eq. (1), was applied. The mechanical model of material with equi-biaxial residual stress indented by a sharp indenter (Berkovich or Vickers) can be considered an axisymmetric sample indented by a conical indenter with 70° of half apex angle [18], as illustrated in Fig. 2. The relationships between the structural steel properties, residual stress, and the characteristics of indentation loading-unloading curves were established in the form of dimensionless functions via extensive finite element (FE) analyses. The proposed method was validated through the results from indentation and tensile tests of structural steels (SS400 and SM490) subjected to residual stress and free stress as well.

$$\sigma = \begin{cases} E\varepsilon & (\varepsilon \le \varepsilon_y) \\ \sigma_y & (\varepsilon_y < \varepsilon < \varepsilon_{st}) \\ \sigma_y[1 + E(\varepsilon - \varepsilon_{st})/(\alpha\sigma_y)]^n & (\varepsilon \ge \varepsilon_{st}) \end{cases} \quad (1)$$

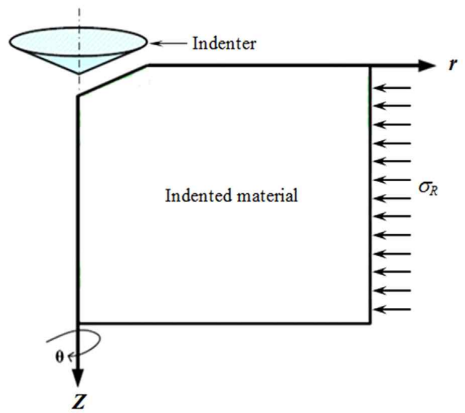


Fig. 2. Indentation model of a sample with equi-biaxial residual stress.

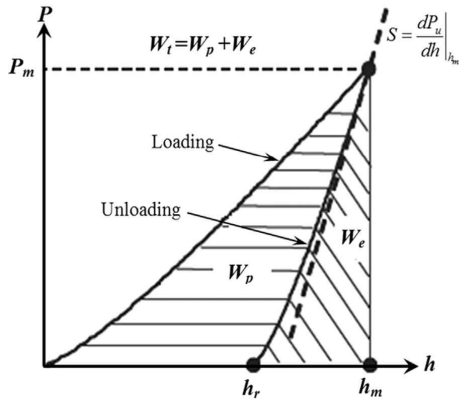


Fig. 3. Typical load-penetration depth curve.

2. Dimensional analysis and finite element simulation

2.1. Dimensional analysis

Fig. 3 illustrates a typical load-penetration depth curve of an unstressed specimen from a sharp indentation. The applied load P during loading can be depicted as a function of the indenter and material properties, as follows:

$$P = P(h, E, \nu, E_i, \nu_i, \sigma_y, n, \alpha) \quad (2)$$

where h is the penetration depth; E, υ, E_i, and υ_i are the elastic modulus and Poisson's ration of the indented material and indenter, respectively.

Using the reduced modulus E_r, which is defined as $E_r = [(1 - \nu^2)/E + (1 - \nu_i^2)/E_i]^{-1}$ [22,23], Eq. (2) can be written as

$$P = P(h, E_r, \sigma_y, n, \alpha) \quad (3)$$

For indentation of a specimen subjected to an equi-biaxial residual stress (σ_R), the applied load during loading can be expressed as

$$P = P(h, E_r, \sigma_y, n, \alpha, \sigma_R) \quad (4)$$

The $\prod$ theorem [24] is applied in dimensional analysis to form Eq. (4) as

$$P = \sigma_y h^2 \Pi_1^0\left(\frac{E_r}{\sigma_y}, n, \alpha, \frac{\sigma_R}{\sigma_y}\right) \quad (5)$$

The total indentation work of the indentation W_t, which is defined as the area under the loading curve from 0 to the maximum depth h_m (Fig. 3), can be determined as

$$W_t = \int_0^{h_m} P dh \quad (6)$$

From Eqs. (5) and (6), with a given indentation maximum depth h_m, the total indentation work (loading work) of indentation can be written in the following form:

$$W_t = \sigma_y h_m^3 \Pi_1^1\left(\frac{E_r}{\sigma_y}, n, \alpha, \frac{\sigma_R}{\sigma_y}\right) \quad (7)$$

Since σ_y and E_r have the same dimensional unit, Eq. (7) then can be written in an alternative form as

$$\frac{E_r h_m^3}{W_t} = \Pi_1\left(\frac{E_r}{\sigma_y}, n, \alpha, \frac{\sigma_R}{\sigma_y}\right) \quad (8)$$

Similarly, the unloading curve of an indentation into a specimen subjected to an equi-biaxial residual stress must be a function of the

indenter and material properties, indentation depth, and residual stress as

$$P_u = P_u(h, h_m, E_r, \sigma_y, n, \alpha, \sigma_R) \quad (9)$$

Eq. (9) becomes a dimensionless function by applying dimensional analysis as

$$P_u = \sigma_y h^2 \Pi_2^0\left(\frac{h}{h_m}, \frac{E_r}{\sigma_y}, n, \alpha, \frac{\sigma_R}{\sigma_y}\right) \quad (10)$$

Note that $P_u = 0$ at the residual impression depth $h = h_r$, leading Eq. (10) to

$$\frac{h_r}{h_m} = \Pi_2^1\left(\frac{E_r}{\sigma_y}, n, \alpha, \frac{\sigma_R}{\sigma_y}\right) \quad (11)$$

The elastic indentation work or unloading work of indentation W_e, which is defined as the area under the unloading curve from the residual impression depth h_r to the maximum depth h_m (Fig. 3), can be determined as

$$W_e = \int_{h_r}^{h_m} P_u dh \quad (12)$$

From Eqs. (10) to (12), the unloading work is obtained as follows:

$$W_e = \int_{h_r}^{h_m} P_u dh = \sigma_y h_m^3 \Pi_2^2\left(\frac{E_r}{\sigma_y}, n, \alpha, \frac{\sigma_R}{\sigma_y}\right) \quad (13)$$

Combining Eqs. (7) and (13) leads to

$$\frac{W_e}{W_t} = \Pi_2\left(\frac{E_r}{\sigma_y}, n, \alpha, \frac{\sigma_R}{\sigma_y}\right) \quad (14)$$

Same as the expression of the loading work in Eq. (7), the unloading work of indentation can also be expressed as the following equation, where W_t is replaced by W_e and the term $(h_m - 0)^3$ is replaced by $(h_m - h_r)^3$:

$$W_e = \sigma_y (h_m - h_r)^3 \Pi_3\left(\frac{E_r}{\sigma_y}, n, \alpha, \frac{\sigma_R}{\sigma_y}\right) \quad (15)$$

The unloading work then can be normalized and expressed in an alternative form as

$$\frac{W_e}{\sigma_y (h_m - h_r)^3} = \Pi_3\left(\frac{E_r}{\sigma_y}, n, \alpha, \frac{\sigma_R}{\sigma_y}\right) \quad (16)$$

Concerning the contact stiffness of indentation S, it is defined as the initial slope of the unloading curve, which can be obtained from Eq. (10) as follows:

$$S = \left.\frac{dP_u}{dh}\right|_{h=h_m} = \sigma_y h_m \Pi_4\left(\frac{E_r}{\sigma_y}, n, \alpha, \frac{\sigma_R}{\sigma_y}\right) \quad (17)$$

Alternatively, Eq. (17) is written as

$$\frac{S}{\sigma_y h_m} = \Pi_4\left(\frac{E_r}{\sigma_y}, n, \alpha, \frac{\sigma_R}{\sigma_y}\right) \quad (18)$$

The four dimensionless functions Π_1, Π_2, Π_3, and Π_4, which correlate the residual stress and material properties with the characteristic parameters of indentation load-depth curves, can be determined by using the results obtained from either experiment of FE analyses. In this study, the FE analyses were conducted and from the obtained dimensionless functions, the residual stress, the yield strength, the strain hardening exponent, and the ratio α can be estimated once the elastic modulus is known.

2.2. Finite element simulations

The nonlinear finite element analysis program ABAQUS [25] was used to simulate the indentation process of structural steel with equi-biaxial residual stress. Considering symmetric conditions, an axisymmetric two-dimensional FE model was adopted. The matrix was modeled as a large cylinder with a radius and height equal or fifty times larger than the contact radius at maximum penetration depth. These dimensions were found to be large enough to approximate a semi-infinite half-space for indentation [26]. A fine mesh near the contact region and a gradually coarser mesh further from the contact region were designed to ensure numerical accuracy and save computational time, leading to a mesh of 10000 four-node bilinear axisymmetric quadrilateral elements CAX4R. At the maximum load, the minimum number of contact elements in the contact zone was ensured to have no less than 16 elements in each FE analysis. Prior to the indentation, an equi-biaxial residual stress (σ_R) was introduced into the specimen by applying pre-stress on the whole specimen along the radial direction. The boundary conditions were applied as follows. The nodes along y axis (the axis of rotation) can move only along the axis itself, and all the nodes on the bottom of the mesh were fixed. The indenter was modeled as a rigid movable cone surface with a half apex angle of 70.3°, and Coulomb's friction behavior was used for the contact between the indenter and the matrix surface. The indentation was displacement controlled with a maximum depth of 2000 nm for all analyses. More than 500 increments were used for both the loading and unloading processes in order to obtain sufficiently smooth P-h curves. Fig. 4 shows the simulation of the indentation process.

To formulate the four dimensionless functions Π_1, Π_2, Π_3, and Π_4, FE analyses were carried out for 400 combinations of different properties, in which the ratio of E/σ_y varied from 50 to 1000 with σ_y varied from 200 to 500, n varied from 0 to 0.5, α varied from 2 to 23, and the ratio of σ_R/σ_y varied from −0.8 to 0.8. The specific values are listed in Table 1. Note that the minus value of σ_R/σ_y indicates compression, and the above ranges cover most combinations of properties and residual stresses for structural steels. For convenience, Poisson's ratio was fixed at 0.3 for all FE analyses since it is a minor factor during indentation process.

3. Finite element analysis results

3.1. Numerical indentation responses

Fig. 5 presents a number of selected indentation curves from numerical analyses, where the effect of residual stress (normalized by σ_R/σ_y ratio), E/σ_y ratio, n, and α on the indentation load-depth curves are shown. As can be seen in Fig. 5a, to indent a given material (i.e., fixed E, σ_y, n and α) to the same depth, a residual tensile stress requires a lower indentation load, whereas a residual compressive stress requires a higher indentation load compared to unstressed material. Moreover, the greater the residual compressive stress intro-

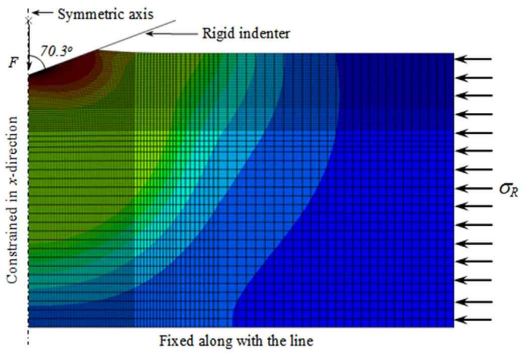


Fig. 4. FE simulation of indentation process.

Table 1
Material properties and residual stresses used for FE analyses.

	E/σ_y	n	α	σ_R/σ_y
400 Combinations of material properties	50	0	2	−0.8
	100	0.15	12	−0.4
Poisson's ratioυ = 0.3	400	0.30	23	0
	700	0.50		0.4
	1000			0.8

duced, the higher indentation load is required, and the greater the residual tensile stress introduced, the less indentation load is required to penetrate the material to the same depth. The effect of the E/σ_y ratio on indentation curves is investigated in Fig. 5b, where other material parameters are fixed and the E/σ_y ratio varied from 50 to 1000 (with σ_y =250 MPa). It is revealed from this figure that when the residual stress and other material properties are fixed, a higher elastic modulus leads to a higher indentation load and larger residual impression depth due to smaller elastic recovery. Similarly, for fixed material properties and a given residual stress, the indentation load for the same maximum penetration depth increases with increasing the strain hardening exponent n, as indicated in Fig. 5c. In contrast, the indentation load for the same maximum penetration depth decreases with increasing the α value when the residual stress and other material properties and are fixed, as illustrated in Fig. 5d. It can also be recognized from this figure that the effect of α on indentation curves tends to decrease when its value is large. Additionally observed from Fig. 5 is that the residual stress, n, and α seem have a minor influence on the contact stiffness, which is defined as the initial slope of the unloading curve, while the change of E leads to a variation of contact stiffness due to the fact that this indentation parameter and the elastic modulus of material are proportional [26].

3.2. Dimensionless functions

The functional forms of Π_1, Π_2, Π_3, and Π_4 in Eqs. (8), (14), (16), and (18), respectively, are constructed using the results obtained from the 400 FE analyses. It is found that the left terms of these four functions are well described by two dimensional third order polynomial equations of E_r/σ_y and σ_R/σ_y at the specific values of n and α. Fig. 6 shows representative fitting surfaces of Π_1, Π_2, Π_3, and Π_4 as the functions of E_r/σ_y and σ_R/σ_y at the fixed values of n =0.15 and α=12, where the dots are the data obtained from FE analyses.

Similarly, the left terms of the four dimensionless functions are also found to be well described by two dimensional third order polynomial equations of n and α at the specific values of E_r/σ_y and σ_R/σ_y. Fig. 7 shows representative fitting surfaces of Π_1, Π_2, Π_3, and Π_4 as the functions of n and α at the fixed values of E_r/σ_y =700 and σ_R/σ_y =0.8,

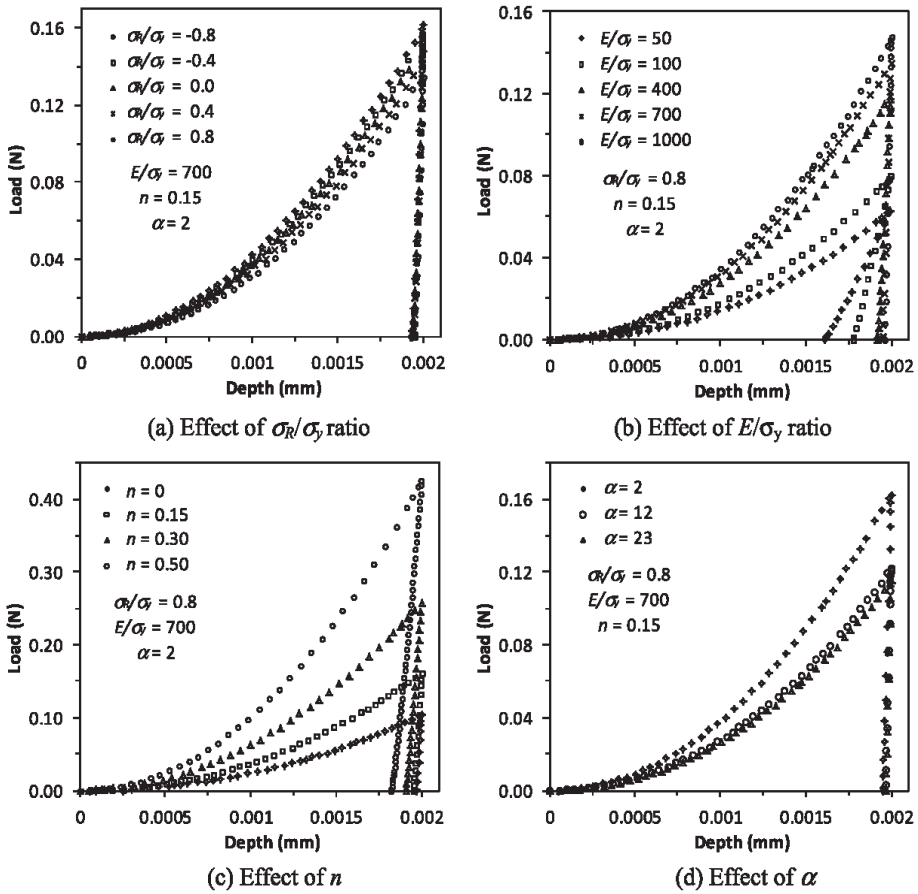


Fig. 5. Effects of material parameters on indentation load-depth curves. (a) Effect of σ_R/σ_y ratio (b) Effect of E/σ_y ratio (c) Effect of n (d) Effect of α.

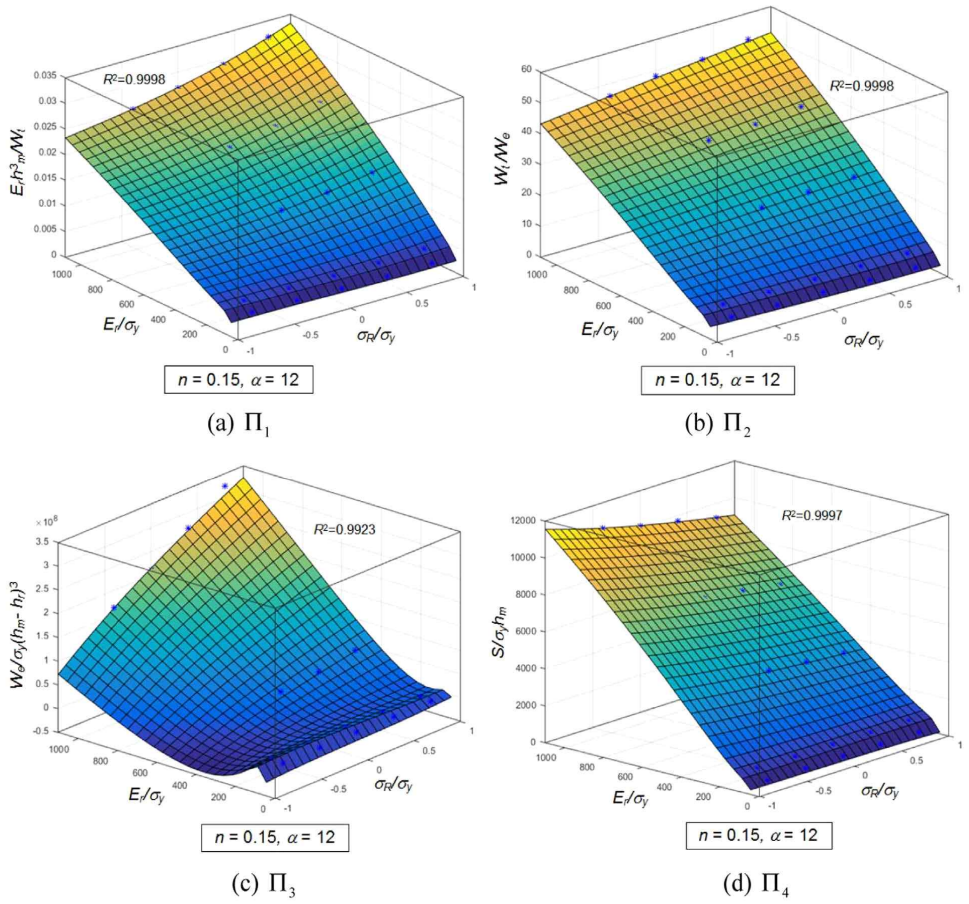


Fig. 6. Fitting surfaces of Π_1, Π_2, Π_3, and Π_4 as the functions of E_r/σ_y and σ_R/σ_y at the fixed values of n =0.15 and α=12. (a) Π_1 (b) Π_2 (c) Π_3 (d) Π_4.

where the dots are the data obtained from FE analyses.

Based on these observations, the four dimensionless functions of Π_1, Π_2, Π_3, and Π_4 are then obtained by fitting all data from 400 FE analyses in the combined forms of two dimensional third order polynomial equations of E_r/σ_y and σ_R/σ_y as well as of n and α, as follows:

$$\frac{E_r h_m^3}{W_t} = \Pi_1\left[ln\left(\frac{E_r}{\sigma_y}\right), \frac{\sigma_R}{\sigma_y}, n, \alpha\right] = \Pi_1(\xi, \lambda, n, \alpha)$$
$$= (a_1 + a_2\xi + a_3\lambda + a_4\xi^2 + a_5\xi\lambda + a_6\lambda^2 + a_7\xi^3 + a_8\xi^2\lambda + a_9\xi\lambda^2 + a_{10}\lambda^3)$$
$$(a_{11} + a_{12}n + a_{13}\alpha + a_{14}n^2 + a_{15}n\alpha + a_{16}\alpha^2 + a_{17}n^3 + a_{18}n^2\alpha + a_{19}n\alpha^2) \quad (19)$$

$$\frac{W_t}{W_e} = \Pi_2\left[\ln\left(\frac{E_r}{\sigma_y}\right), \frac{\sigma_R}{\sigma_y}, n, \alpha\right] = \Pi_2(\xi, \lambda, n, \alpha)$$
$$= (b_1 + b_2\xi + b_3\lambda + b_4\xi^2 + b_5\xi\lambda + b_6\lambda^2 + b_7\xi^3 + b_8\xi^2\lambda + b_9\xi\lambda^2 + b_{10}\lambda^3)$$
$$(b_{11} + b_{12}n + b_{13}\alpha + b_{14}n^2 + b_{15}n\alpha + b_{16}\alpha^2 + b_{17}n^3 + b_{18}n^2\alpha + b_{19}n\alpha^2) \quad (20)$$

$$\frac{W_e}{\sigma_y(h_m - h_r)^3} = \Pi_3\left[\ln\left(\frac{E_r}{\sigma_y}\right), \frac{\sigma_R}{\sigma_y}, n, \alpha\right] = \Pi_3(\xi, \lambda, n, \alpha)$$
$$= (c_1 + c_2\xi + c_3\lambda + c_4\xi^2 + c_5\xi\lambda + c_6\lambda^2 + c_7\xi^3 + c_8\xi^2\lambda + c_9\xi\lambda^2 + c_{10}\lambda^3)$$
$$(c_{11} + c_{12}n + c_{13}\alpha + c_{14}n^2 + c_{15}n\alpha + c_{16}\alpha^2 + c_{17}n^3 + c_{18}n^2\alpha + c_{19}n\alpha^2) \quad (21)$$

$$\frac{S}{\sigma_y h_m} = \Pi_4\left[\ln\left(\frac{E_r}{\sigma_y}\right), \frac{\sigma_R}{\sigma_y}, n, \alpha\right] = \Pi_4(\xi, \lambda, n, \alpha)$$
$$= (d_1 + d_2\xi + d_3\lambda + d_4\xi^2 + d_5\xi\lambda + d_6\lambda^2 + d_7\xi^3 + d_8\xi^2\lambda + d_9\xi\lambda^2 + d_{10}\lambda^3)$$
$$(d_{11} + d_{12}n + d_{13}\alpha + d_{14}n^2 + d_{15}n\alpha + d_{16}\alpha^2 + d_{17}n^3 + d_{18}n^2\alpha + d_{19}n\alpha^2) \quad (22)$$

where $\xi = \ln(E_r/\sigma_y)$ and $\lambda = \sigma_R/\sigma_y$. The fitting coefficients a_i, b_i, c_i, and d_i are listed in Table 2.

4. Reverse analysis

4.1. Principle of reverse analysis

A reverse analysis algorithm is suggested for determining the four unknowns (σ_R, σ_y, n, and α) of structural steel from the four fitting functions (Π_1, Π_2, Π_3, and Π_4). Fig. 8 illustrates the flow chart of the proposed reverse analysis algorithm. From a load–penetration depth

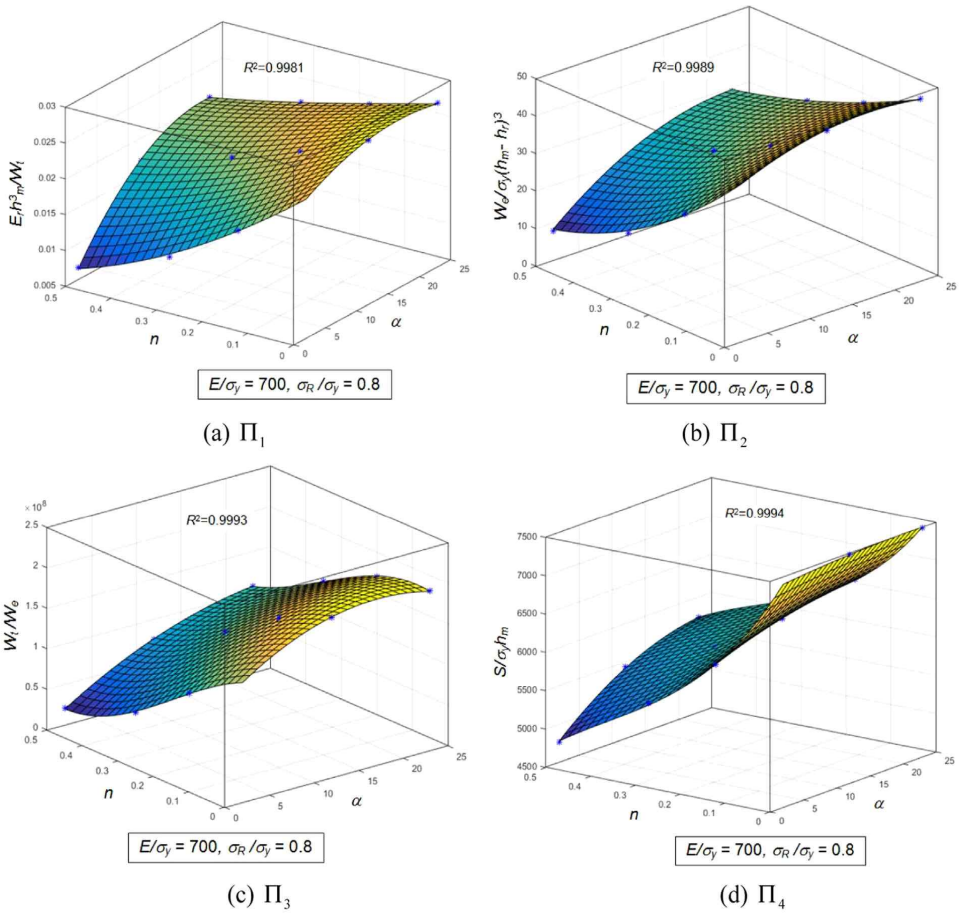


Fig. 7. Fitting surfaces of Π_1, Π_2, Π_3, and Π_4 as the functions of n and α at the fixed values of E_r/σ_y =700 and σ_R/σ_y =0.8. (a) Π_1 (b) Π_2 (c) Π_3 (d) Π_4.

Table 2
Coefficients of the four dimensionless Eqs. (19)–(22).

i	a_i	b_i	c_i	d_i
1	1.3641E −01	−2.1536E +00	−1.0782E +03	−1.0614E +02
2	−9.6358E −02	1.5015E +00	6.8603E +02	7.0062E +01
3	−3.4691E −02	3.9031E −01	1.6916E +02	−6.4594E +00
4	2.2353E −02	−3.5006E −01	−1.4386E +02	−1.5550E +01
5	1.6140E −02	−1.7593E −01	−7.1944E +01	2.8587E +00
6	4.4662E −03	−2.2539E −02	−2.8482E +01	1.0279E +00
7	−1.8240E −03	2.8803E −02	9.9499E +00	1.1832E +00
8	−1.8398E −03	1.9141E −02	7.5327E +00	−3.1759E −01
9	−1.2360E −03	6.5620E −03	6.3735E +00	−2.3778E −01
10	−3.5595E −04	−1.2232E −03	5.0158E −02	5.0408E −02
11	−3.9497E −01	4.7408E +01	9.5994E +04	2.0857E +02
12	9.4761E −01	−1.4770E +02	−1.6373E +05	−3.1408E +02
13	−9.0224E −03	1.2217E +00	4.5108E +03	3.8758E −01
14	−5.9092E −01	1.4179E +02	−3.1196E +05	4.3915E +02
15	−3.7991E −02	4.0390E +00	8.0033E +03	6.4779E +00
16	2.8073E −04	−3.7566E −02	−1.2652E +02	−1.1359E −02
17	−1.4738E −01	−2.6074E +01	5.3088E +05	−3.2378E +02
18	2.5839E −02	−4.0347E +00	−9.5116E +03	−3.1069E +00
19	4.0835E −04	−1.8752E −02	5.1523E +00	−9.0644E −02
R^2	0.9929	0.9941	0.9837	0.9993

curve of indentation experiment, the loading work W_t, unloading work W_e, residual impression depth h_r, maximum penetration depth h_m, and contact stiffness S can be easily measured and determined. The four unknowns (σ_R, σ_y, n, and α) are varied in wide ranges with appropriate increments. The errors of the four dimensionless functions Π_1, Π_2, Π_3, and Π_4 with respect to the measurements from the indentation test are calculated for each combination of residual stress and material properties. The summation of the absolute values of the four errors from Π_1, Π_2, Π_3, and Π_4 is considered as the total error, and the roots (σ_R, σ_y, n, and α) are found by selecting a combination of residual stress and material properties, which leads to the minimum value of the total error.

4.2. Numerical validation of the reverse algorithm

The effectiveness of the proposed reverse algorithm is first checked by using the indentation responses from the FE analyses. The characteristics of indentation load- depth curves (W_t, W_e, h_r, h_m, and S) obtained from the selected FE analyses with different combinations of material properties (E/σ_y, σ_R/σ_y, n, and α) are used as the input data of the reverse algorithm. Fig. 9 shows a comparison between the predicted material properties obtained from the reverse analysis and 25 combinations of input material properties in the numerical

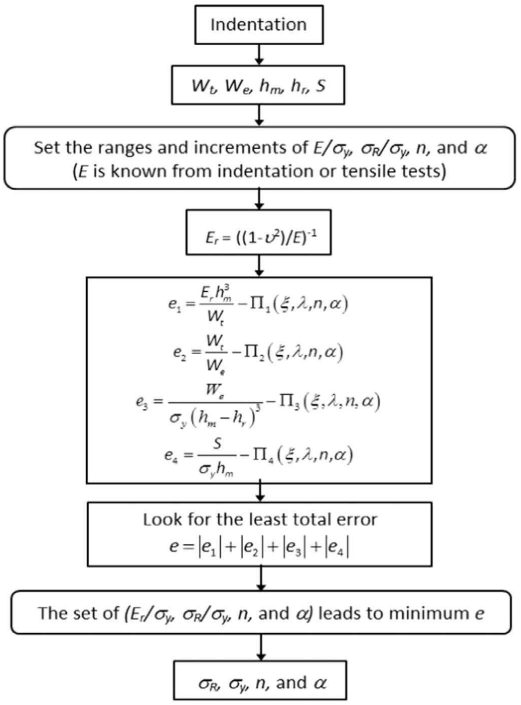


Fig. 8. Flow chart for proposed reverse analysis algorithm.

simulation, where n =0.15, α=12, E/σ_y varied from 50 to 1000, and σ_R/σ_y varied from −0.8 to 0.8. Fig. 10 presents a similar kind of comparison for 12 combinations of input material properties in the numerical simulation, where E/σ_y =700, σ_R/σ_y =0.8, n varied from 0 to 0.5, and α varied from 2 to 23. It is seen from these figures that all calculated combinations well match the input combinations, with all errors of each material property less than 6.5%. Note that the errors can be reduced by using smaller increments of E/σ_y, σ_R/σ_y, n, and α during the reverse analyses. The material properties presented in Figs. 9 and 10 were obtained using the increments of $\Delta E/\sigma_y$ =5, $\Delta\sigma_R/\sigma_y$ =0.01, Δn =0.001, and $\Delta\alpha$=0.5.

4.3. Experimental validation of the reverse algorithm

Two commonly used structural steels (SS400 and SM490) were used to verify the proposed reverse algorithm. The tensile tests were first carried out using an INSTRON testing machine to obtain the properties of SS400 and SM490 steels. The tests were conducted for three specimens of each steel type at room temperature in accordance with ASTM standard [27]. Table 3 lists the elastic modulus, yield strength, strain hardening exponent, and α values observed from the tensile tests of these steels.

Instrumented indentation tests were then performed to appraise the validity of the proposed reverse algorithm. A stress-applying apparatus was designed to allow the introduction of a compressive or tensile stress to the sample by applying a compressive or tensile force and maintaining the stress after releasing the force, as shown in Fig. 11. The operation of the apparatus includes the two following steps: (i) a compressive or tensile force is applied to the sample (by using compressive or tensile testing machine) to introduce a specific compressive or tensile stress into the sample, and (ii) the introduced compressive or tensile stress is then maintained in the sample by screwing in the movable compressive or movable tensile loading nuts, respectively. Note that the applied and maintained stress could be well-defined and measured by both the load cell and the strain gages attached on the sample. In the experiments, the introduced uni-axial stresses were kept lower than the elastic limit of the steels. Three groups of stress states including two different tensile stress levels and one free stress were applied for each material. Due to the limitations of the machine in compressive testing, the compressive pre-stress levels were not taken into consideration for the validity of the proposed algorithm. For the three investigated groups of stress states, nine indentation tests were undertaken for each group using a Nano Hardness Tester made by the Swiss Center for Electronics and Microtechnology. The indentation testing machine is equipped with a Berkovich indenter made of industrial diamond, which has an elastic modulus of 1141 GPa and Poisson's ratio of 0.07. Prior to introducing the stress and indentation tests, the testing surface on the sample was sufficiently polished to be flat and smooth according to the ASTM E3-01 standard [28]. All the indentation tests were performed in displacement control mode with a constant loading rate of 4000 nm/min to the prescribed maximum displacement of 2000 nm and the same unloading rate without holding time according to ISO 14577 and ASTM

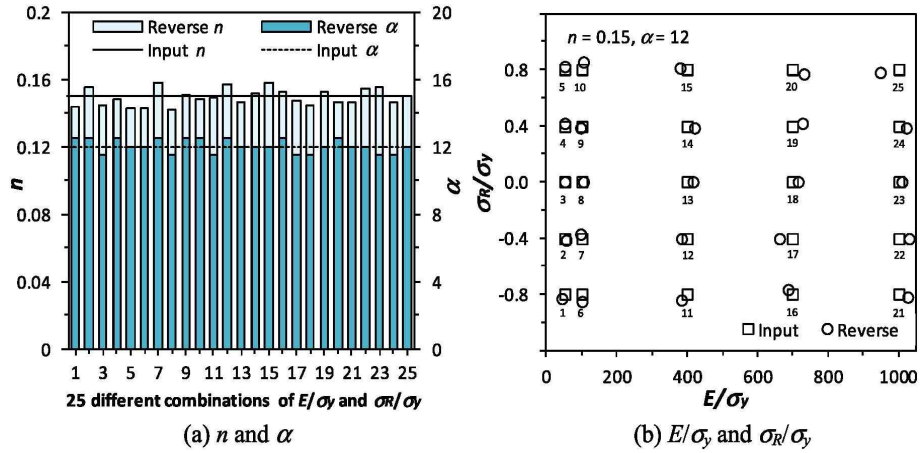


Fig. 9. Comparison between predicted material properties obtained from the reverse analysis and 25 combinations of input material properties (n =0.15, α=12, E/σ_y varied from 50 to 1000, and σ_R/σ_y varied from −0.8 to 0.8) used in the numerical simulation: (a) n and α; and (b) E/σ_y and σ_R/σ_y.

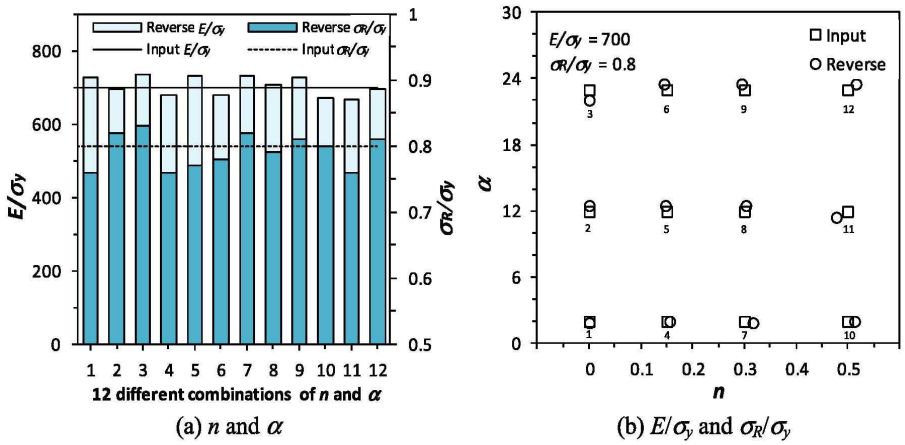


Fig. 10. Comparison between predicted material properties obtained from the reverse analysis and 12 combinations of input material properties (E/σ_y =700, σ_R/σ_y =0.8, n varied from 0 to 0.5, and α varied from 2 to 23) used in the numerical simulation: (a) n and α; and (b) E/σ_y and σ_R/σ_y.

Table 3
Mechanical properties averaged from three tensile tests of each material.

Materials	E (GPa)	σ_y (MPa)	n	α
SS400	198.6	313.6	0.243	9.8
SM490	208.9	395.2	0.230	12.1

E2546-07 standards [29,30]. The installation of the tensile test to introduce the stress into the sample is shown in Fig. 12a, and the indentation test setup is shown in Fig. 12b. Note that the depth of the indented sample at the testing area of 5 mm is large enough to approximate a semi-infinite half-space for indentation with the maximum penetration depth of 2000 nm and the properties of the investigated steels (composite) are always measured from the indentation with this maximum depth instead of the grain properties as indicated in the previous works [20,21].

As for the results, the nine load-penetration depth (P-h) curves obtained from each group of stress states exhibited minor differences from one another. Fig. 13 then presents only the mean curves at each stress level of the SS400 and SM490 to show the effects of residual stress on the indentation load-depth curves, where the solid curves represent the response of free stress materials. It is obvious that samples with the introduced tensile residual stress require less load than the free stress samples to reach to the same penetration depth; the higher the tensile residual stress, the less load is required.

Prior to the validation of the proposed algorithm, the accuracy of the developed FE model was verified by comparing the load-penetration depth curves obtained from FE analyses with those obtained from indentation experiments. The mechanical properties of SS400 and SM490 steels observed from tensile tests and the corresponding introduced residual stresses were used as the input data of the FE analyses. Fig. 14 shows the comparison between load-penetration depth (P-h) curves from FE analysis and selected indentation experiment of SS400 and SM490 steels at the highest stress level. Very good agreement between the FE analysis and selected experimental curves for both steels at the highest stress level can be observed from Fig. 14, indicating that the developed FE simulation is accurate to model the indentation of structural steels subjected to residual stress.

With regard to the total of 36 indentation tests on the 4 stressed samples (2 samples of SS400 and 2 samples of SM490), the indentation loading and unloading works (W_t and W_e), the maximum depth h_m, and the residual impression depth h_r were determined from each indentation curve. The initial unloading slope S value was calculated by first fitting 67% of unloading curve by a power law function $P_u = B(h - h_r)^m$ and then evaluating the derivative at $h = h_m$ [22,23]. These parameters obtained from the indentation tests of 4 groups with tensile residual stresses of both SS400 and SM490 steels are listed in Table 4. The obtained parameters from the indentation tests were then used as input data of the proposed reverse algorithm to calculate the material properties and residual stresses. To reduce the analysis time as well as to obtain the correct material properties and residual stresses, appropriate ranges of E/σ_y, σ_R/σ_y, n, and α were carefully selected and the corresponding fine increments of $\Delta E/\sigma_y$ =2, $\Delta\sigma_R/\sigma_y$ =0.01, Δn =0.001, and $\Delta\alpha$=0.1 were chosen for all reverse analyses. Since the elastic modulus values of the materials are known beforehand, the yield strength σ_y, strain hardening exponent n, α, and residual stress σ_R can be obtained from reverse analysis for all

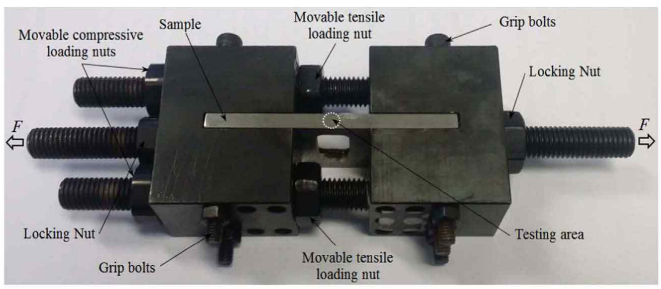
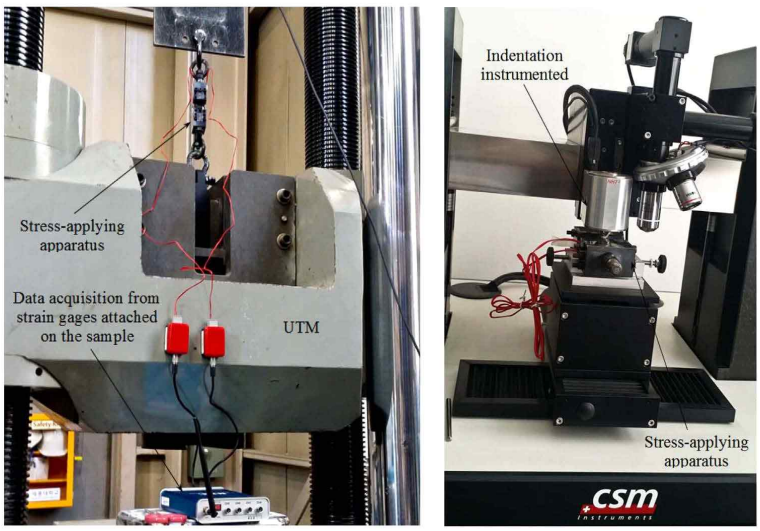


Fig. 11. Stress-applying apparatus.



(a) Tensile test for introduction of residual stress (b) Indentation test

Fig. 12. Installation of (a) tensile test for introduction of residual stress and (b) indentation test. (a) Tensile test for introduction of residual stress (b) Indentation test.

indentation tests on the stressed samples and are presented in Table 5. The relative errors of the material properties and residual stress values estimated using the proposed reverse algorithm when compared to the corresponding tensile properties and nominal introduced stresses of each material are also presented in this table. Note that since the equi-biaxial residual stress is equivalent to the half value of the uni-axial stress, as argued by Giannakopoulos [31], the residual stress values obtained from the reverse algorithm are a half of the final residual stress values listed in Table 5. It is clearly evident that not only the material plastic properties (σ_y, n, and α) but also the residual stress (σ_R) value can be well estimated from each indentation test of stressed samples for both steels. Most indentation tests on stressed samples of SS400 and SM490 steels exhibit relative errors within 15% for the yield strength and the strain hardening exponent, while most relative errors of the estimated α value and the residual stress are less than 20%. These relative error values are acceptable when compared with others results reported in the literature [14,18], and it is believed that the errors could be reduced by using smaller increments of E/σ_y, σ_R/σ_y, n, and α during the reverse analyses. By averaging the obtained material properties and residual stresses from nine indentation tests on each stressed sample, it is recognized that the averaged values of obtained material properties and residual stresses are in very good agreement with the properties observed from tensile tests and introduced stresses for both stress states of SS400 and SM490. Indeed, the relative errors between the averaged values of the obtained material properties and residual stresses from nine tests when compared to the corresponding tensile properties and nominal introduced stresses at each stress state of both materials are in the ranges of −2.3% to 5.5% for yield strength, −0.8% to 5.2% for strain hardening exponent, −2.4% to 6.2% for α value, and −1.5% to 2.7% for residual stress. This observation indicates that the proposed reverse algorithm could provide a good estimation of material properties as well as residual stress introduced in the material the by averaging the obtained values from a large number of indentation tests, specifically nine tests in the present study.

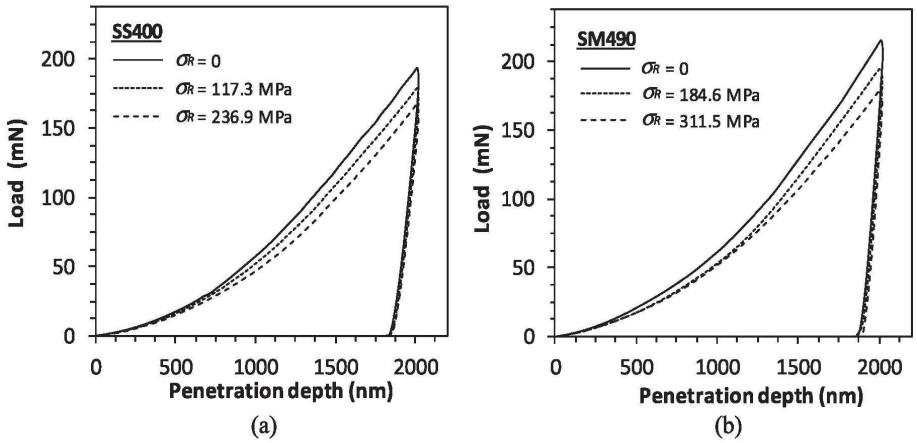


Fig. 13. Mean *P-h* curves of nine indentations in each stress state of (a) SS400 and (b) SM490.

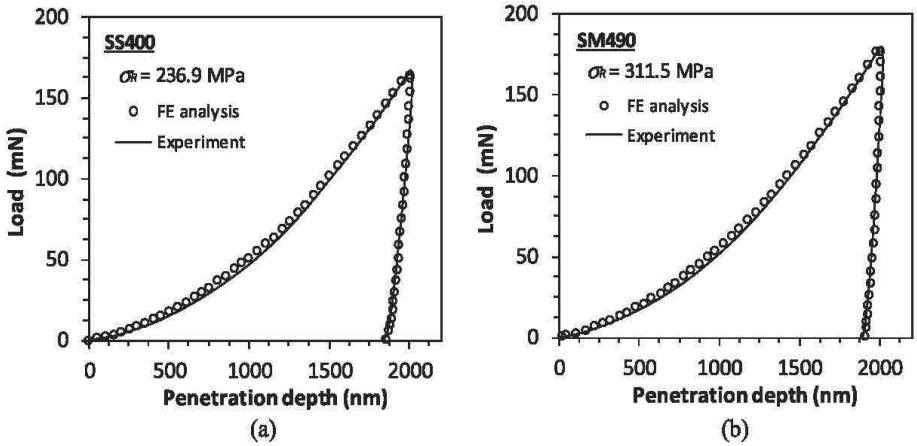


Fig. 14. Comparison between FE analysis and experimental *P-h* curves.

5. Conclusion

In this study, a method that allows estimation of the equi-biaxial residual stress, yield strength, the strain hardening exponent, and the α value of structural steel from the load-depth curve of one sharp indentation test is proposed. Based on the FE analysis results of the indentation process with a large number of different material properties combinations, the effects of residual stress and plastic parameters on the indentation response were investigated, and a reverse algorithm for estimating four unknown quantities (σ_R, σ_y, n, and α) of steel was established. A stress-applying apparatus was designed to allow for the introduction of a compressive or tensile stress to the sample by applying a compressive or tensile force and maintaining the stress after releasing the force. Indentation and tensile tests were performed on tensile stressed samples of SS400 and SM490 steels to verify the accuracy of the proposed reverse algorithm. For most indentation tests of two materials with different residual stress levels, the relative error of the reverse algorithm from a single indentation test is within 15% for material plastic properties (σ_y, n, and α) and less than 20% for residual stress σ_R. The error of the algorithm is demonstrated to be minimized by averaging the results obtained from a large number of indentation tests such as nine tests in this study. Indeed, the relative errors between the averaged values of obtained material properties and residual stresses from nine tests when compared to the corresponding tensile properties and nominal introduced stresses at each stress states of both materials are in the ranges of −2.3% to 5.5% for yield strength, −0.8% to 5.2% for strain hardening exponent, −2.4% to 6.2% for α value, and −1.5% to 2.7% for residual stress. The results indicate that the proposed reverse algorithm in this study can relatively accurately characterize the plastic parameters of structural steel and equi-biaxial residual stress introduced in the steel from indentation.

Acknowledgements

This research was supported by a grant (15CTAP-C098306-01) from the Technology Advancement Research Program funded by the Ministry of Land, Infrastructure and Transport of Korea.

Table 4
Indentation parameters of samples with tensile residual stresses.

	SS400					SM490				
	W_t (N.mm)	W_e (N.mm)	S (N/mm)	h_m (mm)	h_m (mm)	W_t (N.mm)	W_e (N.mm)	S (N/mm)	h_m (mm)	h_m (mm)
(a) σ_R = 117.3 MPa						**(a) σ_R = 184.6 MPa**				
Test 1	0.10893	0.00417	1824.6	0.002018	0.001866	0.13416	0.00587	1984.8	0.002018	0.001842
Test 2	0.10657	0.00393	1864.4	0.002020	0.001875	0.14567	0.00692	1969.7	0.002020	0.001826
Test 3	0.10721	0.00391	1863.0	0.002033	0.001888	0.12530	0.00492	2041.7	0.002033	0.001875
Test 4	0.11595	0.00463	1879.3	0.002018	0.001858	0.13997	0.00634	1992.6	0.002018	0.001833
Test 5	0.11695	0.00473	1881.2	0.002013	0.001851	0.12015	0.00468	2016.4	0.002013	0.001860
Test 6	0.11121	0.00415	1938.6	0.002018	0.001868	0.12825	0.00523	2047.0	0.002018	0.001853
Test 7	0.09955	0.00337	1898.0	0.002021	0.001888	0.11923	0.00445	2080.9	0.002021	0.001872
Test 8	0.10948	0.00429	1820.9	0.002003	0.001849	0.12040	0.00485	1961.3	0.002003	0.001845
Test 9	0.12236	0.00515	1867.4	0.002023	0.001855	0.14628	0.00686	2000.0	0.002023	0.001829
(b) σ_R = 236.9 MPa						**(b) σ_R = 311.5 MPa**				
Test 1	0.09480	0.00312	1867.0	0.002018	0.001892	0.11452	0.00423	2019.3	0.002018	0.001876
Test 2	0.98250	0.00396	1879.9	0.002022	0.001874	0.11083	0.00425	2041.7	0.002022	0.001872
Test 3	0.09996	0.00346	1863.9	0.002021	0.001889	0.11284	0.00403	2060.7	0.002021	0.001882
Test 4	0.96009	0.00360	1858.8	0.002021	0.001879	0.11716	0.00506	1991.8	0.002021	0.001862
Test 5	0.10418	0.00375	1875.8	0.002021	0.001884	0.10888	0.00381	2028.1	0.002021	0.001888
Test 6	0.09991	0.00355	1814.9	0.002022	0.001889	0.11899	0.00501	1953.4	0.002022	0.001859
Test 7	0.90999	0.00368	1859.1	0.002029	0.001884	0.11169	0.00422	2030.8	0.002029	0.001880
Test 8	0.99442	0.00410	1806.0	0.002015	0.001860	0.10290	0.00350	1978.3	0.002015	0.001888
Test 9	0.09120	0.00289	1869.1	0.002017	0.001897	0.11848	0.00452	2028.1	0.002017	0.001869

Table 5
Material properties and residual stress determined using proposed reverse algorithm.

		σ_y (MPa)	% err. σ_y	σ_R (MPa)	% err. σ_R	n	% err. n	α	% err. α
SS400	**(a) σ_R = 117.3 MPa**								
	Test 1	271.3	−13.5%	95.0	−19.0%	0.273	12.4%	7.8	−20.3%
	Test 2	306.5	−2.3%	137.9	17.6%	0.274	12.8%	9.4	−4.0%
	Test 3	278.2	−11.3%	102.9	−12.3%	0.270	11.2%	9.3	−5.0%
	Test 4	341.2	8.8%	122.8	4.7%	0.253	4.0%	10.7	9.2%
	Test 5	355.9	13.5%	113.9	−2.9%	0.259	6.4%	11.9	21.2%
	Test 6	347.2	10.7%	121.5	3.6%	0.209	−13.8%	10.9	11.0%
	Test 7	280.5	−10.6%	126.2	7.6%	0.232	−4.4%	9.5	−3.0%
	Test 8	288.7	−8.0%	92.4	−21.3%	0.276	13.6%	8.6	−12.3%
	Test 9	336.6	7.3%	131.3	11.9%	0.238	−2.0%	8.0	−18.0%
	Ave.	*311.8*	*−0.6%*	*116.0*	*−1.1%*	*0.254*	*4.5%*	*9.6*	*−2.4%*
	STDEV	*31.7*		*15.2*		*0.024*		*1.3*	
	COV[b]	*10.1%*		*13.0%*		*10.0%*		*13.3%*	
	(b) σ_R = 236.9 MPa								
	Test 1	273.6	−12.8%	199.7	−15.7%	0.235	−3.2%	9.5	−3.0%
	Test 2	363.7	16.0%	294.6	24.4%	0.222	−8.8%	11.0	12.0%
	Test 3	283.7	−9.5%	229.8	−3.0%	0.218	−10.4%	7.7	−21.0%
	Test 4	298.2	−4.9%	196.8	−16.9%	0.237	−2.4%	8.5	−13.0%
	Test 5	316.2	0.8%	240.3	1.5%	0.229	−5.6%	10.0	2.5%
	Test 6	293.8	−6.3%	273.2	15.3%	0.280	15.2%	11.1	13.0%
	Test 7	323.5	3.1%	274.9	16.1%	0.227	−6.4%	8.7	−11.0%
	Test 8	329.9	5.2%	260.6	10.0%	0.266	9.6%	9.2	−6.0%
	Test 9	275.8	−12.0%	220.7	−6.9%	0.245	0.8%	11.4	16.0%
	Ave.	*306.5*	*−2.3%*	*243.4*	*2.7%*	*0.240*	*−1.2%*	*9.7*	*−1.2%*
	STDEV	*28.7*		*33.3*		*0.020*		*1.2*	
	COV[b]	*9.2%*		*14.1%*		*8.1%*		*12.3%*	
SM490	**(a) σ_R = 184.6 MPa**								
	Test 1	442.9	12.1%	225.9	22.4%	0.272	18.4%	14.6	21.0%
	Test 2	452.4	14.5%	194.5	5.4%	0.259	12.8%	9.4	−22.0%
	Test 3	392.0	−0.8%	152.9	−17.2%	0.256	11.2%	13.9	15.0%
	Test 4	435.6	10.2%	183.0	−0.9%	0.239	4.0%	10.7	−11.6%
	Test 5	387.7	−1.9%	193.9	5.0%	0.245	6.4%	12.9	7.0%
	Test 6	435.6	10.2%	217.8	18.0%	0.214	−6.8%	13.2	9.0%
	Test 7	400.9	1.5%	208.5	12.9%	0.197	−14.4%	12.6	4.0%
	Test 8	350.5	−11.3%	140.2	−24.1%	0.270	17.6%	10.4	−14.0%
	Test 9	456.3	15.4%	196.2	6.3%	0.225	−2.0%	10.0	−17.0%
	Ave.	*417.1*	*5.5%*	*190.3*	*3.1%*	*0.242*	*5.2%*	*12.0*	*−1.0%*
	STDEV	*40.3*		*33.6*		*0.027*		*1.8*	
	COV[b]	*10.2%*		*18.2%*		*11.8%*		*14.6%*	
	(b) σ_R = 311.5 MPa								
	Test 1	366.3	−7.3%	256.4	−17.7%	0.223	−3.2%	11.3	−7.0%
	Test 2	410.3	3.8%	291.3	−6.5%	0.210	−8.8%	12.7	5.0%
	Test 3	382.1	−3.3%	263.7	−15.4%	0.206	−10.4%	13.1	8.0%
	Test 4	416.7	5.4%	333.4	7.0%	0.224	−2.4%	11.1	−8.0%
	Test 5	360.0	−8.9%	302.4	−2.9%	0.217	−5.6%	12.2	1.0%
	Test 6	433.8	9.8%	373.1	19.8%	0.274	19.2%	14.4	19.0%
	Test 7	426.8	8.0%	371.3	19.2%	0.215	−6.4%	14.2	17.0%
	Test 8	328.7	−16.8%	299.1	−4.0%	0.252	9.6%	12.5	3.0%
	Test 9	404.0	2.2%	270.7	−13.1%	0.232	0.8%	14.3	18.0%
	Ave.	*392.1*	*−0.8%*	*306.8*	*−1.5%*	*0.228*	*−0.8%*	*12.9*	*6.2%*
	STDEV	*33.2*		*41.5*		*0.021*		*1.4*	
	COV[b]	*8.4%*		*13.3%*		*9.0%*		*11.5%*	

a All errors were computed as $(X_{IT} - X_{exp})/X_{exp}$, where X_{IT} represents a variable.
[b] COV is the coefficient of variation.

References

[1] J. Lu, M.R. James (Eds.), Handbook of Measurement of Residual Stresses, Fairmount Press, Liburn, GA, 1996.
[2] K. Masubuchi, Analysis of Welded Structures: Residual StressesDistortion, and their Consequences, Pergamon Press, New York, 1980.
[3] I.C. Noyan, J.B. Cohen, Residual Stress; Measurement by Diffraction and Interpretation, Springer-Verlag, New York, 1987.
[4] V. Hauk, Structural and Residual Stress Analysis by Nondestructive Methods, Elsevier, New York, 1997.
[5] J. Jang, J. Ceram. Process. Res. 10 (3) (2009) 391–400.
[6] L. Xiao, D. Ye, C. Chen, Comp. Mater. Sci. 82 (2014) 476–482.
[7] T.Y. Tsui, W.C. Oliver, G.M. Pharr, J. Mater. Res. 11 (3) (1996) 752–759.
[8] A. Bolshakov, W.C. Oliver, W.M. Pharr, J. Mater. Res. 11 (3) (1996) 760–768.
[9] S. Suresh, A.E. Giannakopoulos, Acta Mater. 46 (16) (1998) 5755–5767.
[10] S. Carlsson, P.L. Larsson, Acta Mater. 49 (2001) 2179–2191.
[11] S. Carlsson, P.L. Larsson, Acta Mater. 49 (2001) 2193–2203.
[12] Y.H. Lee, D. Kwon, Scr. Mater. 49 (2003) 459–465.
[13] X. Chen, J. Yan, A.M. Karlsson, Mater. Sci. Eng. A 416 (2006) 139–149.
[14] M. Zhao, X. Chen, J. Yan, A.M. Karlsson, Acta Mater. 54 (2006) 2823–2832.
[15] Z.H. Xu, X. Li, Acta Mater. 53 (2005) 1913–1919.
[16] J. Yan, A.M. Karlsson, X. Chen, Int. J. Solids Struct. 44 (2007) 3720–3737.
[17] N. Huber, J. Heerens. Acta Mater. 56 (2008) 6205–6213.
[18] Z. Lu, Y. Feng, G. Peng, R. Yang, Y. Huan, T. Zhang, Mater. Sci. Eng. A 614 (2014) 264–272.
[19] T.H. Pham, J.J. Kim, S.E. Kim, Int. J. Mech. Sci. 90 (2015) 151–161.
[20] T.H. Pham, S.E. Kim, J. Constr. Steel Res. 114 (2015) 314–324.
[21] J.J. Kim, T.H. Pham, S.E. Kim, Int. J. Mech. Sci. 103 (2015) 265–274.
[22] W.C. Oliver, G.M. Pharr, J. Mater. Res. 7 (1992) 1564–1583.
[23] W.C. Oliver, G.M. Pharr, J. Mater. Res. 19 (1) (2004) 3–20.
[24] L. Brand, Arch. Ratio. Mech. 1 (1957) 35–45.
[25] Hibbitt, Karlsson, Sorensen, ABAQUS Standard User's Manual, version 6.6, Inc., 2006.
[26] M.Q. Le, Mech. Mater. 46 (2012) 42–56.
[27] ASTM E8/E8M-13a, Standard Test Methods for Tension Testing of Metallic, ASTM International, West Conshohocken, PA, 2013.
[28] ASTM E3-01, Standard Guide for Preparation of Metallographic Specimens, ASTM

International, West Conshohocken, PA, 2007.
[29] ISO 14577, Metallic Materials-Instrumented Indentation Test for Hardness and Materials Parameters, International Organization for Standarlization, Genenva, Switzerland, 2002.
[30] ASTM E2546-07, Standard Practice for Instrumented Indentation Testing, ASTM International, West Conshohocken, PA, 2007.
[31] A.E. Giannakopoulos, J. Appl. Mech. 70 (5) (2003) 638–643.

부록 3.

논문발표 성과

한국전산구조공학회
Computational Structural Engineering Institute of Korea

나노압입으로부터 구조용 강 미세구조의 부피 비를 파악하기 위한 확률적 방법

Probabilistic Approach to Identify Volume Fraction of Microstructures in Structural Steel from Nanoindentation

김 정 중[1] · 호안 팜 타이[2] · 김 승 억[3]

Kim, Jung Joong · Pham, Thai Hoan · Kim, Seung Eock

요 약

본 논문에서는 나노압입 결과로부터 얻은 구조용 강 미세구조의 기계적 특성을 확률적 방법으로 분석하여 부피 비를 파악하는 방법을 소개한다. 구조용 강의 서로 다른 부분에서 수행한 100회의 나노압입 결과로부터 얻은 미세구조의 탄성계수를 분석하여 빈도밀도함수(Frequency Density Function)를 구성한다. 이렇게 구성된 빈도밀도함수를 정규분포 함수들로 합성된 확률밀도함수(probability density Function)로 고려하고, 합성된 PDF를 분해 (deconvolution)하여 각각의 미세구조의 구성 성분피를 파악한다.

핵심용어 : 나노압입, 확률적 방법, 구성 성분비, 확률밀도함수, 디콘볼루션

1. 서 론

미세구조의 화학적 특성을 분석하는 다양한 방법이 개발되어 왔지만, 물리적인 특성, 즉 탄성계수나 강도를 결정하기는 쉽지 않다. 물질 표면의 경도를 조사하여 물질의 강도 및 강성과 비교하는 방법이 금속의 특성을 파악하기 위하여 100여년간 수행되어 왔다 (Hertz 1881). 콘크리트의 특성을 파악하기 위해서도 슈미트 햄머를 이용한 표면 강도는 콘크리트의 특성을 반영함을 알 수 있다. 이러한 이론적인 배경을 바탕으로 나노스케일의 압입시험기를 사용하여 물질을 구성하고 있는 미세구조의 물리적 특성을 파악할 수 있다. 나노압입 시 압입봉의 압입거리를 하중 재하 시와 제거 시에 Fig. 1과 같이 기록하고, 이를 분석하여 물질의 특성을 파악한다(Fischer Cripps 2004).

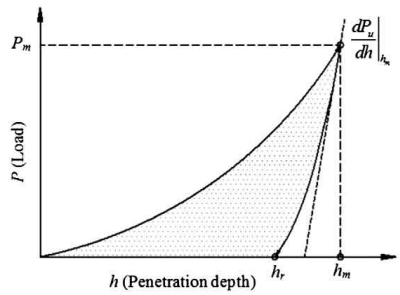


Fig. 1 Typical load-penetration depth curve

가장 많이 사용되는 압입봉의 형태는 삼각 피라미드 형태의 Berkovich tip, 반구형의 spherical 압입봉과 flat ended 압입봉 (Riccardia and Montanari 2004)이다. 다양한 물질에 적용되어 왔으며, 강재와 시멘트의 미세구조 파악에도 많이 사용되고 있다 (Pham et al. 2014; Mondal et al. 2007; Sorell et al. 2008). Berkovich압입봉은 각각의 미세구조를 개별적으로 압입할 수 있기 때문에 각각의 미세구조의 특성을 파악하는데 주로 사용된다. 반면, 구형 압입봉은 보다 넓은 면적을 압입하기 때문에 미세구조로 이루어진 복합체의 특성을 파악한다고 할 수 있다.

2. 본 론

2.1 나노압입

나노압입의 결과로 얻은 제하(unload) 압입깊이 곡선으로부터 탄성계수를 결정하는 방법은 올리버와 파르(Oliver and Pharr 1992)의 방법을 따른다. 이 밖에도 재하(load) 압입깊이 곡선과 제하(unload) 압입깊이 곡선을 모두 이용하여 구조용 강재의 항복강도, 경화지수 등 재료의 강도와 소성 특성을 파악할 수도 있다 (Pham et al. 2015).

[1] 정회원 • 경남대학교 토목공학과 교수 jungkim@kyungnam.ac.kr
[2] 세종대학교 건설환경공학과 pth.thebasic@gmail.com
[3] 세종대학교 건설환경공학과 교수 sekim@sejong.ac.kr

2.2 확률적 해석 방법

삼각 피라미드 형태의 Berkovich 압입봉을 사용하여 나노압입 실험을 수행하였을 경우, 각각의 압입 시 성질이 다른 미세구조를 압입했다고 볼 수 있다. 이 경우 수행된 N번의 실험에 의하여 결정된 N개의 탄성계수를 이용하여 탄성계수 빈도밀도함수를 구성할 수 있다. 빈도밀도함수는 식 (1)과 같은 n개의 정규분포함수의 합으로 이루어진 확률밀도함수로 고려할 수 있다.

$$p(E)=\sum_{i=1}^{n} f_i \frac{1}{\sigma_i\sqrt{2\pi}} exp\left(\frac{-(E-\mu_i)^2}{2\sigma^{2_i}}\right) \quad (1)$$

식에서 n은 미세구조의 수를 나타내며, f_i, σ_i, μ_i는 각각 i번째 미세구조의 부피 비, 탄성계수 표준편차, 탄성계수 평균값을 나타낸다. 식 (1)의 합성 확률밀도함수는 실험으로부터 얻은 탄성계수의 빈도밀도함수와 R^2값이 최대가 되도록 f_i, σ_i, μ_i를 결정하여 얻을 수 있다. 식 (1)이 결정되면 각 미세구조의 부피 비 f_i를 결정할 수 있다.

2.3 사례연구

SS400 구조용강에 100회의 나노압입을 수행하여 탄성계수를 측정하고, Fig. 2와 같이 확률적 방법으로 미세구조의 부피 비를 결정하였다.

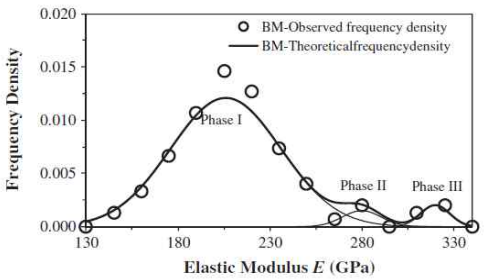


Fig. 2 Deconvolution of nanoindentation results for structural steel SS400 (Pham et al. 2014)

3. 결 론

본 연구에서는 나노압입 실험에 대하여 소개하고 그 결과로부터 얻은 미세구조의 탄성계수 분포를 확률적 방법으로 분석하여 미세구조의 부피 비를 파악하는 방법을 소개하였다. 나노압입 결과로부터 얻은 미세구조의 탄성계수를 분석하여 빈도밀도함수를 구성한다. 이를 정규분포 함수들로 합성된 확률밀도함수로 고려한 후, 회귀분석하여 각각의 미세구조의 구성 성분피를 파악한다.

감사의 글

본 연구는 국토교통부 국토교통기술촉진연구사업의 연구비 지원(15CTAP-C098306-01)에 의해 수행되었습니다.

Reference

Fischer-Cripps, A.C. (2004) Nanoindentation. New York, Springer Science+Business Media, LLC.

Hertz, H. (1881) On the Contact of Elastic Solids, J.Reine Angew. Math., 92, pp. 156-171.

Mondal, P., Shah, S. P., Marks, L. (2007) A reliable technique to determine the local mechanical properties at the nanoscale for cementious materials, Cement and Concrete Research, 37, pp. 1440-1444.

Oliver, W, Pharr, G. (1992) An improved technique for determining hardness and elastic modulus using load and displacement sensing indentation experiments, JournalofMaterialsResearch, 7(6), pp. 1564-1583.

Pham, T.-H., Kim, J.J., Kim, S.-E. (2014) Estimation of Microstructural Cpmpositions in the Weld Zone of Structural Steel Using Nanoindentation, Journal of Constructional Steel Research, 99, pp. 121-128

Pham, T.-H., Kim, J.J., Kim, S.-E. (2015) Estimating Constitutive Equation of Structural Steel Using Indentation, International Journal of Mechanical Science, 90, pp. 151-161

Riccardia, B. and Montanari, R. (2004) Indentation of Metals by a Flat-Ended Cylindrical Punch, Materials Science & Engineering A, 381, pp. 281-291.

Sorelli, L., Constantinides, G., Ulm, F.-J., Toutlemonde, F. (2008) The nano-mechanical signature of ultra high performance concrete by statistical nanoindentation techniques, Cement and Concrete Research, 38, pp. 1447-1456.

Indentation and FE Analysis for Characterization of Mechanical Properties in SM520 Steel Weld Zone

Thai-Hoan Pham[1], Ngoc-Vinh Nguyen[1], Viet-Hung Truong[1], Quang-Viet Vu[1], Viet-Linh Tran[2]
Seung-Eock Kim[1*]
[1]Dept. Of Civil and Environmental Engineering, Sejong University, Seoul, South Korea.
[2]Dept. Of Civil Engineering, Vinh University, Vinh city, Vietnam.
[*]Corresponding author, Dept. Of Civil and Environmental Engineering, Sejong University, 98 Gunjia-dong, Gwangjin-ku, Seoul, 143-747, South Korea.
pth.thebasic@gmail.com, vinhnguyen@sju.ac.kr, truongviethung82@sju.ac.kr, vietvq@vimaru.edu.vn, vietlinh.dhv@gmail.com, sekim@sejong.ac.kr

***Abstract*— Mechanical properties in the weld zone of a popular structural steel SM520 were characterized using indentation and finite element (FE) analysis. Indentation tests were performed across the weld zone including portions of weld metal (WM), base metal (BM), and heat-affected zone (HAZ). Hardness (H), elastic modulus (E), yield strength (σy), and strain hardening exponent (n) were extracted from indentation load-depth curve with the aid of FE analysis. The results showed that H, E, σ_y, and n values in the HAZ decrease in the direction from WM to BM region, the average values of H, E, σ_y, and n in HAZ are highest, whereas WM has a lower E but a higher H, σ_y, and n than does BM.**

Keywords: Indentation; Mechanical properties; SM520 steel; Weld Zone.

I. INTRODUCTION

Welding has been used as an advantageous method to form strong connection for transferring loads between members in steel structures. During the welding process, the temperature change causes solid-state phase transformations, which lead to three different main regions: fusion zone (weld metal-WM), heat-affected zone (HAZ), and base metal (BM) in the weld zone [1]-[3]. The performance of the weld joint is governed by the properties in WM, HAZ, and BM. Therefore, the mechanical properties in WM, HAZ, and BM including hardness (H), elastic modulus (E), yield strength (σ_y), and strain hardening exponent (n) need to be characterized, especially for the weld zone of SM520 steel, which is a very commonly used structural steel in Korea.

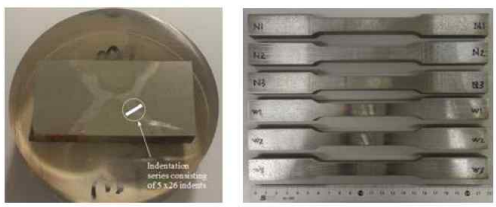
Indentation has been widely used in many engineering fields as a powerful tool for characterization of material properties [4]. While Oliver & Pharr's method is popular for extraction of H and E from the indentation test [5], a method proposed by the authors can be used for estimating σ_y and n of structural steels, which show plastic plateau in their stress-strain curve, from the load-depth curve of indentation [6]. Since indentation test allows accessing to the local properties in the indented area, it has been extensively utilized for investigating the properties of inhomogeneous materials such as steel weld zone.

This study aims to investigate the mechanical properties in the weld zone of SM520 steel by combining the aforementioned methods with the aid of FE analysis. For this purpose, indentation, tensile tests, and FE analysis were carried out.

II. EXPERIMENTAL DETAILS

Two SM520 steel plates with 12 mm thickness were welded in form of double V groove butt (12 mm of width and no root gap) by using metal arc welding. A slice cut across the weld and out from the welded plate was used for indentation specimen. The specimen surface was polished to be smooth and flat in order to reduce the error of indentation tests.

A series of indentation tests consisting of 5 x 26 indenting points was performed across the weld zone using a Nano Hardness Tester machine. The indenting series covered portions of weld metal, heat-affected zone, and base metal. Berkovich indenter made of diamond with elastic modulus of 1141 GPa and Poisson's ratio of 0.07 was employed. A fixed maximum load of 160 mN at a constant loading and unloading rate of 320 mN/min was applied for all indentation tests. Tensile tests were conducted by using an Instron testing machine for three specimens of SM520 (labeled N1, N2, and N3) and three welded specimens (W1, W2, and W3), which were cut out from the welded plate with the same dimensions as SM520 steel specimens. Fig. 1 shows specimens of indentation and tensile tests.



(a) (b)

Fig. 1. Specimens of (a) indentaion and (b) tensile tests.

Acknowledgements: This research was supported by a grant (15CTA P-C098306-01) from Technology Advancement Research Program funded by Ministry of Land, Infrastructure and Transport of Korean.

III. Procedure for Determination of Mechanical Properties from Indentation and FE Analysis

A. Determination of H and E

Fig. 2 illustrates a typical load-depth (*P-h*) curve.

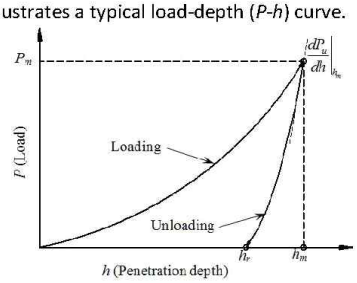


Fig. 2. Typical load-depth (*P-h*) curve.

Hardness and elastic modulus of indented material can be extracted from characteristics of the *P-h* curve, as follows [5]:

$$H = \frac{P_m}{A_c}, \tag{1}$$

$$E_r = \frac{\sqrt{\pi}}{2\beta}\frac{S}{\sqrt{A_c}}, \tag{2}$$

$$E_r = \left[\frac{1-\nu^2}{E} + \frac{1-\nu_i^2}{E_i}\right]^{-1}, \tag{3}$$

where P_m is the maximum applied load; A_c is the projected contact area; E_r is the reduced modulus; S is the initial unloading slope; β is the correlation factor for indenter shape; and E, υ, E_i, and υ_i are the elastic modulus and Poisson's ratio of the indented material and indenter, respectively.

B. Determination of σ_y and n in BM

A method proposed by the authors was used for extracting σ_y and n of structural steel from the *P-h* curve of indentation. In this method, σ_y and n can be determined with respect to α using the following polynomial equations [6]:

$$\frac{E_r^*}{\sigma_y} = \sum_{i=1}^{4}\sum_{j=1}^{4}\sum_{k=1}^{3} a_{ijk} n^{j-1} \alpha^{k-1} \left(\frac{E_r^*}{C}\right)^{i-1}, \tag{4}$$

$$\frac{S}{E_r^* h_m} = \sum_{i=1}^{4}\sum_{j=1}^{4}\sum_{k=1}^{3} b_{ijk} n^{j-1} \alpha^{k-1} \left[\ln\left(\frac{E_r^*}{\sigma_y}\right)\right]^{i-1}, \tag{5}$$

where α is defined as the ratio of the strain at starting point of strain hardening and the yield strain; C is the loading curvature; $E_r^* = \left[\left(1-\nu^2\right)/E\right]^{-1}$; and a_{ijk} and b_{ijk} are coefficients. Since the α value of BM can be obtained from the tensile test of SM520 steel, the proposed method was directly used for determining σ_y and n in BM of the weld zone. The further details of the method can be referred to the literature [5].

C. Determination of σy and n in HAZ and WM

Since the α value of HAZ and WM regions in the weld zone regions in the weld zone could not be obtained from tensile test of the welded specimens, while preparing mini- or micro-specimens from the weld zone that allows determining α value of the weld zones is a rather difficult task due to the small-size of the zones [7], FE analysis is now currently considered an appropriate approach. To obtain the α value of HAZ and WM, the FE analyses of indentation were performed using the nonlinear finite element analysis program ABAQUS [8] for correlating the experimental with the simulated load-penetration depth curves. The material model for structural steel that was used in the previous work was applied in this study [6]. For the set of simulated *P-h* curves, FE analyses were conducted for the total of 560 combinations of different material parameters, in which α varied from 3 to 9 (for every 1), σ_y varied from 325 to 550 (for every 25 MPa), and n varied from 0.18 to 0.25 (for every 0.01). Poisson's ratio was chosen to be 0.3 and elastic modulus of E = 206.3 GPa that was averaged from E values obtained from all indentation tests in HAZ and WM regions was used for all FE analyses. The above ranges of α, σ_y, and n were chosen after paying a special attention to α, σ_y, and n values observed in BM and doing some prior FE analyses in order to reduce the number of FE analyses. The loading part of *P-h* curve drawn up to 160 mN was compared with the experimental curves at the middle indenting column in HAZ and WM regions to determine the corresponding α values and the obtained value of α = 5 and α = 6 was considered the representative α value for HAZ and WM region, respectively. Once α value of HAZ and WM was estimated, the yield strength and strain hardening exponent in HAZ and WM could be determined using (4) and (5).

IV. Results and Discussions

A. Indentation response in the weld zone

The representative *P-h* curves in three regions of the weld zone are presented in Fig. 3. As is seen from this figure, the shape and magnitude of the *P-h* curves change significantly with the individual weld zone, signifying that the indentation response is highly sensitive to the metallurgical condition resulting during the welding. For the present weld zone, the maximum depth in HAZ is smallest, while the depth in BM is larger than that in WM.

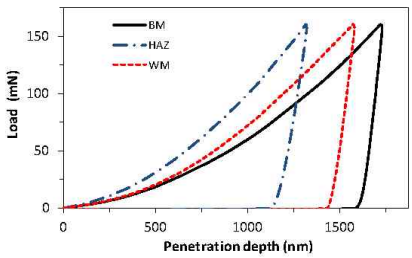
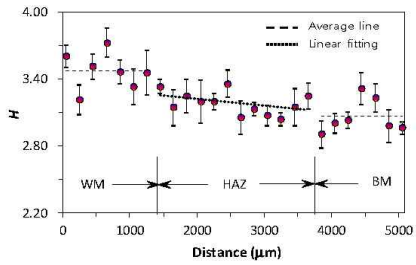


Fig. 3. Representative *P-h* curves in the weld zone.

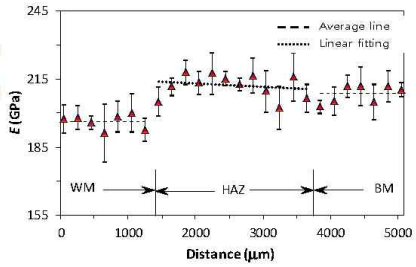
B. Mechanical properties in the weld zone

Fig. 4 shows the distribution of H, E, σ_y, and n across the weld zone, where each data is averaged from 5 values

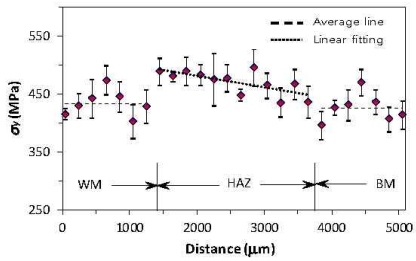
at each indenting column. The standard deviation of the data is also presented in the figure as an error bar. Note in this figure that the dashed lines represent the average values of all data points in the WM and BM regions, while the dotted line is the linear fitting of all values in HAZ regions. As the results, H, E, σ_y, and n values in HAZ gradually increase in the direction from BM to WM region. The average values of all properties in HAZ are highest, while WM has a lower stiffness but a higher hardness, strength, and strain hardening exponent than does BM, as shown in Table 1.



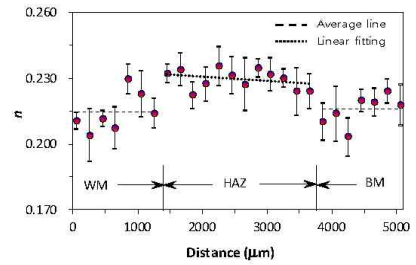
(a) Hardness



(b) Elastic modulus



(c) Yield strength



(d) Strain hardening exponent

Fig. 4. Mechanical properties in the weld zone.

Table 1: Mechanical properties obtained from indentation.

Location	H (GPa)	E (GPa)	σ_y (MPa)	n
BM	3.1	208.6	426.4	0.216
HAZ	3.2	212.2	470.9	0.230
WM	3.5	196.4	434.6	0.214

C. Verification

The results of E, σ_y, and n in BM obtained from indentations are recognized to be agreed well with the tensile test results of SM520 with a small relative error of -1.96%, 0.66%, and 7.46%, respectively, as listed in Table 2.

Table 2: Tensile test results of SM520 steel.

Test	Spe. No	E (GPa)	σ_y	n	α
Tensile	S1	214.4	423.6	0.203	5.9
	S2	212.2	421.7	0.193	6.4
	S3	211.7	425.6	0.207	6.3
	Ave.	212.7	423.6	0.201	6.2
Indentation	BM	208.6	426.4	0.216	
% error		*-1.96*	*0.66*	*7.46*	

To examine the results obtained from indentation tests in HAZ and WM regions, FE analysis of tensile test using ABAQUS program was conducted [8]. The steel and welded specimens for tensile tests were modeled using 8-node element C3D8R. The material model for structural steel used in the previous work [6] was used for the material properties definition of SM520 steel as well as of both HAZ and WM regions. The FE model was first verified by simulating the tensile test of SM520 steel. The properties of SM520 steel in Table 2 were used for the input data in this simulation. Fig. 5 shows the comparison of the failure mode and Fig. 6 shows the comparison of load-strain curve between simulation and experiment of SM520 steel specimen. Good agreement between both the simulated and experimental failure mode and load-strain curve observed from the figures indicates that the developed FE model can be used to accurately simulate the tensile test.



(a) Experiment



(b) FE simulation

Fig. 5. Failure mode of SM520 steel specimen.

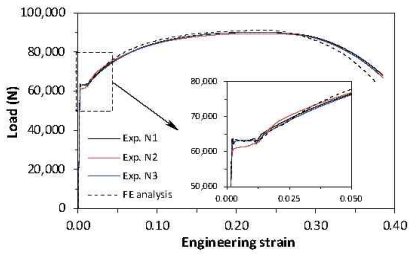
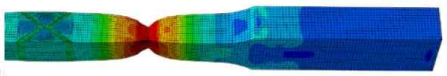


Fig. 6. Comparison of load-strain curve of steel specimen.

The tensile test of welded specimen was then simulated using the developed FE model. The weld portions including WM and HAZ regions were also taken into account and the mechanical properties obtained from indentation tests were used for the definition of the properties in these regions (see Table 1). Fig. 7 shows the comparison of the failure mode and Fig. 8 shows the comparison of load-strain curve between simulation and experiment of the welded specimen. Good agreement between both the simulated and experimental failure mode and load-strain curve observed from these figures indicates that the properties (E, σ_y, and n) determined from indentation tests in HAZ and WM regions are reliable and valid. Concerning the hardness, the values of H = 3.1 GPa, H = 3.2 GPa, and H = 3.5 GPa (Table 1) that represents to the hardness of BM, HAZ, and WM, respectively, are consistent with the related literature [1]-[3].



(a) Experiment



(b) FE simulation

Fig. 7. Failure mode of SM520 steel specimen.

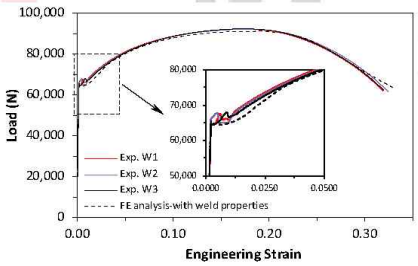


Fig. 8. Comparison of load-strain curve of welded specimen.

V. CONCLUSIONS

In this study, indentation with the aid of FE analysis was used for characterization of the mechanical properties in the weld zone of SM520 steel. Some following conclusions can be drawn from the test and analysis results:

The indentation responses in the weld zone are highly sensitive to the metallurgical conditions during the welding. The maximum penetration depth in HAZ is smallest, while the depth in BM is larger than that in WM.

The mechanical properties in the weld zone determined from the indentation tests with the aid of FE analysis were demonstrated to be valid and reliable by comparing with the results from tensile test, FE simulation, and other literature. For the present weld zone, the hardness, elastic modulus, yield strength, and strain hardening exponent values in the HAZ gradually decrease in the direction from WM to BM region. The average values of mechanical properties in HAZ are highest, while WM has a lower stiffness but a higher hardness, strength, and strain hardening exponent than does BM.

REFERENCES

[1] Z. Boumerzoug, C. Derfouf, and T. Baudin, "Effect of welding on microstructure and mechanical properties of an industrial low carbon steel" J. Eng., Vol. 2, pp. 502-506, 2010

[2] M. Eroglu, M. Aksoy, and N. Orhan, "Effect of coarse initial grain size on microstructure and mechanical properties of weld metal and HAZ of a low carbon steel", Mater. Sci. Eng. A, vol. 269, pp. 59-66, 1999.

[3] A. Gural, B. Bostan, and A.T. Ozdemir, "Heat treatment in two phase region and its effect on welding of a low carbon steel", Mater. Des., vol. 28 (3), pp. 897-903, 2007.

[4] B. Bhushan, Editor, "Handbook of nanotechnology", Springer, Berlin, 2007.

[5] W.C. Oliver and G.M. Pharr, "An improved technique for determining hardness and elastic-modulus using load and displacement sensing indentation experiments", J. Mater. Res., vol. 7, pp. 1564–1583, June 1992.

[6] T.H. Pham, J.J. Kim, S.E. Kim, "Estimating constitutive equation of structural steel using indentation", Int. J. Mech. Sci., vol. 90, pp. 151-161, April 2014.

[7] K.H. Chung *et al.*, "Characterization of mechanical properties by indentation tests and FE analysis – validation by application to a weld zone of DP590 steel", Inter. J. Solids Struct., vol. 46 (2), pp. 344-363, 2009.

[8] Hibbitt, Karlsson, and Sorensen, "ABAQUS Standard User's Manual", version 6.6, Inc., 2006.

Investigating the Relationship between Hardness and Yield Strength of SS400 Steel using Nanoindentation

Ngoc-Vinh Nguyen[1], Viet-Hung Truong[1], Thai-Hoan Pham[2], Seung-Eock Kim[3*]
[1]PhD Student, Dept. Of Civil and Environmental Engineering, Sejong University, Seoul, Korea.
[2]PhD, Dept. Of Civil Engineering, Vinh University, 182 Le Duan, Vinh City, Viet Nam.
[3]Professor, Dept. Of Civil and Environmental Engineering, Sejong University, 98 Gunja-dong, Gwangjin-gu, Seoul, 143-747, Korea.
vinhnguyen@sju.ac.kr, truongviethung82@sju.ac.kr, pth.thebasic@gmail.com, sekim@sejong.ac.kr

Abstract— In this study, Nano Hardness test was carried out at room temperature with different strain rates from 0.002 s^{-1} to 0.2 s^{-1},. A reverse algorithm was used to determine the yield strength from the load-displacement curve of the indentation test. From the obtained yield strength and hardness at different strain rates, the hardness-yield strength relationship was constructed.

Keywords: Hardness; Nanoindentation; Reverse algorithm; Yield strength.

I. INTRODUCTION

Structural steel is one of the most widely used materials in the bridge and building construction due to several advantages, such as the low cost and easy machinability and weldability. The hardness (H) and the yield strength (σ_y) are the important material properties of structural steels. In order to determine the hardness and yield strength, several tests must be carried out, such as the tensile, compressive, and indentation tests, in which the indentation test is a good choice since this test allows extracting both the hardness and yield strength of materials [1]-[3]. Furthermore, the indentation technique has several advantages, such as the short testing time and the low cost.

In early works, the relationship between hardness and yield strength has been constructed by combining the results from tensile and indentation tests [4], [5]. In these studies, the yield strength was obtained from the tensile test, while the hardness was obtained from indentation test. However, determining the H/σ_y ratio by using these both tensile and indentation tests is a high cost and time-consuming task. The relationship between hardness and yield strength was also investigated based on the open literatures for the indentation technique [6]. Although that method is acceptable, the inconsistent input data of the yield strength and hardness values are a limitation of the study because the hardness-yield strength correlation is constructed based on the data collected from seven different studies [6]. The yield strength now can be calculated by using a reverse algorithm for indentation technique [3].

The aim of this study is to investigate the relationship between the hardness and the yield strength by using indentation technique.

Acknowledgements: This research was supported by a grant (15CTAP-C098306-01) from Technology Advancement Research Program funded by Ministry of Land, Infrastructure and Transport of Korean government

II. METHODS

A. Determination of the Hardness

The hardness of the material can be extracted from the load-penetration depth curve of indentation, as follows [1]:

$$H = \frac{P_m}{A_c}, \quad (1)$$

where P_m is a maximum applied load, A_c is the projected contact area. In the indentation technique, the project area is calculated by using the following equation [2]

$$A_c = 24.5h_c^2 + c_1h_c^1 + c_2h_c^{1/2} + c_3h_c^{1/4} + ... + c_8h_c^{1/128}, \quad (2)$$

where h_c is the contact depth.

B. Determination of the Yield Strength

The true stress - strain curve of structural steel can be expressed as follows [3]:

$$\sigma = \begin{cases} E\varepsilon & (\varepsilon \le \varepsilon_y) \\ \sigma_y & (\varepsilon_y \le \varepsilon \le \varepsilon_{st}) \\ \sigma_y[1 + E(\varepsilon - \varepsilon_{st})/(\alpha\sigma_y)]^n & (\varepsilon \ge \varepsilon_{st}) \end{cases} \quad (3)$$

where ε_y is a yield strain, ε_{st} is the strain at the starting-point of strain hardening, α is a plastic property defined as the ratio of ε_{st} and ε_y, E is elastic modulus, and n is strain hardening exponent. The yield strength of structural steel can be determined from the indentation data by using a reverse algorithm, which consists of following dimensionless equations [3]

$$\frac{E_r^*}{\sigma_y} = \Pi_1 = \sum_{i=1}^{4}\sum_{j=1}^{4}\sum_{k=1}^{3} a_{ijk}.n^{j-1}.\alpha^{k-1}.\left(\frac{E_r^*}{C}\right)^{i-1} \quad (4)$$

$$\frac{S}{E_r^* h_m} = \Pi_2 = \sum_{i=1}^{4}\sum_{j=1}^{4}\sum_{k=1}^{3} b_{ijk}n^{j-1}\alpha^{k-1}\left[\ln\left(\frac{E_r^*}{\sigma_y}\right)\right]^{i-1}, \quad (5)$$

where a_{ijk} and b_{ijk} are coefficients, and C is the loading curvature calculated as $C = P_m / h_m^2$.

III. Experiments

A. Specimen Preparation

The specimen for the indentation test is a flat plate with a size of 20 mm x 12 mm x 8 mm. Fig. 1 shows the samples of SS400 steel after being mounted and polished.



Fig. 1. Specimen of structural steel after polishing.

B. Nano Hardness test

Nanohardness tests are carried out at room temperature using Continuous Stiffness Measurement (CSM) technique by controlling a loading strain rate. Berkovich indenter made of industrial diamond with an elastic modulus of 1140 GPa and Poison's ratio of 0.07 is imployed. The maximum displacement is 2000 nm, which is applied to all points during indentation tests.

IV. Results and Discussions

A. Load-Displacement curves

Fig. 2 presents the load-displacement curves of structural steel. The results show that the maximum load increases when the strain rate increases. From the indentation data that are extracted from the load-displacement curves, several material properties can be calculated, such as the hardness and the yield strength.

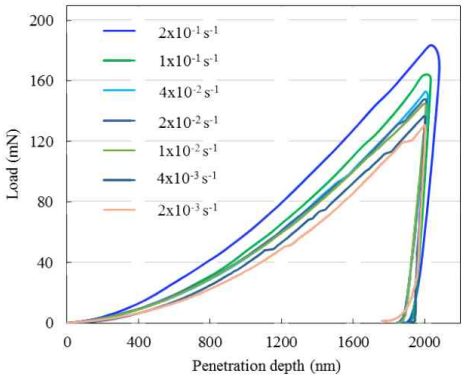


Fig. 2. The load-displacement curves of nanohardness test at different loading strain rates.

B. The Relationship between Yield Strength and Hardness

Fig. 3 shows the correlation between hardness and yield strength. The input data of this correlation are assembled from the hardness and the yield strength values at the different strain rates.

In this study, the relationship between hardness and yield strength is found to be described by an exponent equation as follows:

$$\sigma_y = a\, e^{bH}, \tag{6}$$

where a and b are material dependent constants, which are 71.12 and 0.00089, respectively.

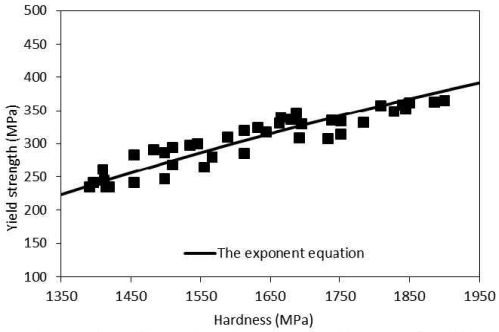


Fig. 3. The relationship between hardness and yield strength.

It can be recognized that (6) well describes the hardness-yield strength relationship with an R-square of 0.85. The correlation between hardness and yield strength constructed based on the indentation results is reliable and acceptable.

V. Conclusions

In this study, the nanoindentation test is performed on structural steel with different strain rate. The relationship between the hardness and the yield strength was investigated based on assembling the values of hardness and yield strength at different strain rates. The hardness-yield strength relationship can be described by an exponent equation.

REFERENCES

[1] Oliver WC, Pharr GM, "An improved technique for determining hardness and elastic-modulus using load and displacement sensing indentation experiments," J Mater Res, vol. 7, pp. 1564–1583, June 1992.

[2] Dao M, Chollacoop N, Van Vliet KJ, Venkatesh TA, Suresh S, "Computational modeling of the forward and reverse problems in instrumented sharp indentation," Acta Mater, vol. 49, pp. 3899–3918, Aug. 2001.

[3] Pham T-H, Kim J-J, Kim S-E, "Estimating constitutive equation of structural steel using indentation," Int J Mech Sci, vol. 90, pp. 151-161, April 2014.

[4] Cahoon JR, Broughton WH, Kutzak AR, "The determination of yield strength from hardness measurements," Metall Trans, vol. 2, pp. 1979–83, July 1971.

[5] Currey JD, Brear K, "Hardness, Young's modulus and yield stress in mammalian mineralized tissues," J Mater Sci Mater, vol. 1, pp. 14–20, June 1990.

[6] Busby JT, Hash MC, Was GS, "The relationship between hardness and yield stress in irradiated austenitic and ferritic steels," J Nucl Mater, vol. 336, pp. 267–278, Sep. 2004.

부록 4.

특허 성과

등록특허 10-1670064

(19) 대한민국특허청(KR)
(12) 등록특허공보(B1)

(45) 공고일자 2016년10월27일
(11) 등록번호 10-1670064
(24) 등록일자 2016년10월21일

(51) 국제특허분류(Int. Cl.)
G01N 3/04 (2006.01) *G01N 3/08* (2006.01)
G01N 3/42 (2006.01)
(52) CPC특허분류
G01N 3/04 (2013.01)
G01N 3/08 (2013.01)
(21) 출원번호 10-2015-0155799
(22) 출원일자 2015년11월06일
심사청구일자 2015년11월06일
(56) 선행기술조사문헌
KR1020110067475 A*
KR1020060070752 A*
KR1020060004429 A
KR1020130043951 A
*는 심사관에 의하여 인용된 문헌

(73) 특허권자
세종대학교산학협력단
서울특별시 광진구 능동로 209 (군자동, 세종대학교)
경남대학교 산학협력단
경상남도 창원시 마산합포구 경남대학로 7 (월영동, 경남대학교 내)
(72) 발명자
김승억
경기도 성남시 분당구 분당로 212, 201동 201호 (분당동, 샛별마을동성아파트)
김정중
경상남도 창원시 마산회원구 양덕로 120 금천빌딩 609호
(74) 대리인
특허법인(유)화우

전체 청구항 수 : 총 2 항 심사관 : 한별

(54) 발명의 명칭 **시험체의 잔류 응력 도입장치**

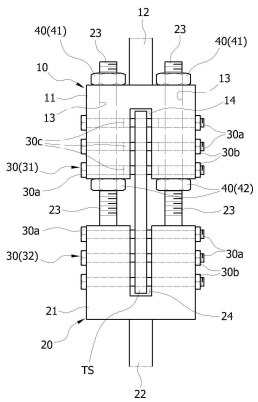
(57) 요 약

본 발명은 시험체의 잔류 응력 도입장치에 관한 것이다.

이를 위하여 본 발명은 몸체의 일단에 UTM을 체결하기 위한 제1 로딩바가 구비되고, 컬럼홀이 몸체의 길이방향으로 형성되며, 시험체가 구비되도록 몸체에 제1 안착홈이 마련되는 제1 파트와 몸체의 일단에 UTM을 체결하기 위한 제2 로딩바가 구비되고, 상기 컬럼홀을 관통하도록 서포팅 컬럼이 몸체의 길이방향으로 형성되며, 시험체가 구비되도록 제2 안착홈이 마련되는 제2 파트와 기 제1,2 파트에 시험체를 고정하는 홀딩수단 및 기 제1,2 파트를 상호 결합하는 고정수단을 포함하는 것을 특징으로 한다.

이로써, 시험체의 단면 위치와 무관하게 균일한 응력분포를 확보하여 추가적인 압입실험을 수행할 수 있다.

대 표 도 - 도2



(52) CPC특허분류
G01N 3/42 (2013.01)
G01N 2203/0016 (2013.01)
G01N 2203/0078 (2013.01)
G01N 2203/0423 (2013.01)

이 발명을 지원한 국가연구개발사업
과제고유번호 15CTAP-C098306-01
부처명 국토교통부
연구관리전문기관 국토교통과학기술진흥원
연구사업명 국토교통기술촉진연구사업
연구과제명 나노압입을 이용한 구조용 강재 용접부의 미세구조 파악 및 정량적 건전성 지표 개발 연구
기 여 율 1/1
주관기관 세종대학교 산학협력단
연구기간 2015.06.24 ~ 2017.06.23

명 세 서

청구범위

청구항 1

몸체(11)의 일단에 UTM을 체결하기 위한 제1 로딩바(12)가 구비되고, 컬럼홀(13)이 몸체(11)의 길이방향으로 형성되며, 시험체(TS)가 구비되도록 몸체(11)에 제1 안착홈(14)이 마련되되, 상기 컬럼홀(13)은 제1 안착홈(14)을 중심으로 대칭되게 상,하부에 각각 형성되는 제1 파트(10)와;

몸체(21)의 일단에 UTM을 체결하기 위한 제2 로딩바(22)가 구비되고, 상기 컬럼홀(13)을 관통하도록 서포팅 컬럼(23)이 몸체(21)의 길이방향으로 형성되며, 시험체(TS)가 구비되도록 제2 안착홈(24)이 마련되되, 상기 서포팅 컬럼(23)은 제2 안착홈(24)을 중심으로 대칭되게 상,하부에 각각 형성되는 제2 파트(20)와;

상기 제1 파트(10)의 몸체(11)와 시험체(TS)를 상하로 관통하는 복수의 제1 홀딩수단(31)과 제2 파트(20)의 몸체(21)와 시험체(TS)를 상하로 관통하는 복수의 제2 홀딩수단(32)으로 구성되되, 복수의 제1,2 홀딩수단(31)(32)은 제1,2 파트(10)(20)의 길이방향 중심축을 기준으로 대칭되게 구비되어 상기 제1,2 파트(10)(20)에 시험체(TS)를 고정하는 홀딩수단(30); 및

상기 제1,2 파트(10)(20)를 상호 결합하는 고정수단(40);을 포함하되,

상기 제2 파트(20)의 서포팅 컬럼(23)은 나사산(23a)이 형성되고, 상기 서포팅 컬럼(23)은 컬럼홀(13)을 관통하여 상기 고정수단(40)의 외측나사(41) 또는 내측나사(42)에 의하여 제1 파트(10)와 결합되어 인가된 압축력 또는 인장력을 바탕으로 형성된 잔류 응력이 고정되어 잔류 응력 도입장치를 분리할 수 있으며, 상기 제1 홀딩수단(31)은 서포팅 컬럼(23)과 간섭되지 않도록 구비되는 크로싱 바(30c)를 포함하되, 상기 크로싱 바(30c)는 상,하부에 구비된 한 쌍의 서포팅 컬럼(23) 사이에 구비되는 것을 특징으로 하는 시험체의 잔류 응력 도입장치.

청구항 2

삭제

청구항 3

삭제

청구항 4

삭제

청구항 5

삭제

청구항 6

제1항에 있어서,

상기 홀딩수단(30)은 크로싱 볼트(30a)와 상기 크로싱 볼트(30a)의 일단을 고정하기 위한 크로싱 너트(30b)로 구성되는 것을 특징으로 하는 시험체의 잔류 응력 도입장치.

청구항 7

삭제

발명의 설명

기 술 분 야

[0001] 본 발명은 시험체의 잔류 응력 도입장치에 관한 것으로, 보다 상세하게는 양단의 제1,2 로딩바를 UTM에 체결하여 외부하중을 인가하고, 서포팅 컬럼을 고정하여 시험체에 균일한 잔류 응력을 도입함으로써, 잔류 응력에 따른 추가적인 압입실험 결과의 차이를 연구하기 위한 시험체의 잔류 응력 도입장치에 관한 것이다.

배 경 기 술

[0002] 인덴테이션(indentation)이란, 시험체의 기계적 성질을 분석하기 위한 방법 중 하나로서, 다양한 형상의 다이아몬드 압입자를 재료에 압입한 후 그 압입자국과 압입 시의 하중을 비교, 분석하여 시험체의 경도나 파괴인성 등을 정밀하게 측정하기 위한 방법이다.

[0003] 한편, 상기 인덴테이션은 다양한 범주의 연구에 사용되고 있으며, 그 범주로서 시험체의 탄소성 거동, 잔류 응력상태의 해석, 박막의 응착력 시험, 파괴특성, 상변화 해석 등에 대한 연구기법으로도 널리 활용되고 있다. 특히, 최근에는 공학기술의 미세화와 소형화에 따라 나노인덴테이션(nanoindentation)의 실험방법이 개발된 바 있다.

[0004] 상기한 인덴테이션을 통한 잔류 응력상태의 해석을 수행하기 위해서는 시험체에 일정한 잔류 응력을 도입하여 잔류 응력이 유지된 상태를 확보하여야 한다.

[0005] 통상적으로 잔류 응력을 도입하기 위한 기구로서 UTM(Universal Testing Machine)을 사용하나, UTM에 고정된 시험체를 바탕으로 추가적인 압입실험을 수행하는 것에는 많은 제약이 따를 수 밖에 없었다.

[0006] 이에 대한민국 실용신안공보 제20-0312482호 '외부하중이 인가된 시편의 나노인덴테이션용 실험 치구'(2003. 04. 23. 등록, 이하 '선행기술문헌'이라 한다)가 제안된 바 있다.

[0007] 상기 선행기술문헌은 시험체에 가해지는 외부하중을 임의로 변화시키면서 이 외부하중이 유지된 상태로 나노인덴테이션 실험을 수행하고자 개발되었으나, 꺾임시험(bending test)을 통하여 외부하중을 인가하는바, 시험체의 단면 위치에 따라 선형의 인장력과 압축력 분포가 도입되어 균일한 응력분포를 확보할 수 없는 문제점이 있었다.

발명의 내용

해결하려는 과제

[0008] 본 발명은 상기한 문제점을 해결하기 위하여 안출된 것으로서, UTM을 이용하여 시험체에 외부하중을 인가하되, 추가적인 압입실험을 수행할 수 있도록 분리할 수 있으며, 시험체의 단면 위치와 무관하게 균일한 응력분포를 확보할 수 있는 시험체의 잔류 응력 도입장치를 제공하는데 그 목적이 있다.

과제의 해결 수단

[0009] 상기한 목적을 달성하기 위하여 본 발명은, 몸체(11)의 일단에 UTM을 체결하기 위한 제1 로딩바(12)가 구비되고, 컬럼홀(13)이 몸체(11)의 길이방향으로 형성되며, 시험체(TS)가 구비되도록 몸체(11)에 제1 안착홈(14)이 마련되되, 상기 컬럼홀(13)은 제1 안착홈(14)을 중심으로 대칭되게 상,하부에 각각 형성되는 제1 파트(10)와; 몸체(21)의 일단에 UTM을 체결하기 위한 제2 로딩바(22)가 구비되고, 상기 컬럼홀(13)을 관통하도록 서포팅 컬럼(23)이 몸체(21)의 길이방향으로 형성되며, 시험체(TS)가 구비되도록 제2 안착홈(24)이 마련되되, 상기 서포팅 컬럼(23)은 제2 안착홈(24)을 중심으로 대칭되게 상,하부에 각각 형성되는 제2 파트(20)와; 상기 제1 파트(10)의 몸체(11)와 시험체(TS)를 상하로 관통하는 복수의 제1 홀딩수단(31)과 제2 파트(20)의 몸체(21)와 시험체(TS)를 상하로 관통하는 복수의 제2 홀딩수단(32)으로 구성되되, 복수의 제1,2 홀딩수단(31)(32)은 제1,2 파트(10)(20)의 길이방향 중심축을 기준으로 대칭되게 구비되어 상기 제1,2 파트(10)(20)에 시험체(TS)를 고정하는 홀딩수단(30); 및 상기 제1,2 파트(10)(20)를 상호 결합하는 고정수단(40);을 포함하되, 상기 제2 파트(20)의 서포팅 컬럼(23)은 나사산(23a)이 형성되고, 상기 서포팅 컬럼(23)은 컬럼홀(13)을 관통하여 상기 고정수단(40)의 외측나사(41) 또는 내측나사(42)에 의하여 제1 파트(10)와 결합되어 인가된 압축력 또는 인장력을 바탕으로 형성된 잔류 응력이 고정되어 잔류 응력 도입장치를 분리할 수 있으며, 상기 제1 홀딩수단(31)은 서포팅 컬럼(23)과 간섭되지 않도록 구비되는 크로싱 바(30c)를 포함하되, 상기 크로싱 바(30c)는 상,하부에 구비된 한 쌍의 서포팅 컬럼(23) 사이에 구비되는 것을 특징으로 한다.

[0010] 삭제

[0011] 삭제

[0012] 삭제

[0013] 삭제

[0014] 또한, 상기 홀딩수단(30)은 크로싱 볼트(30a)와 상기 크로싱 볼트(30a)의 일단을 고정하기 위한 크로싱 너트(30b)로 구성될 수 있다.

[0015] 삭제

발명의 효과

[0016] 이상에서 설명한 바와 같이, 본 발명의 시험체의 잔류 응력 도입장치에 따르면, 양단에 제1,2 로딩바가 구비되어 UTM을 체결하여 시험체에 외부하중을 인가하고, 장치를 UTM으로부터 분리하여 추가적인 압입실험을 수행할 수 있다.

[0017] 또한, 서포팅 컬럼이 컬럼홀을 관통하여 외측나사와 내측나사에 의하여 제1 몸체와 고정되어 인가된 하중이 고정될 수 있다.

[0018] 나아가, 시험체의 단면 위치와 무관하게 균일한 응력분포를 확보할 수 있다.

도면의 간단한 설명

[0019] 도 1은 선행기술문헌에 따른 나노인덴테이션용 실험 치구를 개시한 개념도.

도 2는 본 발명의 일 실시예에 따른 시험체의 잔류 응력 도입장치를 개시한 정면도.

도 3은 본 발명의 일 실시예에 따른 시험체의 잔류 응력 도입장치를 개시한 분해 사시도.

도 4는 본 발명의 일 실시예에 따른 제1 파트를 개시한 단면 사시도.

도 5는 본 발명의 일 실시예에 따른 제2 파트를 개시한 단면 사시도.

도 6 내지 도 9는 본 발명의 일 실시예에 따른 시험체의 잔류 응력 도입장치의 사용방법을 순차적으로 도시한 사시도.

도 10은 본 발명의 일 실시예에 따른 시험체의 잔류 응력 도입장치의 사용상태도.

발명을 실시하기 위한 구체적인 내용

[0020] 이하, 본 발명에 대하여 첨부한 도면을 바탕으로 상세하게 설명한다.

[0021] 도 1은 선행기술문헌에 따른 시험체의 잔류 응력 도입장치를 도시한 것으로, 꺾임시험(bending test)을 통하여 외부하중을 인가하는바, 시험체의 단면 위치에 따라 선형의 인장력과 압축력 분포가 도입되어 균일한 응력분포를 확보할 수 없는 문제점이 있었다.

[0022] 이에 본 발명은 도 2에 도시된 바와 같이 제1,2 파트(10)(20)와 시험체(TS)를 고정하기 위한 홀딩수단(30)을 포함하는 시험체의 잔류 응력 도입장치를 제안한다.

[0023] 도 2에 도시된 바와 같이 상기 제1,2 파트(10)(20)는 몸체(11)(21)의 일단에 UTM을 체결하기 위한 제1,2 로딩바(12)(22)가 구비된다.

[0024] 도 10에 도시된 바와 같이 상기 제1,2 로딩바(12)(22)는 UTM에 체결된 상태에서 상호 외측으로 힘을 가하여 제

1,2 파트(10)(20)에 인장력을 가하거나, 상호 내측으로 힘을 가하여 제1,2 파트(10)(20)에 압축력을 가하게 된다.

[0025] 이후, 후술할 홀딩수단(30)에 의하여 고정된 시험체(TS)에 인장력이 가해지거나 압축력이 가해지게 된다.

[0026] 따라서, 본 발명은 꺾임시험이 아니라 축방향으로 하중을 가하는바, 시험체의 단면 위치와 무관하게 일정한 인장력과 압축력 분포가 도입되어 균일한 응력분포를 확보할 수 있다.

[0027] 이때, 상기 제1,2 로딩바(12)(22)는 나사산이 형성되어 UTM과 나사결합되는 것이 일반적이다.

[0028] 한편, 도 3에 도시된 바와 같이 상기 제1 파트(10)의 몸체(11)는 컬럼홀(13)이 길이방향으로 형성되고, 제2 파트(20)의 몸체(21)는 서포팅 컬럼(23)이 길이방향으로 형성되며, 상기 서포팅 컬럼(23)은 컬럼홀(13)을 관통하여 고정수단(40)에 의하여 결합됨으로써, 상기 제1,2 파트(10)(20)의 몸체(11)(21)가 상호 일체화된다.

[0029] 구체적으로, 상기 제2 파트(20)의 서포팅 컬럼(23)은 나사산(23a)이 형성되고, 상기 서포팅 컬럼(23)은 컬럼홀(13)을 관통하여 외측나사(41) 및/또는 내측나사(42)를 포함하는 고정수단(40)에 의하여 결합될 수 있다.

[0030] 상기 제1,2 파트(10)(20)에 인장력이 가해지면, 제1 몸체(11)의 내측에 구비된 내측나사(42)에 의하여 서포팅 컬럼(23)에 대한 제1 파트(10)의 몸체(11) 위치가 고정될 수 있으며, 반대로 압축력이 가해지면, 제1 몸체(11)의 외측에 구비된 외측나사(41)에 의하여 서포팅 컬럼(23)에 대한 제1 파트(10)의 몸체(11) 위치가 고정될 수 있다. 이로써, 시험체(TS)에 인가된 하중이 고정될 수 있다.

[0031] 또한, 도 4 및 도 5에 도시된 바와 같이 상기 제1,2 파트(10)(20)의 몸체(11)(21)는 각각 제1,2 안착홈(14)(24)이 형성되어 일정한 하중을 인가할 시험체(TS)가 구비된다. 따라서, 상기 제1,2 안착홈(14)(24)은 시험체(TS)에 편심이 작용되지 않도록 제1,2 파트(10)(20)의 몸체(11)(21) 중심에 구비되는 것이 바람직하다.

[0032] 한편, 상기 컬럼홀(13)과 서포팅 컬럼(23)은 제1,2 안착홈(14)(24)을 중심으로 대칭되게 상,하부에 각각 형성되어 시험체(TS)에 편심이 작용되는 것을 예방할 수 있다.

[0033] 이때, 상기 컬럼홀(13)과 서포팅 컬럼(23)는 상,하부에 대칭되게 형성되되, 상,하부에도 각각 복수의 컬럼홀(13)과 서포팅 컬림(23)이 대칭되게 형성되어 폭방향 편심을 방지할 수 있다.

[0034] 한편, 상기 홀딩수단(30)은 제1 파트(10)의 몸체(11)와 시험체(TS)를 상하로 관통하는 복수의 제1 홀딩수단(31)과 제2 파트(20)의 몸체(21)와 시험체(TS)를 상하로 관통하는 복수의 제2 홀딩수단(32)으로 구성될 수 있다.

[0035] 이때, 상기 제1,2 파트(10)(20)의 몸체(11)(21)에는 상기 복수의 제1,2 홀딩수단(31)(32)과 대응되도록 복수의 제1,2 관통홀(15)(25)이 형성될 수 있다.

[0036] 마찬가지로, 편심을 예방하기 위하여 상기 홀딩수단(30)의 복수의 제1,2 홀딩수단(31)(32)은 제1,2 파트(10)(20)의 길이방향 중심축을 기준으로 대칭되게 구비되는 것이 바람직하다.

[0037] 일 실시예로, 상기 홀딩수단(30)은 크로싱 볼트(30a)와 상기 크로싱 볼트(30a)의 일단을 고정하기 위한 크로싱 너트(30b)로 구성될 수 있으며, 각각의 홀딩수단(30)은 제1,2 안착홈(14)(24)에 구비된 시험체(TS)를 관통하여 고정할 수 있다.

[0038] 한편, 제1 파트(10)는 서포팅 컬럼(22)이 관통하는바, 상기 홀딩수단(30)의 제1 홀딩수단(31)은 서포팅 컬럼(23)과 간섭되지 않도록 크로싱 바(30c)를 포함할 수 있다.

[0039] 상기 크로싱 바(30c)는 상,하부에 구비된 한 쌍의 서포팅 컬럼(22) 사이에 구비될 수 있으며, 제1 파트(10)의 몸체(11)에 형성된 제1 관통홀(15) 중 일부는 하부가 개방되지 않은 크로싱 바 삽입홈(15a)이 형성되어, 상기 크로싱 바 삽입홈(15a)에 크로싱 바(30c)를 삽입할 수 있다.

[0040] 한편, 크로싱 바 삽입홈(15a)에는 나사산이 형성되고, 상기 크로싱 바(30c)는 핵사곤 소켓헤드 스크류볼트를 사용하여 내측에 나사결합이 형성되도록 제작할 수 있다.

[0041] 이하, 본 발명의 일 실시예에 따른 시험체의 잔류 응력 도입장치를 이용한 시험방법을 구체적으로 설명한다.

[0042] 도 6에 도시된 바와 같이 시험체(TS)를 제1 안착홈(14)에 안착시키고, 도 7에 도시된 바와 같이 시험체(TS)에 크로싱 볼트(30a) 및 크로싱 바(30c)를 포함하는 제1 홀딩수단(31)이 제1 몸체(11)의 제1 관통홀(15)을 관통되도록 삽입하고, 상기 크로싱 볼트(30a)는 크로싱 너트(30b)를 이용하여 고정한다.

[0043] 이후, 도 8에 도시된 바와 같이 시험체(TS)의 타측도 제2 안착홈(24)에 안착되도록 제2 파트(20)를 구비한다.

[0044] 시험체(TS)가 안착되면, 도 9에 도시된 바와 같이 제2 홀딩수단(32)의 크로싱 볼트(30a)를 상부에서 하부에로 관통시키고, 크로싱 너트(30b)를 이용하여 조임으로써, 시험체(TS)를 고정한다.

[0045] 시험체(TS)의 고정이 완료되면, 제1,2 파트(10)(20)의 제1,2 로딩바(12)(13)를 UTM에 고정하고, 외부하중을 인가한다.

[0046] 외부하중의 인가가 완료되면, 컬럼홀(13)을 관통한 서포팅 컬럼(23)을 고정수단(40)의 내,외측나사(41)(42)를 이용하여 하중에 의한 잔류 응력을 고정하게 된다.

[0047] 잔류 응력이 고정되면, UTM으로부터 본 발명의 시험체의 잔류 응력 도입장치를 분리하여, 추가적인 압입실험을 수행한다.

[0048]

[0049] 이상에서 설명한 본 발명에 따른 시험체의 잔류 응력 도입장치는 상기한 실시예에 한정되지 않고, 이하의 특허청구범위에서 청구하는 본 발명의 요지를 벗어남이 없이 본 발명이 속하는 기술분야에서 통상의 지식을 가진 자라면 누구든지 다양하게 변경하여 실시할 수 있는 범위까지 특허청구범위의 보호범위에 속하는 것으로 보아야 할 것이다.

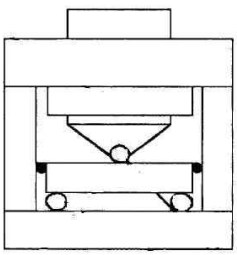
부호의 설명

[0050]

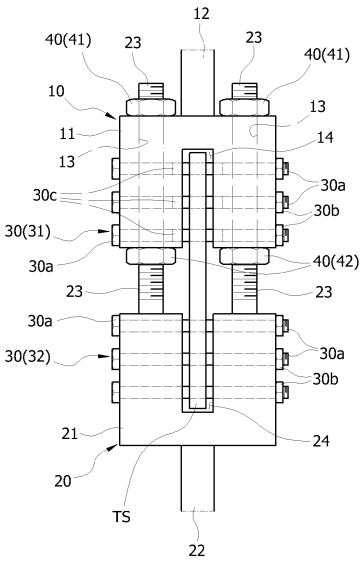
10:제1 파트	11:몸체
12:제1 로딩바	13:컬럼홀
14:제1 안착홈	15:제1 관통홀
20:제2 파트	21:몸체
22:제2 로딩바	23:서포팅 컬럼
24:제2 안착홈	25:제2 관통홀
30:홀딩수단	31:제1 홀딩수단
32:제2 홀딩수단	30a:크로싱 볼트
30b:크로싱 너트	30c:크로싱 바
40:고정수단	41:외측나사
42:내측나사	TS:시험체

도면

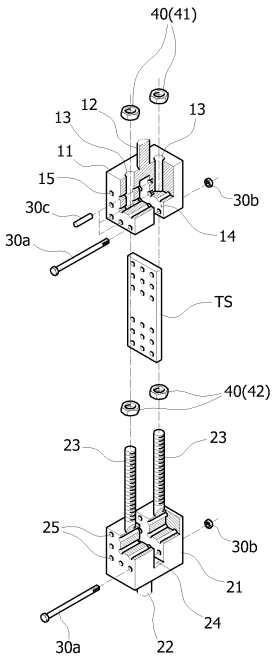
도면1



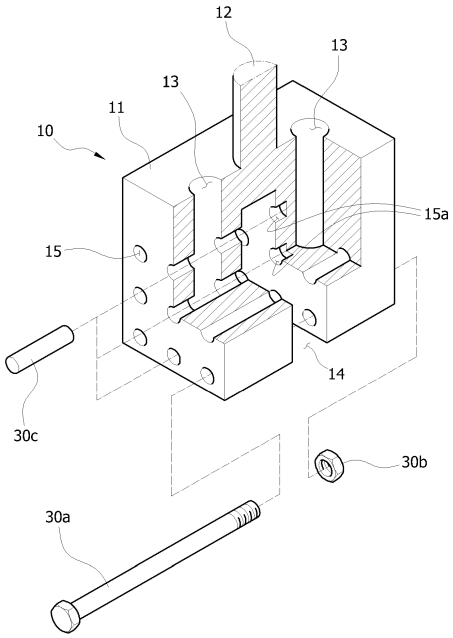
도면2


12
40(41)
23
23
40(41)
10
13
11
14
13
30a
30c
30b
30(31)
40(42)
30a
23
23
30a
30a
30(32)
30b
21
24
20
TS
22

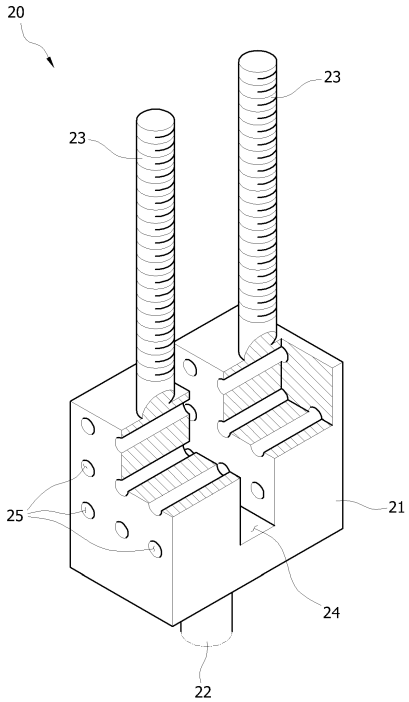
도면3


40(41)
12
13
13
11
15
30b
30c
14
30a
TS
40(42)
23
23
25
30b
21
24
30a
22

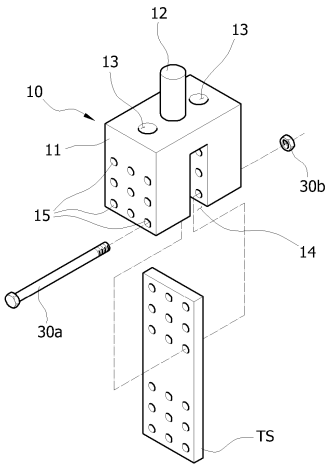
도면4



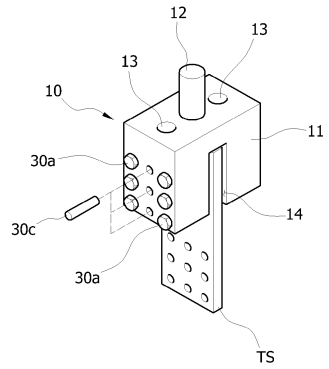
도면5



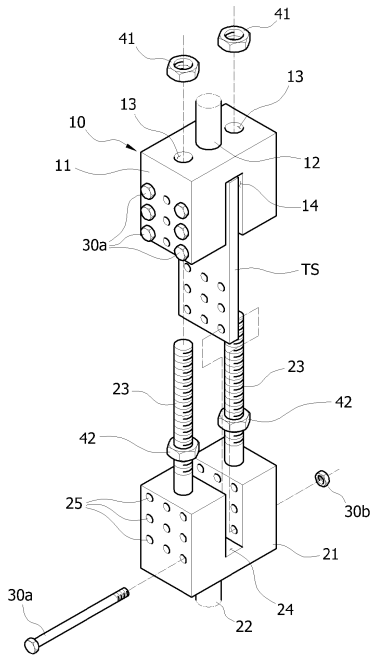
도면6



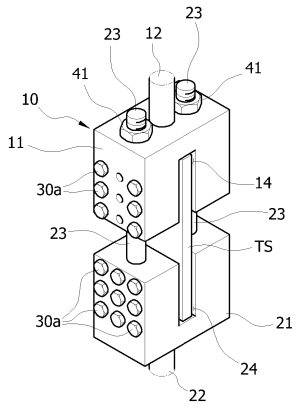
도면7


12
13
13
10
11
30a
14
30c
30a
TS

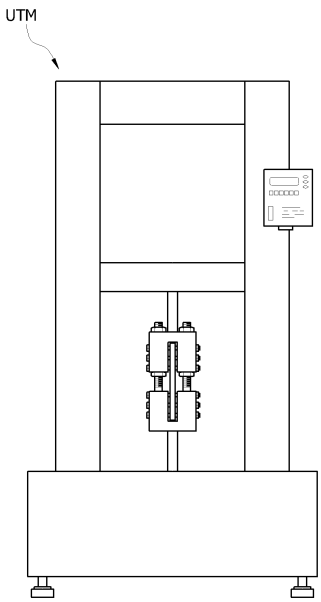
도면8


41
41
13
13
10
11
12
14
30a
TS
23
23
42
42
25
30b
21
30a
24
22

도면9



도면10



관 인 생 략

출 원 번 호 통 지 서

출 원 일 자	2017.04.25
특 기 사 항	심사청구(유) 공개신청(무) 참조번호(P2017217)
출 원 번 호	10-2017-0052870 (접수번호 1-1-2017-0404168-16)
출원인 명칭	세종대학교산학협력단(2-2005-011470-2) 외 1명
대 리 인 성 명	특허법인(유)화우(9-2006-100002-2)
발 명 자 성 명	김승억 김정중
발 명 의 명 칭	구조용 강재 용접부의 건전성 지표 결정 시스템 및 방법

특 허 청 장

<< 안내 >>

1. 귀하의 출원은 위와 같이 정상적으로 접수되었으며, 이후의 심사 진행상황은 출원번호를 통해 확인하실 수 있습니다.

2. 출원에 따른 수수료는 접수일로부터 다음날까지 동봉된 납입영수증에 성명, 납부자번호 등을 기재하여 가까운 우체국 또는 은행에 납부하여야 합니다.
※ 납부자번호 : 0131(기관코드) + 접수번호

3. 귀하의 주소, 연락처 등의 변경사항이 있을 경우, 즉시 [특허고객번호 정보변경(경정), 정정신고서]를 제출하여야 출원 이후의 각종 통지서를 정상적으로 받을 수 있습니다.
※ 특허로(patent.go.kr) 접속 > 민원서식다운로드 > 특허법 시행규칙 별지 제5호 서식

4. 특허(실용신안등록)출원은 명세서 또는 도면의 보정이 필요한 경우, 등록결정 이전 또는 의견서 제출기간 이내에 출원서에 최초로 첨부된 명세서 또는 도면에 기재된 사항의 범위 안에서 보정할 수 있습니다.

5. 외국으로 출원하고자 하는 경우 PCT 제도(특허·실용신안)나 마드리드 제도(상표)를 이용할 수 있습니다. 국내출원일을 외국에서 인정받고자 하는 경우에는 국내출원일로부터 일정한 기간 내에 외국에 출원하여야 우선권을 인정받을 수 있습니다.
※ 제도 안내 : http://www.kipo.go.kr-특허마당-PCT/마드리드
※ 우선권 인정기간 : 특허·실용신안은 12개월, 상표·디자인은 6개월 이내
※ 미국특허상표청의 선출원을 기초로 우리나라에 우선권주장출원 시, 선출원이 미공개상태이면, 우선일로부터 16개월 이내에 미국특허상표청에 [전자적교환허가서(PTO/SB/39)]를 제출하거나 우리나라에 우선권 증명서류를 제출하여야 합니다.

6. 본 출원사실을 외부에 표시하고자 하는 경우에는 아래와 같이 하여야 하며, 이를 위반할 경우 관련법령에 따라 처벌을 받을 수 있습니다.
※ 특허출원 10-2010-0000000, 상표등록출원 40-2010-0000000

7. 종업원이 직무수행과정에서 개발한 발명을 사용자(기업)가 명확하게 승계하지 않은 경우, 특허법 제62조에 따라 심사단계에서 특허거절결정되거나 특허법 제133조에 따라 등록이후에 특허무효사유가 될 수 있습니다.

부록 5.

인력양성

제 C - 7327 호

학 위 수 여 증 명 서

성 명 :	PHAM THAI HOAN
생 년 월 일 :	1983 년 3 월 21 일
학 위 과 정 :	박사과정
소 속 :	대학원
학 과 (전 공) :	건설환경공학과(구조공학)
학위수여일자 :	2015 년 8 월 21 일
학 위 명 :	공학박사
학위등록번호 :	세종대`14(박)087호

위 의 사 실 을 증 명 함.

2016 년 5 월 18 일

세 종 대 학 교 교 무 처 장

* 본 증명서는 자동발급기에서 발급된 것이며, 직인이 없으면 무효임.

세종대학교 SEJONG UNIVERSITY COPY

국문초록

나노압입을 이용한 구조용 강재 용접부의 미세구조 성분과 기계적 특성 연구

세종대학교 대학원

건설환경공학과

Pham Thai Hoan

본 논문에서 제시된 연구의 목적은 나노압입을 사용한 강재의 용접 영역에서 미세구조 구성성분과 기계적 특성을 연구하기 위함이다. 이 논문의 연구는 네 개의 부분으로 구성하였다.

첫 번째로, 강재 SS400 (0.05 wt.% C)의 용접부에 존재하는 미세구조는 나노압입 구성성분 및 광학 현미경을 사용하여 분석한다. 용접부에서 서로 다른 세 곳에 위치한 모재 (BM), 열영향부 (HAZ), 용접재료 (WM)에서 백점 만점으로 점수를 주었다. 마이크로 구조체의 특성으로서 나노압입시험으로부터 얻어지는 기계적 특성을 고려하여, 분해 기법을 이용한 통계적 분석은 미세구조와 BM, HAZ, 및 WM에서 대응하는 부피비를 확인하기 위해서 적용된다. 광학 현미경 관찰과 및 나노압입시험 결과로부터

강재내의 미세구조는 고강도 및 저강도 페리트 (ferrite) 인 두가지 유형을 기계적으로 특징지을 수 있다.

두 번째로는, 나노압입 및 광학 현미경 검사는 강재 (SM490) 용접부에 탄소성 성질의 미세구조 구성성분을 조사하기 위해서 수행된다. 또한, 세 개의 다른 용접부 영역인 BM, HAZ, WM에서 나인그리드 (Nine grid) 실험의 121개 지점에 압입이 가해진다. 각 위치에 121개 나노압입시험 결과의 통계적 분석을 이용하여, 미세구조 구성성분 및 개별 용접부에 대응하는 부피비가 확인된다. 세 가지 미세구조 단계인 BM, HAZ, 그리고 WM은 다른 기계적 성질을 가진 저강성 페리트 (ferrite), 고강성 페리트 (ferrite) 그리고 펄라이트 (pearlite)로 구성된다. 구조해석 응용프로그램을 통해 분해 통계적 분석의 정확성을 확인한다.

세 번째 부분에서는, 압입시험의 하중-압입깊이 곡선으로부터, 소성영역을 비롯한 구조용 강재의 구성방정식을 추정 할 수 있는 새로운 방법을 개발하였다. 강재의 구성적 특성과 깊이곡선에서 압입하중의 특성 사이에 두 가지 무차원의 관계가 도출된다. 나노압입 시뮬레이션을 위한 유한요소모델을 개발하고 강재의 구성적 특성들의 576개 조합을 위한 FE 분석을 수행하였다. 무차원 관계는 FE 결과의 회귀 분석에 의한 다항방정식에 의해서 수립된다. 나노압입과 일축인장압축시험은 FE 모델과 제안된 방정식을 확인하기 위해 수행된다.

마지막으로, 두 개의 강재 SM490과 SS400의 용접부에 대한 기계적 특성은 압입실험, 인장시험, 유한요소(FE) 분석 및 광학 현미경 관찰을 통해 연구되었다. 용접부에 대한 기계적 특성(E, H, σ_y, and n)은 FE 분석을 통해 제안된 방법을 적용한 압입시험 결과로부터 결정된다. 강재시편과 용접시편의 인장시험과 용접부의 등가 탄성계수는 모재 (BM), 열영향부 (HAZ), 용접재료(WM)의 복합적인 작용으로부터 해석된다. 두 강재 용접부의 경우, 용접재료(WM)은 가장 높은 기계적 특성(E, H, σ_y, and

n)의 값을 갖고, 용접재료(WM)에서 모재 (BM)영역 까지 열영향부 (HAZ)내의 기계적 성질이 서서히 감소하는 동안 모재(BM)는 가장 낮은 기계적 특성의 값을 갖는다.

주요어: 나노압입, 구조용 강재, 용접부, 미세구조 구성성분, 기계적 특성, 유한요소해석.

ACKNOWLEDGEMENTS

I wish to express my profound gratitude and sincere respect to my advisor, Prof. Seung-Eock Kim, for his invaluable suggestions, continuous guidance, and enormous support throughout my doctoral studies. The professional knowledge, scientific research method, and especially the kindness from him helped me not only having a lot of confidence to accomplish this dissertation but also improving myself much.

I appreciate all professors in the Dept. of Civil and Environmental Engineering, Sejong University for their enthusiastic instructions and valuable lectures. I am grateful to Prof. Jung J. Kim for his kind guidance and suggestions to this research topic. I also greatly appreciate the dissertation committee members, Profs. Hyuk Chun Noh, Dong Joo Kim, Ki Buem Kim, and Jung J. Kim, for reviewing and giving constructive comments on my thesis.

I would like to thank friends in Bridge and Steel Structure Laboratory at Sejong University for their close friendship and kind assistance. Special thanks to Dr. Duc-Kien Thai for his recommendation of the great trip in South Korea. Many thanks to Vietnamese friends who have been studying and working at Sejong University, for their lofty sentiments and enthusiastic help during the period of overseas study.

Finally, I express my deep gratitude to my family, especially my parents and my wife, for their understanding, encouragement, support, and boundless love. I dedicate this dissertation to my venerable parents, my beloved wife Ha-Hien, and my lovely children Thai-Hung and Bao-Han.

Seoul, June 2015

Pham Thai Hoan

주의

1. 이 최종보고서는 국토교통부에서 시행한 국토교통기술촉진연구사업의 연구보고서입니다.

2. 이 최종보고서 내용을 발표하는 때에는 반드시 국토교통부에서 시행한 사업의 연구개발 성과임을 밝혀야 합니다.

3. 국가과학기술 기밀 유지에 필요한 내용은 대외적으로 발표 또는 공개하여서는 안 됩니다.